SAPIENZA
UNIVERSITÀ DI ROMA

Numerical Modelling of F-Actin Bundles Interacting with Cell Membranes

Scuola di Dottorato in Fisica "Vito Volterra"

Dottorato di Ricerca in Fisica – XXXI Ciclo

Candidate

Alessia Perilli

ID number 1698086

Thesis Advisors

Prof. A. Pelissetto

Prof. C. Pierleoni

A thesis submitted in partial fulfillment of the requirements for the degree of Doctor of Philosophy in Physics

30 October 2018

Numerical Modelling of F-Actin Bundles Interacting with Cell Membranes
Ph.D. thesis. Sapienza – University of Rome

This thesis has been typeset by LaTeX and the Sapthesis class.

Author's email: alessia.perilli@roma1.infn.it

Contents

Papers by the author related to this thesis:

Filament flexibility enhances power transduction of F-actin bundles.
A. Perilli, C. Pierleoni and J.-P. Ryckaert
arXiv:1806.08767v2 [physics.bio-ph]

On the force-velocity relationship of a bundle of rigid bio-filaments.
A. Perilli, C. Pierleoni, G. Ciccotti and J.-P. Ryckaert
The Journal of Chemical Physics **148**, 095101 (2018); doi: 10.1063/1.5001124

On the properties of a bundle of flexible actin filaments in an optical trap.
A. Perilli, C. Pierleoni, G. Ciccotti and J.-P. Ryckaert
The Journal of Chemical Physics **144**, 245102 (2016); doi: 10.1063/1.4954186

Introduction

Answering questions about the fundamental mechanisms that underlie *life* has always aroused mankind's curiosity – and physicists have started turning their heads to the subject as well. Indeed, physics of living systems, or biophysics, is becoming one of the most popular branches of nowadays physics research, with areas of focus ranging across many scales, from structural organization of polymers, to cells dynamics, to collective behaviors of populations (both animal and vegetable). On the cell scale, a fundamental question that has been risen is: *how do cells move?* Because indeed cells move. Tissues are made of thousands cells that do not form a fixed matrix; they crawl, swim, divide, eat. For instance, cell motion in wound healing is essential for a correct restoration of the tissue, while in cancer development it can lead to fatal metastases. What's the motor of these activities? The first model explaining the dynamics of muscle contraction has been formulated in 1954 [1, 2], explaining it through the relative sliding of two types of filaments ("thick" and "thin") dating the beginning of a scientific understanding of the subcellular mechanisms underlying cell motility. In the latest decades, technological progress allowed for increasingly accurate *in-vitro* reconstitution of living systems, where the number of involved actors can be kept under control. It is now well acknowledged that the main responsible for cell motion is *actin*, one of the most abundant proteins in all eukaryotic cells, main component of the *cytoskeleton* – the system of filamentous proteins that determines the cell's shape ensuring its structural stability, located just beneath the cell membrane. Globular actin monomers (*G-actin*) assemble via physical interactions (and not covalent bonds) to form filaments (*F-actin*), and upon monomer addition an amount of chemical energy is released and in some cases further converted into mechanical work. In general, macromolecules showing this ability to store chemical energy and convert it into mechanical energy are called *molecular motors*. In the case of actin filaments, this energy conversion is employed to drive cellular shape changes: polymerizing actin filaments push the cell membrane and deform it (performing mechanical work) to create temporary structures (*e.g.* filopodia, lamellipodia) that serve for instance as probes to explore the surrounding environment or to drive cell migration. In particular, filopodial protrusions are finger-like protuberances made up of bundles of parallel actin filaments enclosed by the cell membrane, and will be the main subject of this thesis. They usually protrude from a lamellipodium (an actin-rich flat projection at the cell's leading edge), with a velocity depending on the resisting load due to membrane tension and to the crowded environment around the cell [3].

Modeling of filopodium growth has been developed over the last twenty years in different directions. Several attempts to directly model a filopodium protruding

against the membrane resistance have been made, *e.g.* in [4] establishing conditions for its onset and size limitations due to actin bundle buckling or to the diffusion of G-actin monomers to the tip. Besides, a more handy approach has been popularly chosen to study the relationship between polymerization forces and the underlying elementary biochemical processes, which is to idealize the cell membrane as a rigid wall, overlooking the membrane elastic response and focusing on the mechanisms and collective strategies put in place by actin filaments to optimize the transduction of chemical into mechanical energy. In addition, the most popular models for the polymerization forces consider *rigid* filaments growing against a rigid obstacle, ruling out filament flexibility as well. The central quantities of interest in these models are typically two: the first is the maximum force that a filament or a bundle of filaments can exert by polymerization, or equivalently the maximum force that they can sustain before stopping their growth, called the *stalling force*. The second is the velocity at which the obstacle (wall) moves under the combined action of the pushing filaments and of an external load, as a function of the applied load, which is the *velocity-load relationship*. Several models for rigid filaments have been developed to give a prediction for these quantities, and two of them will be considered as reference models along this thesis: the *Mean-Field* model [5] and the *Brownian Ratchet* model [6–8]. A fundamental difference between the two is how the work is assumed to be (or results to be) shared among the filaments: according to the mean-field model, the work is equally divided among all the filaments (*Perfect Load Sharing* condition) [5]; the brownian ratchet model, on the other hand, can predict situations where either one filament performs work while the others lag behind (*No Work Sharing* condition), when the filament seeds are lined-up at the same distance from the obstacle [8], or where the presence of the other filaments decreases the work to be performed by a filament against the obstacle by polymerizing (*Partial Work Sharing* condition), when the filament seeds are at appropriate staggered distances from the obstacle [6, 7]. The velocity-load relationships resulting from these models are well different from each other: in particular the velocity at given load increases by increasing the level of work sharing. On the other hand, all these models predict the same expression for the stalling force, Eq. (1.9).

Besides, specific in vitro experiments making use of multi-filament bundles growing against rigid smooth obstacles have been designed [9–12] to directly measure the stalling force or the velocity-load relationship. In particular, an attempt to directly measure the stalling force of an actin bundle was performed in reference [10] by following the relaxation of an actin bundle in an optical trap device, where the filaments growth is opposed by a harmonic force. The bundle was observed to grow displacing the rigid obstacle up to a final trap amplitude corresponding to stalling conditions; at equilibrium, the polymerization force equals the trap restoring force, and hence a measure of the trap amplitude leads to measure the stalling force. Unexpectedly, the force to stall a bundles of 8-10 filaments was found to be slightly larger than the force required to stall a single filament, according to the theoretical predictions. Today the origin of this discrepancy remains unexplained, despite attempts to include hydrolysis of actin-ATP complexes integrated in filaments in the brownian ratchet model framework [13].

The central point of this thesis, and its novelty as well, is the investigation of the *effects of filament flexibility*, overlooked so far, on the static and dynamic

properties of bundles growing against a resisting obstacle, which can be a rigid wall or a flexible membrane. It can be noted that so far, in using rigid filament models, the non rigid character of pushing actin filaments was taken into account indirectly only, by avoiding in *in-vitro* experiments to deal with experimental conditions where manifestation of filament flexibility could become relevant. Anticipating the following, filament flexibility will be shown to have a significant impact on the resulting dynamical properties of the bundles: flexible filaments appear to be more efficient than rigid ones in the power transduction from chemical to mechanical, then improving the level of work sharing in the bundle. A side-effect, relevant only in the case of rigid smooth obstacles though, is that filaments growing too long against a wall have a finite probability to undergo large bending fluctuations leading to an irreversible lateral escape: *escaping* filaments start growing parallel to the obstacle, decoupling their growth from the presence of the load and not pushing it anymore by polymerization. This scenario, which is an exclusive feature of filaments growing in slit pores with no lateral constraints, could have indeed influenced the outcome of the unexplained experiment [10].

This thesis is divided in two parts. The first part will be focused on models of filaments growing against rigid obstacles, referring to a limited – yet relevant – set of experimental and theoretical conditions. Chapter 1 provides an introductory overview of the subject, presenting the reference models for rigid filaments and some of the experiments performed to measure the stalling force and the velocity-load relationship. In Chapter 2 the statistical mechanics framework of bundles of flexible filaments growing in an optical trap set up, mimicking the experimental conditions of ref. [10], will be built and results on their equilibrium properties will be presented. These results will provide a further validation of the popular expression for the stalling force given by the previous models (*i.e.* mean-field and brownian ratchet), which results valid also for flexible filaments within differences of few percents. Here, the issue of escaping filaments is discussed and precise conditions on the trap strength, determining the trap amplitude (and hence the bundle length) at equilibrium, to avoid the escaping regime will be given. Chapter 3 is focused on the non-equilibrium dynamics of bundles in optical trap: the time evolution of the system is reformulated through a Markovian description, particularly suitable for numerical realizations of the process, and stochastic dynamics simulations are performed using a classical Gillespie algorithm [19]. First, we show that the velocity-load relationship, which is usually obtained using a constant external load exerted on the obstacle, can be equivalently and more efficiently obtained using an optical trap set up, thanks to a wide timescales separation between the wall relaxation and the (de)polymerization events: the load change results to be very slow compared to both the time interval between two (de)polymerization events and the time needed by the filaments to relax afterwards, implying that on the short timescale the filaments feel a load which is essentially constant. The velocity-load relationship for a flexible bundle will be generalized to include the bundle degree of flexibility, λ, defined as the ratio of the filaments contour length over a threshold bundle characteristic length beyond which flexibility effects become detectable. We will show that flexibility considerably enriches the theoretical scenario filling the gap between the multi-filaments brownian ratchet model [6, 7] and the classical mean field Perfect Load Sharing condition [5]: for $\lambda \leq 1$ the behavior is essentially rigid, for $\lambda > 1$ flexibility effects manifest as an

enhancement of the power of transduction of chemical into mechanical energy, as a result of an improved level of work sharing among the filaments. The Perfect Load Sharing condition, though, remains an unreachable upper limit because of the onset of escaping filaments.

The second part of this thesis will deal with actin filaments growing against a cell membrane, with the purpose of generalizing the above models to more realistic situations, in particular the formation of filopodial protrusions in living cells or in *in-vitro* recostitutions on GUV (Giant Unilamellar Vesicles). In such situations, filaments employ the transduction of chemical energy into mechanical to deform a flexible membrane, instead of pushing and displacing a rigid obstacle. Chapter 4 will present an introduction to the subject of *biomembranes*, phospholipid bilayers behaving as quasi-2D fluids, where lipids can diffuse laterally, and embedding the cell cytoskeleton. The chapter will conclude with the aforementioned popular model [4] that has been a pioneering attempt to mathematically model filopodial protrusions. Chapter 5 will be focused on the elastic properties of biomembranes, which are fundamental to understand how they oppose to the deformations induced by the growth of the underlying pushing filaments. First, a simple continuum model will be introduced to describe membrane deformations and the related energy variations, then a differential geometry approach will be followed, within which the most popular Helfrich theory [14] for the membrane bending energy in terms of the membrane principal curvatures shall be discussed. In this chapter three different methods will be presented to calculate the membrane surface tension, an important quantity to determine the membrane elastic response to external deforming forces. The first route to the surface tension is via the analysis of the height fluctuations of a flat membrane at equilibrium, making use of the Helfrich free energy [14,65]; the second is by a virial expression relating the surface tension to the forces acting between the membrane constituents [95]; the last one is by a relationship between the radius of a tubular protrusion pulled out of the membrane and its elastic coefficients [105]. Chapter 6 will present the numerical model of the membrane that has been developed to perform simulations of the membrane+filaments system: in particular, the membrane will be described as a network of beads which are connected by bonds (tethers) to form a triangular network (*triangulated surface model* [15–18]). These vertices are also subject to excluded volume interactions and the curvature energy is discretized based on the angles between the neighboring triangle faces. Filaments, on the other hand, are modeled again as discrete wormlike chains with the number of monomers changing in time by adding or removing subunits, with explicit bonding, bending and excluded volume interactions between them. The time evolution of the system will be simulated via a Molecular Dynamics approach, numerically integrating the Langevin equations that are assumed to describe its dynamics. A popular method to model the fluidity of the membrane is to introduce a Monte Carlo procedure by which bonds are flipped to the diagonal of two adjacent triangles [15–18] (see Fig. 6.4); this method will be shown to correctly reproduce the fluid-like behavior by analyzing the beads mean square displacement in the long time limit. Moreover, in order to allow for membrane deformations, Grand-Canonical Monte Carlo insertion/deletion moves are introduced in the algorithm following the pioneering work of ref. [19]: beads are inserted in or deleted from the network using a Monte Carlo procedure such that the surface triangulation remains always valid. Simulations of membranes in absence

of pushing filaments will be exploited to study the membrane surface tension using the aforementioned different methods and the results so obtained will show that the model presented in this thesis can be considered a valid coarse-grained description of this complex system. Finally, the time evolution of the full system (membrane and filaments) will be simulated, with the filaments growing from small sizes, hitting the initially flat membrane and causing its deformation, leading to the onset of a filopodial protrusion (in conditions such that the membrane cannot rigidly shift under the push). The results here presented are preliminary only, and the model is based on assumptions (namely a sufficiently wide timescale separation between the membrane relaxation and the filament (de)polymerizations – the membrane is considered always at equilibrium between two chemical events) which still need to be verified deeply. Once validated, though, this model could be exploited to produce simulations of this complex system with remarkable efficiency and extract informations on the dynamics of the system otherwise inaccessible. Moreover, it could be easily enriched with known mechanisms – like free monomer diffusion, length-dependent free monomer density or filaments lateral branching – and hence made more realistic.

Part I

Actin Filaments

Chapter 1

Cytoskeletal filaments and polymerization forces

...the elegance and robustness of biological systems never cease to amaze me. Exciting opportunities await those willing to embrace the challenge of learning a new field and applying the experimental and analytical tools of physical science to biological questions. Quantitative biology is alive and growing, and the potential impacts on health, disease, and technology are enormous. There is no time like the present to peer into the microscope and see what's crawling by.

D. A. Fletcher

The difference between active (or living) and passive (or non-living) matter is commonly pictured as related to the ability of the first to generate directed, purposeful motion. Any living organism – even those who seem immobile for long times, like plants – experiences a constant self-organized motion at cellular level: cells do not form a passive interconnected matrix, but they crawl, swim, slide, change shape, divide. A very familiar example of cell's shape change is the contraction of muscle cells; a less familiar but very important example of cellular activity is the locomotion of macrophages who chase, capture and remove hostile cells and material from the surrounding environment. Most of these cellular activities are related to that of the cytoskeletal proteins, which have the capability to convert chemical energy into mechanical work. In particular, in many cases the chemical energy to be converted into mechanical work comes from the (de)polymerization (growth and shrinking) of cytoskeletal filaments, and the forces arising in this process are referred to as polymerization forces*.*

In this introductive chapter, a (simplified) description of the cytoskeleton will be provided in Section 1.1, introducing the most important processes driven by actin polymerization forces – lamellipodial and filopodial protrusions in particular. Section 1.2 will be devoted to the experiments which in the last few decades have aimed to directly measure the polymerization forces, and finally in Section 1.3 the most popular modeling approaches to quantitatively interpret the phenomenon (Mean

Field [5] and Brownian Ratchet model [6, 7]) will be reviewed; these models will be deemed reference models all along the first part of the thesis.

1.1 The Cytoskeleton

The number of cells in a human body largely exceeds the number of stars in the Milky Way, yet not so many varieties of cells exist: only about 200 cell types for about 10^4 total cells in our body [20]. These kinds of cell differ by their functions and capabilities and by their shape: some cells are spherical (like certain varieties of bacteria), some cylindrical (like the baterium *E. coli*), some are elongated with extended branched structures (like neurons), some adopt a biconcave shape (like red blood cells). Notwithstanding, the basic structure of the cell is roughly the same for all of them: a soft, fluid lipid bilayer (the *cell* or *plasma membrane*) encloses the whole cell and divides it from the external environment, and a network of filamentous proteins (the *cytoskeleton*) ensures the needed rigidity, regulates the cell shape, exerts forces and produces motion.

The cytoskeletal filaments are in general linear structures, which spontaneously assemble from globular protein monomers, by binding to each other through weak non-covalent bonds. There are three types of cytoskeletal filaments: *microtubules*, *intermediate filaments* and *actin filaments* (or *microfilaments*). They are usually classified with respect to their thickness, but they also differ by their stiffness, which can be quantitatively given in terms of a unique parameter: the *persistence length*, ℓ_p, which can be defined as the polymer contour length beyond which the orientational correlation is lost[1]. These three types of cytoskeletal filaments have also different structures and functions, in particular:

Microtubules are stiff hollow cylindrical structures, with persistence lengths in the range 100 μm–6 mm [21]; they are also the thickest, with a diameter of about 25 nm, and they are made of 13 adjacent protofilaments, which in turn are made up of a sequence of tubulin dimers (see Fig. 1.1a, top). Microtubules are *polar*, i.e. their two ends are not equivalent: the *plus end* or *barbed end* exhibits a large frequency of dimers binding (*polymerization rate*), while at the the *minus end* or *pointed end* the detachment of dimers occurs with a rate similar to or higher than attachment, resulting in a slowly growing or shrinking tail. This polarity allows microtubules to move by *treadmilling*: in this process, the pointed end adds dimers at the same rate at which the barbed end looses them, so that the total length of the microtubule stays the same while its center of mass moves in the direction of the plus end. Microtubules are also able to exert relevant pushing forces: during mitosis, for instance, they polymerize forming a temporary structure that catches the chromosomes and push them in opposite directions in the dividing cell [20, 22].

Intermediate filaments (Fig. 1.1a, middle) are the most flexible of all cytoskeletal filaments ($\ell_p \simeq 0.3 \div 1.0$ μm) while they are intermediate in diameter (8 to 12 nm) [23]. There are several classes of intermediate filaments (like *keratin* or *neurofilaments*), and different types belong to different cells. They are not

[1] See Chapter 2 for a precise definition of ℓ_p.

polar, and thus they do not treadmill, and their main role is then thought to be related to structural and elastic properties of the cell, but they do not enter into cellular motility and dynamics.

Actin filaments are the principal constituents of the cytoskeleton, actin being the most abundant protein in all eukaryotic cells, and one of the most highly conserved: this means that it has changed very little throughout evolution – suffice it to say that our actin differs by no more than 20% from that of algae, for instance. Actin filaments (Fig. 1.1a, bottom) are made of two interwoven protofilaments and are the thinnest, with a typical diameter of 7 nm [23] – they are also called *microfilaments* – but they have an intermediate persistence length ($\ell_p \simeq 15 \div 17$ μm). Their subunits are globular-actin monomers (or G-actin) which are polar by nature, because of their asymmetric structure, and this lets actin filaments treadmill. These globular subunits contain ATP (adenosine triphosphate) which hydrolyzes into ADP (adenosine diphosphate) after polymerization; this hydrolysis implies an energy release and determines a weakening of the polymeric bonds, making depolymerization easier. Moreover, actin filaments can use this energy release due to polymerization to produce forces which are not only very significant, but also a key player in cellular motility: they are involved in many processes happening in the cell, like division, fertilization or crawling motion.

These three filament types organize themselves in separate structures, with different typical arrangements. In particular, microtubules radiate across the cell volume from the microtubule-organizing center, the site where microtubule formation begins and free-ends of microtubules attract to; intermediate filaments extend from a ring surrounding the nucleus to the plasma membrane and are associated with cell attachment sites; actin microfilaments are highly concentrated at the periphery of the cell where they form a three-dimensional network just beneath the membrane. Besides, the cytoskeleton must be able to rapidly adapt to external stimuli or environmental changes – like red blood cells passing through capillaries which are narrower than the cells themselves (in their rest disc shape): they have to deform to fit through these vessels. The cytoskeleton has therefore evolved into a highly dynamic structure: its filaments constantly grow and shrink, associate and dissociate each other via linking auxiliary proteins, or form temporary structures beneath the membrane [23]. Individual actin filaments, in particular, can switch between two structures, bundles and networks, which play different roles in the cell. In bundles, which can be extensile or contractile, actin filaments are cross-linked into closely packed parallel arrays. Extensile bundles can create fingerlike protrusions of the plasma membrane, such as intestinal microvilli. Contractile bundles are involved in processes like cellular division during mitosis, when they form the so called contractile ring. Conversely, actin filaments in networks are loosely crosslinked in orthogonal arrays that form three-dimensional meshworks with the properties of semisolid gels. When needed, filaments from the network can be recruited to bundle with others and protrude beneath the membrane, or they can form flat, quasi-2D, structures extending at the leading edge of a crawling cell (see Fig. 1.1b): a cyclic repetition of leading-edge-protrusion and rear-retraction lets the cell move forward. The actin-rich finger-like protrusions beneath the membrane are called

filopodia (plural of *filopodium*), the flat structures are called *lamellipodia* (plural of *lamellipodium*).

The key of all these activities carried by microfilaments is *polymerization* (and *depolymerization*), i.e. the linear assembly (and disassembly) of subunits via physical interactions, as mentioned above. The energy gained in (de)polymerizing can than be converted into purposeful mechanical work (*e.g.* the membrane deformation during crawling motion, a bacterium being pushed away, or the split of the two newborn cells during cytokinesis in cell division).

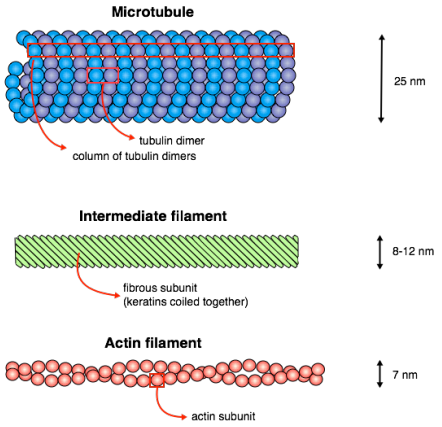

(a) Schematic representation of the three kinds of cytoskeletal filaments: from top down, (i) a microtubule, where a tubulin dimer is indicated, (ii) an intermediate filament, with the keratin subunit indicated, and (iii) an actin filament, with an actin monomer indicated. For every case, the typical thickness is also shown.

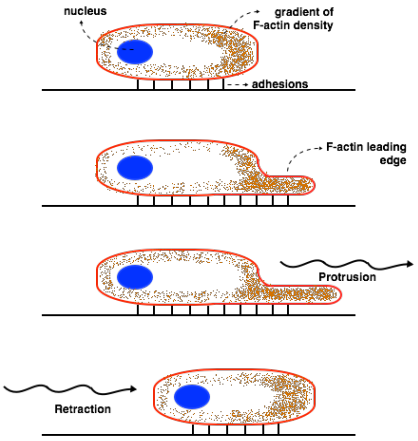

(b) Schematic of a crawling cell. Actin filaments gather in the front of the cell with the plus ends facing the direction of motion, and by polymerization produce protrusive forces. The cell moves by using cycles of leading-edge protrusion, establishment of new adhesions to the substrate, deadhesion and actin-myosin-dependent retraction of the rear of the cell.

Figure 1.1

In real tissues, by the way, cellular motility is the result of many processes involving a possibly large number of actors, including secondary or auxiliary proteins, each with a specific task: a very important family of these are the *motor proteins* (*myosin*, *kinesin* and *dynesin*) which are able to convert chemical energy, usually stored in high-energy chemical bonds or transmembrane proton gradient, into mechanical work, walking along the cytoskeletal tracks [24]. The mechanisms regulating the mutual action of actin filaments and myosin, for instance, have been intensively studied and modelled, and for long time it has been thought that actin and myosin had to work necessarily together to produce motion. It is now known that many kinds of movement or the production of forces at the cellular level do not require motor proteins, being based on the solely polymerization-depolymerization mechanism of microtubules and actin filaments [24]: in the following, I will focus on the so-called *polymerization forces*, which are the forces generated exclusively by

polymerization.

1.1.1 Cellular motility and polymerization forces

The common belief that myosin was fundamental to cell motility came from the fact that for long time the most studied form of actin-dependent movement had been skeletal muscle contraction, where the energy conversion from chemical to mechanical is obtained through ATP hydrolysis by myosin. During the 70's, the observation of non-muscle myosin in crawling cells led to the assumption that myosin produced the forces needed to crawl [25]. After 1987, however, this assumption had to be rejected since it had been observed that *Dictyostelium* amoebae, which failed to express the native myosin, nonetheless exhibited many forms of cell movement [26]. Later, it had been observed [27] that actin filaments polymerizing inside a lipid vesicle could deform it both in presence and in absence of various actin-binding proteins. It is now accepted that actin or microtubule polymerization rather than myosin ATP hydrolysis provides pushing forces, while contractile forces appear to be dependent on myosin motor activity [28]. Nowadays, a quite large number of motility-related processes is known to be led by actin polymerization, from embryonic development, wound healing, immune response and tissues development [29]. Fertilization, for instance, appears to be driven by polymerizing actin filaments. Much studied is the case of the sea cucumber *Thyone*: once the sperm cell has reached the egg, it produces an acrosomal protrusion[2] made of fast polymerizing actin filaments enclosed by the membrane. This lets the sperm fuse with the egg membrane and accomplish the fertilization process [24, 30]. Similarly, the unicellular biflagellated alga *Chlamydomonas* fulfils fertilization via a membrane protrusion (the so-called *fertilization tubule*) filled by actin, which resembles the *Thyone* acrosomal protrusion [24, 31], and by which they attach and fuse with the mating cell's membrane. Actin polymerization appears to be the leading process also in cellular crawling motion, as mentioned above. In general, cells crawling on a substrate present a gradient of F-actin concentration along the cytoskeleton, with larger density in the part of the cell pointing towards the direction of motion: there, the cell protrudes a *lamellipodium* beyond which new adhesion points to the substrate are created, and then it undergoes a phase of de-adhesion and rear retraction[3] (see Fig. 1.1b). The periodic repetition of this scheme makes the cell crawl. Techniques like electron and immunofluorescence microscopy [32] or fluorescence photoactivation [33, 34] have allowed to monitor the movement and the growth of labelled actin filaments in crawling cells with a remarkable accuracy: it has been observed that in fish epithelial keratocytes – among the most motile cells known – actin microfilaments did not move with respect to the cell substratum, nor slide across one another (as happens in contraction with myosin), but they propelled the leading edge of the cell by rapid polymerization [34].

In the last decades, the ability to perform experiments on *in vitro* reconstituted systems with a controlled number of purified proteins allowed to identify the actors involved in the cell motility with increasing precision. Much of what we know about cell motility indeed comes from reconstituted *in vitro* experiments on bacteria like *Listeria monocytogenes* and *Shigella flexneri* [35], which can move inside a

[2] The *acrosome* is a cap-like organelle covering half of the head of the spermatozoa.
[3] The retraction mechanism is related to the myosin action, as said above.

host infected cell by protruding actin-reach comet tails: using pure components of the actin cytoskeleton to reconstitute sustained movement in those bacteria [35] allowed to claim that propulsion in *Lysteria* and *Shigella* is actin-based, and does not require myosin. It is now recognized that not only bacteria, but also viruses [36, 37], endosomes [38] and endogenous vesicles [39] employ actin polymerization for intracellular motility.

The experimental techniques developed in the last two decades have allowed not only to observe the correlation between actin polymerization and propulsion of the leading edge in crawling cells, but also to directly measure the force that a bundle of filaments can exert or the velocity at which an obstacle is pushed by the polymerization of few actin filaments. In the next section I will review some of the experiments aimed to the direct measurement of the polymerization forces.

1.2 Measuring the polymerization forces

In the beginning of the 90's it was then accepted that assembly and disassembly of cytoskeletal filaments (actin filaments and microtubules) can produce forces which are relevant for cellular motility. One of the questions related to the phenomenon which arose in the following years was the maximum amount of force that could be generated by a microfilament or a microtubule: this is called the *stalling force*, because an external force, opposite to the growth direction, with the same intensity, would cause the filament to stall. It is worth remarking again that the polymerization force is the force related to the solely polymerization mechanism, and so if a filament is pushed with a force large enough, it will stop polymerizing. If a growing filament faces an obstacle which responds with a force smaller than the stalling force, its polymerization can make the obstacle move with a certain velocity; this velocity, which is roughly the same as the filament's growth velocity, depends on the force that the obstacle is opposing to the filaments' growth. The entire curve v vs F constitutes the *velocity-load relationship*, one of the main concept used to understand the phenomenon of polymerization forces.

In the following subsections some of the experiments aimed to the direct measurement of the polymerization forces or the velocity-load relationship will be reviewed.

1.2.1 Experiments on microtubules

In 1997 the stalling force of a single microtubule has been measured for the first time [9] using an experimental system in which growing microtubules were made to push against an immobile barrier: glass coverslips were etched with long channels, and the walls of such channels acted as barriers. Short microtubule seeds were attached to the channels and let grow. Of all the random growth directions only those roughly perpendicular to the walls were taken into account. To calibrate the force measurement, the flexural rigidity of the microtubules was measured using a thermal fluctuations analysis. The force was measured by analyzing the shape of the microtubules obtained by electron microscopy (buckling analysis). Biotin was added to label the microtubules and streptadivin to attach microtubules to the support. The information extracted from the experiment led to the measurement not only of the polymerization force, which resulted to be on the order of 4 pN, but

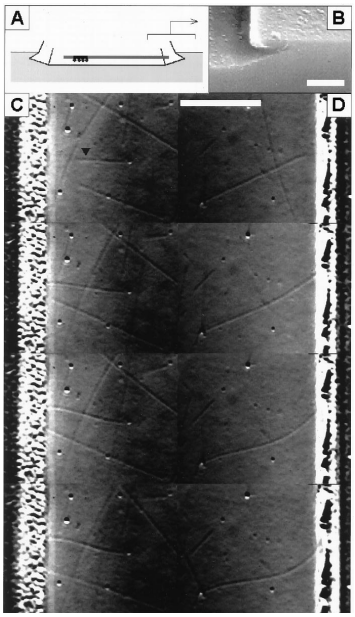

(a) Experimental set up to study the force produced by growing microtubules. (A) Achemati representation of the set-up (side view): the seed, coupled to biotin and attached to the streptadivin-coated substrate, is shown in black; the microtubule is shown in gray. An overhang at the top of the channel was created to prevent the microtubule to bend and grow upwards sliding on the wall. (B) Wall with overhang shown by electron microscopy imaging. (C) A microtubule, indicated by an arrow, starts growing towards the wall, stalled by it. (D) An escaping microtubule: after reaching the wall, its growth goes on parallel to the wall. Scale bar: 10 μm. From [9].

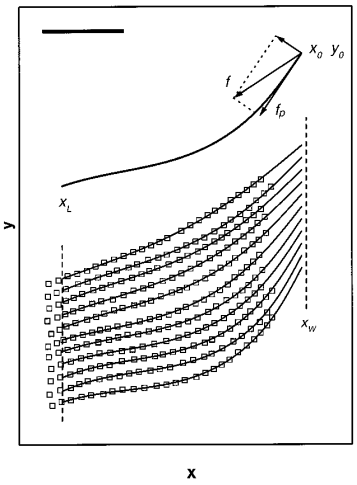

(b) Analysis of the microtubule buckling shape. Open squares show the hand recovered shape of a microtubule while the solid lines represent fits to the shape of an elastic rod. It is assumed that a force f was applied at the contact point of the microtubule with the wall (x_0, y_0). This contact point remained fixed in time and was chosen to produce the best combined fit over the entire time sequence. The magnitude and the direction of the force f at each time point were obtained by these fits. Scale bar: 5 μm. From [9].

Figure 1.2

also of the velocity-load relationship. They found a velocity which decreased as the external force started to act (i.e. when the filaments approached the barrier), and in particular they found a decay which could be well fitted by a decreasing exponential. We shall see in the following section the theoretical predictions and interpretations of this result. Another important observation made by the authors concerned the ways the microtubules could bend to accomodate the growth once they started to feel compressed by the walls. The upwards bending was prevented by the realization of an overhang on the walls of the channels. The growth of some filaments was critically slowed down with their barbed end pivoting around a fixed contact point with the wall. Other filaments, on the contrary, found the way to avoid stalling by sliding along the wall and go on growing unconstrained in a direction roughly

perpendicular to the initial growing direction. These filaments, to which I will refer as *escaping filaments* hereafter, did not exert any polymerization force, since the barbed end was free to grow, and they were discarded from the analysis.

Few years later, in 2003, a new technique has been proposed for the measurement of the pushing forces generated by growing microtubules: the optical trap [40], where forces of the order of the pN can be measured by monitoring the displacement of an object trapped in a harmonic potential. The authors indeed questioned the validity of the buckling analysis performed in [9] to get the stalling force, adding that this method needed the rigidity of the microtubules to be known. This parameter, by the way, required elaborate analysis to be obtained and might depend strongly on the growth conditions. To measure the stalling force, on the contrary, they employed a multiple optical trap with a pair of beads biochemically connected to a microtubule segment, trapped by an asymmetric "keyhole" shaped potential: fast time sharing of the laser beam was used to trap one bead tightly, while the other bead was only kept perpendicular to the pushing direction. This would prevent the microtubules to slide and escape. With this method, they measured the force as time passed and observed a steep rise corresponding to a maximum value of 1.2 ± 0.2 pN. Besides, to get the stalling force they didn't use the keyhole trap but a stiffened bundle of ~ 20 cross-linked microtubules, held by two trapped beads in front of a fixed barrier, at ~ 5 μm from it. Only one of the two beads was tightly connected to the bundle and the displacement of this bead was monitored to measure the force on it. They observed two sharp jumps, followed by two distinct plateaus, in the force as a function of time: they were interpreted as the effect of two microtubules of the bundle coming subsequently in contact with the barrier. They constructed the velocity-load relationship from the force and the displacement observed and they extracted two stall forces at ~ 1.2 pN and ~ 3 pN for the single- and double-microtubule case respectively. The authors ended by envisioning the possibility to use the same experimental apparatus for analogous measurements on single actin filaments.

1.2.2 Experiments on actin filaments

In the last two decades much effort had been made in understanding and setting the theoretical basis of the origin of the forces generated by actin polymerization, while experimental progress lagged behind. There had been some attempt to directly measure the force generated by actin networks [41, 42], from which however it cannot be extrapolated the force generated by a single filament [10], and only one published measurement on a single actin filament [43]: in this latter experiment they used evanescent wave fluorescence microscopy to observe assembly of actin filaments which were polymerized on slides preincubated with formin and myosin to attach both the barbed and the pointed ends of the filament to the substrate. The force was extrapolated observing the bending profile of the filament as it grew and bent between the adhesion points, giving an estimate force per filament equal (at least) to 1.3 pN[4] in condition where 2 pN were expected from theoretical predictions. This experiment, however, didn't allow to obtain important information on e.g. the dependence of the growth velocity on the external load, or how the filament growth

[4] The experimental design prevented the authors to measure forces larger than 1.3 pN.

approached the stalling situation. Moreover, the barbed end of the filament was clamped by the formin protein, and it was not possible to extrapolate from the outcome the behavior of free-barbed-end filaments.

In 2007 the stalling force of a bundle of few actin filaments was measured using an optical trap set-up [10], as suggested in [40]. In this experiment, a *Limulus* acrosomal bundle of 8-10 filaments was attached to a 1 μm-radius polystyrene bead, which was in turn put in a keyhole optical trap and positioned few nanometers far from a microfabricated barrier. After actin monomers had been introduced into the flow cell, filaments started to grow, pushing the bead away from the wall and from the minimum of the trapping potential. Measuring the displacement of the bead and knowing the strength constant of the trap, the polymerization force could be inferred. The authors used two different trap constants for two different actin monomers concentrations, and in any case they observed a monotonic increase of the bead-wall distance, up to the establishment of a plateau, corresponding to the stalling force. The outcome of this experiment, although, was quite weird: the stalling force that was measured was smaller than what predicted by any known model (see later), much closer to the force predicted by a single filament rather than 8-10. The full understanding of this result is still missing, despite of the several attempts that have been made, as it shall be detailed in the following. Indeed, this unexpected experimental outcome had been the very first inspiration of the present work.

The last experiment I shall present in this section has been performed in 2014, with the goal of measuring the velocity-load relationship for a bundle of actin filaments [12]. The experimental setup was made up of supermagnetic beads, which were meant as a tool to simultaneously manipulate actin filaments, apply forces to them and measure their reaction to the external load. Some of the beads were coated with gelsolin molecules acting as polymerization seeds. The beads were then put in an appropriate magnetic field which induced a magnetic dipole on them and kept them organized in chains, attracting each other. Also formins were introduced in the system to provide a stiffening of the bundles and make them grow radially from the surface of the spheres. As filaments started growing, they pushed and separated the beads against the (constant) magnetic force. The authors measured the bead-to-bead distance, increasing with time, and from this they could measure the bundle growth velocity. Note that each (v, F) data point was obtained through a single experiment at some value of the external force, and to get a different point a new experiment at a different value of the external force had to be performed. This implies issues related to the reproducibility of the experiment, and in order to get reliable data, they checked that no reorganization or damage occurred when applying the magnetic field. Along with this experimental work, a theoretical interpretation was provided, as I shall detail in the following section. The authors analyzed the power of transduction of the chemical energy into mechanical work, and they tried to interpret the observed maximum power in terms of the number of filaments pushing the bead. Interestingly, they suggested that the actin machinery in cells responds to the external forces by tuning appropriately the number of filaments at the leading edge.

In the next section, the modelling approach that has been adopted to describe the phenomenon of polymerization forces, and the experimental results briefly reported so far will be reconsidered and interpreted within these models.

1.3 Modelling the polymerization forces

Actin filaments, as well as microtubules, show persistence lengths quite large compared to the typical lengths observed in experiments. For actin, $\ell_p \approx 15\mu$m and the observed length range was $(0.15 \div 0.9)\mu$m in [10] and $(0.25 \div 0.5)\mu$m in [12]. Hence, it can be claimed with good approximation that actin filaments, as well as microtubules, are stiff filaments, and indeed the main models commonly used to describe them are models of fully rigid rods. Here I shall give some common ingredients of these models and some basic notation which will be used throughout the remaining of the thesis.

Let's consider an actin filament in a solution of free monomers, which can be incorporated in the filament by polymerization with a rate U_0 (time rate of monomer capture, with units of $[time]^{-1}$). The rate at which the filament looses monomers by depolymerization is denoted as W_0 (time rate of monomer release). Reasonably, the polymerization rate depends on the free monomer concentration ρ_1, since in absence of available free monomers it is impossible to polymerize. In particular, the number of polymerization events is proportional to the free monomer concentration,

$$U_0 = k_{on}\rho_1 \tag{1.1}$$

where k_{on} is the polymerization rate constant, with units of $[concentration \cdot time]^{-1}$ [20]. Conversely, the depolymerization rate is independent of ρ_1,

$$W_0 = k_{off} \tag{1.2}$$

with k_{off} the depolymerization rate constant, with units of $[time]^{-1}$ [20]. The typical values which are commonly adopted in the literature and will be used in this work are $k_{on} = 11.6\ \mu M^{-1}s^{-1}$ and $k_{off} = 1.4\ s^{-1}$ [20,43][5]. Since the polymerization rate grows with the monomer density while the depolymerization one stays constant, there will be a value of the monomer concentration which makes the two rates identical: this is the *critical concentration*, ρ_{1c}, given by

$$\rho_{1c} = \frac{k_{off}}{k_{on}} \tag{1.3}$$

which is $\rho_{1c} = 0.12\ \mu$M using the aforementioned values for the rates. I will denote the free monomer concentration divided by this value as the *reduced* free monomer concentration, $\hat{\rho}_1 = \rho_1/\rho_{1c} = U_0/W_0$: $\hat{\rho}_1 > 1$ means that the polymerization rate is larger than the depolymerization one and the filament will grow on average; $\hat{\rho}_1 < 1$,

[5] A complete description would take into account the fact that both U_0 and W_0 depend on the state of the attaching or detaching actin monomer: it can be an ATP–monomer or an ADP one, but here I neglect this distinction and make the approximation that an attaching monomer always contains ATP and a detaching monomer always contains ADP. The rates indicated in the text refer to these two states: $U_0 \equiv U_0^{ATP}$ and $W_0 \equiv W_0^{ATP}$.

conversely, implies a polymerization rate smaller than the depolymerization one and a net decrease in the filament length.

When a monomer is added to the filament, its length increases by an amount equal to d_0: in the case of actin filaments, which are made of two strands coiled together, this quantity equals half the diameter of a monomer, which gives $d_0 = 2.7$ nm.

In the following subsections I shall review the most popular and employed models, to which my results will be compared in the next chapters.

1.3.1 Mean Field model

Let's consider a filament with the pointed end anchored to some substrate and the barbed end free to (de)polymerize. There is a difference ΔG between the Gibb's free energy of a free monomer and that of a monomer attached to the filament: if this difference is negative (free energy of the subunit in solution smaller than the free energy of the subunit in the filament), the filament spontaneously elongates by adding monomers to the free end, otherwise it shrinks. These situations corresponds to free monomer concentrations larger and smaller than ρ_{1c} (or equivalently $\hat{\rho}_1 > 1$ and $\hat{\rho}_1 < 1$) respectively. If $\Delta G > 0$ ($\hat{\rho}_1 > 1$), an excess of free energy is released by the polymerization event and this amount of energy can be converted in another form of energy, *e.g.* mechanical work. To see this, let's consider the same anchored filament but in proximity to a mobile barrier to which a force opposite to the growth direction is applied. When the growing end comes in contact with it, the filament can still polymerize as long as it can push the obstacle far away by a step of d_0, the filament incremental size per added monomer. The gain in free energy is now lowered by an amount Fd_0, where F is the magnitude of the applied (compressive) force. However, as long as the overall energy difference is still negative, the process is energetically favourable, and the filament will grow pushing the obstacle forward. In this situation, it is reasonable to assume that the (de)polymerization rate constants depend on the resistance of the obstacle, $k_{on}(F) \equiv k'_{on}$ and $k_{off}(F) \equiv k'_{off}$[6]. Let's now see how this dependence can be assessed through a thermodynamic approach.

The chemical potential of free monomers in solution with density ρ_1 can be written as [5]

$$\mu_{sol} = \mu^0_{sol} + k_B T \ln \rho_1 \tag{1.4}$$

where μ^0_{sol} is an ideal term, k_B is the Boltzmann constant and T the absolute temperature. Let's denote by μ_{fil} the monomer chemical potential when attached to the filament, which is taken independent of the force or the length (*i.e.* the filament is considered to be incompressible and no finite length effect is considered) [5]. Once a monomer passes from the solution to the filament's tip, the free energy changes are $-\mu_{sol}$ in the solution, $+\mu_{fil}$ in the filament and Fd_0 in the load. The sum of these contributions, $\mu_{fil} + Fd_0 - \mu_{sol}$, can be positive, negative or zero depending on the free monomers concentration. If the concentration is equal to the critical concentration for the applied value of F (*i.e.* at equilibrium), $\rho_1 = \rho'_{1c}$, then the

[6] Primes indicate the quantity in presence of the load.

sum is zero and:

$$\begin{aligned}\mu_{fil} + Fd_0 = \mu_{sol} &= \mu^0_{sol} + k_B T \ln \rho'_{1c} \\ &= \mu^0_{sol} + k_B T \ln \frac{k'_{off}}{k'_{on}}.\end{aligned} \tag{1.5}$$

If $F = 0$, to have equilibrium ($\mu_{sol} = \mu_{fil}$) the free monomer density must be $\rho_1 = \rho_{1c}$, and then $W_0 = k_{off} = \rho_{1c} k_{on} = U_0$:

$$\mu_{fil} = \mu^0_{sol} + k_B T \ln \rho_{1c} = \mu^0_{sol} + k_B T \ln \frac{k_{off}}{k_{on}}. \tag{1.6}$$

This relationship for μ_{fil} holds for any value of F or ρ_1, since it has been taken as constant. The quantity that drives monomers to assembly onto the filament is the difference between the chemical energy of the free monomer in solution and the chemical energy of the incorporated monomer, which is, from Eqs. (1.4) and (1.6):

$$\Delta\mu = \mu_{sol} - \mu_{fil} = k_B T \ln \frac{\rho_1}{\rho_{1c}} = k_B T \ln \hat{\rho}_1 \tag{1.7}$$

with $\hat{\rho}_1$ the reduced concentration introduced above. At equilibrium, $\Delta\mu = Fd_0$, Eq. (1.5) holds and the filament does not grow nor shrink – it stalls, and F is equal to the *stalling force*:

$$F_{stall} = \frac{k_B T}{d_0} \ln \hat{\rho}_1. \tag{1.8}$$

Eq. (1.8) applies to a single filament, but if we consider a bundle of filaments, treated as non-interacting, independent and identical, giving a mean-field character to the treatment, the total stalling force will be the sum of N_f identical forces, and hence the stalling force of a bundle of N_f filaments will be

$$F^{\text{MF}}_{stall} = N_f \frac{k_B T}{d_0} \ln \hat{\rho}_1. \tag{1.9}$$

Eq. (1.9), obtained for the first time by Hill in [5], is a very important expression, which will recur all along this thesis as a fundamental point of reference.

From Eqs. (1.5) and (1.6), it is possible to write the formal dependence of the (de)polymerization rates on the external force,

$$k'_{on} = k_{on} \exp\left(-a\beta F d\right) \tag{1.10}$$

$$k'_{off} = k_{off} \exp\left((1-a)\beta F d\right) \tag{1.11}$$

introducing a dimensionless parameter, a, sometimes referred to as "load factor" [8], which expresses how the effect of the external load is distributed between the polymerization and the depolymerization rate constants (note that the ratio between the constants does not depend on this parameter).

The same approach can be used to obtain the *velocity-load relationship* for a bundle of N_f filaments, which is the velocity v at which an obstacle moves when loaded with a force F and pushed by N_f growing filaments, as a function of F. The velocity-load relationship which is usually attributed to Hill's work has indeed derived later in [11, 44] with a very straightforward argument starting from Hill's work [5].

Let's consider a bundle of filaments growing freely with rates U_0 and W_0; each monomer addition leads to an increase in the bundle length by d_0, each removal to a shrinkage by d_0. If the free monomer density is large enough, the polymerization rate exceeds the depolymerization rate and the average growth velocity of the bundle will be simply $v_0 = d_0(U_0 - W_0)$. Now, as stated previously, if a filament is subjected to an external force F, his (de)polymerization rates will change, according to Eqs. (1.10) and (1.11). Considering a bundle of N_f filaments, each filament must perform an average work equal to Fd_0/N_f for the addition of a subunit. If the assumption is made that the depolymerization rate does not depend on the applied force ($a = 1$ in Eqs. (1.10) and (1.11)), the popular velocity-load relationship can be written:

$$v^{\mathrm{MF}}(F \mid N_f, \rho_1) = d_0 \left[U_0 \exp\left(-\beta \frac{F d_0}{N_f} \right) - W_0 \right] \tag{1.12}$$

$$= dW_0 \left[\hat{\rho}_1 \exp\left(-\beta \frac{F d_0}{N_f} \right) - 1 \right] \tag{1.13}$$

where the parametric dependence on the number of filaments N_f and the free monomers density ρ_1 has been indicated explicitly. The velocity is correctly zero for $F = F_{stall} = N_f \frac{k_B T}{d} \ln \hat{\rho}_1$. In this mean field model, every filament in the bundle is considered to be independent of the others and equivalent to all the others. From Eq. (1.13) one can get the power of transduction of chemical energy into mechanical work, which is simply the velocity times the force, $P^{\mathrm{MF}}(F \mid N_f, \rho_1) = F v^{\mathrm{MF}}(F \mid N_f, \rho_1)$. Each filament in the bundle is sustaining an external force equal to $f = F/N_f$, and every filament performs the same amount of work: $P^{\mathrm{MF}}(F \mid N_f, \rho_1) = N_f f v^{\mathrm{MF}}(f \mid N_f = 1, \rho_1) = N_f P^{\mathrm{MF}}(f \mid N_f = 1, \rho_1)$, *i.e.* the power developed by the multi-filament bundle is N_f times the power developed by a single filament against a load $f = F/Nf$. Eq. (1.13) maximizes the power of transduction of chemical energy into mechanical work, and it has been coined as the *Perfect Load Sharing* (PLS) condition [44].

Eq. (1.13), although very popular, has turned out to be inadequate to quantitatively interpret experimental data [9, 11, 12], predicting a velocity sistematically larger than observed. This discrepancy led to the formulation of more microscopic models, which could give a mechanistic explanation of how the free energy gained in polymerization can be transducted into mechanical work – these models will be reviewed in the following subsection.

1.3.2 Brownian Ratchet models

The idea of interpreting the pushing mechanism of growing *rigid* filaments as a rectified brownian motion has been proposed in [7], invoking popular Feynmann's ratchet mechanism. Let's consider a particle diffusing in one dimension, subject to periodic boundaries through which it can pass only in one direction (the same for all the boundaries): in the end, the motion of the particle, brownian by nature, will result in a net displacement in one of the two directions. In this case, the barriers act as *ratchets* and their effect is to rectify the brownian motion. Let's see how this concept applies to the case of filaments polymerizing in contact with a mobile barrier.

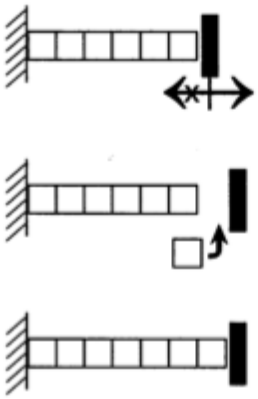

Figure 1.3. Schematic representation of the Brownian Ratchet model for a single filament: the seed is anchored on the left to a fixed substrate and the free end faces a perpendicular mobile wall. If the gp opened by thermal fluctuations between the filament's tip and the wall is equal to or wider than d_0 a monomer can intercalate. From [24].

Let's consider a rigid filament, pictured as a linear array of monomers, grafted at one end to a fixed wall and growing at the other end against a second mobile wall with diffusion coefficient D, which during his motion remains always perpendicular to the growth direction (see Fig. 1.3). This latter wall is pushed by a force F towards the filaments' tips. Since the filaments are rigid and grow straight, this is a unidimensional problem, de facto. Moreover, the filaments' tips constitute a reflecting barrier for the wall, which cannot go beyond it. Being the filament rigid and the monomers incompressible, the only way for the filament to attach a subunit is that the gap between its tip and the wall be larger or equal to d_0, the incremental size per attached monomer. The wall, besides, fluctuates and a gap of sufficient width can open from time to time and a monomer can intercalate. Once this attachment has occurred, the wall fluctuations will be pushed forward: the monomer intercalation acts as a ratcheting mechanism.

Let's denote by y the distance between the wall and the filament's tip. If $y \geq d_0$, there is a probability per unit of time U_0 that a monomer will attach to the tip, which is equivalent to the transition $y \to y - d_0$. Detachment is always allowed, regardlessly of y, and occurs with a probability per unit of time W_0. This is equivalent to a jump $y \to y + d_0$. Let's define the probability density $c(y,t)$ such that $\int_a^b c(y,t)dy$ is the probability to have $y \in (a,b)$ at time t. It is easy to write the time evolution of $c(y,t)$ [7] in terms of a Fokker-Plank equation, taking into account the diffusion of the wall and the jump terms due to polymerization/depolymerization events:

$$\frac{\partial c}{\partial t} = D\frac{\partial^2 c}{\partial y^2} + \frac{DF}{k_B T}\frac{\partial c}{\partial y} + U_0\left[c(y+d_0,t) - \Theta\left(y-d_0\right)c(y,t)\right] + W_0\left[\Theta\left(y-d_0\right)c(y-d_0,t) - c(y,t)\right] \tag{1.14}$$

where $\Theta(\cdots)$ is the Heaviside step function and accounts for the minimum gap size

to allow for polymerization, $y \geq d_0$. The fact that the wall cannot penetrate the filament tip translates into a reflecting boundary condition at $y = 0$:

$$-D\frac{\partial c(0,t)}{\partial y} - \frac{DF}{k_B T}c(0,t) = 0. \tag{1.15}$$

Moreover, $c(y,t)$ is required to be continuous at $y = d_0$. Once the steady state solution $c(y)$ is found, the velocity can be obtained as follows:

$$v = d_0 \left(\frac{U_0 \int_{d_0}^{\infty} c(y)dy - W_0 \int_0^{\infty} c(y)dy}{\int_0^{\infty} c(y)dy} \right). \tag{1.16}$$

The numerator is the net rate of polymerization, meant as the average number of monomers inserted minus the average number of monomers detached per unit of time; again, the integral multiplying U_0 starts from d because polymerization can occur only for $y \geq d_0$. When $W_0 \ll U_0$ depolymerization can be neglected, and a trascendent expression for the velocity-load relationship can be written down [7] and, interestingly enough, in the case of polymerization and depolymerization velocities ($U_0 d_0$ and $W_0 d_0$) much smaller than $2D/d_0^2$ (which is the ideal ratchet velocity), this expression reduces to Eq. (1.13) for $N_f = 1$.

In the case of a single rigid filament, the wall fluctuations are the only way to open a gap of adequate size for polymerization, $y \geq d_0$. Besides, when considering a bundle of N_f with a suitable disposition of filaments, a new "subsidy" mechanism arises. To see this, one more detail needs to be specified: the longitudinal disposition of the first monomer of each filament, or its seed, as it will be called hereafter. Let's denote by h_n the coordinate of the n-th seed, with $n = 1, \ldots, N_f$, and let's consider a distribution of these h_n which we call *staggered* or *homogeneous*: their average is 0, the distance between two adjacent seeds, $h_n - h_{n-1}$, is equal to d_0/N_f for every n and $-d_0/2 < h_n < d_0/2$ for every n. A choice which satisfies these condition is:

$$h_n = \left[\frac{2n-1}{N_f} - 1 \right] \frac{d_0}{2}. \tag{1.17}$$

Fig. 1.4 reports a sketch of a staggered bundle: the grey area is the width of the grafting wall where seeds are placed, X_n is the position of the n-th tip along the x axis, and the maximum of all the X_n is denoted by X^*. Note that because of the seeds arrangement, at any given time only one filament can be in contact with the wall. If j_n is the number of monomers in the n-th filament, the length of the filament will be $L_{cn} = (j_n - 1)d_0$ and

$$X_n = h_n + (j_n - 1)d_0. \tag{1.18}$$

L is the wall position and the condition $L \geq X^*$ must always be satisfied (reflecting boundary condition), as stated before in words. The aforementioned subsidy effect is a consequence of the disposition of the seeds: from the definition of h_n, it can be seen that the distance between the wall (supposed to be on average adjacent to the most advanced tip or little apart) and the second most advanced tip is an

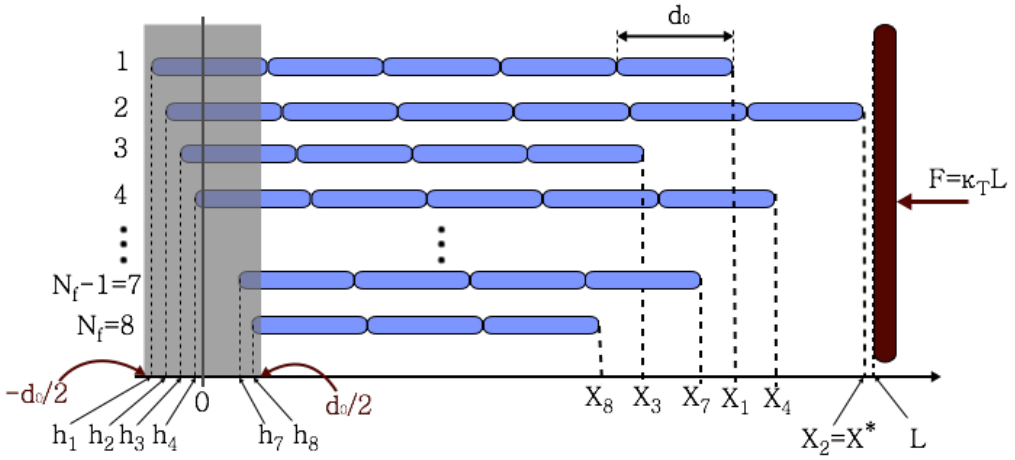

Figure 1.4. Sketch of a bundle of $N_f = 8$ filaments facing a mobile wall (brown vertical section), with a staggered disposition of the seeds.

integer multiple of d_0/N_f, which can be less than d_0. In this case, to allow for polymerization, the minimum gap to be opened between the wall and the most advanced tip is mFd_0/N_f, with m integer $1 \leq m < N_f$, which is smaller than d_0. Hence because of the presence of the other filaments, it becomes easier to polymerize for each of them. Note that this subsidy effect does not occur in the case of an "unstaggered" disposition of the seeds, $h_n = 0$ for every n: in that case the gap to be opened to polymerize is always d_0 at least.

From this latter model, the velocity-load relationship can be found [6, 7] and numerically solved within certain approximations [12]. Let's denote by p_m the probability to find a filament at distance md_0/N_f from the most advanced tip. Note that only one filament tip can be found at a given distance md_0/N_f, because of the seeds disposition. Moreover, only filaments with $m = 1, \ldots, N_f$ can contribute to the wall displacement, resulting in an average forward velocity [12]

$$v^+ = U_0 \left\{ d_0 \exp\left(-\frac{Fd_0}{k_B T}\right) + \sum_{m=1}^{N_f - 1} \exp\left[-\left(d_0 - \frac{md_0}{N_f}\right) \frac{F}{k_B T} \right] p_m \left(d_0 - \frac{md_0}{N_f}\right) \right\} \tag{1.19}$$

where the exponential factor takes into account the decrease of the polymerization rate due to the presence of the load (it has been taken $a = 1$ in Eqs. (1.10) and (1.11)) and in the sum the factor $(d_0 - md_0/N_f)$ is the distance by which the wall needs to be displaced to allow for monomer intercalation, for $m = 1, \ldots, N_f - 1$. Besides, depolymerization of the leading filament causes a decrease in the bundle length and a backwards motion of the wall. Considering the depolymerization rate as independent of the load, one gets the average backwards velocity as:

$$v^- = W_0 \left\{ p_1 \frac{d_0}{N_f} + \sum_{m=2}^{N_f} \left[m p_m \prod_{k=1}^{m-1} (1 - p_k) \right] \frac{d_0}{N_f} + \prod_{m=1}^{N_f - 1} (1 - p_m)\, d_0 \right\} \tag{1.20}$$

where the first term in brackets takes account of the probability that the second longest filament is at a distance d_0/N_f from the most advanced, the second term takes into account the probability p_m that the second longest is at a distance md_0/N_f with $m \geq 2$ and that none of the others is closer, and the last term takes into account the probability $\prod_{k=1}^{m-1}(1-p_k)$ that no filament is at a distance md_0/N_f with $1 \leq m < N_f$: in this latter case the depolymerization of the longest filament leads to a wall displacement equal to d_0 and the depolymerized filament remains the most advanced filament in the bundle. The average wall velocity will be $v^{\mathrm{BR}} = v^+ - v^-$ [12] (the superscript BR stays for Brownian Ratchet).

Now, to solve Eqs. (1.19) and (1.20), the probability p_m must be found. Let's consider the forward (in the direction of the wall) and the backward (in the opposite direction) flux of monomers at a distance md_0/N_f from the wall, Φ_m^+ and Φ_m^-. The first one is given by $\Phi_m^+ = U_0 p_{m+N_f} - p_n v^{\mathrm{BR}}/d_0$, because polymerization at a tip which is $(m+N_f)d_0/N_f$ apart from the wall can occur with rate U_0 (it isn't in contact with the wall neither before nor after polymerization), while polymerization at a tip at distance md_0/N_f from the wall occurs with a reduced rate, which is taken into account by the factor v^{BR}/d_0. Similarly, the minus flux is $\Phi_m^- = W_0 p_m$. At steady state, $\Phi_m^+ = \Phi_m^-$, which gives:

$$\begin{aligned}
p_{m+N_f} &= \left(\frac{W_0 + v^{\mathrm{BR}}/d_0}{U_0}\right) p_m \\
p_{m+2N_f} &= \left(\frac{W_0 + v^{\mathrm{BR}}/d_0}{U_0}\right) p_{m+N_f} = \left(\frac{W_0 + v^{\mathrm{BR}}/d_0}{U_0}\right)^2 p_m \\
&\dots \\
p_{m+iN_f} &= \left(\frac{W_0 + v^{\mathrm{BR}}/d_0}{U_0}\right)^i p_m \qquad m = 1, \dots, N_f - 1, i \in \mathbf{N}
\end{aligned} \tag{1.21}$$

Besides, these probabilities must satisfy the condition

$$\sum_{i=0}^{\infty} p_{m+iN_f} = 1 \tag{1.22}$$

because a given tip can be found only at distances which are multiples of d_0/N_f. This sum can be calculated straightforwardly, giving the expression of p_m and finally leading to:

$$p_{m+iN_f} = \frac{v_0 - v^{\mathrm{BR}}}{d_0 U_0} \left(\frac{W_0 + v^{\mathrm{BR}}/d_0}{U_0}\right)^i \tag{1.23}$$

where $v_0 = (U_0 - W_0)d_0$ is the growth velocity in absence of the load. The probability p_{m+iN_f} results thus to be independent of m: the average density of filament is constant within each interval $[id_0, (i+1)d_0]$. Then, in Eqs. (1.19) and (1.20) one can replace $p_m = p_0 = \frac{v_0 - v^{\mathrm{BR}}}{d_0 U_0}$ which gives finally:

$$\begin{aligned}
v^{\mathrm{BR}} = U_0 \Bigg\{ & d_0 \exp\left(-\frac{F d_0}{k_B T}\right) + \sum_{m=1}^{N_f - 1} \exp\left[-(N_f - m)\frac{d_0}{N_f}\frac{F}{k_B T}\right] \frac{v_0 - v^{\mathrm{BR}}}{U_0}\frac{(N_f - m)}{N_f} \Bigg\} \\
- W_0 \Bigg\{ & \frac{v_0 - v^{\mathrm{BR}}}{N_f U_0} \left[\sum_{m=1}^{N_f - 1} m \left(\frac{v^{\mathrm{BR}} + d_0 W_0}{d_0 U_0}\right)^{m-1}\right] + \left(\frac{v^{\mathrm{BR}} + d_0 W_0}{d_0 U_0}\right)^{N_f - 1} d_0 \Bigg\}
\end{aligned} \tag{1.24}$$

Interestingly enough, the stalling force given by this equation is the same as that calculated in the mean field approach,

$$F_{stall} = N_f \frac{k_B T}{d_0} \ln \hat{\rho}_1 \tag{1.25}$$

as it can be checked substituting $v^{\mathrm{BR}} = 0$ and $F = F_{stall}$ in Eq. (1.24).

Eq. (1.24) is a polynomial equation in v^{BR} to be solved. As proposed in [45], it can be done by using the Newton-Raphson method: introducing $w = v^{\mathrm{BR}}/d_0 W_0$, one can rewrite Eq. (1.24) as follows:

$$\begin{aligned}\phi(w) = \frac{\hat{\rho}_1}{N_f}\Bigg\{ & N_f \exp\left(-\frac{F d_0}{k_B T}\right) \\ & + \sum_{m=1}^{N_f-1} \exp\left[-\left(d_0 - \frac{md}{N_f}\right)\frac{F}{k_B T}\right]\left(1 - \frac{1+w}{\hat{\rho}_1}\right)(N_f - m)\Bigg\} \\ & - \frac{1}{N_f}\left[\left(1 - \frac{1+w}{\hat{\rho}_1}\right)\sum_{m=1}^{N_f-1} m\left(\frac{1+w}{\hat{\rho}_1}\right)^{m-1} + N_f\left(\frac{1+w}{\hat{\rho}_1}\right)^{N_f-1}\right] - w = 0\end{aligned} \tag{1.26}$$

To apply the method, the derivative of this expression is required,

$$\begin{aligned}\phi'(w) = & -\frac{1}{N_f}\Bigg\{\sum_{m=1}^{N_f-1} \exp\left[-\left(d_0 - \frac{md}{N_f}\right)\frac{F}{k_B T}\right](N_f - m)\Bigg\} \\ & + \frac{1}{\hat{\rho}_1 N_f}\Bigg\{\sum_{m=1}^{N_f-1} m\left(\frac{1+w}{\hat{\rho}_1}\right)^{m-2}\left[\frac{1+w}{\hat{\rho}_1} - \left(1 - \frac{1+w}{\hat{\rho}_1}\right)(m-1)\right]\Bigg\} \\ & - \frac{1}{\hat{\rho}_1}(N_f - 1)\left(\frac{1+w}{\hat{\rho}_1}\right)^{N_f-2} - 1.\end{aligned} \tag{1.27}$$

Using an initial guess for w – which can be taken equal to the mean field velocity Eq. (1.13) – the whole velocity-load can be obtained.

Fig. 1.5 shows the two curves corresponding to Eq. (1.13) (mean field model) and Eq. (1.24) (brownian ratchet model) for $N_f = 32$ and $\hat{\rho}_1 = 2.5$: the two start at the same point for $F = 0$, and meet at the same value of the stalling force, where $v^{\mathrm{BR}} = v^{\mathrm{MF}} = 0$. For intermediate values of F, the mean field prediction is systematically higher than the brownian ratchet model.

Unstaggered Brownian Ratchet model

Let's consider, for sake of completeness, the case where filaments have their seeds in an *unstaggered* disposition, *i.e.* precisely lined up at the same distance from the moving wall. This configuration characterize the "Unstaggered Brownian Ratchet" model for rigid filaments [8], according to which more than one filament can be in contact with the wall at the same time, and the wall position is identified with the position of the longest filament(s). Yet, this model leads to the so-called "no load sharing" condition for the filaments in the bundle. Let's suppose that more than one

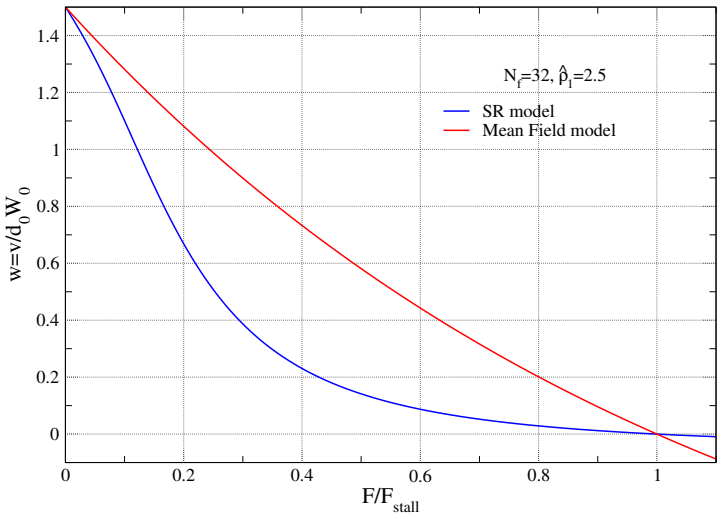

Figure 1.5. Velocity-load relationships obtained within the mean field and the brownian ratchet models. The y axis reports the dimensionless velocity v^{BR}/d_0W_0, while the x axis reports the force normalized by the stalling value. The value at $F = 0$ is the same for the two models, as well as the value of the stalling force. The figure has been realized for $N_f = 32$ and $\hat{\rho}_1 = 2.5$.

filament is in contact with the wall. In order for one of these filaments to polymerize, the wall must be moved away by a distance d_0, but only the filament on which the monomer is added will perform work. The polymerization rate of this filament is supposed to be lowered by the presence of the wall to a value $U(F) < U_0$. The other filaments, after this polymerization, can polymerize as there were no barrier, with bulk rate U_0. The same applies to depolymerization: W_0 changes to a load-dependent value $W(F)$ only if depolymerization occurs at the tip of the longest filament with all the other filaments shorter than this. If this is the case, the depolymerizing filament produces work since depolymerization leads to a back move of the wall by a step d_0: in general, work is associated only with those (de)polymerization events implying a motion of the barrier. By construction, so, only one filament per time can perform mechanical work against the wall[7]. Polymerization and depolymerization rates in presence of an external load are related to each other by Eqs. (1.10) and (1.11), which have been employed in [8] fixing the load factor to $a = 1$, meaning that the polymerization rate carries all the force dependence while the depolymerization rate stays constant.

Given this "no-load sharing" model, the master equations for the time evolution of the filament sizes have been written and solved analytically in the $N_f = 2$ case, numerically in the $N_f > 2$ cases for which a mean-field approach has been

[7] A sharing of the load would occur if there are (only) two filaments in contact with the barrier and they undergo (de)polymerization in exactly the same time, but this event has a negligible occurrence probability.

developed [8]. The authors found a wall velocity at given load much smaller than what predicted by the SR model, while they found the same stalling force as Eq. (1.9); yet, in the case of unstaggered bundles it is convenient introducing an "apparent" stalling force, defined there as the load at which the velocity drops to less than an arbitrary fraction α of the load-free velocity, $v_0 = d_0(U_0 - W_0)$. Notice that this load-free velocity is the same as in the SR model: at zero load there is no coupling between the filaments, which behave independently of each other so that the mutual seeds disposition does not matter. This apparent stalling force is significantly lower than the stalling force and it grows logarithmically with the number of filaments, rather than linearly like the real stalling force. This implies that the larger the bundle, the larger the difference between the real and the apparent stalling force. It could be a significant quantity in real experiments, where the parameter α can be chosen in relation to the limit resolution in the velocity measurement, for instance.

Another interesting outcome of this model was that near the apparent stalling force the system is found to undergo a transition between two regimes: a non-condensed regime at low forces where filament sizes have a spread distribution and a condensed regime where filaments accumulate near the wall. The indicator for such transition is the number of filaments in contact with the wall, N_0, which was observed to go from 1 to N_f as the force increased: at the apparent stalling force, $N_0 \simeq \alpha N_f$.

This unstaggered brownian ratchet is very instructive, however it hasn't been as popular as the corresponding staggered version, which has been usually employed to interpret experimental result, as reported in the following.

1.3.3 Interpretation of the experimental measurements

To close this introductory chapter, let's see how the experimental measurements reviewed in Section 1.2 have been interpreted within the mean-field and the SR model.

In [9], the authors fitted the experimental velocity-load relationship with an exponentially decaying function as Eq. (1.13), finding it reasonable to assume, as the only effect of force, a decrease in the polymerization rate; yet, they didn't exclude that both the polymerization and the depolymerization rates could be affected by the external force. However, the large uncertainty associated to their measurements prevented them from reliably measure the stalling force. Moreover, comparing the microtubules flexural rigidity obtained from the fit with the one got from direct measurements, they concluded that they observed a velocity decreasing faster with F than predicted by Eq. (1.13), suggesting that the perfect load sharing scenario did not apply in their case.

In [43], the authors observed polymerization of a tethered individual actin filament and expected a stalling force calculated with Eq. (1.9) or Eq. (1.25) of the order of 2 pN and they observed a force at least equal to 1.3 pN; the experimental design prevented them to give more accurate measurements, or to get the velocity-load relationship. Conversely, the use of the optical trap set-up in [10] allowed the authors to get a quite neat measurement of the stalling force, which was rather different from expectations. They observed the growth of an actin bundle of 8-10 filaments and got a curve F vs time which led to a plateau, corresponding to the stalling

force. They used two different actin concentrations, 2 μM and 4 μM, and to get a prediction from Eq. (1.9) they measured the apparent critical concentration for their experimental conditions; they got 0.8 pN and 1.0 pN *per filament* for 2 μM and 4 μM respectively, so for a bundle of 8-10 filaments they expected a force 8-10 times larger. The plateaus they observed, on the other hand, were 1.0 pN and 1.5 pN respectively, much closer to the values expected for a single filament in the same conditions. The origin of this result is still unexplained, despite the attempt by the authors to relate it to the buckling phenomenon. To anticipate the following, in this work the answer to this question is sought by introducing an explicit treatment of the flexibility in the filament model. Finally, the authors in [10] didn't provide an estimate of the velocity-load relationship, although the performed measurements could have produced it almost effortlessly.

As for the experiment [12], where bundles growing between two magnetic beads have been employed to get the velocity-load curve, the authors claimed that their data could be successfully fitted by the SR model, Eq. (1.24), while the unstaggered model prediction was too low to fit experimental data. The authors used that law to fit the experimental data using N_f as a fitting parameter: they obtained $N_f \approx 100$, which was considered a reasonable number by the authors. They also directly measured the mechanical power transducted from the filaments to the load, $P = vF$, and they observed that for small values of the load the behavior was close to an ideal regime where filaments polymerized without being affected from the wall; as the load increases, the power reaches a maximum and then falls to zero at stalling. Again, this behavior is predicted by the brownian ratchet model. The authors, moreover, concluded that the level of work sharing among the filaments was intermediate between the perfect load sharing and the no-load sharing scenarios. However, because of the large experimental uncertainty, the agreement could be qualitative only; moreover, they explored a limited range of load values, remaining quite far from stalling.

Chapter 2

A Statistical Mechanics model for semiflexible filaments

The physical behavior of linear polymers such as actin filaments or microtubules strongly depends on the ratio between their persistence length*, qualitatively introduced in Chapter 1, and their contour length. On length scales much smaller than the persistence length, thermal fluctuations can be neglected while bending energy determines the polymer shape, which will tend to be straight: this is the case of* rigid *filaments. On length scales larger than the persistence length, conversely, thermal fluctuations play a crucial role in determining the polymer shape, and this is the case of* flexible *filaments. There is an in-between class of polymers, said* semiflexible*, for which the typical length scales are comparable with their persistence length. Although often treated as rigid, actin filaments belong to this latter class of polymers, and one of the most suitable model to describe them is the* worm-like chain model*.*

Previous studies [46] on worm-like chains grafted at one end perpendicular to a plane and compressed at the other end by another wall, parallel to the grafting surface, have established the (microscopically averaged) force that the chain exerts on the confining wall; this force is not due to any interaction potential between the chain and the wall, but only to the decrease in the number of possible configurations of the chain, and therefore it is said to have entropic *origin. We will make use of this expression, established for fixed-size filaments, to model* growing *filaments against a (fixed or mobile) rigid wall: an adiabatic approximation based on the wide timescale separation between the chemical events (slow) and the time needed by the chain to equilibrate (fast), will let us consider the chains as always at equilibrium between two successive (de)polymerization events and use the known expression [46] for the average force exerted by living filaments on a confining wall. Moreover, in the case of mobile obstacles, an additional timescale separation between wall diffusion, chemical events and filaments relaxation will allow us to use the same expression [46] to build the Statistical Mechanics framework of* living *semiflexible filaments growing against a* mobile *wall. One issue that arises when considering flexible filaments growing against an obstacle is the possibility of occurrence of* escaping filaments*: for trap amplitudes beyond a specific threshold, filaments can bend so much that they start growing parallel to the obstacle, not participating to the polymerization forces anymore. In optical trap the occurrence of escaping filaments can be controlled by*

properly choosing the trap strength constant; a quantitative criterion for this choice shall be given in the following. The formalism developed will be exploited to study the equilibrium properties of the bundles, e.g. *the equilibrium distribution function for the wall position or for the number of filaments touching the wall. From the equilibrium average wall position in optical trap, in particular, the stalling force can be calculated, provided that the probability of escaping filaments is negligible.*

This chapter is structured as follows: after giving a general definition of the persistence length, some of the most popular models for semiflexible polymers are reviewed in Section 2.1, with particular emphasis on the worm-like chain (WLC) model in Section 2.1.2. Within the WLC model, the entropic force generated by compressed filaments is derived in Section 2.2 following [46]. In Section 2.3 a novel Statistical Mechanics framework for a bundle of semiflexible filaments growing in contact with a moving obstacle is built. In particular, the case of an optical-trap-like potential is studied in detail, and in Section 2.4 results for semiflexible bundles in optical trap are presented.

This chapter is based on the results presented in [47].

2.1 Flexible and semiflexible filaments

Thermal forces cause flexible filaments undergo fluctuations in shape which may be crucial to their structure: shape fluctuations in a very flexible object may be so relevant to lead it to loose its structure. On the other hand, if a biological object (be it a protein or a cell or an organism) has a structure, which in most cases is intimately related to its functionality, this structure is meant to be maintained over time. Then, cytoskeletal filaments must be rigid enough so that thermal fluctuations don't perturb their shape too much: the *persistence length* of a filament, ℓ_p, is the most important parameter describing this resistance to thermal fluctuations. Several intuitive definitions of ℓ_p may be given – it can be defined as the filament length over which thermal bending becomes appreciable, or as the distance over which the orientations of two filament segments become uncorrelated [48].

To see how a filament bends in response to external forces, the simplest approach is to invoke the continuous elasticity theory [49]. Let's consider a small segment of length L_c, which can be seen as an elastic rod, bent into a circular arc of radius R. For sake of simplicity, let's consider the filament constrained in a plane (2D). The curvature, which is $1/R$, in the limit of small deformations will be proportional to the bending moment, M, via a constant of proportionality known as *flexural* or *bending rigidity*, κ [49]:

$$M = \kappa \frac{1}{R}, \tag{2.1}$$

which is the analogous of the Hooke's law for a spring.

In order to apply Eq. (2.1), known as *beam equation*, let's rewrite it in a different form. Let $[x(s), y(s)]$ be the position of a point along the filament, where s is the arc length, *i.e.* the contour distance from the end chosen as origin. Let $\theta(s)$ the tangent angle, defined by

$$\tan\theta(s) = \frac{\sin\theta(s)}{\cos\theta(s)} = \frac{dy}{ds} \Big/ \frac{dx}{ds} \tag{2.2}$$

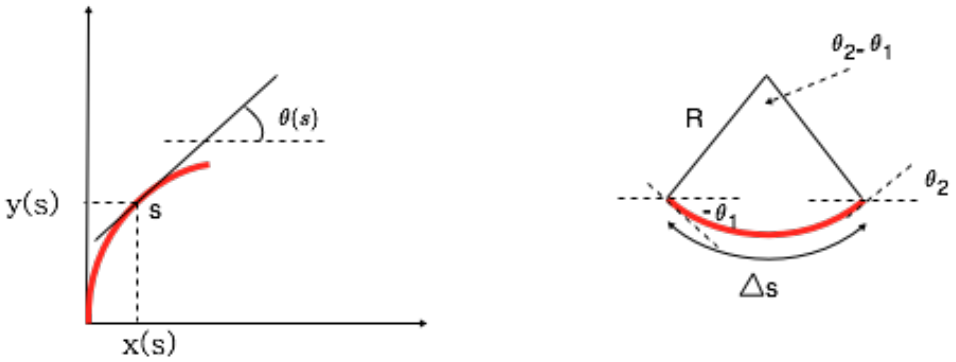

Figure 2.1. Segment of filament with circular shape or radius R. Over the arc length Δs, the tangent angle increases by $\Delta\theta = \theta_2 - \theta_1$, and for a circle it is true that $R = \Delta s/\Delta\theta$. In the general case, the local radius of curvature is $R = ds/d\theta$ and the curvature is its inverse.

which is the angle between the tangent to the filament at s and the horizontal axis. Moreover, as shown in Fig. 2.1, $d\theta/ds = 1/R$, with R radius of curvature [48], so that Eq. (2.1) becomes:

$$M(s) = \kappa \frac{d\theta(s)}{ds}. \tag{2.3}$$

The corresponding bending energy is the integral of the moment with respect to the curvature, like the potential energy is the integral of the force with respect to displacement. Let's denote the curvature $\frac{d\theta}{ds}$ by $\mathcal{C}$ (and $\frac{d\theta}{ds}(L_c)$ by $\mathcal{C}_0$):

$$\Delta U = \left[\int_0^{\mathcal{C}_0} \kappa \mathcal{C} \cdot d\mathcal{C}\right] \Delta s = \frac{1}{2}\kappa \mathcal{C}_0^2 \Delta s = \frac{1}{2}\kappa \left(\frac{d\theta}{ds}(L_c)\right)^2 \Delta s \tag{2.4}$$

which in the limit of small length becomes

$$\frac{dU}{ds} = \frac{1}{2}\kappa \left(\frac{d\theta}{ds}\right)^2. \tag{2.5}$$

The energy per unit length is thus proportional to the square of the curvature: all the information about the filament's shape is enclosed in $\theta(s)$ and its derivative. The persistence length can be related to this tangent angle, as it can be obtained from the average of the cosine of $\theta(s) - \theta(0)$. Let's define $f(s) = \langle \cos(\theta(s)) \rangle$ (where $\langle \cdots \rangle$ denotes a time or ensemble average) and let's assume, without loss of generality, $\theta(0) = 0$. Considering an arc length increment Δs, the correspondent increment in $f(s)$ will be:

$$\begin{aligned}
\Delta f = \frac{df}{ds}\Delta s &\approx f(s + \Delta s) - f(s) \\
&= \langle \cos(\theta(s + \Delta s)) \rangle - \langle \cos(\theta(s)) \rangle \\
&= \langle \cos(\theta(s + \Delta s) - \theta(s) + \theta(s)) \rangle - \langle \cos(\theta(s)) \rangle \\
&= \langle \cos(\Delta\theta + \theta(s) \rangle - \langle \cos(\theta(s)) \rangle
\end{aligned}$$

where $\Delta\theta = \theta(s + \Delta s) - \theta(s)$. Since the angles $\Delta\theta$ and $\theta(s)$ are statistically independent [48], we can write

$$\begin{aligned}\frac{df}{ds}\Delta s &\approx \langle \cos\Delta\theta \cos\theta(s)\rangle - \langle \sin\Delta\theta \sin\theta(s)\rangle - \langle \cos(\theta(s))\rangle \\ &= \langle \cos\Delta\theta\rangle\langle \cos\theta(s)\rangle - \langle \sin\Delta\theta\rangle\langle \sin\theta(s)\rangle - \langle \cos(\theta(s))\rangle \\ &= \langle \cos\Delta\theta\rangle \left[\langle \cos\Delta\theta\rangle - 1\right] \end{aligned} \tag{2.6}$$

since the average of the sine terms is zero. We thus have:

$$\begin{aligned}\frac{df}{ds} &\approx \frac{\langle \cos\Delta\theta - 1\rangle}{\Delta s} f(s) \approx -\frac{1}{2}\left\langle \frac{(\Delta\theta)^2}{\Delta s}\right\rangle f(s) \\ &= -\frac{1}{2}\left\langle \left(\frac{\Delta\theta}{\Delta s}\right)^2 \Delta s\right\rangle f(s) = -\frac{\langle \Delta U\rangle}{\kappa} f(s) \\ &= -\frac{k_B T}{2\kappa} f(s) \end{aligned} \tag{2.7}$$

where in the last line the equipartition theorem has been used, with k_B the Boltzmann constant and T the absolute temperature. The solution of this differential equation is an exponential decay with decaying length scale equal to $2\kappa/k_B T$. In 3D there are two independent angular degrees of freedom, so that the average energy in the short segment is twice and [48, 49]

$$\langle \cos\left[\theta(s) - \theta(0)\right]\rangle = \exp\left(-\frac{k_B T s}{\kappa}\right). \tag{2.8}$$

So as $\theta(s)$ differs from $\theta(0)$, the cosine of their difference decreases and when the two angle are uncorrelated, their difference can be any angle between 0 and 2π with equal probability, and the average of its cosine is zero. The persistence length is the decaying length scale of this exponential and it is related to the bending rigidity κ by:

$$\ell_p = \frac{\kappa}{k_B T}. \tag{2.9}$$

The persistence length is thus proportional to the bending rigidity, as one would expect, and inversely proportional to the temperature: if the temperature is higher, thermal fluctuations become more important and bending more pronounced.

Moreover, it can be shown [49] that the bending rigidity of an elastic rod can be written in terms of the Young's modulus E: $\kappa = EI$, with I the moment of inertia of the rod's cross section A_{cross}, $I = \int_{A_{cross}} r^2 dS$. If the section of the rod is circular with diameter D, this integral gives $I = \frac{\pi}{32} D^4$; in general, $I \propto D^4$ and the persistence length $\ell_p = EI/k_B T \propto D^4$ strongly increases with the filament diameter, which is an intuitive result. Besides, actin filaments, which are thinner than intermediate filaments (see Section 1.1), are also stiffer (their persistence length is larger): this apparent inconsistency is due to the fact that large supramolecular assemblies often form helices to increase the rigidity, and this is the case of the double-stranded helical structure of F-actin [50].

Finally, there is another quantity which is related to the persistence length and which can be useful in the measurement of the persistence length itself: it is the

end-to-end distance, R_{EE}. This length is at most equal to L_c, and it drops below this value as the filament bends. It can be shown that the mean-squared end-to-end distance is:

$$\langle R_{\text{EE}}^2 \rangle = 2\ell_p^2 \left[\exp\left(-\frac{L_c}{\ell_p} \right) - 1 + \frac{L_c}{\ell_p} \right]. \tag{2.10}$$

Measuring the end-to-end distance instead of the cosine of the tangent angles is an easier and more practical approach in the case of semiflexible filaments: the persistence length of actin filaments, indeed, has been first estimated using this method [51].

Beyond this simple elastic model, several models coming from a statistical mechanics approach have been formulated to interpret the behavior of single polymers. In the following subsections two of these models for flexible and semiflexible polymers in solution will be briefly revised.

2.1.1 Freely-jointed chain model

The most simple model for a single polymer in solution is the *freely-jointed chain* model, useful in describing proteins like antibodies that contain globular or rigid colloids jointed by flexible regions – these proteins are said to have *segmental flexibility* [48]. In the freely-jointed chain, monomers are described as points at positions $\{\mathbf{r}_n\}$ with $n = 0, 1, \ldots, N$. Two adjacent monomers n and $n-1$ are connected by the bond vector

$$\mathbf{d}_n = \mathbf{r}_n - \mathbf{r}_{n-1} \tag{2.11}$$

for $n = 1, \ldots, N$. The length of these bond vectors is fixed at a value d_0, while the angle between two successive bonds can take any value with the same probability. This translates into a probability distribution for the bond $\mathbf{d}$ given by

$$\psi(\mathbf{d}) = \frac{1}{4\pi d_0^2} \delta(|\mathbf{d}| - d_0). \tag{2.12}$$

The end-to-end vector joining the first and the last monomers, $\mathbf{R}_{\text{EE}}(N) = \mathbf{r}_N - \mathbf{r}_0$, has zero average, while the mean-squared end-to-end distance is:

$$\begin{aligned} \langle [R_{\text{EE}}(N)]^2 \rangle &= \langle (\mathbf{R}_{\text{EE}}(N-1) + \mathbf{d}_{N-1})^2 \rangle \\ &= \langle [R_{\text{EE}}(N-1)]^2 + 2R_{\text{EE},x}(N-1) d_0 \sin\theta\cos\phi \\ &+ 2R_{\text{EE},y}(N-1) d_0 \sin\theta\sin\phi \\ &+ 2R_{\text{EE},z}(N-1) d_0 \cos\theta + b^2 \rangle \\ &= \langle [R_{\text{EE}}(N-1)]^2 \rangle + d_0^2 = \cdots = N d_0^2 \end{aligned} \tag{2.13}$$

so that the typical end-to-end distance increases like the square root of the number of bonds, $\bar{R} = \sqrt{\langle [R_{\text{EE}}(N)]^2 \rangle} = \sqrt{N} d_0$. Comparing this result with Eq. (2.10), in the limit of $N \gg 1$, with $L_c = N d_0$, the persistence length is found to be $\ell_p = d_0/2$.

Suppose now that the chain is fixed at one end, while a force tries to stretch it at the other end. The chain will reasonably tend to align with the direction of the force, but in the meantime it will react to this stretching as a consequence of

its tendency to maximize entropy: when the chain is pulled, the number of possible configurations decreases, and the corresponding decrease in entropy costs free energy. We ask now how the end-to-end distance along the direction of the force depends on the applied force (*force-displacement relationship*). To simplify the treatment, let's consider the stretching of a freely-jointed chain in two dimensions and let's F be a horizontal force. If the n-th segment forms an angle θ with F, the corresponding potential energy of the segment will be $U = -Fd_0 \cos\theta$. The probability that this segment is in the angular strip $(\theta, \theta + d\theta)$ is proportional to the area of the strip, $2\pi \sin\theta \; d\theta$, multiplied by the Boltzmann factor $\exp(-U/k_BT)$. The average value of $\cos\theta$ is thus:

$$\begin{aligned}\langle\cos\theta\rangle &= \frac{\displaystyle\int_0^\pi \cos\theta \;\exp(Fd_0\cos\theta/k_BT)\sin\theta \; d_0\theta}{\displaystyle\int_0^\pi \exp(Fd_0\cos\theta/k_BT)\sin\theta \; d\theta} \\ &= \frac{\displaystyle\int_{-1}^1 y \;\exp(xy)dy}{\displaystyle\int_{-1}^1 y \;\exp(xy)dy} = \frac{\exp(x)+\exp(-x)}{\exp(x)-\exp(-x)} - \frac{1}{x} = \coth(x) - \frac{1}{x} \equiv \mathcal{L}(x)\end{aligned} \tag{2.14}$$

with $x = Fd_0/k_BT$. $\mathcal{L}(x)$ is the Langevin function, which goes from zero to one as F increases. The average extension of the curve, $\langle X\rangle = Nd_0\langle\cos\theta\rangle$ thus increases from zero to Nd_0, the length of the completely stretched chain. The slope at the origin of the Langevin function is 1/3, how can be found expanding in Taylor series around the origin. Hence for small forces we have:

$$F = \frac{3k_BT}{Nd_0^2}\langle X\rangle, \tag{2.15}$$

i.e. the freely jointed chain when stretched with small forces behaves like a spring of constant $3k_BT/Nd_0^2$, proportional to the temperature (similarly to rubber-like materials) and inversely proportional to N and d_0 (and hence to ℓ_p): it means that is easier to align a stiff polymer than a very flexible one, as a consequence of the entropic nature of the polymer elasticity [48].

2.1.2 Worm-like chain model

The freely-jointed chain model is not very realistic, for instance it does not take into account that at short length polymers are stiff: for a model to be suitable for *semi*-flexible filaments like actin, it must consider the free energy cost due to bending. This can be done in a discrete model similar to the freely jointed chain, introducing a next-neighbours interaction analogous to that of the Ising or Heisenberg model, which accounts for the bending energy cost [52]. This is done by defining the following internal energy:

$$E\{\mathbf{t}_n\} = -K_b \sum_{n=1}^{N-1} \mathbf{t}_n \cdot \mathbf{t}_{n+1} = -K_b \sum_{n=1}^{N-1} \cos\theta_n \tag{2.16}$$

where $\mathbf{t}_n = \mathbf{d}_n/d_0$ are the bond versors, with $\mathbf{d}_n$ defined in Eq. (2.11), θ_n is the angle between $\mathbf{t}_n$ and $\mathbf{t}_{n+1}$ and K_b is a measure of the bending rigidity, with energy dimensions. The miminum of this energy is attained for $\{\theta_n = 0\}_{n=1,\dots,N-1}$, and as two bonds deviate from the straight configuration the energy rises proportionally to the bending rigidity parameter. Given this bending internal energy, the partition function for this chain will be thus

$$\mathcal{Z}_N = \prod_{n=1}^{N-1} \int_0^\pi d\theta_n \; 2\pi \sin\theta_n \; \exp\left(\beta K_b \cos\theta_n\right) = \left(\frac{4\pi}{\beta K_b}\sinh(\beta K_b)\right)^{N-1} \tag{2.17}$$

with $\beta = 1/k_B T$, while the Boltzmann distribution giving the probability for a set of angles $\{\theta_n\}_{n=1,N-1}$ is

$$p(\{\mathbf{t}_n\}_{n=1,\dots,N-1}) = \frac{1}{\mathcal{Z}_N}\exp(-\beta E(\{\mathbf{t}_n\})_{n=1,\dots,N-1}) \tag{2.18}$$

Let's now calculate the mean-squared end-to-end distance, from which we will extract the persistence length of the worm-like chain:

$$\langle [R_{\mathrm{EE}}(N)]^2\rangle = \left\langle \left(\sum_{n=1}^{N} \mathbf{d}_n\right)^2 \right\rangle = d_0^2 \sum_{n,m=1}^{N} \langle \mathbf{t}_n \cdot \mathbf{t}_m\rangle \tag{2.19}$$

for which the correlation between bonds along the chain is needed. Let's first evaluate the correlation between nearest neighbours:

$$\begin{aligned}
\omega_1 = \langle \mathbf{t}_n \cdot \mathbf{t}_{n+1}\rangle = \langle \cos\theta_n\rangle &= \frac{1}{\mathcal{Z}_N}\prod_{m=1}^{N-1}\int_0^\pi d\theta_m \; 2\pi\sin\theta_m \; \cos\theta_n \; \exp\left(\beta K_b\cos\theta_m\right) \\
&= \frac{1}{\mathcal{Z}_N}\int_0^\pi d\theta_n \; 2\pi\sin\theta_n \; \cos\theta_n \; \exp\left(\beta K_b\cos\theta_n\right) \; \mathcal{Z}_{N-1} \\
&= \coth\left(\beta K_b\right) - \frac{1}{\beta K_b} = \mathcal{L}(\beta K_b)
\end{aligned} \tag{2.20}$$

Let's denote the correlation between two bonds separated by $l = m - n$ $(m > n)$ bonds by $\omega_l = \langle \mathbf{t}_n \cdot \mathbf{t}_{n+l}\rangle$. Note that for each bond vector, only its projection along the preceding bond is transmitted to the next one: $\mathbf{t}_n \cdot \mathbf{t}_{n+l} = \prod_{k=1}^{l} \mathbf{t}_{n+k-1} \cdot \mathbf{t}_{n+k}$, which finally leads to:

$$\begin{aligned}
\langle \mathbf{t}_n \cdot \mathbf{t}_{n+l}\rangle &= \frac{1}{\mathcal{Z}_N}\prod_{m=1}^{N-1}\int_0^\pi d\theta_m \; 2\pi\sin\theta_m \; \exp\left(\beta K_b\cos\theta_m\right) \; (\mathbf{t}_n \cdot \mathbf{t}_{n+l}) \\
&= \frac{1}{\mathcal{Z}_N}\prod_{m=1}^{N-1}\int_0^\pi d\theta_m \; 2\pi\sin\theta_m \; \exp\left(\beta K_b\cos\theta_m\right) \; \prod_{k=1}^{l}(\mathbf{t}_{n+k-1} \cdot \mathbf{t}_{n+k}) \\
&= \frac{1}{\mathcal{Z}_N}\prod_{m=1}^{N-1}\int_0^\pi d\theta_m \; 2\pi\sin\theta_m \; \exp\left(\beta K_b\cos\theta_m\right) \; \prod_{k=1}^{l}\cos\theta_{n+k} \\
&= \left(\frac{\displaystyle\int_0^\pi d\theta \; \sin\theta \; \exp\left(\beta K_b\cos\theta\right) \; \cos\theta}{\frac{4\pi}{\beta K_b}\sinh(\beta K_b)}\right)^l \\
&= \left(\coth(\beta K_b) - \frac{1}{\beta K_b}\right)^l
\end{aligned} \tag{2.21}$$

Note that the last calculated quantity coincides with Eq. (2.8), and the two are equal if we define the persistence length as

$$\ell_p \equiv \frac{d_0}{\log\left(\coth(\beta K_b) - \frac{1}{\beta K_b}\right)} \underset{\beta K_b \gg 1}{\approx} d_0 \beta K_b. \tag{2.22}$$

Hence, comparing Eq. (2.22) with Eq. (2.9), the parameter K_b results related to the bending rigidity κ via the relation $K_b = \kappa/d_0$. We can now calculate the mean-squared end-to-end distance using the identity $\frac{\langle [R_{\text{EE}}(N)]^2 \rangle}{d_0^2} = \sum_{n=1}^{N} \langle t_n^2 \rangle + 2 \sum_{n<m} \langle \mathbf{t}_n \cdot \mathbf{t}_m \rangle$:

$$\begin{aligned}
\frac{\langle [R_{\text{EE}}(N)]^2 \rangle}{d_0^2} &= N + 2 \sum_{n=1}^{N} \sum_{m=n+1}^{N} \exp\left(-\frac{1}{\beta K_b}(m-n)\right) = N + 2 \sum_{n=1}^{N} \sum_{l=1}^{N-n} \exp\left(-\frac{1}{\beta K_b} l\right) \\
&= N + 2 \sum_{n=1}^{N} \left[\frac{1 - \exp\left(-\frac{1}{\beta K_b}(N-n-1)\right)}{1 - \exp\left(-\frac{1}{\beta K_b}\right)} - 1 \right] \\
&= \frac{1 + \exp\left(-\frac{1}{\beta K_b}\right)}{1 - \exp\left(-\frac{1}{\beta K_b}\right)} N - 2 \frac{\exp\left(-\frac{1}{\beta K_b}\right) - \exp\left(-\frac{1}{\beta K_b}(N+1)\right)}{\left(1 - \exp\left(-\frac{1}{\beta K_b}\right)\right)^2} \\
&\underset{N \gg 1}{\approx} \frac{1 + \exp\left(-\frac{1}{\beta K_b}\right)}{1 - \exp\left(-\frac{1}{\beta K_b}\right)} N
\end{aligned} \tag{2.23}$$

Again, the mean-squared end-to-end distance, in the long-chain limit, scales proportionally to N, similarly to the freely jointed chain model.

This model, known as Kratky-Porod model [52], is mostly used in its continuum version, the so called wormlike chain (WLC) model. It is obtained by letting simultaneously $d_0 \to 0$ and $N \to \infty$ while keeping $L_c = N d_0$ constant; from Eq. (2.22) it must be also $K_b \to \infty$, in order to keep ℓ_p constant, being both ℓ_p and κ physical quantities independent of the microscopic description of the model. Taking these limits in the second line of Eq. (2.23) and using Eq. (2.22) in the $\beta K_b \gg 1$ limit give $\langle [R_{\text{EE}}(L_c)]^2 \rangle = 2\ell_p L_c \left(1 - \frac{\ell_p}{L_c}(1 - \exp(L_c/\ell_p))\right)$, which is the same as Eq. (2.10). It is interesting to note that this model contains both the rigid and flexible limiting behaviors, obtainable by tuning the ratio between the contour and the persistence length:

$$\langle [R_{\text{EE}}(L_c)]^2 \rangle \approx \begin{cases} L_c^2 & L_c \ll \ell_p \\ 2\ell_p L_c & L_c \gg \ell_p \end{cases} \tag{2.24}$$

The last limit coincides with the mean-squared end-to-end distance of a freely jointed chain (Eq. (2.13) with $\ell_p = d_0/2$).

The free energy of a continuous worm like chain can be obtained from Eq. (2.16) using the identity $\mathbf{t}_n \cdot \mathbf{t}_{n+1} = -\frac{1}{2}\left[(\mathbf{t}_{n+1} - \mathbf{t}_n)^2 - 2\right]$ and taking the aforementioned

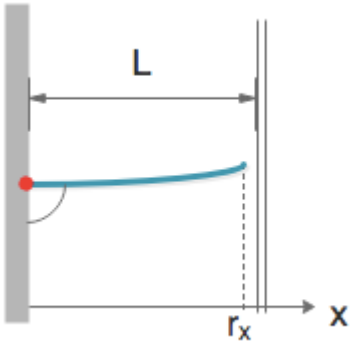

Figure 2.2. Grafted WLC (light blue) confined by a fixed wall (double vertical line) at distance L from its grafting point (red spot). r_x is the position of the free end along the direction perpendicular to the wall.

limits:

$$E_{wlc} = \lim_{d_0 \to 0, N \to \infty} \left[\frac{\ell_p}{2\beta} \sum_{n=1}^{-1} N d_0 \left(\frac{\mathbf{t}_{n+1} - \mathbf{t}_n}{d_0} \right)^2 \right] = \frac{\ell_p}{2\beta} \int_0^{L_c} ds \left(\frac{\partial \mathbf{t}}{\partial s} \right)^2 \tag{2.25}$$

having left out a constant term. s is the arc length variable, $\mathbf{t}(s)$ the tangent versor at s and $\partial \mathbf{t}/\partial s$ is the local curvature of the chain.

The elastic energy of the WLC model parametrized in terms of the arc length s, Eq. (2.25), is the most commonly used form of the bending energy of a worm like chain and, basing on it, the force generated by a confined WLC will be calculated in the next section, following [46].

2.2 Entropic forces generated by a confined passive worm-like chain

Let's consider a wormlike chain of fixed contour length (or number of monomers) that is grafted at one end to a wall and confined by a second wall at the other end, which is otherwise free to fluctuate: it will exert a force on this latter wall due to the steric constraint it imposes and this force is said to be *entropic*.

Let's take the simplest case of a grafted WLC with the grafted end perpendicular to the wall, and the obstacle wall parallel to the grafting plane (see Fig. 2.2). Let's x be the direction perpendicular to the wall and parallel to the filament's grafting direction, L the distance between the grafted end and the wall and r_x the position of the filament's end along the x direction. The presence of the confining wall determines a constraint on the filament's tip position, namely $r_x \leq L$. Since we are interested in the force due to the filament confinement, we will consider lengths $L_c \geq L$, so that the chain feels the presence of the wall.

To derive the average force that the filament exerts on the wall, let's first consider an interaction potential between the tip and the wall, $U(L - r_x(L_c))$, which is a

steep potential rapidly rising for $r_x \to L$. Later on, this potential will be turned into a hard wall potential. The partition function can be written as a path integral over all filament configurations compatible with the boundary conditions:

$$\mathcal{Z}_{/\!/}(L) = \int \mathcal{D}\left[\mathbf{r}(s)\right] \exp(-\beta(H+U)) \tag{2.26}$$

where $\beta H = \frac{\ell_p}{2} \int_0^{L_c} ds \, (\partial \mathbf{t}(s)/\partial s)^2$ and the measure is taken such that $\mathcal{Z}_{/\!/}(L) = 1$ for $U = 0$. The ensemble-averaged force acting perpendicularly to the wall is:

$$\langle f_{/\!/} \rangle(L) = \frac{1}{\mathcal{Z}_{/\!/}(L)} \int \mathcal{D}\left[\mathbf{r}(s)\right] \exp(-\beta(H+U)) \frac{\partial U}{\partial r_x(L_c)} \tag{2.27}$$

and since the wall potential depends only on the difference between L and r_x,

$$\begin{aligned} \langle f_{/\!/} \rangle(L) &= k_B T \frac{\partial}{\partial L} \ln \mathcal{Z}_{/\!/}(L) \\ &= -\frac{\partial}{\partial L} \mathcal{F}_{/\!/}(L) \end{aligned} \tag{2.28}$$

where the *compression* or *confinement* free energy of the confined chain $\mathcal{F}_{/\!/}(L) = -k_B T \ln \mathcal{Z}_{/\!/}(L)$ has been defined. If we now go to the hard wall limit ($U = 0$ for $r_x(L_c) < L$, $U = \infty$ otherwise), the partition function becomes:

$$\mathcal{Z}_{/\!/}(L) = \int \mathcal{D}\left[\mathbf{r}(s)\right] \exp(-\beta H) \Theta(L - r_x(L_c)) \equiv \langle \Theta(L - r_x(L_c)) \rangle_0 \tag{2.29}$$

where the subscript 0 means that the average is taken in the absence of the wall-tip potential (with respect to the solely bending Hamiltonian) and $\Theta(x)$ is the Heaviside step function: a given configuration is taken into account only if the tip is at the left of the wall. Thus, the free energy results from a measure of the number of the configurations compatible with the constraints, and each configuration is weighted by a Boltzmann factor for the bending energy.

We can rewrite Eq. (2.29) in terms of the probability to find the r_x at x, regardlessly of the transverse components, $P_{/\!/}(x) = \langle \delta(x - r_x(L_c)) \rangle$:

$$\begin{aligned} \mathcal{Z}_{/\!/}(L) &= \int \mathcal{D}\left[\mathbf{r}(s)\right] \exp(-\beta H) \Theta(L - r_x(L_c)) \\ &= \int \mathcal{D}\left[\mathbf{r}(s)\right] \exp(-\beta H) \int_{-L_c}^{L_c} dx \; \delta(x - r_x(L_c)) \Theta(L - x) \\ &= \int_{-L_c}^{L_c} dx \; \Theta(L - x) \langle \delta(x - r_x(L_c)) \rangle_0 \\ &= \int_{-L_c}^{L} dx \; P_{/\!/}(x) \end{aligned} \tag{2.30}$$

which expresses the *restricted* partition function as the cumulative distribution function corresponding to the probability density $P_{/\!/}(x)$. Eq. (2.28) thus becomes:

$$\begin{aligned} \langle f_{/\!/} \rangle(L) &= k_B T \frac{\partial}{\partial L} \ln \mathcal{Z}_{/\!/}(L) \\ &= k_B T \frac{P_{/\!/}(L)}{\mathcal{Z}_{/\!/}(L)}. \end{aligned} \tag{2.31}$$

2.2.1 Worm-like chain in the weak bending limit

To calculate the entropic force $\langle f_{/\!/}\rangle(L)$ is then necessary the knowledge of the probability distribution of the filament's tip position. As detailed in Appendix A.1, this distibution function is found to be, in the weak bending limit ($\ell_p \gg L_c$):

$$P_{/\!/}(x) = \frac{2\ell_p}{L_c^2}\sum_{k=1}^{\infty}(-1)^{k+1}\lambda_k \exp\left(-\frac{\lambda_k^2(L_c-x)\ell_p}{L_c^2}\right) \tag{2.32}$$

where $\lambda_k = \frac{\pi}{2}(2k-1)$. The integral in Eq. (2.30) can be explicitely evaluated now, giving:

$$\begin{aligned}\mathcal{Z}_{/\!/}(L) &= \int_{-L_c}^{L_c} dx\, P_{/\!/}(x) - \int_{-L}^{L_c} dx\, P_{/\!/}(x) = 1 - \int_{-L}^{L_c} dx\, P_{/\!/}(x) \\ &= 1 - 2\sum_{k=1}^{\infty}(-1)^{k+1}\lambda_k^{-1} + 2\sum_{k=1}^{\infty}(-1)^{k+1}\lambda_k^{-1}\exp\left(-\frac{\lambda_k^2(L_c-L)\ell_p}{L_c^2}\right) \\ &= 2\sum_{k=1}^{\infty}(-1)^{k+1}\lambda_k^{-1}\exp\left(-\frac{\lambda_k^2(L_c-L)\ell_p}{L_c^2}\right)\end{aligned} \tag{2.33}$$

since $2\sum_{k=1}^{\infty}(-1)^{k+1}\lambda_k^{-1} = 1$. From this expression it results that the dependence of the reduced partition function on L, L_c and ℓ_p appears through the ratio

$$\eta \equiv \ell_p\frac{L_c - L}{L_c^2} \qquad \text{for } L_c > L \tag{2.34}$$

which can be defined as a *reduced compression* of the filament, which takes into account its stiffness: for given L, L_c, the larger ℓ_p the larger the reduced compression. The restricted partition function exhibits the scaling property $\mathcal{Z}_{/\!/}(L|L_c,\ell_p) = \tilde{\mathcal{Z}}_{/\!/}(\eta)$, as well as the confinement free energy $\tilde{\mathcal{F}}_{/\!/}(\eta) = -k_BT\ln\tilde{\mathcal{Z}}_{/\!/}(\eta)$, and the average force becomes:

$$\begin{aligned}\langle f_{/\!/}\rangle(L,L_c) &= \frac{L_c^2}{\ell_p}\frac{\partial\tilde{\mathcal{F}}_{/\!/}(\eta)}{\partial\eta} \\ &= \frac{\pi^2}{4}\frac{\ell_p k_BT}{L_c^2}\tilde{\mathfrak{f}}(\eta)\end{aligned} \tag{2.35}$$

where we have implicitly defined the the dimensionless scaling function

$$\tilde{\mathfrak{f}}(\eta) \equiv \frac{4}{\pi^2}\frac{\partial\tilde{\mathcal{F}}_{/\!/}(\eta)}{\partial\eta}. \tag{2.36}$$

This reduced force is a rapidly increasing function of the reduced compression, going from zero to one in the interval $0 \le \eta \lesssim 0.2$, then it reaches a plateau and it stays constant, equal to 1 (see inset of Fig. 2.3). Small compressions indeed correspond to larger L, and for $L \to L_c$ ($\eta \to 0$) the probability for the tip to overlap with the wall gets smaller and smaller until for $L = L_c$ only the straight configuration is such that $r_x = L$. For large enough compressions (when $\tilde{\mathfrak{f}}(\eta) = 1$), the force exerted on the wall is equal to the Euler buckling force, $f_b = \frac{\pi^2}{4}\frac{\ell_p k_BT}{L_c^2}$, independent of L.

The length L_c such that $\eta = 0.2$ depends on the persistence length of the filament: at given L, the larger ℓ_p, the smaller the L_c that gives $\eta = 0.2$. Actin filaments, in which we are interested, have a persistence length $\ell_p \simeq 15$ μm and typical lengths in the cytoskeleton going from 10 nm to 1μm: for $L_c = 1\mu$m, it is sufficient that L be just 1% smaller than L_c, to have $\tilde{\mathfrak{f}}(\eta) = 1$. Thus actin filaments, as soon as compressed, exert a force equal to the Euler buckling force, $f_b = \frac{\pi^2}{4}\frac{\ell_p k_B T}{L_c^2}$.

2.2.2 Beyond the weak bending limit

When considering longer chains, *i.e.* increasing the ratio between the contour length and the persistence length, the reduced force $\tilde{\mathfrak{f}}(\eta)$ deviates from the universal behavior described above, increasing with η even for $\eta > 0.2$. Monte Carlo simulations on grafted (discrete) wormlike chains [53] have shown that the deviation from the plateau appeared at a η value inversely proportional to the chain contour length L_c. In those simulations, where L_c was kept constant while varying L, for increasing η (and hence decreasing L) the force rapidly increases and eventually becomes independent of L_c: this is reasonable, since if the chain is strongly bent against the obstacle, only a portion $\sim \pi L/2 \ll L_c$ of the contour length closer to the grafting point remains under compression, while the remaining part is free to lay parallel to the wall (or better to fluctuate inside the slit without pushing the wall) [54].

The reduced forces for large bent chains with different L_c show a universal behavior when plotted as a function of $\gamma = \frac{L_c - L}{L_c} = \frac{L_c}{\ell_p}\eta$, see Fig. 2.3: the force reaches the unitary plateau at a γ value which depends on L_c, but for $\gamma \gtrsim 0.1$ all the points depart from the plateau and collapse on the same curve. This behavior results to be well fitted by the following function:

$$\tilde{\tilde{\mathfrak{f}}}(\gamma) = \frac{a + b\gamma^2}{(1-\gamma)^2} + 1 \tag{2.37}$$

with $a = 0.044(5)$ and $b = 0.28(1)$ fitting parameters [54].

The full expression of the adiabatic force exerted by a wormlike chain of contour length L_c on a rigid wall at distance L from its seed is thus:

$$\langle f_{/\!/}\rangle(L, L_c) = \frac{\pi^2}{4}\frac{\ell_p k_B T}{L_c^2} \times \begin{cases} \tilde{\mathfrak{f}}\left(\gamma\frac{\ell_p}{L_c}\right) & \gamma < 0.1 \quad \text{weak bending} \\ \frac{a+b\gamma^2}{(1-\gamma)^2} + 1 & \gamma \geq 0.1 \quad \text{strong bending} \end{cases} \tag{2.38}$$

covering the whole compression range, from weak to strong bending. It is interesting to evaluate the infinite-L_c limit of the reduced force Eq. (2.38): when $L_c \gg L$, $\gamma \to 1$ and $\tilde{\tilde{\mathfrak{f}}}(\gamma)$ diverges, while the Euler buckling force goes to zero so that in the end we have:

$$\langle f_{/\!/}\rangle\left(\frac{L}{L_c} \to \infty\right) = \frac{\pi^2}{4} k_B T \ell_p \frac{a+b}{L^2} \tag{2.39}$$

independent of L_c. In this regime the force exerted by the filament is dominated by the elastic response due to pure bending, and not by the constraints imposed on the Brownian fluctuations.

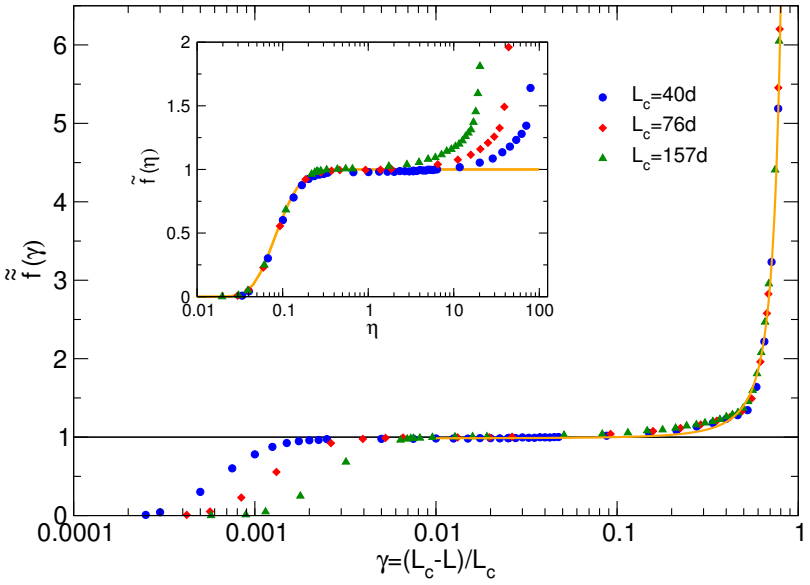

Figure 2.3. Reduced force exerted by a discrete wormlike chain against a smooth rigid wall as a function of the reduced compression $\gamma = \frac{L_c - L}{L_c} = \frac{L_c}{\ell_p}\eta$ for three different L_c values. The force grows from zero to the unitary plateau within a small range of γ depending on L_c and departs from it at $\gamma \simeq 0.1$. The orange solid line is the fitting function Eq. (2.37). In the inset, the same reduced force as a function of $\eta = \gamma \frac{\ell_p}{L_c}$, and the orange curve is the reduced force Eq. (2.36). From [54].

In this section we have derived the force that a passive (*i.e.* non growing) WLC exerts on a fixed obstacle, both in the limit of weak and large bending. In the following sections, I will apply this result to the case of *living* filaments facing a fixed or mobile wall, focusing on equilibrium conditions.

2.3 Bundle of grafted living semiflexible filaments in an optical trap setup

By *living filaments* we denote filaments that grow and shrink by adding and loosing monomers (via polymerization and depolymerization events) at their free end. These filaments will be modeled as discrete WLC, for which the results of the previous sections will be applied, with variable number of bonds (or monomers, equivalently). I recall (see Chapter 1) that by ρ_1 I indicate the density of free monomers, by $\hat{\rho}_1$ its reduced value such that if $\hat{\rho}_1 > 1$ filaments will tend to grow; $\hat{\rho}_1$ is also equal to the ratio between the polymerization rate U_0 and the depolymerization rate W_0. Moreover let's denote by d_0 the incremental size per added monomer ($d_0 = 2.7$ nm for actin filaments) and by μ_1 the chemical potential of free monomers in solution.

In this section, the Statistical Mechanics framework describing a bundle of

filaments in an optical trap setup will be built. I'll first discuss the single grafted filament case growing against a fixed obstacle [53], then I'll generalize to the case of a bundle of filaments, first facing a fixed wall and then growing in an optical trap setup [47].

2.3.1 Single grafted living filament growing against a fixed wall: escaping filament issue and non-escaping criteria

Let's consider a single filament enclosed in a rectangular box at temperature T, attached by one end to one of the bases of the cuboid and immersed in an ideal solution of free monomers that can bind to the free end of the filament. Let A be the transverse area and L the height of the box, with $L \ll \ell_p$. The filament has a variable number of monomers j and contour length $L_c = (j-1)d_0$; I will consider $j = 2$ as the permanent seed of the filament, in order to keep its orientation fixed, perpendicular to the grafting plane. It implies that if $j = 2$, the filament cannot loose any other monomer, but it can only polymerize.

A living filament in supercritical conditions ($\hat{\rho}_1 > 1$) will tend to grow, reaching an average length that will depend on the control variables $\hat{\rho}_1$ and L: one can expect that the filament will either be stalled by the wall or, thanks to its flexibility, bend enough to continue growing at the free end, sliding along the wall at L (see Fig. 2.4). When this last scenario occurs, the filament is said to be *escaping*, and we identify a filament as escaping as it becomes longer than a critical size,

$$z^*(L) = \mathrm{int}\left(\frac{\pi L}{2d_0}\right) \tag{2.40}$$

corresponding to a planar configuration which covers a quarter of a circle of radius L ($\mathrm{int}(x)$ indicates the integer part of the argument x). In Fig. 2.4 three cases are depicted: a filament just touching the wall (a), a filament bent and possibly stalled (b), and an escaping filament (c) (monomers exceeding the threshold $z^*(L)$ are drawn in red). In [55] the occurrence of escaping filaments was denoted as *pushing catastrophe*, distinguishing between this phenomenon and the classical Euler buckling instability, at variance with most of the literature where the term buckling is often used inappropriately.

When considering *equilibrium* situations, as for the calculation of the stalling force for instance, the escaping condition must be avoided, because the unhidered growth of the filament prevents the establishment of a true statistical equilibrium, but at most a stationary non-equilibrium state sets up. The *non-escaping regime* can be attained tuning the control variables $\hat{\rho}_1$ and L in such a way that the statistical weight of filaments of size $j \geq z^*(L)$ becomes negligibly small. In this case, the bias on the statistical mechanics averages will be negligible as well.

Let's denote by $\alpha_j(L)$ the ratio between the canonical partition function of a filament of size $j \geq 2$ and the canonical partition funciton of the same grafted filament in absence of the wall. This latter quantity is a function of L and j, equal to one for $L_c \leq L$ and rapidly decaying to zero for $L_c > L$; it corresponds to $\mathcal{Z}_{/\!/}(\tilde{\eta})$ of the last section [46, 53]: as a function of η, the α factor is equal to one for $\eta = 0$ and rapidly decreasing to zero for $\eta > 0$.

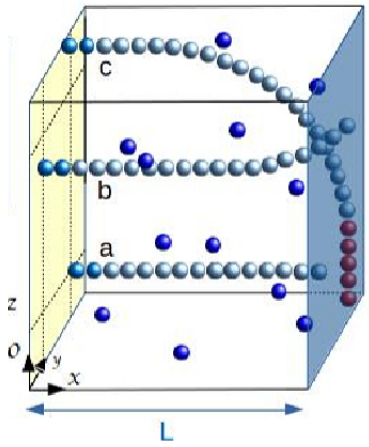

Figure 2.4. (a) A grafted filament with size $z(L)$ (see Eq. (2.51)) which corresponds to the longer size for which the filament does not interact with the wall at L; (b) a slightly bent grafted filament with net polymerization arrested by the wall; (c) an escaping filament polymerizing along the obstacle while subject to a bending mechanical force by the wall. Monomers in excess with respect $z^*(L)$ are represented in red. Adapted from [54]

It can be shown [53] (see Appendix A.2) that the grand-canonical partition function of a single growing filament in a fixed wall ensemble, can be written as the product of single filament and free monomers partition functions:

$$\begin{aligned}\Xi^R(A, L, T, \mu_1, N_f = 1) &= \Xi^{free}(A, L, T, \hat{\rho}_1) \times \Xi^{fil}(L, T, \hat{\rho}_1) \\ &= \exp\left(\beta \frac{AL}{K_0} \hat{\rho}_1\right) \times \left[\left(\frac{q_2^0 \Lambda^6}{K_0^2}\right) D(L, \hat{\rho}_1)\right] \end{aligned} \tag{2.41}$$

where K_0 is the equilibrium constant for the polymerization/depolymerization reaction in absence of loads (see Appendix A.3), $\Lambda = \sqrt{\beta h^2 / 2\pi m}$ is the free monomers de Broglie wavelength, and q_2^0 is the partition function of the grafted dimers (seeds). The factor

$$D(L, \hat{\rho}_1) = \sum_{j=2}^{z^*(L)} \alpha_j(L)\, \hat{\rho}_1^j \tag{2.42}$$

is the single living filament partition function, given the wall at L and the free monomers reduced density $\hat{\rho}_1$ [47, 53]. The link between the free monomers reduced density and the free monomers chemical potential is found to be (see Appendix A.2):

$$\hat{\rho}_1 = \frac{K_0}{\Lambda^3} \exp(\beta \mu_1) \tag{2.43}$$

like for an ideal gas. The filament size distribution at given wall position and reduced density, $P(j|L, \hat{\rho}_1)$, and the corresponding average size of the filament, $l_{fil}(L, \hat{\rho}_1)$, in

the grand canonical ensemble, are:

$$P(j|L,\hat{\rho}_1) = \frac{\alpha_j(L)\,\hat{\rho}_1^j}{D(L,\hat{\rho}_1)} \tag{2.44}$$

$$l_{fil}(L,\hat{\rho}_1) = \frac{\sum_{j=2}^{z^*(L)} j\;\alpha_j(L)\,\hat{\rho}_1^j}{D(L,\hat{\rho}_1)} = \hat{\rho}_1 \frac{\partial \ln D}{\partial \hat{\rho}_1}. \tag{2.45}$$

Moreover, the single living filament average force, $f_\perp(L,\hat{\rho}_1)$ is found to be given by the derivative with respect to L of k_BT times the logarithm of the single filament partition function Eq. (2.42) [53] (see Appendix A.2):

$$\begin{aligned}\beta f_\perp(L,\hat{\rho}_1) &= \frac{\partial \ln D}{\partial L} = \frac{\sum_{j=2}^{z^*(L)} \frac{\partial \alpha_j(L)}{\partial L}\,\hat{\rho}_1^j}{D} \\ &= \sum_{j=2}^{z^*(L)} \frac{\partial \ln \alpha_j(L)}{\partial L}\,P(j|L,\hat{\rho}_1) = \sum_{j=2}^{z^*(L)} \beta \bar{f}_j(L)\,P(j|L,\hat{\rho}_1)\end{aligned} \tag{2.46}$$

where the compression mean force potential and associated mean force at fixed j have been defined as

$$w_j(L) = -k_BT \ln \alpha_j(L) \tag{2.47}$$

$$\bar{f}_j(L) = -\frac{\partial w_j(L)}{\partial L}. \tag{2.48}$$

Note that Eq. (2.47) is the same as the confinement free energy $\mathcal{F}_{/\!/}(\eta)$ defined in Section 2.2 [46]. The mean force Eq. (2.48) is the microscopically averaged force[1] that a filament of size j exerts on the wall at L, and corresponds to Eqs. (2.35) and (2.36). The average force of a *living* filament, Eq. (2.46), is the average of this mean force weighted by the probability for the filament to have j monomers, given the wall at L.

It is worth observing that we are expressing the force exerted by a *living* filament as an average of the forces exerted by *passive* filaments, using the same expression obtained for a worm-like chain at equilibrium. It can be argued that the polymerization/depolymerization processes necessarily imply some non-equilibrium transient, with possible consequences on the force as well: however, our strategy is correct as long as there is a well defined timescales separation between the characteristic time of polymerization/depolymerization events, τ_{chem}, and the characteristic time needed by the filament to re-equilibrate after a (de)polymerization event, τ_{micro}. We will always consider situations such that the *adiabatic approximation*

$$\tau_{micro} \ll \tau_{chem} \tag{2.49}$$

is valid. The typical actin polymerization timescale realized in vitro is $\tau_{chem} \sim W_0^{-1} \sim 10^{-2}$ s, while the normal mode relaxation time of a worm-like chain is found to be [56]

$$\tau_{micro} = \frac{4\pi\eta}{\ell_p \kappa_B T q^4} \tag{2.50}$$

[1] This force is an average over the internal degrees of freedom

with $q = (n+1/2)\pi/L_c$ and η is the solvent viscosity (water). Inputing values for actin, the longest relaxation time results $\tau_{micro} \sim 10^{-9}$ s, *i.e.* $\tau_{micro}/\tau_{chem} \sim 10^{-7}$ [19].

Returning to the living filament force, clearly only configurations corresponding to $L_c > L$ will contribute to the average force. Indeed, the lower bound in the sums of Eq. (2.46) can be subsituted by $j = z(L)+1$, where $z(L)$ is the maximum number of monomers in the filament before it feels the presence of the wall:

$$z(L) = \mathrm{int}\left(\frac{L}{d_0}\right) + 1. \tag{2.51}$$

The upper boundary is $z^*(L)$ because we don't want filaments to become escaping: as already said, this will not affect the validity of these ensemble averages as long as the probability for a filament to have z^* monomers is negligibly small. We quantify this requirement by imposing that the probability $P(z^*)$ be much smaller than $P(z)$:

$$\frac{P(z^*|L,\hat{\rho}_1)}{P(z|L,\hat{\rho}_1)} = \frac{\alpha_{z^*}(L)}{\alpha_z(L)}\hat{\rho}_1^{z^*-z} = \alpha_{z^*}(L)\hat{\rho}_1^{z^*-z} \ll 1 \tag{2.52}$$

since $\alpha_z(L) = 1$. Let's take this ratio equal to a small quantity $\zeta \gtrsim 0$. Taking the logarithm of both sides and using Eq. (2.47), we find:

$$-\beta w_{z^*}(L) + (z^*(L) - z(L))\ln\hat{\rho}_1 = \ln\zeta. \tag{2.53}$$

The mean force potential $w_{z^*}(L)$ is the work that has to be performed to compress a filament of size $z^*(L)$ to make it fit the space limited by the presence of the wall: for a constant force, it would be equal to the product of this force times the compression $(z^*(L) - z(L))d_0 = (\frac{\pi}{2} - 1)\, L$. Limiting to the weak bending regime and making the approximation that the reduced force $\tilde{\mathrm{f}}(\eta)$ is constant over the whole compression region, so that the filament force is $\pi^2\ell_p k_B T/4L_c^2$ (with $L_c = (z^*(L)-1)d_0 = \pi/2\ L$), we get:

$$-\frac{\pi^2\ell_p}{4\left(\frac{\pi}{2}L\right)^2}\left(\frac{\pi}{2}-1\right)L + \left(\frac{\pi}{2}-1\right)\frac{L}{d_0}\ln\hat{\rho}_1 = \ln\zeta \tag{2.54}$$

from which a criterion for the maximum value of L is obtained (in the small ϵ limit):

$$L_{max} = \sqrt{\frac{\ell_p d_0}{\ln\hat{\rho}_1}} + \frac{d_0\ln\zeta}{(\frac{\pi}{2}-1)\ln\hat{\rho}_1} \equiv L_l + \delta_\zeta \tag{2.55}$$

with $d_\zeta < 0$ for $\zeta < 1$. If we take $\zeta = 10^{-3}$, for a typical value of $\hat{\rho}_1 = 2.5$, using $\ell_p = 5370 d_0$ for actin, we get for instance $L_{max} = 69.5 d_0$. Decreasing $\hat{\rho}_1$, the maximum pore width increases: for $\hat{\rho}_1 = 1.7$, $L_{max} = 88.4 d_0$. For comparison, the measurement of the polymerization force in the optical trap setup [10] in supercritical conditions at $\hat{\rho}_1 = 1.7$ (see Fig 4b of that reference), involves an elongation of $L \simeq 200$ nm which corresponds to about $L = 74 d_0$, compatible with the present definition of the non-escaping regime.

The mean force potential $w_j(L)$ is an important quantity useful to understand the effect of flexibility on the polymerization mechanism of a confined filament: Fig. 2.5 shows the mean force potential as a function of L for two successive sizes j (red line) and $j+1$ (blue line), for $j = 30$ (left) and $j = 60$ (right). The free

energy $w_j(L)$ is a linearly decaying function of L for $L < L_c$, while it's constant for $L > L_c$, with $L_c = (j-1)d_0$. The observed linear decay is a related to the fact that the compression force in the weak bending limit is constant, for large enough compressions ($\eta \gtrsim 0.2$). The non-linearity region which joints the linear decay and the constant region, corresponding to the increasing region of the force ($0 < \eta < 0.2$), is too small to be appreciated in the plot: for the red curve in the left panel ($j = 30$, $L_c = 29d_0$), the non-linear region would extend between $28.97d_0$ and $29d_0$. The vertical distance between the red and the blue profile corresponds to the free energy difference between the two filament states j and $j+1$, or the free energy change per added/removed monomer. In the plateau regions this difference is $k_BT \ln \hat{\rho}_1$, otherwise it is a function of L. We chose an arbitrary energy difference threshold equal to $2.5k_BT$, which corresponds to a ratio between $P(j+1)$ and $P(j) \sim 0.1$ (so that the probability of having size $j+1$ is still not negligible with respect to j): it can be seen from the figure (the red dotted line is $\beta w_j + 2.5$) that in the case $j = 30$ $\Delta w = 2.5$ for $L \simeq 29.7d_0$, while in the case $j = 60$ it happens for $L \simeq 59d_0$. It can be interpreted as follows: for a filament of size $j = 30$ and contour length $L_c = 29d_0$ to polymerize and jump to the next size $j = 31$ with a non-negligible probability, the wall must be at least at $L = 29.7d_0$. For a filament of size $j = 60$ and contour length $L_c = 59d_0$, polymerization can happen with non-negligible probability even if the wall is at $L = 59d_0$ or less. Flexibility hence increases the capability of a filament to polymerize when in contact with a barrier, and this effect is more and more pronounced as the filament size increases.

Note that in the case of a rigid filament, conversely, in order for it to polymerize, the wall position must be at least $L = L_c + d_0 = jd_0$ regardlessly of j, since the filament can't bend nor compress.

2.3.2 Bundle of living filaments growing against a fixed wall

The results obtained for the single filament can be readily generalized for a bundle of filaments [47], making the assumption that filaments are independent. Since we don't introduce steric interactions between filaments and since the confining wall is taken as rigid and planar, the transverse positions of their seeds along the grafting plane are irrelevant, while their longitudinal positions are not. Let's denote by h_n the longitudinal position of the n-th seed, $n = 1, \dots N_f$, as in Section 1.3.2, and let's take them in the staggered disposition defined in Eq. (1.17). I recall that the staggered or homogeneous seeds disposition is such that seeds are placed at regularly spaced depths along x, $|h_n - h_{n+1}| = d_0/N_f$, and distributed around zero, $\sum_{n=1}^{N_f} h_n = 0$, determining a grafting thickness $\sim d_0$ (see Fig. 1.4).

All the relevant quantities defined in the last section remain the same, but they become specific for each filament n, with the wall position L replaced by the seed-wall distance $L_n = L - h_n$, with $n = 1, \dots, N_f$. In the condition that filaments are independent, the average bundle force will be the sum of the single filament

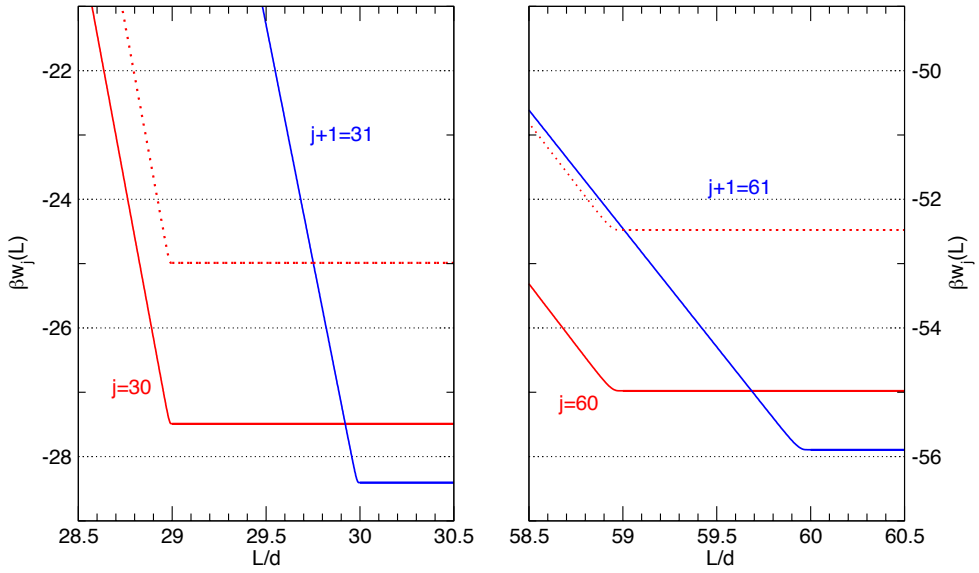

Figure 2.5. Mean force potential w_j as a function of L for filaments of successive sizes j (red solid line) and $j+1$ (blue line), for $j = 30$ (left panel) and $j = 60$ (right panel). The red dotted line corresponds to $w_j + 2.5k_BT$, and the point where it intersects the blue line is the minimum L at which the filament can be found with size $j+1$ with non-negligible probability. This happens for $L \simeq 29.7d_0$ in the $j = 30$ case and for $L \simeq 59d_0$ in the $j = 60$ case: the longer filament can polymerize even if it's already under compression, while the shortest filament must have the wall at least $0.7d_0$ larger than L_c. From [54].

mean forces Eq. (2.46):

$$F_{bun}(L) = \sum_{n=1}^{N_f} f_\perp(L_n, \hat{\rho}_1) \tag{2.56}$$

$$f_\perp(L_n, \hat{\rho}_1) = \sum_{j_n=z_n+1}^{z_n^*} P(j_n|L_n, \hat{\rho}_1)\ \bar{f}_j(L_n) \tag{2.57}$$

with $z_n = \mathrm{int}(L_n/d_0) + 1$, $z_n^* = \mathrm{int}(\pi L_n/2d_0)$ and $P(j_n|L_n, \hat{\rho}_1)$ given by Eq. (2.44).

In the case of a bundle of filaments, an interesting quantity is the number of filaments N_0 hitting the wall – hence having size larger than the corresponding z_n. The average value of N_0, which parametrically depends on L and $\hat{\rho}_1$, can be written as the sum of the probability for each filament to have size larger than z_n:

$$N_0(L, \hat{\rho}_1) = \sum_{n=1}^{N_f} \sum_{j_n=z_n+1}^{z_n^*} P(j_n|L_n, \hat{\rho}_1). \tag{2.58}$$

This quantity is a number between 0 – no filaments hitting the wall – and N_f – all the filaments hitting the wall.

Note that in the case of perfectly rigid filaments, N_0 vanishes identically. Also, in that case the concept of force becomes ill-defined since the potential of mean

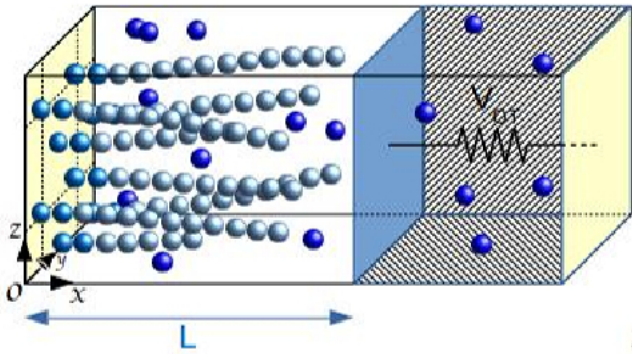

Figure 2.6. Bundle of semiflexible filaments grafted normally to a planar wall on the left and growing against a mobile loaded wall on the right. The optical trap potential is represented by a spring of constant κ_{T}, such that the force acting on the wall is $F = -\kappa_{\mathrm{T}} L$ ($V_{OT} = \frac{1}{2}\kappa_{\mathrm{T}} L$). Adapted from [54].

force of a filament of contour length L_c is either zero for $L_n \geq L_c$ or infinite for $L_n < L_c$. Correspondingly, $P(j_n|L_n, \hat{\rho}_1)$ goes to zero for $L_n < L_c$. Again, flexibility considerably enriches the scenario of the possible behaviors of grafted living filaments, which, depending on their length, can simultaneously touch the wall (while *staggered* rigid filaments cannot) contributing to the total force acting on it.

2.3.3 Bundle of living filaments growing in an optical trap

As detailed in Section 1.2.2, Footer *et al.* [10] measured the force exerted by a bundle of actin filaments in an optical trap set-up, where the growth occurred against a harmonic force. This kind of potential ensures that, in absence of escaping filaments, a true equilibrium state is eventually reached, where the trap force equals the bundle stalling force. Mimicking this experimental set-up, we construct an equivalent simple model, as depicted in Fig. 2.6, where the bundle, grafted on the left wall, grows against the wall on the right, which is now let free to move under the combined action of the growing filaments and of a spring connected to it and resembling the optical trap potential. Being κ_{T} the spring strength constant and its rest length equal to the total extent of the box (left and right chambers enclosing the bundle and the spring respectively, see Fig. 2.6), then the force acting on the wall is $F = -\kappa_{\mathrm{T}} L$, with L distance between the grafting and the moving wall.

Now the wall position is a random variable as well, and at equilibrium its position will have a probability distribution depending on the free monomers reduced density (and hence on the force they are able to exert, see Eqs. (2.44), (2.46) and (2.57)) and the trap strength, $\mathcal{P}^{\mathrm{OT}}(L|\hat{\rho}_1, \kappa_{\mathrm{T}}) \equiv \mathcal{P}^{\mathrm{OT}}(L)$. The joint distribution function for the wall position and filament sizes is given by the product of the wall position

probability function and the single filament size distributions Eq. (2.44):

$$p(L, j_1, \ldots, j_{N_f}|\hat{\rho}_1) = \mathcal{P}^{\mathrm{OT}}(L) \prod_{n=1}^{N_f} P(j_n|L_n, \hat{\rho}_1) \tag{2.59}$$

$$= \frac{\exp\left(-\beta\frac{\kappa_{\mathrm{T}}L^2}{2}\right) \prod_{n=1}^{N_f} \alpha_{j_n}(L_n)\hat{\rho}_1^{j_n}}{\int_{2d_0}^{L_R} dL' \exp\left(-\beta\frac{\kappa_{\mathrm{T}}L'^2}{2}\right) \prod_{n=1}^{N_f} D(L'_n, \hat{\rho}_1)} \tag{2.60}$$

where the compressional energy stored in the spring is $V_{OT} = \frac{1}{2}\kappa_{\mathrm{T}}L^2$. The equilibrium distribution for the variable L is (see Appendix A.4)

$$\mathcal{P}^{\mathrm{OT}}(L|\hat{\rho}_1, \kappa_{\mathrm{T}}) \equiv$$

$$\mathcal{P}^{\mathrm{OT}}(L) = \begin{cases} \dfrac{\exp\left(-\beta\frac{\kappa_{\mathrm{T}}L^2}{2}\right) \prod_{n=1}^{N_f} D(L_n, \hat{\rho}_1)}{\int_{2d_0}^{L_R} dL' \, \exp\left(-\beta\frac{\kappa_{\mathrm{T}}L'^2}{2}\right) \prod_{n=1}^{N_f} D(L'_n, \hat{\rho}_1)} & 2d_0 < L < L_R \\ 0 & \text{otherwise} \end{cases} \tag{2.61}$$

The condition $\mathcal{P}^{\mathrm{OT}}(L_R) = 0$ will not be an artefact provided that the choice of L_R and κ_{T} is adequate. Through this distribution, the average wall position and bundle force can be formally expressed as follows:

$$\langle F_{bun}\rangle^{\mathrm{OT}} = \int_{2d_0}^{L_R} dL' \, \mathcal{P}^{\mathrm{OT}}(L')F_{bun}(L') \tag{2.62}$$

$$\langle L\rangle^{\mathrm{OT}} = \int_{2d_0}^{L_R} dL \, \mathcal{P}^{\mathrm{OT}}(L')L' \tag{2.63}$$

where $F_{bun}(L)$ is given by Eq. (2.56). The measurement of the force in [10] has been achieved by monitoring the bead displacement; in these conditions, the measured force must be compared with this average over the L distribution, Eq. (2.62). It can be shown (see Appendix A.4) that these two quantities are proportional, $\langle F_{bun}\rangle^{\mathrm{OT}} = \kappa_{\mathrm{T}}\langle L\rangle^{\mathrm{OT}}$, so that the measured displacement times the trap constant is equivalent to the optical trap average (over L) of the bundle force expression, satisfying mechanical equilibrium. The average bundle force at equilibrium corresponds to the stalling force for the bundle.

To determine the third quantity of interest, *i.e* the number of filaments touching the wall in the optical trap ensemble, it is convenient to define a relative size for each filament with respect to the wall, $m_n = j_n - z_n$. The marginal distributions of these filament relative sizes, for each filament n, are:

$$Q^{\mathrm{OT}}(m_n|\hat{\rho}_1) = \int_{2d_0}^{L_R} dL \, \mathcal{P}^{\mathrm{OT}}(L)Q(m_n|L_n, \hat{\rho}_1) \tag{2.64}$$

$$Q(m_n|L_n, \hat{\rho}_1) = Q(j_n - z_n|L_n, \hat{\rho}_1) = P(m_n + z_n|L_n, \hat{\rho}_1) \tag{2.65}$$

so that

$$\langle x_0\rangle^{\rm OT} \equiv \frac{\langle N_0\rangle^{\rm OT}}{N_f} = \frac{1}{N_f}\int_{2d_0}^{L_R} dL\ \mathcal{P}^{\rm OT}(L) N_0(L,\hat{\rho}_1) \tag{2.66}$$

$$= \frac{1}{N_f}\int_{2d_0}^{L_R} dL\ \mathcal{P}^{\rm OT}(L) \sum_{n=1}^{N_f}\sum_{m_n=1}^{z_n^*(L_n)-z_n(L_n)} Q(m_n|L_n,\hat{\rho}_1)$$

$$= \frac{1}{N_f}\sum_{n=1}^{N_f}\sum_{m_n=1}^{z_n^*(L_n)-z_n(L_n)} Q^{\rm OT}(m_n|\hat{\rho}_1) \tag{2.67}$$

is the average fraction of touching filaments, going from 0 to 1. It is the optical trap average (over L) of the probability for the single filaments to have size $j_n > z_n$.

Non-escaping filaments criteria in optical trap

In Eq. (2.40) the critical size $z^*(L)$ has been defined as the maximum number of monomers before a filament becomes escaping, and the condition on the maximum pore size L_{max} has been obtained in Eq. (2.55). So far, we have imposed that a filament with size $z^*(L)$ cannot polymerize ($U_n(z^*(L)) = 0$), and we have obtained the maximum pore size by imposing that the probability of reaching the size $z^*(L)$ was negligibly small. In an optical trap set-up, the wall fluctuates around its equilibrium average position, and the condition on L in the fixed-wall ensemble translates into a condition on the trap strength $\kappa_{\rm T}$, taking into account the wall fluctuations. Intuitively, since larger $\kappa_{\rm T}$'s allow for smaller trap widths, there will be a minimum value for this parameter minimizing the probability of escaping filaments.

In the optical trap apparatus L results to be a random variable with a Gaussian distribution [47, 53] with a variance given by $\sigma_L^{\rm OT} = \sqrt{k_B T/\kappa_{\rm T}}$, and therefore a safe choice for the average wall position the optical trap is

$$\langle L\rangle^{\rm OT} < L_{max} - 3\sqrt{\frac{k_B T}{\kappa_{\rm T}}} = \sqrt{\frac{\ell_p d_0}{\ln\hat{\rho}_1}} + \delta_\zeta - 3\sqrt{\frac{k_B T}{\kappa_{\rm T}}} \tag{2.68}$$

Knowing $\langle L\rangle^{\rm OT}$ related to the bundle stalling force through $\langle L\rangle^{\rm OT} = F_{stall}/\kappa_{\rm T}$, Eq. (2.68) provides a condition for the maximum value of $\kappa_{\rm T}$ that can be used for given N_f and $\hat{\rho}_1$. A weaker trap would let the filaments become too long and eventually escape. In Section 2.4 results for the averages and distributions will be presented and the practical meaning of this condition on $\kappa_{\rm T}$ will become clear.

A special case: rigid filaments growing in an optical trap

It is instructive to apply the above treatment to the simple case of rigid filaments, for which $\ell_p = \infty$. In this case, the wall factor $\alpha_j(L)$ is either 1 for $L > L_c$, or 0 otherwise: this lets us evaluate analitically first the single fixed-wall filament size distribution $P(j|L,\hat{\rho})$ Eq. (2.44), and then the expressions for the $\mathcal{P}^{\rm OT}(L)$ and $\langle L\rangle^{\rm OT}$ Eqs. (2.61) and (2.63).

Note that a rigid filament cannot bend, so the presence of the wall will always stop the filament growth, independently of its length, without the occurrence of escaping filaments. Moreover, given the wall position L, the maximum possible size

for the n-th filament is $z_n(L_n)$, since it cannot bend nor penetrate the wall. The single filament partition function, then, is given by (see Eq. (2.42) for the definition)

$$D(L_n,\hat{\rho}_1)=\begin{cases}\displaystyle\sum_{j_n=2}^{z_n^*}\alpha_{j_n}(L_n)\hat{\rho}_1^{j_n}=\sum_{j_n=2}^{z_n}\hat{\rho}_1^{j_n}=\frac{\hat{\rho}_1^2}{\hat{\rho}_1-1}\left(\hat{\rho}_1^{z_n-1}-1\right) & 2d_0<L<\infty\\ 0 & \text{otherwise}\end{cases}. \tag{2.69}$$

Denoting by $\mathcal{N}$ the normalization of the wall position distribution function (the denominator in Eq. (2.61)), this quantity will be given by:

$$\mathcal{N}=\int_{2d_0}^{\infty}dL'\ \exp\left(-\beta\frac{\kappa_{\mathrm{T}}L'^2}{2}\right)\prod_{n=1}^{N_f}\frac{\hat{\rho}_1^2}{\hat{\rho}_1-1}\left(\hat{\rho}_1^{z_n(L')-1}-1\right) \tag{2.70}$$

Let's take, for simplicity, the case of a single filament, $N_f=1$:

$$\begin{aligned}\mathcal{N}&=\frac{\hat{\rho}_1^2}{\hat{\rho}_1-1}\int_{2d_0}^{\infty}dL'\ \exp\left(-\beta\frac{\kappa_{\mathrm{T}}L'^2}{2}\right)\left(\hat{\rho}_1^{\,\mathrm{int}(L'/d_0)}-1\right)\\ &=\frac{\hat{\rho}_1^2}{\hat{\rho}_1-1}\sum_{i=2}^{\infty}\int_{id_0}^{(i+1)d_0}dL'\ \exp\left(-\beta\frac{\kappa_{\mathrm{T}}L'^2}{2}\right)\left(\hat{\rho}_1^{i}-1\right)\\ &=\frac{\hat{\rho}_1^2}{\hat{\rho}_1-1}\sum_{i=2}^{\infty}\left(\hat{\rho}_1^{i}-1\right)\int_{id_0}^{(i+1)d_0}dL'\ \exp\left(-\beta\frac{\kappa_{\mathrm{T}}L'^2}{2}\right)\\ &=\frac{\hat{\rho}_1^2}{\hat{\rho}_1-1}\sum_{i=2}^{\infty}\left(\hat{\rho}_1^{i}-1\right)\frac{d_0}{\sqrt{2}\sigma}\int_{i/\sqrt{2}\sigma}^{(i+1)/\sqrt{2}\sigma}dy\ \mathrm{e}^{-y^2}\\ &=\frac{\hat{\rho}_1^2 d_0}{\hat{\rho}_1-1}\sqrt{\frac{\pi}{2}}\sigma\sum_{i=2}^{\infty}\left(\hat{\rho}_1^{i}-1\right)\left[\mathrm{erfc}\left(\frac{i}{\sqrt{2}\sigma}\right)-\mathrm{erfc}\left(\frac{i+1}{\sqrt{2}\sigma}\right)\right]\end{aligned} \tag{2.71}$$

where $\sigma=(\sqrt{\beta\kappa_{\mathrm{T}}d_0^2})^{-1}$. The second equivalence arises splitting the integral into a sum of integrals performed over the ranges of continuity of the step-shaped $\mathrm{int}(L/d)$ appearing in the integrand.

With this result, Eq. (2.61) can be readily written:

$$\mathcal{P}^{\mathrm{OT}}(L)=\sqrt{\frac{2\kappa_{\mathrm{T}}}{\pi k_BT}}\frac{\left(\hat{\rho}_1^{\,\mathrm{int}(L/d_0)}-1\right)\exp\left(-\beta\frac{\kappa_{\mathrm{T}}L^2}{2}\right)}{\sum_{i=2}^{\infty}\left(\hat{\rho}_1^{i}-1\right)\left[\mathrm{erfc}\left(i\sqrt{\frac{\beta\kappa_{\mathrm{T}}d_0^2}{2}}\right)-\mathrm{erfc}\left((i+1)\sqrt{\frac{\beta\kappa_{\mathrm{T}}d_0^2}{2}}\right)\right]} \tag{2.72}$$

With similar procedures (see Appendix A.6), the average trap length can be explicitly evaluated, giving:

$$\langle L\rangle^{\mathrm{OT}}=\sqrt{\frac{2k_BT}{\pi\kappa_{\mathrm{T}}}}\frac{\sum_{i=2}^{\infty}\left(\hat{\rho}_1^{i}-1\right)\left[\exp\left(-\beta\frac{i^2d_0^2\kappa_{\mathrm{T}}}{2}\right)-\exp\left(-\beta\frac{(i+1)^2d_0^2\kappa_{\mathrm{T}}}{2}\right)\right]}{\sum_{i=2}^{\infty}\left(\hat{\rho}_1^{i}-1\right)\left[\mathrm{erfc}\left(i\sqrt{\frac{\beta\kappa_{\mathrm{T}}d_0^2}{2}}\right)-\mathrm{erfc}\left((i+1)\sqrt{\frac{\beta\kappa_{\mathrm{T}}d_0^2}{2}}\right)\right]} \tag{2.73}$$

This expression, formally complicated, results to be in very close agreement with Hill's force Eq. (1.8) divided by κ_{T}. For the present optical trap ensemble, indeed,

the link with Hill's expression can be made mathematically more transparent noting that Eq. (2.73) can alternatively be expressed as

$$\langle L\rangle^{\mathrm{OT}} = \frac{1}{\kappa_{\mathrm{T}}}\frac{k_BT}{d_0}\ln\hat{\rho}_1 \times \left(\frac{\displaystyle\int_{2d_0}^{\infty} dx\ \hat{\rho}_1^{\mathrm{int}(x)} \exp\left(-\frac{\kappa_{\mathrm{T}}d_0^2}{2k_BT}x^2\right)}{\displaystyle\int_{2d_0}^{\infty} dx\ \hat{\rho}_1^{\mathrm{int}(x)} \exp\left(-\frac{\kappa_{\mathrm{T}}d_0^2}{2k_BT}x^2\right) - \sqrt{\frac{\pi k_BT}{2\kappa_{\mathrm{T}}d_0^2}}}\right) \tag{2.74}$$

where $x = L/d_0$ (see Appendix A.6). The r.h.s. of Eq. (2.74) is equal to $F_{stall}/\kappa_{\mathrm{T}}$ given by Eq. (1.8), multiplied by a term whose deviations from unity are marginal and decrease to zero as κ_{T} decreases ($\langle L\rangle^{\mathrm{OT}}$ goes to ∞). Indeed, Eq. (2.74) times κ_{T}, converges exponentially fast to Hill's value Eq. (1.8) when κ_{T} goes to zero (the length of the filament goes to infinity), for a given $\hat{\rho}_1 > 1$. This statistical mechanics proof of the well known Hill's formula, otherwise demonstrated by thermodynamic arguments, is an original result of this work [47].

The relative size optical trap distribution function Eq. (2.64) can be calculated along the same lines:

$$\begin{aligned}
Q^{\mathrm{OT}}(m) &= \int_{2d_0}^{\infty} dL\ \mathcal{P}^{\mathrm{OT}}(L)\frac{\hat{\rho}_1-1}{\hat{\rho}_1^2\left(\hat{\rho}_1^{z(L)-1}-1\right)}\hat{\rho}_1^{m+z(L)} \\
&= \sqrt{\frac{2\kappa_{\mathrm{T}}}{\pi k_BT}}\frac{\hat{\rho}_1-1}{\hat{\rho}_1^2}\ \hat{\rho}_1^{m}\frac{\displaystyle\int_{2d_0}^{\infty} dL\ \exp\left(-\beta\frac{\kappa_{\mathrm{T}}L^2}{2}\right)\hat{\rho}_1^{\mathrm{int}(L/d_0)}}{\displaystyle\sum_{i=2}^{\infty}\left(\hat{\rho}_1^{i}-1\right)\left[\mathrm{erfc}\left(i\sqrt{\tfrac{\beta\kappa_{\mathrm{T}}d_0^2}{2}}\right)-\mathrm{erfc}\left((i+1)\sqrt{\tfrac{\beta\kappa_{\mathrm{T}}d_0^2}{2}}\right)\right]} \\
&= \sqrt{\frac{2\kappa_{\mathrm{T}}}{\pi k_BT}}\frac{\hat{\rho}_1-1}{\hat{\rho}_1^2}\ \hat{\rho}_1^{m}\frac{\displaystyle\sum_{i=2}^{\infty}\int_{id_0}^{(i+1)d_0} dL\ \hat{\rho}_1^{i}\exp\left(-\beta\frac{\kappa_{\mathrm{T}}L^2}{2}\right)}{\displaystyle\sum_{i=2}^{\infty}\left(\hat{\rho}_1^{i}-1\right)\left[\mathrm{erfc}\left(i\sqrt{\tfrac{\beta\kappa_{\mathrm{T}}d_0^2}{2}}\right)-\mathrm{erfc}\left((i+1)\sqrt{\tfrac{\beta\kappa_{\mathrm{T}}d_0^2}{2}}\right)\right]} \\
&= \frac{\hat{\rho}_1-1}{\hat{\rho}_1^2}\ \frac{\displaystyle\sum_{i=2}^{\infty}\hat{\rho}_1^{i}\left[\mathrm{erfc}\left(i\sqrt{\tfrac{\beta\kappa_{\mathrm{T}}d_0^2}{2}}\right)-\mathrm{erfc}\left((i+1)\sqrt{\tfrac{\beta\kappa_{\mathrm{T}}d_0^2}{2}}\right)\right]}{\displaystyle\sum_{i=2}^{\infty}\left(\hat{\rho}_1^{i}-1\right)\left[\mathrm{erfc}\left(i\sqrt{\tfrac{\beta\kappa_{\mathrm{T}}d_0^2}{2}}\right)-\mathrm{erfc}\left((i+1)\sqrt{\tfrac{\beta\kappa_{\mathrm{T}}d_0^2}{2}}\right)\right]}\ \hat{\rho}_1^{m}
\end{aligned} \tag{2.75}$$

In Appendix A.7, the same calculations for a bundle of N_f filaments are reported. In general, the stalling force of a bundle of rigid filaments results to be given by

$$F_{stall}^{rigid} = \langle F\rangle^{\mathrm{OT}} = \kappa_{\mathrm{T}}\langle L\rangle^{\mathrm{OT}} = N_f\frac{k_BT}{d_0}\ln\hat{\rho}_1. \tag{2.76}$$

In the next section, results for the equilibrium statistical mechanics averages and distributions for rigid and flexible filaments, for both $N_f = 1$ and $N_f > 1$, will be presented, using the results obtained in this chapter.

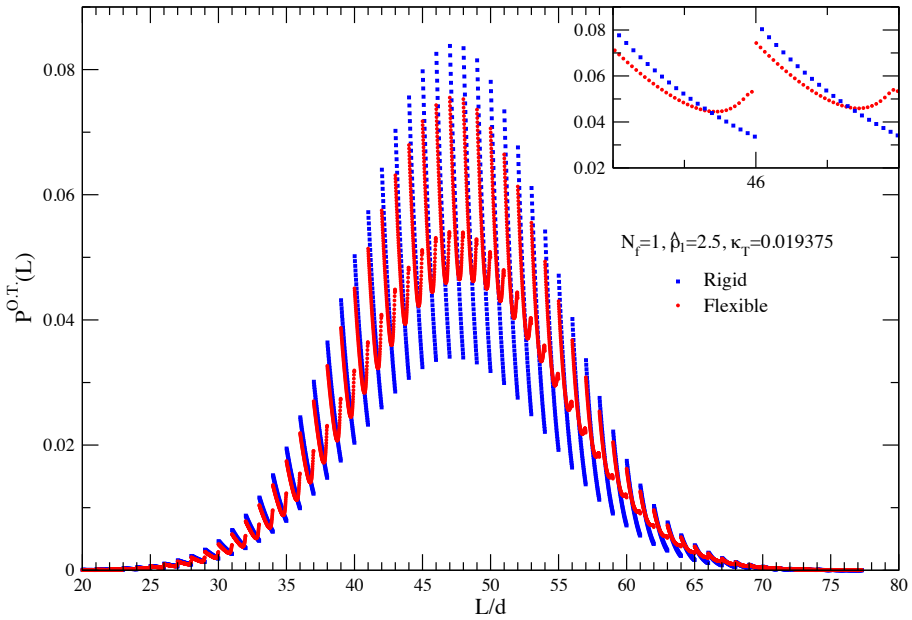

Figure 2.7. Equilibrium distribution function $\mathcal{P}^{\mathrm{OT}}(L)$ Eq. (2.61) for a single filament at $\hat{\rho}_1 = 2.5$ with $\kappa_{\mathrm{T}} = 0.019375\frac{k_B T}{d_0^2}$, rigid (blue squares) and flexible (red dots) cases. Inset: detail of the distributions in the range $L \in [45; 47]$ to show the reduction in discontinuity induced by the flexibility. From [47].

2.4 Equilibrium Statistical Mechanics results for a bundle of semiflexible filaments in an optical trap setup

In this section, I show results obtained within the model specified in the latter sections, via numerical integration of the equilibrium distribution function $\mathcal{P}^{\mathrm{OT}}(L)$ Eq. (2.61). I compare rigid and flexible behaviors, for both single filaments and bundles. I will show results for $\hat{\rho} = 2.5$ and $\hat{\rho} = 1.7$, typical values for *in vitro* experiments [10, 12]. Several values of κ_{T} have been used, chosen such that $F_{stall}/\kappa_{\mathrm{T}} \leq L_{max} - 3\sqrt{k_B T/\kappa_{\mathrm{T}}}$ (see Eq. (2.68)), using Eq. (2.76) for F_{stall}: it will be a reasonable estimate for flexible filaments as well, provided that the effects of flexibility on the stalling force are moderate.

2.4.1 Rigid and flexible single filaments

The equilibrium distribution function $\mathcal{P}^{\mathrm{OT}}(L)$ Eq. (2.61) for a single filament at $\hat{\rho}_1 = 2.5$ and $\kappa_{\mathrm{T}} = 0.019375\frac{k_B T}{d_0^2}$ is shown in Fig. 2.7 for both the rigid (red circles) and flexible (blue squares) case. The expected wall equilibrium average position from Eq. (1.9) is $L^{\mathrm{MF}} = N_f \frac{k_B T}{d_0 \kappa_{\mathrm{T}}} \ln \hat{\rho}_1 = 47.29 d_0$. In both cases, the wall position distribution function exhibits discontinuities at L values equal to integer multiples of d_0 due to the fact that in Eq. (2.72) the dependence on L comes in through the integer part of L/d_0. The magnification in the inset shows how flexibility reduces the height of these jumps. Note that the jumps are such that $\mathcal{P}^{\mathrm{OT}}(L \to n d_0{}^-) < \mathcal{P}^{\mathrm{OT}}(L \to n d_0{}^+)$; these discontinuities occur at all the possible

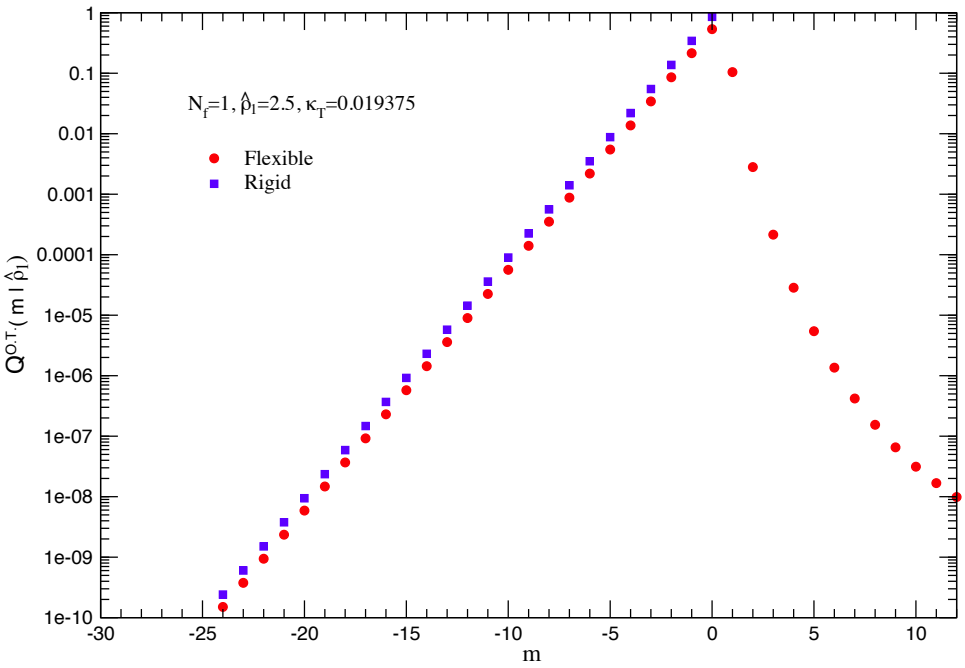

Figure 2.8. Single filament relative size distribution, Eq. (2.64), at $\hat{\rho}_1 = 2.5$ in an optical trap with $\kappa_{\rm T} = 0.019375\frac{k_BT}{d_0^2}$, for the rigid (blue squares) and flexible (red circles) cases. From [47].

positions of the rigid filament's tip $(j-1)d_0$, and given the tip at a position $(j-1)d_0$ the wall will be with most probability in contact with it, on its right, because of the condition $L \geq (j-1)d_0$. In the case of a flexible filament, instead, the wall can be also at positions $L \geq (j-1)d_0$ and this leads to the reduction of the height of the discontinuities.

A remarkable thing to notice is that the averages of L over these two distributions is almost the same: $\langle L\rangle^{\rm OT} = 47.58d_0$ in the flexible case and $\langle L\rangle^{\rm OT} = 47.29d_0$ in the rigid case, the latter being in agreement with the mean field prediction $L^{\rm MF}$ up to the 9th decimal place.

As for the stalling force, in the case of flexible filament $F_{stall} = \kappa_{\rm T}\langle L\rangle^{\rm OT} = 0.9219\frac{k_BT}{d_0}$, only 0.6% larger than the mean field prediction Eq. (1.9).

The single filament relative size distribution, Eq. (2.64) (Eq. (2.75) for the rigid case) , is shown in Fig. 2.8 for the same case ($\hat{\rho}_1 = 2.5$ and $\kappa_{\rm T} = 0.019375\frac{k_BT}{d_0^2}$), for both the rigid (blue squares) and the flexible (red circles) case. In the case of the rigid filament, only negative values of m (*i.e.* $j \leq z$) are possible, while in the flexible case m can assume also positive values (*i.e.* $j > z$), with rapidly decreasing probability. The negative-m tails are equal for the two cases (the flexible case is a bit lower because of normalization) and increase like $\hat{\rho}_1^m$. Eq. (2.67), in the case of single flexible filament, gives the ratio of the permitted filament's lengths touching the wall during the Brownian fluctuations of the wall inside the trap. It is equal to the area subtended by the positive-m tail of $Q^{\rm OT}(m)$, and for the case shown in Fig. 2.8, $\langle x_0\rangle^{\rm OT} = 0.005528 \sim 0.6\%$.

2.4.2 Bundles of rigid and flexible filaments

We compare now averages and distribution functions of homogeneous bundles of flexible and rigid filaments with $N_f = 8$ and $\kappa_T = 0.1333 \frac{k_B T}{d_0^2}$, which gives L^{MF} corresponding roughly to the limit of the escaping regime, where flexibility effects are expected to be larger. The number of filaments has been initially chosen to resemble the bundle used in experiment [10]. Fig. 2.9a shows the wall position distribution

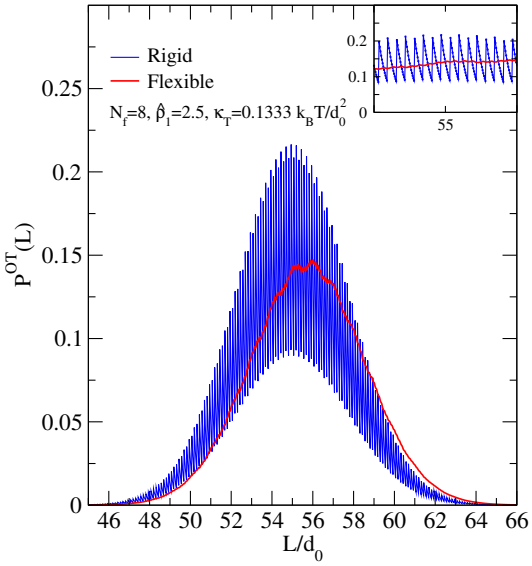

(a) Wall position distribution function in the optical trap ensemble for $N_f = 8$, $\kappa_T = 0.1333 \frac{k_B T}{d_0^2}$ giving $L^{MF} = 54.99 d_0$, for both rigid (blue line) and flexible (red line) filaments. From [47].

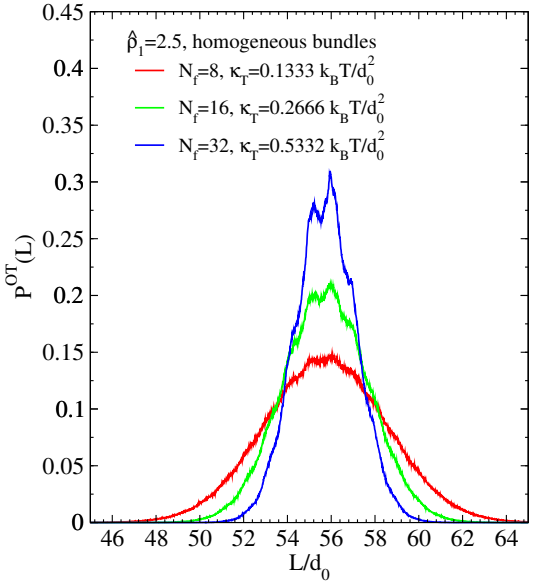

(b) Wall position distribution function in the optical trap ensemble for $N_f = 8$, 16 and 32 and $\kappa_T = 0.1333 \frac{k_B T}{d_0^2}$, $0.2666 \frac{k_B T}{d_0^2}$ and $0.5332 \frac{k_B T}{d_0^2}$ respectively. From [47].

Figure 2.9

functions for both the rigid (blue line) and flexible (red line) bundles. Both the rigid and the flexible distribution functions have an overall bell shape, but the rigid case remains discontinuous (with a distance between two successive jumps of $\Delta L = d_0/8$ now) while in the flexible case the wall position distribution function becomes continuous although with some local oscillations arising from the limited flexibility of the single filaments (see inset of Fig. 2.9a). $\mathcal{P}^{OT}(L)$ of the flexible model is slightly shifted towards larger L values: again, flexibility determines a modest enhancement of the stalling force and hence a larger average position of the trap. We obtain $\langle L \rangle^{OT} = 54.99 d_0$ for the rigid model again in perfect agreement with Hill's prediction ($54.99 d_0$), and $\langle L \rangle^{OT} = 55.75 d_0$ for the flexible model. The corresponding stalling forces are $F_{stall} = 7.33 d0$ for the rigid bundle ($F^{MF}_{stall} = 7.33 d0$) and $F_{stall} = 7.43 d0$ for the flexible bundle (1.4% larger than the mean field prediction).

Flexibility thus manifests through a slight increase in the stalling force, already detectable for a single filament but more enhanced for $N_f = 8$. Starting from this observation, we investigated cases of homogeneous bundle with different N_f but same $\langle L \rangle^{OT} \approx L^{MF} = N_f \frac{k_B T}{d_0 \kappa_T} \ln \hat{\rho}_1 = 54.99 d_0$ (the deviation from the mean

field prediction is still expected to be within few percents even for larger bundles), scaling $\kappa_{\rm T}$ proportionally to N_f. We picked $N_f = 8$, 16 and 32, and Fig. 2.9b shows the corresponding distribution functions: in any case the shape of $\mathcal{P}^{\rm OT}(L)$ is well represented by a Gaussian function centred at $\langle L\rangle^{\rm OT}$ with a width decreasing as $\sigma_L^{\rm OT} \sim \kappa_{\rm T}^{-1/2} \sim N_f^{-1/2}$ (hence a narrower profile for increasing N_f). Around the maximum some roughness is visible and increasing with N_f: the curve for 8 filaments is smoother than the one for 16 and the one for 32 filaments, which exhibit some apparently irregular "protuberances" at the top. Increasing the trap strength, this irregularities become more pronounced and the curves for 8 filaments become rapidly oscillating. The increase of roughness in the behavior must be related to the increasing stiffness of the trap: the value of κ_T needed to have the same average length of the trap for the different bundles is proportional to N_f, therefore the stronger trap is for larger N_f value.

The average trap length is found to be $\langle L\rangle^{\rm OT} = 55.75 d_0$ independently of N_f (differences arise at the third decimal place, see Table 2.1). Thus the stalling force $F_{stall} = \langle F\rangle^{\rm OT}$ is proportional to N_f: $F_{stall} = 7.43\frac{k_BT}{d_0}$ for $N_f = 8$, $F_{stall} = 14.86\frac{k_BT}{d_0}$ for $N_f = 16$ and $F_{stall} = 29.73\frac{k_BT}{d_0}$ for $N_f = 32$. In any case the calculated bundle force is $\sim 1.4\%$ larger than the mean field prediction.

Let's further define the bundle force equilibrium distribution as:

$$\begin{aligned}\mathcal{P}^{\rm OT}(F_{bun}) &\equiv \left\langle \delta\left(F_{bun} - \sum_{n=1}^{N_f} \bar{f}_{j_n}(L_n)\right)\right\rangle \\ &= \int_0^{L_R} dL \sum_{\{j_n\}} \delta\left(F_{bun} - \sum_{n=1}^{N_f} \bar{f}_{j_n}(L_n)\right)\left[\prod_{n=1}^{N_f} P(j_n|L_n,\hat{\rho}_1)\right]\mathcal{P}^{\rm OT}(L)\end{aligned} \tag{2.77}$$

where $\sum_{n=1}^{N_f} \bar{f}_{j_n}(L_n)$ is the sum of the forces exerted by each filament when the configuration of the filament sizes is $\{j_n\} = \{j_1, \ldots, j_n \ldots, j_{N_f}\}$, given by Eq. (2.48).

Fig. 2.10a shows the bundle force distribution functions for the same three cases as above, which show peaks at specific values of the force in the low-force range and have a roughly Gaussian overall shape. The amplitude of the peaks decreases strongly with N_f, to become barely visible for $N_f = 32$. Despite the peculiar differences of $\mathcal{P}^{\rm OT}(F_{bun})$ for the three bundles, as already said, the average bundle force per filament does not depend on N_f and is $\langle F\rangle^{\rm OT}/N_f = 0.9289\frac{k_BT}{d_0}$ to be compared to the mean field value $F_{stall}^{\rm MF} = 0.9163\frac{k_BT}{d_0}$, again a genuine effect of flexibility since fully rigid bundles provide results in perfect agreement with the mean field theory. The position of the maximum of the Gaussian envelope and the average force values are extensive with N_f while the position of the peaks at small force values does not depend on N_f, suggesting that they are related to single filament behaviors. Indeed, the distance between adjacent peaks is roughly equal to the value of the buckling force $f_b = \frac{\pi^2}{4}\frac{\ell_p k_B T}{L_c^2} \approx 4.3\frac{k_BT}{d_0}$ with $L_c \approx \langle L\rangle^{\rm OT} \approx 55.75 d_0$. To better understand the origin of these peaks, let's define the joint distribution function for the wall position

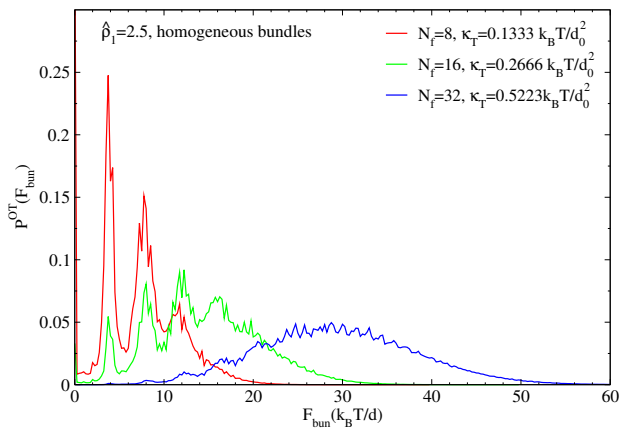

(a) Bundle force distribution function in the optical trap ensemble for $N_f = 8$, 16 and 32 and $\kappa_T = 0.1333\frac{k_BT}{d_0^2}$, $0.2666\frac{k_BT}{d_0^2}$ and $0.5332\frac{k_BT}{d_0^2}$ respectively.

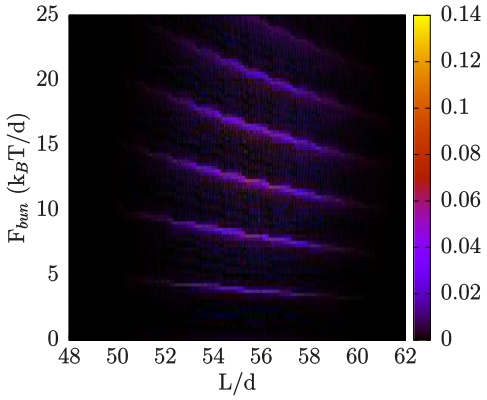

(b) Colormap of $\mathcal{P}^{\mathrm{OT}}(L, F_{bun})$, Eq. (2.78) for the $N_f = 16$ case. From [47].

Figure 2.10

and bundle force $\mathcal{P}^{\mathrm{OT}}(L, F_{bun})$ as

$$\mathcal{P}^{\mathrm{OT}}(L, F_{bun}) = \sum_{\{j_n\}} \delta\left(F_{bun} - \sum_{n=1}^{N_f} \bar{f}_{j_n}(L_n)\right) \prod_{n=1}^{N_f} P(j_n|L_n, \hat{\rho}_1)\mathcal{P}^{\mathrm{OT}}(L). \tag{2.78}$$

Fig. 2.10b shows a colormap of $\mathcal{P}^{\mathrm{OT}}(L, F_{bun})$ for the $N_f = 16$ case; these data have been obtained through a Monte Carlo sampling of the wall position, according to $\mathcal{P}^{\mathrm{OT}}(L)$, and then of the filament sizes, according to $P(j_n|L_n, \hat{\rho}_1)$, from which histograms were calculated. The joint probability distribution function presents some very specific features as well: it is composed by a sequence of crest and valleys roughly alternating in the F_{bun} direction and extending in the L direction. The crests in the low forces region are almost parallel to the L axis, while they gradually tilt by negative angles moving along the force axis. Integrating these crests over L to get the marginal $\mathcal{P}^{\mathrm{OT}}(F_{bun})$ determines the peaks observed in Fig. 2.10a, pronounced for small forces and disappearing for large ones. Along the individual crests, the force decreases with L, in agreement with the buckling force expression $\sim L_c^{-2}$. It is plausible to associate each crest to a specific number of "buckled“ filaments (in the sense of compressed enough to exert a force equal to $f_b = \frac{\pi^2}{4}\frac{\ell_p k_B T}{L_c^2}$, see Section 2.2), so that in Fig. 2.10b the first crest (from bottom up) is due to a single filament pushing the wall, the second is due to two filaments, and so on. The same applies to Fig. 2.10a: each peak arises from the contribution to the bundle force of an integer number of filaments.

Let's additionally define the distribution function of the number of touching

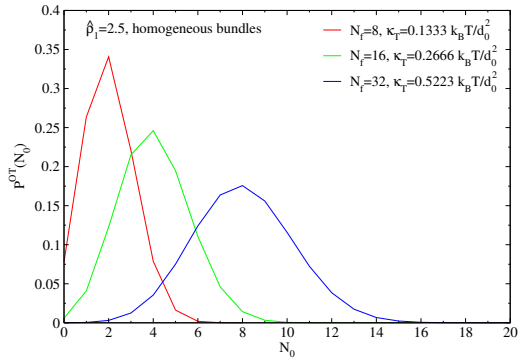

Figure 2.11. Optical trap distribution function of the number of touching filaments for $N_f = 8$, 16 and 32 and $\kappa_T = 0.1333\frac{k_BT}{d_0^2}$, $0.2666\frac{k_BT}{d_0^2}$ and $0.5332\frac{k_BT}{d_0^2}$ respectively.

filaments N_0 in the optical trap:

$$\mathcal{P}^{\rm OT}(N_0) \equiv \left\langle \delta\left(N_0 - \sum_{n=1}^{N_f}\Theta(j_n - z_n - 1)\right)\right\rangle$$
$$= \int_0^{L_R} dL \sum_{\{j_n\}} \delta\left(N_0 - \sum_{n=1}^{N_f}\Theta(j_n - z_n - 1)\right)\left[\prod_{n=1}^{N_f} P(j_n|L_n,\hat{\rho}_1)\right]\mathcal{P}^{\rm OT}(L) \tag{2.79}$$

as the marginal of the joint distribution function for L and N_0 defined as

$$\mathcal{P}^{\rm OT}(L,N_0) = \sum_{\{j_n\}} \delta\left(N_0 - \sum_{n=1}^{N_f}\Theta(j_n - z_n - 1)\right)\left[\prod_{n=1}^{N_f} P(j_n|L_n,\hat{\rho}_1)\right]\mathcal{P}^{\rm OT}(L) \tag{2.80}$$

Fig. 2.11 shows the distribution function $\mathcal{P}^{\rm OT}(N_0)$ for the same three cases as above: they are all bell-shaped functions with the average shifted towards larger N_0 as N_f increases, yet the corresponding fraction of touching filaments is the same for the three cases, $\langle x_0\rangle^{\rm OT} = N_0/N_f \sim 25\%$. If we define the average force per filament as $\langle x_0\rangle^{\rm OT}F_{stall}/N_f$, it is $\sim 3.7k_BT/d_0$ in any case, slightly smaller than (but still in good agreement with) the single filament buckling force $f_b = \frac{\pi^2}{4}\frac{\ell_p k_BT}{(\langle L\rangle^{\rm OT})^2} \sim 4.3k_BT/d_0$. This small discrepancy comes probably from the fact that we have approximated the average filament length with the average wall position, but filaments are flexible and compressed, and hence their average contour length may exceed $\langle L\rangle^{\rm OT}$. Nevertheless, given its modest extent, it is still reasonable to interpret the single filament behavior through a two-state model, where filaments are either too short to touch the wall or in their compressed state contributing to the force by a finite amount equal to $f_b(L_c) \propto L_c^{-2} \approx L^{-2}$. In this two-state model, a living bundle of given length can adjust the number of touching filaments to tune the force to be applied to resist to the external load. In this optical trap system, indeed, the equilibrium bundle force

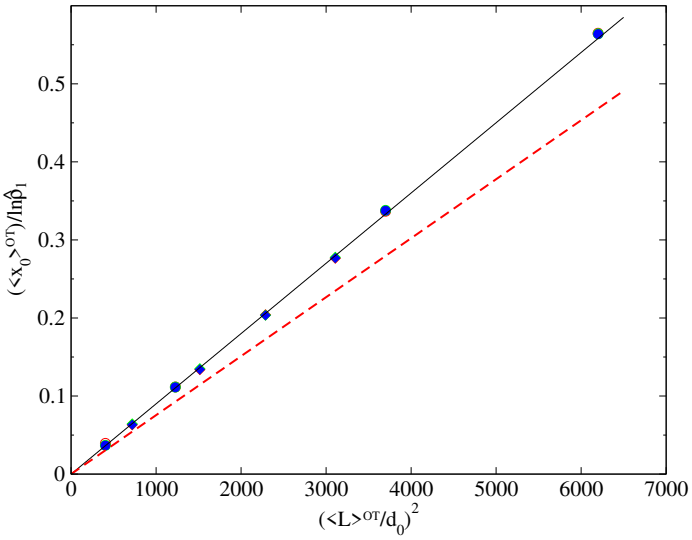

Figure 2.12. Average number of touching filaments, divided by $\ln\hat{\rho}_1$ as a function of the average wall position squared. The dashed red line is Eq. (2.82).

can be related to the average number of touching filaments as follows:

$$\begin{aligned}\langle F_{bun}\rangle^{\mathrm{OT}} &= \int_0^{L_R} dL\ \mathcal{P}^{\mathrm{OT}}(L)\ F_{bun}(L) \\ &= \int_0^{L_R} dL\ \mathcal{P}^{\mathrm{OT}}(L) \sum_{n=1}^{N_f} \sum_{j_n=z_n+1}^{z_n^*(L_n)} \frac{\pi^2}{4}\frac{\ell_p k_B T}{L_{c,j_n}^2}\tilde{\mathfrak{f}}(\eta_{j_n}) P(j_n|L_n) \\ &\approx \frac{\pi^2}{4}\frac{\ell_p k_B T}{(\langle L\rangle^{\mathrm{OT}})^2}\int_0^{L_R} dL\ \mathcal{P}^{\mathrm{OT}}(L) \sum_{n=1}^{N_f} \sum_{j_n=z_n+1}^{z_n^*(L_n)} P(j_n|L_n) = \frac{\pi^2}{4}\frac{\ell_p k_B T}{(\langle L\rangle^{\mathrm{OT}})^2} N_f \langle x_0\rangle^{\mathrm{OT}}\end{aligned} \tag{2.81}$$

where we approximated $L_{c,j}^2$ by $(\langle L\rangle^{\mathrm{OT}})^2$ and $\tilde{\mathfrak{f}}(\eta_{j_n}) = 1$. We can make the further approximation $\langle F\rangle^{\mathrm{OT}} \approx F_{stall}^{\mathrm{MF}} = N_f \frac{k_B T}{d_0}\ln\hat{\rho}_1$, to get:

$$\frac{\langle x_0\rangle^{\mathrm{OT}}}{\ln\hat{\rho}_1} \approx \frac{4}{\pi^2}\frac{1}{\ell_p d_0}\left(\langle L\rangle^{\mathrm{OT}}\right)^2. \tag{2.82}$$

Fig. 2.12 shows $\frac{\langle x_0\rangle^{\mathrm{OT}}}{\ln\hat{\rho}_1}$ as a function of $(\langle L\rangle^{\mathrm{OT}})^2$ for three homogeneous bundles with $N_f = 8$, 16 and 32 for four different κ_{T}/N_f at $\hat{\rho}_1 = 2.5$ (squares) and four at $\hat{\rho}_1 = 1.7$ (circles).

It is worth emphasize that the choice of the trap strength is crucial in order to get reliable results (not spoiled by the presence of escaping filaments): the range of κ_{T} values that let remain in the non-escaping regime can be determined as follows:

since the optical trap average stalling force is not much different from the mean field prediction Eq. (1.9), the average trap length will be $N_f \frac{k_B T}{d_0} \ln \hat{\rho}_1 / \kappa_{\rm T}$ and Eq. (2.68) becomes:

$$\frac{N_f \frac{k_B T}{d_0} \ln \hat{\rho}_1}{\kappa_{\rm T}} < \sqrt{\frac{\ell_p d_0}{\ln \hat{\rho}_1}} - 3\sqrt{\frac{k_B T}{d_0 \kappa_{\rm T}}} \tag{2.83}$$

which gives the minimum value of $\kappa_{\rm T}$ not to have escaping filaments. For $N_f = 8$ and $\hat{\rho}_1 = 2.5$, for instance, $\kappa_{\rm T}^{min} = 0.1287$.

In Fig. 2.12 data points corresponding to the same $\kappa_{\rm T}/N_f$ and $\hat{\rho}_1$ but different N_f collapse on top of each other. We can see that indeed the average fraction of touching filaments scales as $(\langle L \rangle^{\rm OT})^2$, but the slope estimated by Eq. (2.82) is $15 - 20\%$ smaller: the number of touching filaments results slightly larger than predicted by mean field theory. This is a further effect of filament flexibility: since the average polymerization force is slightly larger than the mean field stalling force, Eq. (2.82) underestimates the observed average fraction of touching filaments.

To conclude this section, Table 2.1 reports numerical results for all the mentioned cases. We report averages and RMS fluctuations for $\langle L \rangle^{\rm OT}$, $\langle F_{bun} \rangle^{\rm OT}$ and $\langle N_0 \rangle^{\rm OT}$. We have investigated two values of the reduced free monomers density, $\hat{\rho}_1 = 1.7$ and 2.5, and three values of the number of filaments in the bundle, $N_f = 8$, 16 and 32. For each specific case $(\hat{\rho}_1, N_f)$ we have selected the trap strength $\kappa_{\rm T}$ in order to cover the entire range of significant trap lengths and avoid the escaping-filaments bias. In all cases the thermal equilibrium fluctuations are in agreement with the prediction in Eq. (2.68), so that $\langle L \rangle^{O.T.}$ is well inside $L_{max} \pm 3\sigma_L^{\rm OT}$, as required to avoid escaping filaments. Moreover, trap fluctuations decrease as $\kappa_{\rm T}^{-1/2} \sim N_f^{-1/2}$. Results show, as expected, that rescaling $\kappa_{\rm T}$ with N_f provides indeed traps with the same average length, to a rather good approximation. In general, the computed average values are systematically larger than Hill's predictions by few percents. The larger deviations are observed for longer traps while shorter traps are closer to the corresponding mean field values $L^{\rm MF}$. As discussed, this behavior is ascribable to filaments' flexibility.

2.5 Concluding remarks

As a final observation, let's discuss about the results of reference [10]: they observed the growth of $N_f \approx 8$ filaments anchored to a polystyrene bead, controlled by a harmonic force in an optical trap apparatus, and growing against an immobile surface. As filaments grew, pushed the bead backwards against the harmonic force, up to the establishment of an equilibrium position, corresponding to a harmonic force equal to the stalling force. Two free monomers concentrations were used: $\rho_1 = 4$ μM and 2 μM ($\hat{\rho}_1 = 2.5$ and 1.7 respectively). The measured latex bead displacement at equilibrium was $\langle L \rangle^{\rm OT} \approx 900$ nm $\approx 300 d_0$ at $\hat{\rho}_1 = 2.5$ and $\langle L \rangle^{\rm OT} \approx 180$ nm $\approx 70 d_0$ at $\hat{\rho}_1 = 1.7$. Given the trap strength, $\kappa_{\rm T} = 0.0035 k_B T / d_0^2$ in the first case and $\kappa_{\rm T} = 0.011 k_B T / d_0^2$ in the second, the two trap lengths corresponded to apparent stalling forces equal to $\langle F_{bun} \rangle^{\rm OT} \approx 1.05\ k_B T / d_0 = 1.6$ pN and $\langle F_{bun} \rangle^{\rm OT} \approx 0.72\ k_B T / d_0 = 1.1$ pN respectively. Eq. (1.9) gives, for these parameters, $F_{stall}^{\rm MF} = 6.31\ k_B T / d_0$ and $4.25\ k_B T / d_0$ respectively. To interpret these results, they based on the following criterion: if the force was smaller than the single filament buckling force at the

Table 2.1. Average values of the wall positions, the polymerization force and the number N_0 and the fraction x_0 of filaments touching the wall and respective RMS fluctuations for the selected values of the κ_{T}, $\hat{\rho}_1$ and N_f for homogeneous bundles. All values are expressed in reduced units based on length d and energy k_BT. The first column labels different parameter sets.

N_f	$\hat{\rho}_1$	κ_{T}	L^{MF}	$\langle L\rangle^{\mathrm{OT}}$	σ_L^{OT}	F_{stall}^{MF}	$\langle F_{bun}\rangle^{\mathrm{OT}}$	σ_F^{OT}	$\langle N_0\rangle^{\mathrm{OT}}$	$\sigma_{N_0}^{\mathrm{OT}}$	$\langle x_0\rangle^{\mathrm{OT}}$
8	1.7	0.05500	78.1818	78.7368	4.3182	4.2450	4.3312	0.04350	2.3977	0.2796	0.2997
		0.07075	60.0004	60.8220	3.7902		4.3032	0.1535	1.4293	0.2129	0.1787
		0.1221	34.7668	35.0241	2.8727		4.2765	0.9910	0.4737	0.1490	0.05921
		0.2122	20.0048	20.0896	2.1745		4.2630	3.7011	0.1598	0.1383	0.01998
	2.5	0.1333	54.9912	55.7469	2.7661	7.3303	7.4311	0.3056	2.0272	0.2625	0.2534
		0.1550	47.2924	47.8241	2.5570		7.4127	0.5433	1.4957	0.2369	0.1870
		0.1900	38.5807	38.9259	2.3049		7.3959	1.0466	0.9817	0.2146	0.1227
		0.2750	26.6557	26.8178	1.9130		7.3728	2.8637	0.4633	0.2009	0.05791
16	1.7	0.1100	78.1818	78.7439	3.0699	8.4900	8.6618	0.02488	4.7895	0.3835	0.2993
		0.1415	60.0004	60.8219	2.6823		8.6063	0.06557	2.8687	0.2777	0.1793
		0.2443	34.7668	35.0098	2.0308		8.5529	0.6766	0.9459	0.1639	0.05912
		0.4245	20.0048	20.0856	1.5375		8.5279	3.3587	0.3132	0.1396	0.01957
	2.5	0.2666	54.9912	55.7456	1.9559	14.6606	14.8618	0.1444	4.0714	0.3304	0.2545
		0.3100	47.2924	47.8236	1.8080		14.8253	0.2865	2.9844	0.2846	0.1865
		0.3800	38.5807	38.9259	1.6298		14.7918	0.6584	1.9793	0.2408	0.1237
		0.5500	26.6557	26.8186	1.3526		14.7503	2.2412	0.9425	0.2038	0.05890
32	1.7	0.2200	78.1818	78.7411	2.1705	16.9801	17.3230	0.04285	9.5716	0.5321	0.2991
		0.2830	60.0004	60.8213	1.8966		17.2124	0.07504	5.7321	0.3756	0.1791
		0.4886	34.7668	35.0098	1.4360		17.1058	0.3562	1.8876	0.1964	0.05899
		0.8490	20.0048	20.0856	1.0872		17.0525	2.6196	0.6215	0.1423	0.01942
	2.5	0.5332	54.9912	55.7449	1.3830	29.3213	29.7232	0.1544	8.1150	0.4368	0.2536
		0.6200	47.2924	47.8233	1.2785		29.6504	0.2155	5.9646	0.3645	0.1864
		0.7600	38.5807	38.9258	1.1524		29.5836	0.3716	3.9302	0.2929	0.1228
		1.100	26.6557	26.8187	0.9564		29.5006	1.4525	1.8542	0.2216	0.05794

observed average length, $f_b = \frac{\pi^2}{4}\frac{k_B T \ell_p}{(\langle L \rangle^{\mathrm{OT}})^2}$, then the measurement was considered reliable and the measured force identified with the stalling force, otherwise the measure was discarded as considered meaningless. The first case ($\hat{\rho}_1 = 2.5$) fitted this latter condition, and hence it was rejected. The second case ($\hat{\rho}_1 = 1.7$) instead fell into the former condition and therefore was considered a correct measure of the bundle polymerization force. According to our analysis related to the occurrence of escaping filaments, instead, both the adopted trap constants were too weak to impede the phenomenon, hence the probability of having escaping filaments was not negligible. A reasonable explanation for the small force that has been measured is that most of the filaments in the bundle were escaped, contributing with an elastic force as discussed in Section 2.2.2.

To conclude and resume this chapter, the statistical mechanics formalism for a homogeneous bundle of filaments growing in an optical trap setup has been developed, basing on the expression for the passive worm-like chain entropic force found in [46], in the approximation that the characteristic timescale of chemical reactions $\tau_{chem} \sim W_0^{-1}$ is large compared to the chain relaxation time τ_{micro}. The interest in the optical trap set up is that it allows to establish a genuine equilibrium state, which can be treated through the equilibrium statistical mechanics tools. The model was built to explicitly include flexibility in the filament modelling, yet it can be applied to rigid filaments as well, for which exact expressions for the probability distribution of the wall position and its expected value. This last expression, in particular, reduced to the well-known mean field expression Eq. (1.9) [5] in the $\kappa_{\mathrm{T}} \to 0$ limit. Taking into account flexibility made us distinguish between two different regimes: the *stalling regime* where filaments are compressed and exert a force equal to the Euler buckling force $\frac{\pi^2}{4}\frac{k_B T \ell_p}{L_c^2}$, and the *escaping regime* where filaments bend so much that they grow sliding along the opposite wall, not pushing it by polymerization anymore but only resisting with the elastic force due to bending. In the non-escaping regime, attained by properly choosing κ_{T} and $\hat{\rho}_1$ flexibility seems to have the effect of slightly enhancing the stalling force, with an intensity slightly increasing with the average bundle length (and hence the degree of flexibility). Yet this amplification amounts to at most few percent, and the stalling force can thus be considered roughly equal to the mean field prediction Eq. (1.9), and independent of the bundle length. The second interesting observation is that the number of filament in permanent contact with the wall scales like $(\langle L \rangle^{\mathrm{OT}})^2$: since each filament provides a contribution to the total force proportional to $L_c^{-2} \sim (\langle L \rangle^{\mathrm{OT}})^{-2}$, and since the total force must remain L-independent, the number of pushing filaments must scale like the trap amplitude squared.

In the next chapter, the same formalism will be applied to a non-equilibrium situation: we will follow the filaments growing from the seeds up to the establishment of the wall equilibrium position (or up to the point they become escaping), like they actually did in [10], and we will extract the velocity-load relationship for homogeneous bundles of semiflexible filaments.

Chapter 3

Stochastic Dynamics simulations of semi-flexible filaments growing against a load

The last chapter has been focused on the equilibrium properties of a stalled bundle of semiflexible filaments in an optical trap apparatus, building the equilibrium Statistical Mechanics framework for this system. The stalling force, the average bundle length, the average number of filaments touching the wall have been calculated, all at equilibrium. If we now want to access information on quantities like the velocity-load relationship, we have to move to non-equilibrium conditions, and reformulate the problem following a more suitable approach: the time evolution of the filaments+wall system can be written in terms of a Markov process, which can be numerically solved by producing statistically correct trajectories simulating the time evolution of the system, using e.g. *a classical Gillespie algorithm [57]. We will consider the relaxation of the system in an optical trap set up, where filaments start growing in contact with the wall from a small size up to stalling, when in absence of escaping filaments the polymerization force equals the trap force. Following the wall position in time, the instantaneous wall velocity and the corresponding force opposing the filaments growth can be calculated and, in principle, the velocity-load curve constructed. Notice that from a single optical trap relaxation almost the entire $v(F)$ relationship can be obtained, while a single experiment in constant load set up provides a single point on the curve (one stationary velocity for one value of the force). The equivalence between the two protocols will be ensured again by the wide timescale separation between the change of the load (slow) and the time interval over which the chemical events take place and the bundle tips relax (fast). This separation of timescales implies that during the slow variation of the trap amplitude, and thus of the load, the distribution of the filament lengths (with respect to the position of the obstacle) remains equivalent to the distribution in a hypothetical constant load experiment with the load value set to the optical trap load at the current stage of the relaxation process. This finding holds for any value of N_f and trap strength in the non-escaping regime which emphasizes the general character of the results.*

This chapter is organized as follows: in Section 3.1 the time evolution of the system is written in terms of a Fokker-Planck equation for the joint probability

distribution function for the wall position and filament sizes. These equations will be handled to get a discrete Markov chain in continuous time, and the simulation algorithm will be presented. A further approximation for rigid filaments will simplify the problem and allow for a more efficient algorithm. In Section 3.2 results from this approach are presented for bundles in optical trap set up (flexible and rigid filaments) and under constant load (rigid filaments only). In Section 3.3 it will be shown how flexibility determines a considerable enhancement of the power ($v \times F$) of transduction of chemical into mechanical energy, with respect to the rigid case. For short filaments (strong traps) the effect of flexibility is negligible and the power closely follows the behavior predicted by the Brownian Ratchet model for rigid filaments (Partial Load Sharing). As the bundle length increases (weaker traps), the power progressively increases towards the Perfect Load Sharing mean field behavior given by Eq. (1.13)*, indicating that flexibility induces better work sharing capacities in the bundle. However, this behavior cannot be reached without incurring in the escaping filament regime described here within the same unified approach. A simple* ansatz *combining linearly the Perfect Load Sharing and the rigid brownian ratchet behaviors provides a satisfactory description of the data in the non-escaping regime.*

This chapter is based on the results presented in [45, 54].

3.1 Fokker-Planck Equations and stochastic dynamics simulation algorithm

Let's consider a bundle of N_f filaments, grafted at the pointed end to a planar substrate with a staggered disposition of the seeds (see Eq. (1.17)), and growing against a moving wall, opposing a force $F(L)$ (generically depending on the wall position) to the bundle growth, as sketched in Fig. 1.4. At a given time, our system can be represented by a set of variables for the wall position and the filament sizes, namely $\{L, j_1, \ldots, j_{N_f}\}$ (j_n number of monomers in the n-th filament, see Chapter 2). Since filaments grow and shrink and the wall moves, these variables depend on time, and since they change in a stochastic fashion, they form a set of stochastic variables. The wall undergoes a diffusive motion with diffusion coefficient D; filaments polymerize and depolymerize with rates (see Appendix A.5)

$$W_{j_n}(L) = W_0 \tag{3.1}$$

$$U_{j_n}(L) = \frac{\alpha_{j_n+1}(L)}{\alpha_{j_n}(L)}\, U_0 \tag{3.2}$$

with the wall factors $\alpha_{j_n}(L)$ defined in Section 2.3.1 (see Appendix A.2, Eq. (A.20)). Note that this notation can be applied to both the flexible and rigid cases: in the latter, $\alpha_{j_n}(L) = \Theta(L - (j_n - 1)d_0 - h_n)$, *i.e.* filaments can only polymerize when the gap between their tip and the wall is larger than or equal to d_0. In the flexible case, instead, $\alpha_{j_n}(L)$ is a smooth function also equal to one for $L > (j_n - 1)d_0 + h_n$, but allowing for non-zero $U_{j_n}(L)$ for a range of wall positions $L < (j_n - 1)d_0 + h_n$, depending on the filament's persistence and contour lengths.

Let $\mathcal{P}_{j_1,\ldots,j_{N_f}}(L, t)$ be the time-dependent joint distribution function for the set $\{L, j_1, \ldots, j_{N_f}\}$: its time evolution can be described by a set of Fokker-Planck

equations[1] mixing a continuous process in space for the wall diffusion and a discrete process for the filaments' sizes. For the model defined above, we have:

$$\begin{aligned}
&\frac{\partial \mathcal{P}_{j_1,\dots,j_{N_f}}(L,t)}{\partial t} + \frac{\partial}{\partial L} J_{j_1,\dots,j_{N_f}}(L,t) \\
&= U_0 \sum_{n=1}^{N_f} \left[(1-\delta_{2,j_n}) \frac{\alpha_{j_n}(L)}{\alpha_{j_n-1}(L)} \mathcal{P}_{j_1,\dots,j_n-1,\dots,j_{N_f}}(L,t) - \frac{\alpha_{j_n+1}(L)}{\alpha_{j_n}(L)} \mathcal{P}_{j_1,\dots,j_n,\dots,j_{N_f}}(L,t) \right] \\
&+ W_0 \sum_{n=1}^{N_f} \left[\mathcal{P}_{j_1,\dots,j_n+1,\dots,j_{N_f}}(L,t) - (1-\delta_{2,j_n}) \mathcal{P}_{j_1,\dots,j_n,\dots,j_{N_f}}(L,t) \right]
\end{aligned} \tag{3.3}$$

where the probability current density is

$$J_{j_1,\dots,j_{N_f}}(L,t) = -D \left[\frac{\partial \mathcal{P}_{j_1,\dots,j_{N_f}}(L,t)}{\partial L} - \frac{F(L)}{k_B T} \mathcal{P}_{j_1,\dots,j_{N_f}}(L,t) \right]. \tag{3.4}$$

$F(L)$ is a generic L-dependent compressive load applied to the obstacle: the particular cases of a harmonic (optical trap) load $F(L) = -\kappa_T L$ and a constant load $F < 0$ will be investigated in the following. Eq. (3.3) contains the wall diffusion part $\frac{\partial}{\partial L} J_{j_1,\dots,j_{N_f}}(L,t)$ in the l.h.s, which is continuous in space, and the stochastic jumps for the filament sizes in the r.h.s., which describes a discrete process. The red term indicates the polymerization event $j_n - 1 \to j_n$, the blue term is for the polymerization event $j_n \to j_n + 1$, the green term is for the depolymerization $j_n + 1 \to j_n$, the purple term is for the depolymerization $j_n \to j_n - 1$. These latter sink and source terms are written assuming that transitions can only occur between adjacent microscopic states defined as states with all the j_n identical, except one that can change by one unit. The δ functions ensure that filaments cannot be smaller than $j_n = 2$ (the seed).

The general normalization condition for the joint distribution function is

$$\int_{2d_0}^{L_R} \sum_{j_1=2}^{z_1^*(L)} \cdots \sum_{j_{N_f}=2}^{z_{N_f}^*(L)} \mathcal{P}_{j_1,\dots,j_{N_f}}(L,t)\, dL = 1. \tag{3.5}$$

where L_R is the total length of the box enclosing filaments, free monomers and wall (see Fig. 2.6). Note that in the case of flexible filaments, only with a harmonic force (or a generic L-dependent force) it is possible to reach an equilibrium situation with an average wall position much smaller than L_R, so that the boundary condition $\mathcal{P}^{EQ}_{j_1,\dots,j_{N_f}}(L_R) = 0$ can be applied with no biases and the occurrence probability of escaping filaments is minimized, as discussed in Section 2.3.3. Conversely, in the case of a constant load, as long as there is an imbalance between the external force F and the bundle stalling force, the wall will keep moving in one of the two possible directions, until all the filaments either become too short to further depolymerize ($F > F_{stall}$) or get escaping ($F < F_{stall}$).

In order to solve Eq. (3.3) and get rid of its mix discrete-continuous character, it is convenient to approximate it by a purely discrete process by discretizing the wall position with a grid step $\delta = d_0/M$ with M integer and $M \gg 1$. The wall is hence

[1] It is a set of equations, one for each set $\{j_1, \dots, j_{N_f}\}$.

allowed to move by backward or forward jumps of width δ, and in the variables set the position L is substituted by the discrete variable

$$k = \text{int}\left[\frac{L}{\delta}\right] \tag{3.6}$$

so that the diffusive part of Eq. (3.3) becomes a finite difference equation in k. The whole process can be thus seen as a discrete Markov chain in continuous time, where the system, given a state $\{k, j_1, \ldots, j_n, \ldots, j_{N_f}\}$, can jump to another state which differs from the previous by only one variable by ± 1 units, namely $\{k, j_1, \ldots, j_n \pm 1, \ldots, j_{N_f}\}$ or $\{k \pm 1, j_1, \ldots, j_n, \ldots, j_{N_f}\}$. The time interval between two successive jumps is a random variable as well, but continuous. Each state is hence connected to $2(N_f + 1)$ possible states, and the probabilities for each jump depend only on the current values of the variables (which is a characteristic of Markov processes). A continuous time Markov process can always be described by the vectorial *forward* equation [58]

$$\frac{d\mathbf{P}}{dt} = \mathbf{P}\mathrm{Q} \tag{3.7}$$

where $\mathbf{P}(t)$ is the probability vector field and Q is the generator matrix of the Markov chain. In our case $\mathbf{P}(t) \equiv \{\mathrm{P}_{k,j_1,\ldots,j_{N_f}}(t)\}$ and the Q-matrix elements contain the (de)polymerization rates for the filament and the forward/backward jump rates for the wall, and they can be obtained starting from Eqs. (3.3) and (3.4), as reported in Appendix A.8 [59]. Denoting by $F_{k+1/2}$ the forward jump rate from $k\delta$ to $(k+1)\delta$ and by $B_{k+1/2}$ the backward jump rate from $(k+1)\delta$ to $k\delta$, they read:

$$F_{k+1/2} = \frac{D}{\delta^2}\frac{\Delta\Phi_{k+1/2}}{k_B T\left(\exp\left(-\frac{\Delta\Phi_{k+1/2}}{k_B T}\right) - 1\right)} \tag{3.8}$$

$$B_{k+1/2} = -\frac{D}{\delta^2}\frac{\Delta\Phi_{k+1/2}\exp\left(-\frac{\Delta\Phi_{k+1/2}}{k_B T}\right)}{k_B T\left(\exp\left(-\frac{\Delta\Phi_{k+1/2}}{k_B T}\right) - 1\right)} \tag{3.9}$$

whose final expression will depend on the choice of the external potential, being Φ the potential related to the external load, and $\Delta\Phi_{k+1/2}$ the difference between this potential at sites $k+1$ and k respectively. For the two cases we will consider we have:

$$\Delta\Phi_{k+1/2} = \begin{cases} F\delta & \text{constant load,} \\ \frac{1}{2}\kappa_{\mathrm{T}}\delta^2\left((k+1)^2 - k^2\right) & \text{optical trap.} \end{cases} \tag{3.10}$$

The non-zero matrix elements of the Q-matrix for the Markov process can now be explicitly written:

$$\mathrm{Q}_{\{k,j_1,\ldots,j_n\ldots,j_{N_f}\},\{k+1,j_1,\ldots,j_n\ldots,j_{N_f}\}} = F_{k+1/2} \tag{3.11}$$

$$\mathrm{Q}_{\{k,j_1,\ldots,j_n\ldots,j_{N_f}\},\{k-1,j_1,\ldots,j_n\ldots,j_{N_f}\}} = B_{k-1/2} \tag{3.12}$$

$$\mathrm{Q}_{\{k,j_1,\ldots,j_n\ldots,j_{N_f}\},\{k,j_1,\ldots,j_n+1\ldots,j_{N_f}\}} = U_{j_n}(k\delta) \tag{3.13}$$

$$\mathrm{Q}_{\{k,j_1,\ldots,j_n\ldots,j_{N_f}\},\{k,j_1,\ldots,j_n-1\ldots,j_{N_f}\}} = W_0 \tag{3.14}$$

$$\mathrm{Q}_{\{k,j_1,\ldots,j_n\ldots,j_{N_f}\},\{k,j_1,\ldots,j_n\ldots,j_{N_f}\}} = -F_{k+1/2} - B_{k-1/2} - \sum_{n=1}^{N_f}\left(U_{j_n}(k\delta) + W_0\right) \tag{3.15}$$

where I have used Eqs. (3.1) and (3.2) for the filaments (de)polymerization rates. The row sums of this matrix are zero, as required for the generator matrix of a Markov process,

$$\sum_{\{k',j'_1,\ldots,j'_n\ldots,j'_{N_f}\}} \mathrm{Q}_{\{k,j_1,\ldots,j_n\ldots,j_{N_f}\},\{k',j'_1,\ldots,j'_n\ldots,j'_{N_f}\}} = 0. \tag{3.16}$$

This matrix has a huge dimensionality – still finite if we limit the filaments sizes and the wall position to the non-escaping regime – and the analytical solution of Eq. (3.7) is not a feasible route. Nonetheless, given a state $\{k, j_1, \ldots, j_n \ldots, j_{N_f}\}$ only $2(N_f + 1)$ possible finite states exist, and the rates of going to any of them are given in Eqs. (3.11) to (3.15) and can be easily calculated. This allows us to calculate, for a given state, the probability to go to any of the accessible states, suggesting to rather simulate the time evolution of the system. Indeed, the numerical solution of Eq. (3.7) can be obtained by producing a number of realizations of the discrete Markov chain, from which histograms and averages can be calculated. To do this we employed the Gillespie algorithm [57], by which, given an initial state, the next one is determined by picking one of the accessible states, following certain probabilistic rules and producing statistically correct trajectories. Let's denote by $i_0 \equiv \{k, j_1, \ldots, j_n \ldots, j_{N_f}\}$ the current state of the system. At each step two random variables are sampled: the time interval to the next jump τ and the final state i_m (or equivalently the index of the jump m). From general Markov chain theory, τ is known to have an exponential distribution with a parameter given by $-\mathrm{Q}_{i_0 i_0} = -\sum_{i_m \neq i_0} \mathrm{Q}_{i_0 i_m}$, while the probability for the m-th state is given by the ratio between $\mathrm{Q}_{i_0 i_m}$ and $|\mathrm{Q}_{i_0 i_0}|$ [58]. The algorithm, at each time step, follows this scheme:

1. Given i_0, every non-zero $\mathrm{Q}_{i_0 i_m}$ is calculated.
2. The time interval to the next move is determined using the direct method following from the standard inversion method of the Monte Carlo theory [60]: a random number $r_1 \in [0, 1]$ is generated from a uniform distribution and
$$\tau = \frac{1}{|\mathrm{Q}_{i_0 i_0}|} \ln \frac{1}{r_1}. \tag{3.17}$$
3. The index of the next move is determined similarly: a second random number $r_2 \in [0, 1]$ is sampled and m is taken as the smallest integer satisfying the following relation
$$\sum_{n=1}^{m-1} \frac{\mathrm{Q}_{i_0 i_n}}{|\mathrm{Q}_{i_0 i_0}|} < r_2 \leqslant \sum_{n=1}^{m} \frac{\mathrm{Q}_{i_0 i_n}}{|\mathrm{Q}_{i_0 i_0}|}. \tag{3.18}$$
4. The state vector is updated to $i_0 \to i_m$ and the time incremented by τ.
5. repeat from point 1., or end the simulation.

The state vector $\{k, j_1, \ldots, j_n \ldots, j_{N_f}\}$ is stored for the calculation of histograms and averages.

The system evolution will be governed by different timescales, relative to different processes: the already defined τ_{chem} (typical time interval between two

(de)polymerizations), τ_{micro} (characteristic time needed for a chain to re-equilibrate after a (de)polymerization), and the timescale related to the diffusive motion of the wall, $\tau_D = d_0^2/D$. To get an idea of the value of τ_D we can consider the experiment [10], where the moving obstacle was a polystyrene bead of ~ 1 μm of diameter; considering water as solvent and applying the Stoke's law, we have $D = \frac{k_B T}{6\pi R\eta} \approx 2.2 \times 10^{-4}$ nm^2/s, with $\eta = 10^{-3}$ Pa·s the water viscosity, $R = 1$ μm the bead radius and $k_B T = 4.14$ k$_B$T. Thus $\tau_D \approx 3.3 \times 10^{-5}$ s $\approx 5 \times 10^{-5} \tau_{chem}$; defining $\epsilon = \tau_D/\tau_{chem}$, in typical *in vitro* experiments $\epsilon \ll 1$[2]. In the case of rigid bundles the limit $\epsilon \to 0$ can be taken, according to which the wall immediately re-equilibrates after any change of the position of the most advanced tip (*i.e.* the wall position distribution function is always equal to its equilibrium form) and the problem simplified. In this way, the elimination of the fast motion of the wall allows to go to longer times, since the dimensionality of the problem is reduced. We will see this in the next subsection.

3.1.1 Fokker-Planck equation in the $\epsilon = 0$ limit

Let's consider the case of a bundle of rigid filaments growing against an external load. Given the wide timescale separation ($\epsilon \ll 1$), it is convenient to rewrite Eq. (3.3) in such a way to put in evidence the parameter ϵ and take the limit $\epsilon = 0$ [45], thanks to which the wall and filaments motions can be separated. The interest of this limit is justified by the fact that in *in vitro* experiments with actin bundles coupled to colloidal particles (*e.g.* the optical trap experiment [10]), the typical value of this timescales ratio is $\epsilon \ll 1$, as anticipated. Let's define $\tilde{t} = W_0 t$, $x = \frac{L}{d_0}$ and $f = \frac{F d_0}{k_B T}$ and multiply Eq. (3.3) by $\frac{d_0^2}{D}$ to get:

$$\begin{aligned}
&\epsilon \frac{\partial \widetilde{\mathcal{P}}_{j_1,\dots,j_{N_f}}(x,\tilde{t}\,)}{\partial \tilde{t}} + \frac{\partial}{\partial x}\widetilde{J}_{j_1,\dots,j_{N_f}}(x,\tilde{t}\,) \\
&= \epsilon \left\{ \hat{\rho}_1 \sum_{n=1}^{N_f} \left[(1-\delta_{2,j_n}) \frac{\alpha_{j_n}(x)}{\alpha_{j_n-1}(x)} \widetilde{\mathcal{P}}_{j_1,\dots,j_n-1,\dots,j_{N_f}}(x,\tilde{t}\,) - \frac{\alpha_{j_n+1}(x)}{\alpha_{j_n}(x)} \widetilde{\mathcal{P}}_{j_1,\dots,j_{N_f}}(x,\tilde{t}\,) \right] \right. \\
&\left. + \sum_{n=1}^{N_f} \left[\widetilde{\mathcal{P}}_{j_1,\dots,j_n+1,\dots,j_{N_f}}(x,\tilde{t}\,) - (1-\delta_{2,j_n}) \widetilde{\mathcal{P}}_{j_1,\dots,j_{N_f}}(x,\tilde{t}\,) \right] \right\}
\end{aligned} \tag{3.19}$$

with

$$\widetilde{J}_{j_1,\dots,j_{N_f}}(x,\tilde{t}\,) = -\frac{\partial}{\partial x}\widetilde{\mathcal{P}}_{j_1,\dots,j_{N_f}}(x,\tilde{t}\,) - f(x)\widetilde{\mathcal{P}}_{j_1,\dots,j_{N_f}}(x,\tilde{t}\,) \tag{3.20}$$

the probability current density in the reduced units. $f(x) = \frac{F d_0}{k_B T}$ for the constant load, $f(x) = -\frac{\kappa_T d_0 x}{k_B T}$ for the optical trap.

If we now let ϵ go to zero, we have the simple equation

$$\frac{\partial}{\partial x}\widetilde{J}^{(0)}_{j_1,\dots,j_{N_f}}(x,\tilde{t}\,) = -\frac{\partial^2 \widetilde{\mathcal{P}}^{(0)}_{j_1,\dots,j_{N_f}}(x,\tilde{t}\,)}{\partial x^2} + \frac{\partial}{\partial x}\left[-f(x)\widetilde{\mathcal{P}}^{(0)}_{j_1,\dots,j_{N_f}}(x,\tilde{t}\,) \right] = 0 \tag{3.21}$$

which can be integrated analytically. Since we are considering rigid filaments, the integration interval goes from the position of the most advanced tip, $x^* =$

[2] It can sometimes go close to 1 for a very large colloidal particle in a crowded environment.

$\max_{n=1,\dots,N_f}\{x_n\}$ with $x_n = \frac{X_n}{d_0} = j_n - 1 + \frac{h_n}{d_0}$ (see Fig. 1.4 and Section 1.3.2), up to infinity. The boundary conditions on the probability and the probability current density read

$$\widetilde{\mathcal{P}}^{(0)}_{j_1,\dots,j_{N_f}}(x,\tilde{t}\,)|_{x<x^*(t)} = 0 \qquad \widetilde{\mathcal{P}}^{(0)}_{j_1,\dots,j_{N_f}}(x,\tilde{t}\,)|_{x=\infty} = 0 \tag{3.22}$$

$$\widetilde{J}^{(0)}_{j_1,\dots,j_{N_f}}(x,\tilde{t}\,)|_{x=x^*(t)} = 0 \qquad \widetilde{J}^{(0)}_{j_1,\dots,j_{N_f}}(x,\tilde{t}\,)|_{x=\infty} = 0. \tag{3.23}$$

Integrating Eq. (3.21) once and applying these conditions, the general solution results to be

$$\widetilde{\mathcal{P}}^{(0)}_{j_1,\dots,j_{N_f}}(x,\tilde{t}\,) = a(j_1,\dots,j_{N_f},\tilde{t}\,)\exp\left(-\int_x^\infty dx'\; f(x')\right) \tag{3.24}$$

where $a(j_1,\dots,j_{N_f},\tilde{t}\,)$ is a generic L-independent pre-factor incorporating the time and $\mathbf{j}$ dependencies.

Besides, the joint probability distribution function can be written also as the product of the marginal distribution for the subset $\{j_1,\dots,j_{N_f}\}$ times the conditional probability distribution for x:

$$\widetilde{\mathcal{P}}^{(0)}_{j_1,\dots,j_{N_f}}(x,\tilde{t}\,) = \widetilde{P}^{(0)}(j_1,\dots,j_{N_f},\tilde{t}\,)\widetilde{\Pi}^{(0)}(x|j_1,\dots,j_{N_f},\tilde{t}\,) \tag{3.25}$$

and comparing this expression with the general solution Eq. (3.24), we can write

$$\widetilde{\mathcal{P}}^{(0)}_{j_1,\dots,j_{N_f}}(x,\tilde{t}\,) = \widetilde{P}^{(0)}(j_1,\dots,j_{N_f},\tilde{t}\,)\widetilde{\Pi}^{(0)}_{EQ}(x|j_1,\dots,j_{N_f}) \tag{3.26}$$

since the x dependence in Eq. (3.24) is explicit and time-independent. The explicit expression for the normalized equilibrium wall distribution function, conditional to the set of filament sizes, $\widetilde{\Pi}^{(0)}_{EQ}(x|j_1,\dots,j_{N_f})$, can be found by choosing the type of force acting on the wall. For the two cases of constant load and optical trap we have:

$$\widetilde{\Pi}^{(0)}_{EQ}(x|j_1,\dots,j_{N_f}) = \begin{cases} \dfrac{f\exp(-fx)}{\exp\left(-fx^*\right)} & \text{constant load,} \\ \sqrt{\dfrac{2\tilde{\kappa}_T}{\pi}}\;\dfrac{\exp\left(-\frac{1}{2}\tilde{\kappa}_T x^2\right)}{\operatorname{erfc}\left(\sqrt{\frac{1}{2}\tilde{\kappa}_T}x^*\right)} & \text{optical trap.} \end{cases} \tag{3.27}$$

with $\tilde{\kappa}_T = \frac{\kappa_T d_0^2}{k_B T}$. We can furthermore calculate the average wall position, given the filaments' sizes:

$$\langle L\rangle^{(0)} = d_0\int_{x^*}^\infty dx\; x\;\widetilde{\Pi}^{(0)}_{EQ}(x|j_1,\dots,j_{N_f}) = \begin{cases} X^* + \dfrac{k_B T}{F} & \text{constant load,} \\ \sqrt{\dfrac{2}{\tilde{\kappa}_T\pi}}\dfrac{\exp\left(-\frac{1}{2}\tilde{\kappa}_T(x^*)^2\right)}{\operatorname{erfc}\left(\sqrt{\frac{1}{2}\tilde{\kappa}_T}x^*\right)} & \text{optical trap.} \end{cases} \tag{3.28}$$

In the constant load case, for $F \to \infty$ the average wall position becomes equal to the position of the most advanced tip, X^*, and the wall position distribution function becomes a delta function: the wall is constantly forced to lie against the

most advanced filament's tip. The same occurs in the case of the optical trap when $\kappa_{\mathrm{T}} \to \infty$.

Note that Eq. (3.26) is still a time-dependent function because the set of filament sizes changes in time by single monomer (de)polymerization events. The limit $\epsilon = 0$ implies that each time a filament polymerizes or depolymerizes, the wall immediately re-equilibrates according to its equilibrium distribution Eq. (3.27). To get the joint distribution function Eq. (3.26), we need to consider Eq. (3.19) up to first order in ϵ. By doing so, as detailed in Appendix A.9, we can write Eq. (A.94) in a vectorial form like Eq. (3.7),

$$\frac{d\mathbf{P}_0}{dt} = \mathbf{P}_0 \mathrm{Q}^{(0)} \tag{3.29}$$

where we went back to the dimensional variables, using the relation $\widetilde{P}_0(j_1, \ldots, j_{N_f}, \tilde{t}\,)d\tilde{t} = P_0(j_1, \ldots, j_{N_f}, t)dt$, and $\mathrm{Q}^{(0)}$ is the generator matrix. This matrix connects adjacent states, *i.e.* states different from each other only for one variable by ± 1 unit: $\{j_1, \ldots, j_n, \ldots, j_{N_f}\}$ and $\{j_1, \ldots, j_n \pm 1, \ldots, j_{N_f}\}$ for any $n = 1, \ldots, N_f$. Given a state, hence, $2N_f$ possible final states exist. The matrix elements can be readily written by regarding Eq. (A.94):

$$Q^{(0)}_{\{j_1,\ldots,j_n,\ldots,j_{N_f}\}j_1,\ldots,j_n+1,\ldots,j_{N_f}} = U_{j_n} = U_0 A^{(n)}(j_1, \ldots, j_n, \ldots, j_{N_f}) \tag{3.30}$$

$$Q^{(0)}_{\{j_1,\ldots,j_n,\ldots,j_{N_f}\}j_1,\ldots,j_n-1,\ldots,j_{N_f}} = W_{j_n} = W_0 \tag{3.31}$$

$$Q^{(0)}_{\{j_1,\ldots,j_n,\ldots,j_{N_f}\}j_1,\ldots,j_n,\ldots,j_{N_f}} = -\sum_{n=1}^{N_f} (U_{j_n} + W_{j_n}) \tag{3.32}$$

with

$$A^{(n)}(j_1, \ldots, j_n, \ldots, j_{N_f}) = \begin{cases} \exp\left(-f(x^{*'} - x^*)\right) & \text{constant load,} \\ \dfrac{\operatorname{erfc}\left(\sqrt{\tilde{\kappa}_T/2}\, x^{*'}\right)}{\operatorname{erfc}\left(\sqrt{\tilde{\kappa}_T/2}\, x^*\right)} & \text{optical trap} \end{cases} \tag{3.33}$$

where $x^{*'} \geq x^*$ is the most advanced tip's position once filament n has polymerized ($j_n \to j_n + 1$). These factors correct the polymerization rates, and take into account the reduction in U_0 due to the presence of the wall (see Appendix A.9).

Eq. (3.29) can be solved numerically using the same scheme described above for the $\epsilon > 0$ case. In this case the filament sizes will be evolved sampling the new state, and the wall position is assumed to be equal to the average Eq. (3.28). In the following sections, results for the rigid and flexible cases will be presented and compared with those given by the traditional models reviewed in Section 1.3, in order to outline the effects of flexibility on the bundle dynamical behavior.

3.2 Stochastic Dynamics simulations

3.2.1 Units and parameters

Length, time and energy units are taken as d_0, W_0^{-1} and k_BT. For actin $d_0 = 2.7$ nm; experimental information gives $W_0^{-1} = 1.4$ s; $k_BT = 4.14 \times 10^{-21}$ J at room

temperature. The model requires to fix the wall diffusion coefficient D, which is equivalent to fixing the dimensionless parameter $\epsilon = \frac{d_0^2 W_0}{D}$. As discussed in the previous section, experimental information on ϵ gives $\epsilon = 5 \times 10^{-5}$ for actin, using $D = 2.2 \times 10^{-4}$ nm^2/s for a micron-seized bead in water. In the case of rigid filaments, for which the most advanced filament tip's position act like a reflecting barrier for the wall, we can take the approximation $\epsilon = 0$. In the case of flexible filaments, the realistic value of ϵ is far too small to sample both the filament sizes and the wall position: computing time would be essentially spent to observe the wall diffusion next to a bundle of quasi-fixed filament sizes. Hence, empirically we decided to adopt a thousandfold larger value, $\epsilon = 5 \times 10^{-2}$, having tested that the time scale separation is still sufficient to represent the wall dynamics generated by the much lower experimental value of ϵ, as explained later on. The timescales separation indeed

$$\tau_{micro} \ll \tau_D \ll \tau_{chem} \tag{3.34}$$

is still satisfied if we take a thousandfold larger D and lets us consider the filaments and the wall at equilibrium between two successive chemical events.

3.2.2 Equilibrium simulations of semiflexible bundles

In order to verify the robustness of the algorithm, equilibrium simulations in optical trap were first realized and compared with the results presented in the previous chapter. We reproduced each of the cases reported in Table 2.1, obtaining in any case averages in perfect agreement with those obtained by numerical integration. To give an example, Fig. 3.1 shows the wall position equilibrium distribution function for the case $N_f = 16$, $\hat{\rho}_1 = 2.5$ and $\kappa_{\mathrm{T}} = 0.2666 \frac{k_B T}{d_0^2}$, showing a good agreement between between stochastic dynamics (red points) and numerical integration (black line) results.

Besides equilibrium distributions and averages, the stochastic dynamics approach lets investigate dynamical features even at equilibrium, like the wall position time correlation function for instance. Anticipating the following, this correlation function can be related to the velocity-load relationship, in particular its slope at stalling, which in turn can be connected with an additional friction acting on the wall, which we call *chemical*. To see this, it is convenient to write the time evolution of the wall position in terms of a Langevin equation: indeed, the coefficients appearing in the Fokker-Planck Eq. (3.3) may be derived from a stochastic Langevin equation [61] for the wall dynamics, coupled to Master equations for the time evolution of the filament sizes. The Langevin equation for the wall motion in an optical trap-like potential reads:

$$M \frac{d^2 L(t)}{dt^2} = F_{bun}(t) - \kappa_{\mathrm{T}} L(t) - \xi \frac{dL(t)}{dt} + R(t) \tag{3.35}$$

where M is the mass of the obstacle, $F_{bun}(t)$ the bundle force, depending on time through the the filament sizes and wall position time dependence, $\xi = \frac{k_B T}{D}$ is the friction coefficient and $R(t)$ a white random noise,

$$\langle R(t) \rangle = 0 \tag{3.36}$$

$$\langle R(t+\tau) R(t) \rangle = 2 \xi k_B T \delta(\tau), \tag{3.37}$$

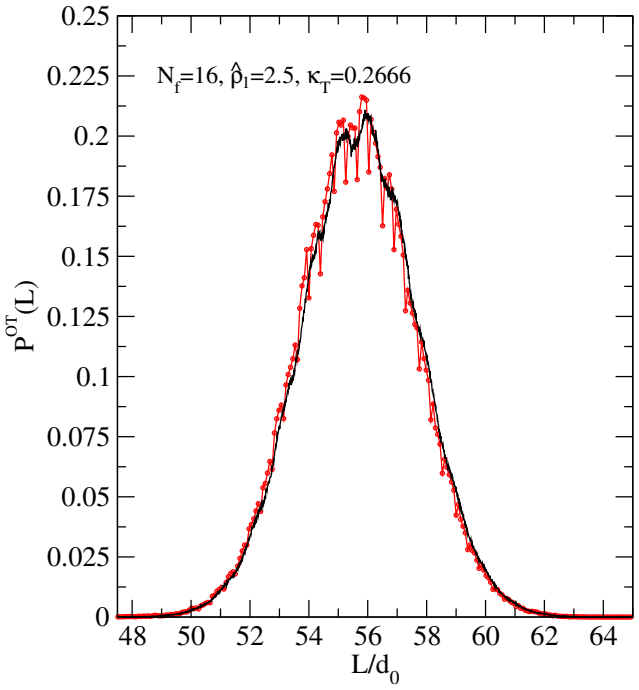

Figure 3.1. Wall position equilibrium distribution function for $N_f = 16$, $\hat{\rho}_1 = 2.5$ and $\kappa_{\mathrm{T}} = 0.2666 \frac{k_B T}{d_0^2}$, data from stochastic dynamics (red points) and numerical integration (black line) are shown.

the last identity arising from the Fluctuation-Dissipation Theorem. Since the inertial relaxation time of the wall, $\tau_{inertia} = M/\xi$, is very fast (of the order of 10^{-7} s according to the experimental setup [10] for a micron radius bead of mass $M = 4\pi R^3 \rho \sim 10^{-15}$ Kg in water, $\xi = 1.9 \times 10^{-8}$Js/m^2) compared to the diffusion time, we can take the over-damped limit of Eq. (3.35):

$$\xi \frac{dL(t)}{dt} = F_{bun}(t) - \kappa_{\mathrm{T}} L(t) + R(t) \tag{3.38}$$

In Chapter 2 we have seen that both for the rigid and the flexible case the stalling force is given by Eq. (1.9) in rather good approximation, and in an optical trap the equilibrium average wall position will be given roughly by $\langle L \rangle^{\mathrm{OT}} \approx L^{\mathrm{MF}} = F^{\mathrm{MF}}_{stall}/\kappa_{\mathrm{T}}$, with a variance $\sigma_L^{\mathrm{OT}} \approx \sqrt{k_B T/\kappa_{\mathrm{T}}}$. It is convenient to rewrite Eq. (3.35) in terms of the displacement from the equilibrium position, $\Delta L(t) = L(t) - \langle L \rangle^{\mathrm{OT}}$:

$$\begin{aligned} \xi \frac{d\Delta L(t)}{dt} &= F_{bun}(t) - \kappa_{\mathrm{T}} \left(\langle L \rangle^{\mathrm{OT}} + \Delta L(t) \right) + R(t) \\ &= (F_{bun}(t) - F_{stall}) - \kappa_{\mathrm{T}} \Delta L(t) + R(t). \end{aligned} \tag{3.39}$$

Let's focus on the difference $F_{bun}(t) - F_{stall}$: it represents the fluctuations at equilibrium (*i.e.* near stalling) of the bundle force with respect to its equilibrium average value. It can be related to the wall velocity, assuming that it exists a univocal velocity-load relationship $v(F)$: when the wall is loaded with a force F, it moves

with a stationary velocity v. Around stalling, where the velocity is strictly zero, it is possible to expand $v(F)$ around F_{stall}, and truncating to the first order:

$$\begin{aligned} v(F) &= v(F)\Big|_{F_{stall}} + \left.\frac{dv(F)}{dF}\right|_{F_{stall}} (F - F_{stall}) + \dots \\ v(F) &\approx \left.\frac{dv(F)}{dF}\right|_{F_{stall}} (F - F_{stall}) \\ &\equiv -\frac{1}{\gamma}\,(F - F_{stall}) \end{aligned} \tag{3.40}$$

where the aforementioned *chemical friction* γ has been defined as minus the inverse of the slope of $v(F)$ at stalling; it is indeed a friction coefficient with a chemical (and not hydrodynamic) origin., *i.e.* related to the filaments' chemical activity (polymerization/depolymerization). Assuming that at any time the external force $F(t)$ is equal to $F_{bun}(t)$ (mechanical equilibrium) plus random fluctuations to be reabsorbed into the white noise, and substituting $v(F(t)) = \frac{d\Delta L(t)}{dt}$ Eq. (3.39) becomes:

$$(\xi + \gamma)\,\frac{d\Delta L(t)}{dt} = -\kappa_{\mathrm{T}}\Delta L(t) + R'(t) \tag{3.41}$$

where the noise has been redefined in order to include the chemical friction coefficient:

$$\langle R'(t)\rangle = 0 \tag{3.42}$$

$$\langle R'(t+\tau)R'(t)\rangle = 2\,(\xi+\gamma)\,k_B T\delta(\tau). \tag{3.43}$$

Eq. (3.41) can be solved choosing the initial wall position $L(t=0) = L_0$, giving:

$$\begin{aligned} L(t) = \langle L\rangle^{\mathrm{OT}} &+ (L_0 - \langle L\rangle^{\mathrm{OT}}) \exp\left(-\frac{\kappa_{\mathrm{T}}}{\xi+\gamma}\,t\right) \\ &+ \frac{1}{\xi+\gamma}\int_0^t dt'\,\exp\left(-\frac{\kappa_{\mathrm{T}}}{\xi+\gamma}\,(t-t')\right) R'(t') \end{aligned} \tag{3.44}$$

Taking the average over the noise realization of both sides of Eq. (3.44) and using Eq. (3.42), we find that the wall relaxes towards the equilibrium position exponentially, with fluctuations exponentially decaying in time, with a characteristic time $\tau^{\mathrm{OT}} = \frac{\xi+\gamma}{\kappa_{\mathrm{T}}}$:

$$\langle L(t)\rangle = \langle L\rangle^{\mathrm{OT}} + (L_0 - \langle L\rangle^{\mathrm{OT}}) \exp\left(-\frac{\kappa_{\mathrm{T}}}{\xi+\gamma}\,t\right) \tag{3.45}$$

The same is expected for the velocity and the bundle force:

$$\langle v(t)\rangle = \frac{d\Delta L(t)}{dt} = -\frac{\kappa_{\mathrm{T}}}{\xi+\gamma}\,(L_0 - \langle L\rangle^{\mathrm{OT}}) \exp\left(-\frac{\kappa_{\mathrm{T}}}{\xi+\gamma}\,t\right) \tag{3.46}$$

$$\langle F_{bun}(t)\rangle = \kappa_{\mathrm{T}}\langle L\rangle^{\mathrm{OT}} = F_{stall} + \kappa_{\mathrm{T}}\left[(L_0 - \langle L\rangle^{\mathrm{OT}}) \exp\left(-\frac{\kappa_{\mathrm{T}}}{\xi+\gamma}\,t\right)\right] \tag{3.47}$$

Note that the averages in the l.h.s. of the last three equations, $\langle\cdots\rangle$, are time-dependent averages over the noise realization, while $\langle L\rangle^{\mathrm{OT}}$ is an average over the equilibrium optical trap ensemble (see Section 2.3.3).

From Eq. (3.44) we can calculate the time correlation function of the wall position as well:

$$\begin{aligned}\langle L(t+\tau)L(t)\rangle &= \left\langle \left(\langle L\rangle^{\mathrm{OT}} + (L_0 - \langle L\rangle^{\mathrm{OT}})\, \mathrm{e}^{-\frac{\kappa_{\mathrm{T}}}{\xi+\gamma}\,(t+\tau)} + \frac{1}{\xi+\gamma}\int_0^t dt'_1\, \mathrm{e}^{-\frac{\kappa_{\mathrm{T}}}{\xi+\gamma}\,(t+\tau-t'_1)} R'(t'_1) \right) \right. \\ &\quad \left. \times \left(\langle L\rangle^{\mathrm{OT}} + (L_0 - \langle L\rangle^{\mathrm{OT}})\, \mathrm{e}^{-\frac{\kappa_{\mathrm{T}}}{\xi+\gamma}\,(t)} + \frac{1}{\xi+\gamma}\int_0^t dt'_2\, \mathrm{e}^{-\frac{\kappa_{\mathrm{T}}}{\xi+\gamma}\,(t-t'_2)} R'(t'_2) \right) \right\rangle \\ &= \langle L\rangle^{\mathrm{OT}} \left[\langle L\rangle^{\mathrm{OT}} + (L_0 - \langle L\rangle^{\mathrm{OT}}) \left(\mathrm{e}^{-\frac{\kappa_{\mathrm{T}}}{\xi+\gamma}\,(t+\tau)} + \mathrm{e}^{-\frac{\kappa_{\mathrm{T}}}{\xi+\gamma}\,t} \right) \right] \\ &\quad + (L_0 - \langle L\rangle^{\mathrm{OT}})^2\ \mathrm{e}^{-\frac{\kappa_{\mathrm{T}}}{\xi+\gamma}\,(2t+\tau)} \\ &\quad + \frac{1}{(\xi+\gamma)^2}\int_0^{t+\tau} dt'_1 \int_0^t dt'_2\, \mathrm{e}^{-\frac{\kappa_{\mathrm{T}}}{\xi+\gamma}\,(2t+\tau-t'_1-t'_2)} \langle R'(t'_1)R'(t'_2)\rangle. \end{aligned} \tag{3.48}$$

Let's calculate the last integral separately, using Eq. (3.43):

$$\begin{aligned} I &= \int_0^{t+\tau} dt'_1 \int_0^t dt'_2\, \mathrm{e}^{-\frac{\kappa_{\mathrm{T}}}{\xi+\gamma}\,(2t+\tau-t'_1-t'_2)} \langle R'(t'_1)R'(t'_2)\rangle \\ &= 2(\xi+\gamma)k_B T \int_0^{t+\tau} dt'_1 \int_0^t dt'_2\, \mathrm{e}^{-\frac{\kappa_{\mathrm{T}}}{\xi+\gamma}\,(2t+\tau-t'_1-t'_2)} \delta(t'_1 - t'_2) \\ &= k_B T\, \frac{(\xi+\gamma)^2}{\kappa_{\mathrm{T}}} \left(\mathrm{e}^{-\frac{\kappa_{\mathrm{T}}}{\xi+\gamma}\,\tau} - \mathrm{e}^{-\frac{\kappa_{\mathrm{T}}}{\xi+\gamma}\,(2t+\tau)} \right). \end{aligned} \tag{3.49}$$

Plugging this result into Eq. (3.48) and taking the limit of large time t while keeping τ constant, we obtain:

$$\langle L(t+\tau)L(t)\rangle \sim (\langle L\rangle^{\mathrm{OT}})^2 + \frac{k_B T}{\kappa_{\mathrm{T}}} \exp\left(-\frac{\kappa_{\mathrm{T}}}{\xi+\gamma}\,\tau \right) \tag{3.50}$$

which is a function of the time difference τ only. The characteristic time of the exponential decay is again $\tau^{\mathrm{OT}} = \frac{\xi+\gamma}{\kappa_{\mathrm{T}}}$. To get the chemical friction γ, one can extract the characteristic time of the time correlation function for the wall position obtained by numerical simulations, or the velocity-load relationship, if known. We can use the mean field Eq. (1.13) and the brownian ratchet Eq. (1.24) to get the corresponding predictions: in the former case

$$\gamma^{\mathrm{MF}} = -\left(\left. \frac{dv^{\mathrm{MF}}(F)}{dF} \right|_{F_{stall}} \right)^{-1} = \frac{k_B T}{W_0 d_0^2} N_f \tag{3.51}$$

giving values of the order of $N_f \geq 1$ in program units, while the hydrodynamic friction ξ is of the order of $10^{-5}\, \frac{k_B T}{W_0 d_0^2}$: the dominating friction is thus the chemical one, giving a characteristic time $\tau^{\mathrm{OT}}_{\mathrm{MF}} = \frac{\gamma^{\mathrm{MF}}+\xi}{\kappa_{\mathrm{T}}} \approx \frac{\gamma^{\mathrm{MF}}}{\kappa_{\mathrm{T}}}$, independent of the number of filaments at fixed $\langle L\rangle^{\mathrm{OT}}$ (in this case κ_{T} scales proportionally to N_f, as well as γ^{MF}).

In the brownian ratchet model the expression for γ is a bit more complicated:

$$\gamma^{\mathrm{SR}} = -\left(\left.\frac{dv^{\mathrm{SR}}(F)}{dF}\right|_{F_{stall}}\right)^{-1} = \frac{k_B T}{W_0 d_0^2}\, N_f\, \frac{1+A}{B} = \gamma^{\mathrm{MF}}\, \frac{1+A}{B} \tag{3.52}$$

$$A = N_f^{-1} \sum_{m=1}^{N_f-1} m\hat{\rho}_1^{-m} + (N_f-1)\,\hat{\rho}_1^{-(N_f-1)} - N_f^{-1} \sum_{m=1}^{N_f-1} m\hat{\rho}_1^{-m}\,[1-(\hat{\rho}_1-1)(m-1)] \tag{3.53}$$

$$B = N_f\,\hat{\rho}_1^{1-N_f}\left[1+\sum_{m=1}^{N_f-1}\hat{\rho}_1^m\left(1-\hat{\rho}_1^{-1}\right)\left(\frac{N_f-m}{N_f}\right)^2\right] \tag{3.54}$$

and can be calculated numerically. The factor $\frac{1+A}{B}$ is larger than one, so that $\gamma^{\mathrm{SR}} \geq \gamma^{\mathrm{MF}}$ for any N_f (the equality holding for $N_f = 1$). Fig. 3.2 shows the ratio

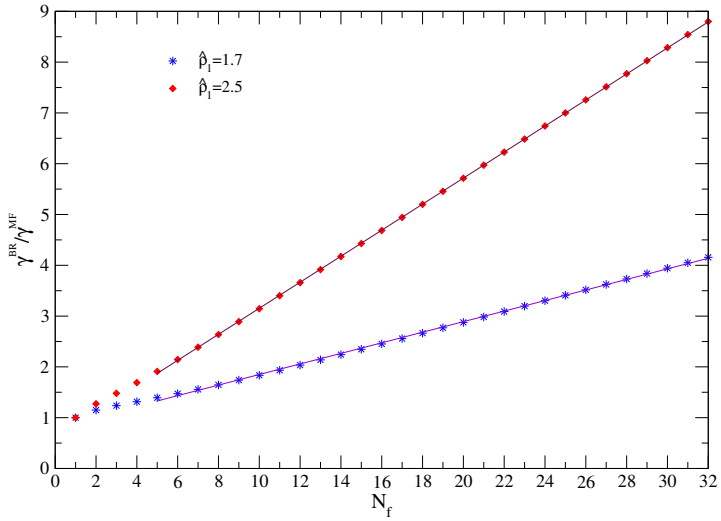

Figure 3.2. $\theta^{\mathrm{SR}} = \frac{\gamma^{\mathrm{SR}}}{\gamma^{\mathrm{MF}}}$ as a function of N_f for two different reduced densities, $\hat{\rho}_1 = 1.7$ and 2.5. The behavior is linear for $N_f \geq 5$, $\gamma^{\mathrm{SR}} = \gamma^{\mathrm{MF}}(aN_f + b)$ with $a = 0.1040 \pm 0.0005$ and $b = 0.81 \pm 0.01$ for $\hat{\rho}_1 = 1.7$, and $a = 0.2563 \pm 0.0002$ and $b = 0.590 \pm 0.005$ for $\hat{\rho}_1 = 2.5$. The solid lines indicate these linear laws.

between γ^{SR} and γ^{MF}, $\theta^{\mathrm{SR}} = \frac{\gamma^{\mathrm{SR}}}{\gamma^{\mathrm{MF}}} = \frac{\tau^{\mathrm{SR}}}{\tau^{\mathrm{MF}}}$ as a function of N_f for two different reduced densities, $\hat{\rho}_1 = 1.7$ and 2.5: for N_f large enough ($N_f \geq 5$), the observed behavior is linear, $\gamma^{\mathrm{SR}} = \gamma^{\mathrm{MF}}(aN_f + b)$, with parameters given in the figure caption and represented by the solid lines.

From the stochastic dynamic simulations of homogeneous flexible bundles in optical trap, we have computed the time correlation function for the wall position normalized to one, $C_L(t) = \dfrac{\langle L(t+t_0)L(t_0)\rangle - (\langle L\rangle^{\mathrm{OT}})^2}{\langle (L(t_0))^2\rangle - (\langle L\rangle^{\mathrm{OT}})^2}$, averaging over different

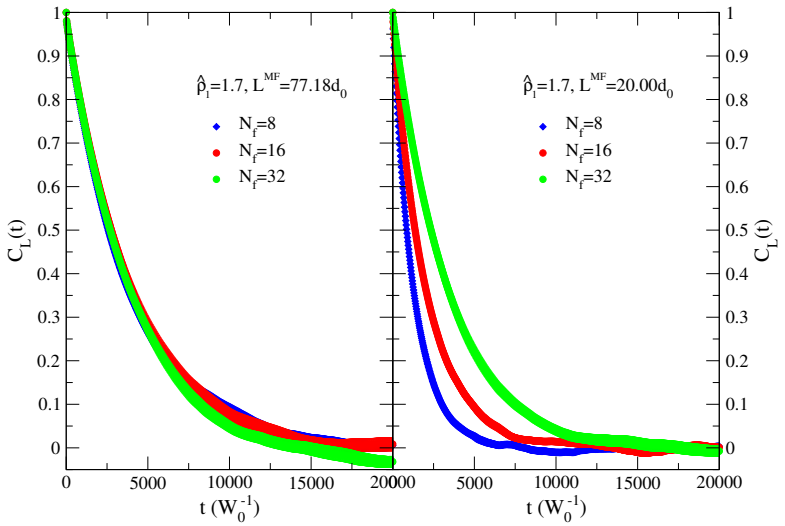

Figure 3.3. Time autocorrelation functions of the wall position for the indicated values of N_f, $\hat{\rho}_1$ and L^{MF}.

trajectories and over t_0 along the trajectories. Fig. 3.3 shows the wall time autocorrelation functions for $N_f = 8$, 16 and 32 flexible bundles and the indicated values of $\hat{\rho}_1$ and L^{MF} and Table 3.1 reports the decay times of the wall position correlation functions, together with the mean field and brownian ratchet (SR) prediction, the ratio between τ^{SR} and τ^{MF} (θ^{SR}) and the ratio between the observed τ^{OT} and τ^{SR} (θ^{OT}). It can be noted that the observed time constants are not too different for different N_f at given L^{MF} when κ_T is not too large (long bundles), while for larger values of κ_T (shorter bundles) τ^{OT} increases with N_f. This observation could be connected with the wall distance distribution: as already said, the roughness of the L distribution increases with increasing the trap strength and the number of filaments in the bundle. This increase in roughness signals the presence of a very rough wall effective potential, that is obtainable taking the logarithm of the distribution: it is not so surprising that diffusing in such a rough potential is slower than diffusing in a smooth potential surface.

As for $\theta^{\mathrm{OT}} = \frac{\tau^{\mathrm{OT}}}{\tau^{\mathrm{MF}}}$, for small trap sizes (large κ_T) the observed values of τ^{OT} are quite different from the mean field values and θ^{OT}'s are quite large; at given L^{MF} they increase with $\hat{\rho}_1$ and N_f. Increasing the trap average size, $\theta^{\mathrm{OT}} \to 1$ for every N_f: the time constants of the exponential decay of the wall position time autocorrelation function become closer to the mean field prediction as κ_T decreases (hence, as the bundle length increases). These factors are shown as functions of L^{MF} in Fig. 3.4 for all the inspected values of N_f, $\hat{\rho}_1$ and κ_T. The dotted horizontal line $\theta^{\mathrm{OT}} = 1$ indicates the mean field limiting behavior, attained for very long (and hence very flexible) bundles.

Table 3.1. Observed decay times for the wall position correlation function for the selected values of the κ_T, $\hat{\rho}_1$ and N_f for homogeneous bundles, in W_0^{-1} units. The mean field prediction for the wall average position, $L^{\rm MF}$ (d_0), the predicted values of the time constant, $\tau^{\rm MF}$ (W_0^{-1}) and $\tau^{\rm SR}$ (W_0^{-1}), and the ratios $\theta^{\rm SR} = \frac{\tau^{\rm SR}}{\tau^{\rm MF}}$ and $\theta^{\rm OT} = \frac{\tau^{\rm OT}}{\tau^{\rm MF}}$ are also shown (in program units).

N_f	$\hat{\rho}_1$	$\kappa_{\rm T}$	$L^{\rm MF}$	$\tau^{\rm MF}$	$\tau^{\rm SR}$	$\theta^{\rm SR} = \frac{\tau^{\rm SR}}{\tau^{\rm MF}}$	$\tau^{\rm OT}$	$\theta^{\rm OT} = \frac{\tau^{\rm OT}}{\tau^{\rm MF}}$
8		0.2112			62.35	1.646	59.6 ± 0.9	1.57 ± 0.03
16	1.7	0.4245	20.00	37.88	92.88	2.452	95 ± 2	2.51 ± 0.05
32		0.8490			157.47	4.157	155 ± 5	4.1 ± 0.1
8		0.1221			107.85	1.646	102 ± 2	1.55 ± 0.06
16	1.7	0.2443	34.75	65.62	160.90	2.452	141 ± 3	2.15 ± 0.06
32		0.4886			272.78	4.157	183 ± 5	2.76 ± 0.09
8		0.07075			186.11	1.646	154 ± 4	1.36 ± 0.05
16	1.7	0.1415	60.00	113.07	277.25	2.452	161 ± 4	1.43 ± 0.06
32		0.2830			470.03	4.157	173 ± 5	1.53 ± 0.05
8		0.05500			239.41	1.646	181 ± 4	1.24 ± 0.03
16	1.7	0.1100	77.18	145.45	356.64	2.452	186 ± 8	1.28 ± 0.05
32		0.2200			604.64	4.157	183 ± 5	1.27 ± 0.04
8		0.2550			82.72	2.637	73 ± 1	2.32 ± 0.03
16	2.5	0.5500	26.65	31.37	147.00	4.686	120 ± 2	4.12 ± 0.08
32		0.6200			276.06	8.800	165 ± 5	5.7 ± 0.1
8		0.1900			111.02	2.637	90 ± 1	2.13 ± 0.04
16	2.5	0.3100	38.58	42.10	197.28	4.686	113 ± 2	2.69 ± 0.05
32		0.6200			370.48	8.800	139 ± 3	3.29 ± 0.08
8		0.1550			136.10	2.637	93 ± 1	1.80 ± 0.02
16	2.5	0.3100	47.29	51.61	241.84	4.686	114 ± 2	2.18 ± 0.05
32		0.6200			416.15	8.800	121 ± 3	2.35 ± 0.05
8		0.1221			172.78	2.637	108 ± 5	1.63 ± 0.07
16	2.5	0.2443	60.00	65.52	306.89	4.686	95 ± 2	1.63 ± 0.03
32		0.4886			576.58	8.800	111 ± 2	1.70 ± 0.04

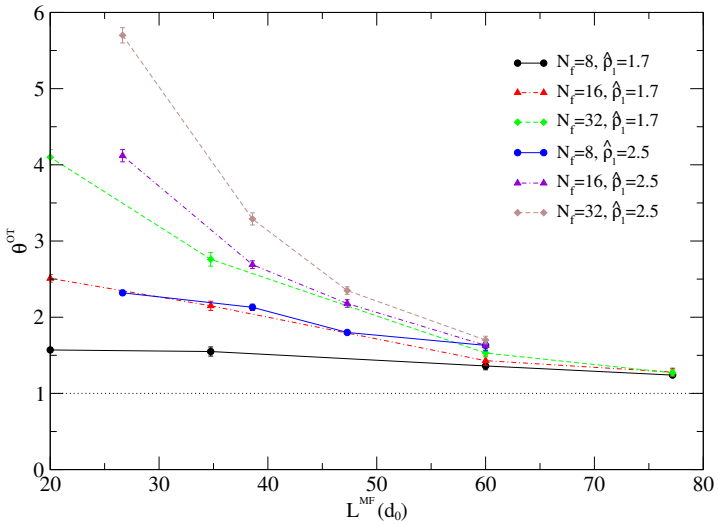

Figure 3.4. Ratio between the observed time constant for the exponential decay of the wall correlation function as a function of L^{MF} for all the inspected values of N_f, $\hat{\rho}_1$ and κ_T.

3.2.3 Non-equilibrium simulations

The main purpose of this approach is to study the non-equilibrium behavior of bundles of actin filaments growing against a mobile wall, when this moves with a non-zero average velocity. We ask if it is possible to extract the full velocity-load relationship from an optical trap experiment, where the obstacle is monitored from its initial position up to equilibrium (stalling). To answer this question, we need to analyze once more the timescales involved in the problem. In constant load experiments, the obstacle is seen to move with a constant velocity, which depends on the applied force, pointing out the existence of a local equilibrium between the force exerted by the filaments and the load [3]. What about the optical trap? In this set up, the wall position evolves in time and so does the load ($F(t) = \kappa_T L(t)$). How does the wall respond to this continuous change in the applied force? Let's denote by $\tau_{wall}^{micro}(F)$ the relaxation time needed by the wall to adjust to a change of the external force, and by τ^{OT} the characteristic time of the evolution of the wall towards stalling in the optical trap set-up. As long as $\tau_{wall}^{micro}(F)$ is much smaller than τ^{OT}, the trap relaxation can be considered as a sequence of quasi-stationary non-equilibrium states for the bundle/wall system, still in equilibrium on the long time needed by the load to change in the optical trap set up[4].

If this timescale separation holds, an optical trap relaxation experiment (*i.e.*

[3] According to our model this is possible only for a limited range of L values in the case of flexible filaments, because of the occurrence of escaping filaments.

[4] This is the same timescale discussed in the previous section in accordance to the Fluctuation Dissipation Theorem.

the time evolution of the wall-bundle system from a non-equilibrium condition until stalling) can be used to extract a load-velocity relationship which is *de facto* equivalent to the relationship usually obtained via constant load experiments. To verify if this is the case, we have analyzed results for rigid filaments both in constant load and in optical trap set up, as detailed in the following.

Rigid filaments in constant load and optical trap set up

We have computed the relaxation toward the stationary state for a homogeneous bundle of $N_f = 32$ rigid living filaments at reduced density $\hat{\rho}_1 = 2.5$ pressing against a constant load F. We have chosen various values of F in the range $0.05 < F/F_{stall} < 1.25$ with $F_{stall} \equiv F_{stall}^{\mathrm{MF}}$ being the stalling force Eq. (1.9). We have used the $\epsilon = 0$ algorithm to produce 10^3 independent trajectories, starting at time 0 with all filament sizes set to the same value $j_n = 500$. This size has been chosen to avoid the bias at short lengths $j_n = 2$ where depolymerization is forbidden[5], taking into account that length does not affect the rigid filaments' behavior. In two cases ($F = 0.6F_{stall}$ and $F = 0.9F_{stall}$), we used the $\epsilon > 0$ algorithm setting a very large persistence length ($\ell_p \sim 5 \times 10^5 d_0$) to produce 10^3 trajectories and compare the results from the two approaches. In these cases we started with an initial wall position $L_0 = 5d_0$ and filament sizes distributed according to the equilibrium distribution Eq. (2.44). In any case we have observed an asymptotic long-time stationary state where the wall moved with constant velocity, preceded by a transient behavior exponentially decaying in time. To determine the microscopic relaxation time of the wall, we have calculated the average wall position as a function of time over all the trajectories, denoted by $\langle L \rangle_t$, and fitted its asymptotic time evolution as $\langle L \rangle_t = C + v_{stat} t + C' \exp\left(-t/\tau_{wall}^{micro}\right)$. Moreover, fitting the asymptotic behavior of the mean square elongation $\sigma_L^2(t) = \langle L^2 \rangle_t - \langle L \rangle_t^2 \underset{t\to\infty}{\approx} 2\Gamma t$ [62] provides us with information on the bundle diffusion coefficient Γ, related to the diffusion of the wall induced by the pushing filaments. Panel (a) of Fig. 3.5 reports the relaxation time τ_{wall}^{micro} for a homogeneous bundle of $N_f = 32$ rigid filaments, obtained using the $\epsilon = 0$ algorithm, as a function of the load reduced by the stalling force Eq. (1.9). The relaxation times are of the order of W_0^{-1}, except at small loads, where it diverges. We will come back on the consequences of this divergence later on. The bundle diffusion coefficient Γ is shown in panel (b) of Fig. 3.5 as a function of the reduced force F/F_{stall}. Here the red points have been obtained using the $\epsilon > 0$ algorithm: note the consistency between the values of Γ coming from the two approaches. The bundle diffusion coefficient increases for $F \to 0$ as well, relatedly to the divergence of τ_{wall}^{micro} in the same limit.

With the same analysis that provides the relaxation time, we can obtain the stationary velocity of the wall for each value of the external load. Plotting these stationary velocities as a function of the load gives the velocity-load relationship.

Let's now consider the bundle/wall relaxation in an optical trap apparatus. We have used both the $\epsilon = 0$ and the $\epsilon > 0$ algorithms, starting in the former case with all initial filaments sizes $j_n = 6$ for any n and in the latter case from an initial wall position $L_0 = 5d_0$ and the filament sizes distributed according to Eq. (2.44). The

[5] This could be the case for values $F > F_{stall}$ and consequent negative velocities.

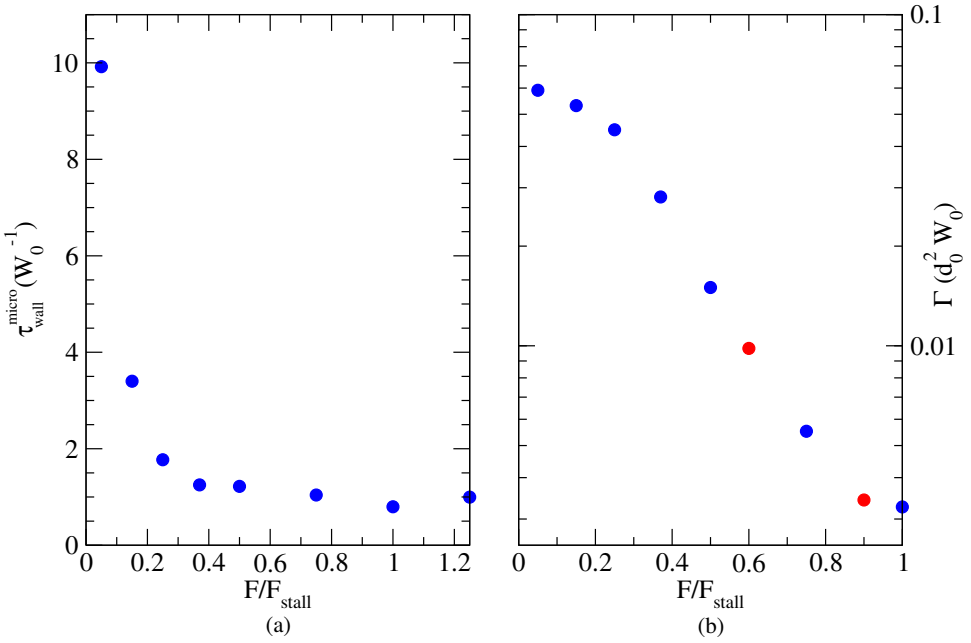

Figure 3.5. (a) Load dependence of the relaxation time τ_{wall}^{micro} for a homogeneous bundle of $N_f = 32$ rigid filaments growing against a constant load F at $\hat{\rho}_1 = 2.5$. (b) Diffusion coefficient Γ of the bundle. Blue symbols ($\epsilon = 0$ algorithm) and red symbols ($\epsilon > 0$ algorithm) refer to the stationary part of the constant load stochastic dynamics experiment mentioned in (a). From [54].

evolution of the wall position, and hence of the optical trap force $\langle F \rangle_t = \kappa_T \langle L \rangle_t$, from the small initial values to stalling is expected to occur at long time with an exponential behavior according to Eq. (3.47). Fitting the long-time part of the average behavior with this law gives information on the optical trap relaxation time τ^{OT}. Fig. 3.6 shows the relaxation toward stalling of the average force as a function of time for three cases: the blue and red points are obtained by the two different algorithms $\epsilon = 0$ and $\epsilon = 0.05$ and the same $\kappa_T = 0.25$. Note that this latter value is thousandfold larger than the experimental one [10], still data points perfectly superimpose with those obtained with $\epsilon = 0$, proving that the dynamics at finite (but small enough) ϵ is representative of the infinitely fast wall diffusion limit. The green points are obtained with the $\epsilon = 0$ algorithm with a larger $\kappa_T = 0.4511$. In any case the final plateau is in perfect agreement with the mean field prediction Eq. (1.9) represented by a dotted horizontal line. The dashed lines above the data points are the best fits of the exponential asymptotic behavior Eq. (3.47), providing the reported estimates of τ^{OT}. The mean field and brownian ratchet predictions for the two κ_T values are

$$\kappa_T = 0.25\text{:}\ \tau^{\mathrm{MF}} = 128\ W_0^{-1},\ \tau^{\mathrm{SR}} = 1126.4\ W_0^{-1}$$

$$\kappa_T = 0.4511\text{:}\ \tau^{\mathrm{MF}} = 70.94\ W_0^{-1},\ \tau^{\mathrm{SR}} = 624.25\ W_0^{-1}$$

The optical trap values are

$$\kappa_T = 0.25\text{:}\ \tau^{\mathrm{OT}} = (1185 \pm 50)\ W_0^{-1},\ \epsilon = 0.05$$

$$\kappa_T = 0.25\text{:}\ \tau^{\mathrm{OT}} = (1164 \pm 10)\ W_0^{-1},\ \epsilon = 0$$

$$\kappa_T = 0.4511\text{:}\ \tau^{\mathrm{OT}} = (654 \pm 10)\ W_0^{-1},\ \epsilon = 0$$

all in quite good agreement with the brownian ratchet predictions. In any case, the important observation to be made is that the adiabatic separation $\tau_{wall}^{micro} \ll \tau^{\mathrm{OT}}$ is verified, except at vanishing loads.

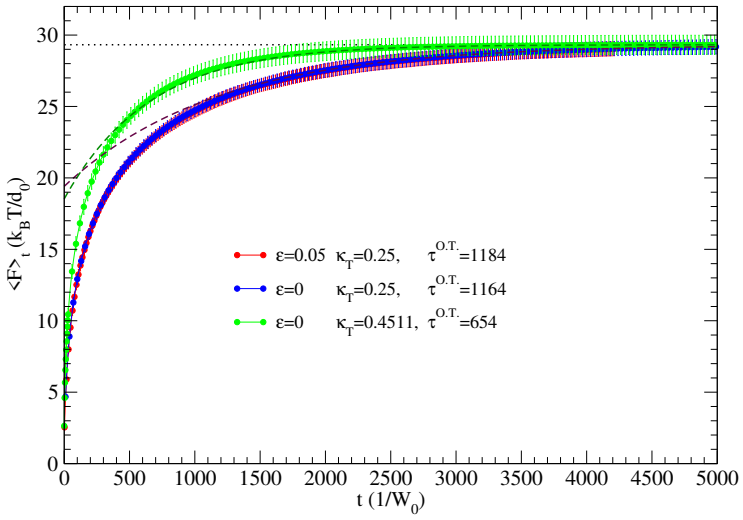

Figure 3.6. Non-equilibrium relaxation of the average optical trap force $\langle F \rangle_t = \kappa_T \langle L \rangle_t$ as a function of time for staggered bundles of $N_f = 32$ rigid filaments at $\hat{\rho}_1 = 2.5$ and the indicated κ_T values. The associated Root Mean Square Deviation (RMSD) $\kappa_T \sigma_L(t)$ is also shown. The final plateau value of the relaxations is compatible with the value F_{stall} given by Eq. (1.9) indicated by a horizontal dotted black line. The dashed lines represent the best fit of an exponential asymptotic behavior Eq. (3.47), providing estimates of τ^{OT} and hence of the chemical friction γ defined by Eq. (3.40). From [45].

Numerical differentiation of the wall position along the non-equilibrium trajectory always lets us get the velocity as a function of time; at each timestep we thus know the velocity at which the wall is moving and the force to which it is subject. Plotting the velocity as a function of the force (eliminating the time dependence) provides the full velocity-load relationship, from very small forces up to stalling. Fig. 3.7 shows the velocity-load relationship obtained by both constant load (red circles)

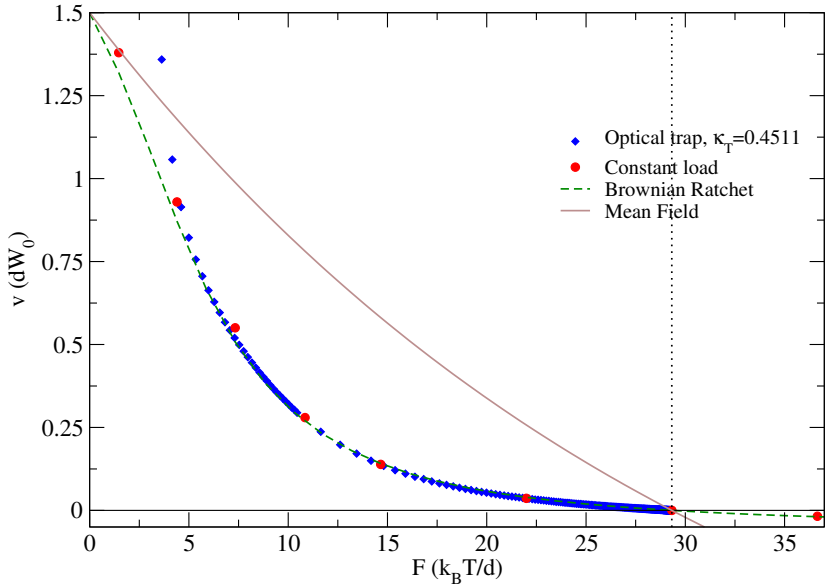

Figure 3.7. Velocity-load relationship for a homogeneous bundle of $N_f = 32$ rigid filaments at $\hat{\rho}_1 = 2.5$ ($\epsilon = 0$). The stationary velocity data points (red filled circles) are obtained as the asymptotic slope of $\langle L \rangle_t$ for constant force runs at each shown load value. Error bars are less than symbol sizes. The dashed green line is Démoulin *et al.*Õs theoretical estimate of $v^{\text{SR}}(F)$ based on Eq. (1.24) [12]. The solid line is the mean field velocity Eq. (1.13). The blue points show the velocity-load relationship obtained by the optical trap relaxation at $\kappa_T = 0.4511 \frac{k_B T}{d_0^2}$. Stalling is indicated by the vertical dotted line at $F = 29.32 \frac{k_B T}{d_0}$. From [45].

and optical trap (blue symbols), together with the brownian ratchet prediction $v^{\text{SR}}(F)$ based on Eq. (1.24) [12] (green dashed line) and the mean field prediction Eq. (1.13) [5, 11] (continuous brown line). A vertical dotted line represents the stalling force $F = 29.32 \frac{k_B T}{d_0}$. It is evident that the constant load simulations on rigid filaments give results in full agreement with the brownian ratchet model, while the mean field prediction always overestimates the wall velocity; the agreement between the observed velocity and the brownian ratchet prediction is less good at small forces, but this can be a consequence of the approximations made in Démoulin *et al.*'s theory [12] (yet very good, despite the approximations) to get the expression for the velocity Eq. (1.24), which is plotted. The optical trap results are also in agreement with the brownian ratchet model prediction, except at small loads: for too small forces the relaxation time τ_{wall}^{micro} has been found to diverge and the adiabatic separation, ensuring the equivalence between the constant load and optical trap dynamics, doesn't hold anymore. The fact that an optical trap experiment can be used to get almost the whole velocity-load relationship is an interesting result, which could be useful in designing experiments: during the relaxation the force varies

between zero and stalling and, tuning appropriately the experimental parameters, the system will go through stationary non-equilibrium states, where time by time its velocity is the same as in a constant load experiment with a value of the force equal to the optical trap load at that time. A single experiment thus potentially gives the entire load-velocity relationship, while a constant load experiment provides just a single point of that relationship.

Let's now see how and if this applies to flexible filaments and whether flexibility modifies somehow the velocity-load relationship of a bundle of filaments in optical trap.

Flexible filaments in optical trap set up

We have produced trajectories for $N_f = 32$ flexible filaments (flexibility is expected to display more evident effects for larger bundles) at $\hat{\rho}_1 = 2.5$ and several values of κ_T (10^3 trajectories for each case), also in the escaping regime, using for the average filament force the full expression Eq. (2.38) describing both the weak compression and the escaping regime. In order to highlight the effects of flexibility, we compare results for flexible and rigid bundles at the same thermodynamic conditions in Fig. 3.8. The top panel shows the average wall relaxation $\langle L \rangle_t$ of both a flexible bundle (actin $\ell_p = 5370.371 d_0$) and a fully rigid bundle (one of the cases shown in Fig. 3.6), with $\kappa_T = 0.4511 k_B T/d_0^2$ giving $L^{\text{MF}} = F_{stall}/\kappa_T = 65 d_0$ from Eq. (1.9), a value small enough to prevent the occurrence of escaping filaments and yet large enough to let flexibility effects manifest. Simulations started with the wall at initial position $L_0 = 5 d_0$ and the filament sizes distributed according to Eq. (2.44) and were run for a time window of $700 W_0^{-1}$. The relaxation towards stalling is similar to the rigid case, $\langle L \rangle_t \sim \langle L \rangle^{\text{OT}} - A \exp(-t/\tau^{\text{OT}})$ where τ^{OT} is the final relaxation time and A the amplitude of the slowest relaxation mode which depends on the initial conditions. The observed asymptotic value of the wall position, $\langle L \rangle^{\text{OT}}$, is equal to L^{MF} (indicated by the horizontal solid line) in the case of rigid filaments, slightly larger in the case of flexible filaments, as expected from the equilibrium results of Section 2.4. Fits, represented in the figure by dashed lines, provide $A = 65.9 d_0$, $\tau^{\text{OT}} = 128 W_0^{-1}$ and $A = 21.8 d_0$, $\tau^{\text{OT}} = 653 W_0^{-1}$ for flexible and rigid filaments respectively: the separation between the timescale of the load change τ^{OT}, the chemical events timescale τ_{chem} and the microscopic relaxation time τ_{wall}^{micro} in the case of flexible filaments is still wide enough to guarantee that during the slow variation of the trap amplitude, and thus of the load, the distribution of the filament lengths (with respect to the position of the obstacle) remains equivalent to the distribution in a hypothetical constant load experiment with load value set to $\kappa_T \langle L \rangle_t$ at the current stage of the relaxation process. This finding holds for any value of N_f and κ_T in the non-escaping regime which emphasizes the general character of the results.

The vertical bars on the data indicate the standard deviation of $\langle L \rangle_t$ which is seen to evolve rapidly towards its predicted equilibrium value $\sigma_L^{\text{OT}} = \sqrt{k_B T/\kappa_T} = 1.489 d_0$ for rigid filaments, while we measure $\sigma_L^{\text{OT}} = 1.5178 d$ for flexible filaments. This rather limited value of σ_L at all times is a unique characteristic of the optical trap apparatus, allowing to obtain rather precise measurements already with a limited number of relaxations. In real experiments, a single relaxation could still provide a

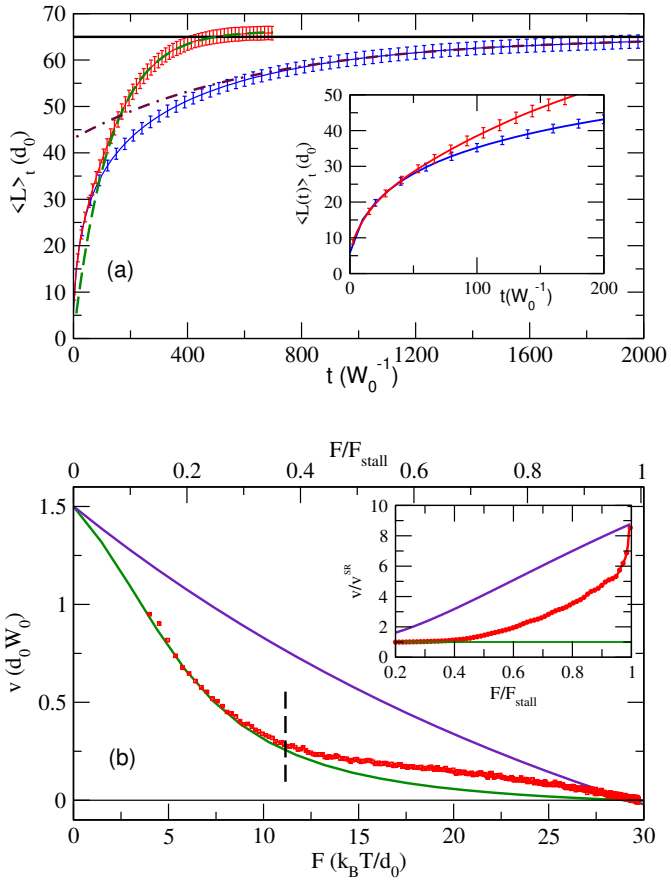

Figure 3.8. Panel (a): Relaxation of a staggered bundle of N_f filaments subject to optical trap load with trap strength $\kappa_T = 0.4511 k_B T/d_0^2$ at $\hat{\rho}_1 = 2.5$. Results for rigid (blue line) and flexible (red line) models. The horizontal line represents the value $L^{\rm MF} = F_{stall}/\kappa_T = 65 d_0$ from Eq. (1.9), while the flexible model has the slightly larger asymptotic value, in agreement with the theoretical prediction $\langle L\rangle^{\rm OT} = 66.1877 d_0$ (see Section 2.4, [47]). The vertical bars on the data indicate the standard deviation of $\langle L\rangle_t$ which is seen to evolve rapidly towards its predicted equilibrium value $\sigma_L^{\rm OT} = \sqrt{k_B T/\kappa_T} = 1.489 d_0$ (we measure $\sigma_L^{\rm OT} = 1.5178 d$ for flexible filaments). Exponential fits to the long time behavior for both models are shown by dashed and dot-dashed lines. The inset is an enlargement of the region where flexible and rigid model behaviors start diverging from each other. Panel (b): Red circles represent $\langle v\rangle_t = d\langle L\rangle_t/dt$ versus $\langle F\rangle_t = \kappa_T \langle L\rangle_t$ for flexible filaments as obtained in an optical trap experiment. The green line is the brownian ratchet prediction (that we have seen to be valid for rigid filaments), and the purple curve represents the mean field behavior. The vertical dashed line indicates the point where the flexible model data start to deviate from the rigid behavior. Inset: velocity relative to the brownian ratchet adiabatic solution versus the load reduced by the stalling force: mean field (purple line), flexible model (red points). From [54].

reliable measurement.

In the inset, a magnification of the first part of the relaxation process is shown: at very small lengths, the rigid and flexible behaviors are indistinguishable, while for $\langle L\rangle_t \gtrsim 25$ the flexible trajectory starts to deviate from the rigid one.

The bottom panel of Fig. 3.8 reports the wall velocity $v(t) = d\langle L\rangle_t/dt$, obtained by numerical differentiation, and plotted as a function of the time dependent load $F(t) = \kappa_T\langle L\rangle_t$ for both rigid and flexible bundles. Rigid model behavior is represented by the approximate solution of ref. [12] which we have seen to be very accurate [45]. On the same plot I also report the mean field behavior Eq. (1.13). The $v(F)$ data for the flexible model at the chosen κ_T value closely follow the rigid bundle curve up to $F \approx 11.3 k_B T/d_0$ (i.e. $F/F_{stall} \approx 0.38$, indicated by the vertical bar in the bottom panel of the figure), corresponding to $L \approx 25 d_0$ at that κ_T value. This behavior suggests that the velocity for flexible bundles is function not only of the external load but also of the bundle length. As stalling is approached, the $v(F)$ data get closer to the mean field curve: the inset in the bottom panel shows the ratio between the $v(F)$ data and the brownian ratchet prediction (red points) and between v^{MF} and the brownian ratchet prediction (purple line). The red points move from 1 at small loads to the purple line for the load approaching stalling, the deviation starting at $F/F_{stall} \approx 0.38$.

Anticipating a bit the following, the observed strong reduction of τ^{OT} due to flexibility is a manifestation of a new polymerization mechanism for flexible filaments, in which the monomer addition inside a tip-wall gap smaller than d_0 is made possible by a bending fluctuation: this mechanism, adding up to the subsidy effect discussed for bundles staggered rigid filaments in Chapters 1 and 2, improves the work repartition over the filaments as the fraction of filaments simultaneously touching the wall is related to the load sharing capacities of the filaments in the bundle. When filaments are short, the buckling force $f_b = \frac{\pi^2}{4}\frac{k_B T \ell_p}{L_c^2}$ (see Chapter 2) is rather large and few filaments (just a single one acting sporadically for very tight traps) are able to sustain the entire load. Therefore in a very short trap the dynamic behavior of the flexible bundle is equivalent to the rigid model behavior, as seen in the top panel of Fig. 3.8 for $L < (25 \div 30) d_0$. When filaments get longer, the single filament buckling force becomes weaker and a significant fraction of filaments has to be recruited simultaneously to sustain the increasingly large external load. As L further increases, all filaments would be recruited to act permanently and the mean field picture, where filaments perfectly share the load, would become valid as all the filaments would work simultaneously. This situation however is never reached in the present model because thermal bending fluctuations cause filaments to escape before the perfect load sharing condition is reached, as discussed later on.

3.3 Analysis of the filament flexibility effects

Flexible filaments display a enhanced polymerization capability with respect to rigid filaments, because they can exploit bending fluctuations to intercalate monomers and grow against a loaded obstacle. Let's imagine that a filament needs to compress by $n\delta$ ($\delta = d_0/N_f$) to intercalate a monomer: this compression plus the monomer addition, followed by the filament relaxation displacing the wall against the external force is energetically possible only if the difference in the free energy between the initial and final state satisfies the following

$$n\delta f_b - k_B T \ln \hat{\rho}_1 = n\delta \frac{\pi^2}{4}\frac{k_B T \ell_p}{L_c^2} - k_B T \ln \hat{\rho}_1 \sim k_B T \tag{3.55}$$

where $n\delta f_b$ is the compression free energy difference in the weak bending condition, where filaments exert a force equal to the buckling force f_b, and $-k_BT\ln\hat{\rho}_1$ is the gain in free energy due to polymerization. This relation gives a n-dependent effective length

$$\bar{L}(n) \approx \sqrt{\frac{n\pi^2\ell_p d_0}{4N_f(1+\ln\hat{\rho}_1)}} \tag{3.56}$$

for a bundle of N_f filaments at reduced density $\hat{\rho}_1$, at which flexibility effects start to manifest. In a staggered bundle, $n = 1, \ldots, N_f - 1$: in the case $N_f = 32$ at $\hat{\rho}_1 = 2.5$ we would have $\bar{L}(1) = 14.70d_0$ and $\bar{L}(31) = 81.85d_0$. We have seen that divergence between the flexible and rigid velocity-load relationship started at $\langle L\rangle_t \approx 25d_0$, which corresponds approximately to $n = 3$. To see whether this value is fortuitous, let's observe a comparison between different N_f bundles at the same $L^{\mathrm{MF}} = 80d_0$ ($\kappa_T = 0.011453N_fk_BT/d_0^2$). Fig. 3.9 shows the velocity obtained by the relaxation

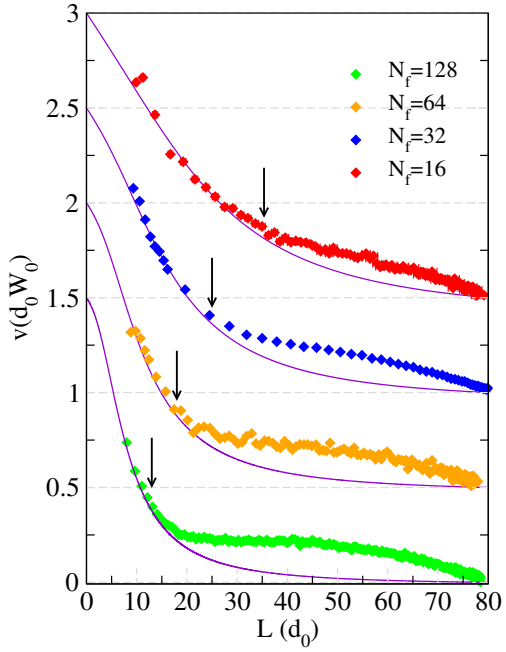

Figure 3.9. Flexible bundle velocity in optical trap as a function of the wall position for $N_f = 16$, 32, 64 and 128, $\hat{\rho}_1 = 2.5$ and $\kappa_T = 0.011453N_fk_BT/d_0^2$. The curves are shifted by 0.5 vertically to make the plot clearer. Vertical arrows indicate the value $\bar{L}(3)$ at which flexibility effects start manifesting through a deviation from the rigid brownian ratchet behavior. From [54].

experiments in optical trap as a function of the wall position for any case; the curves are shifted by 0.5 vertically to make the plot clearer. We empirically observe that in all cases $\bar{L}(3)$, indicated by vertical arrows in the figure, signals the beginning of the flexible regime. Hence, we assume that the crossover size between rigid and flexible behavior for a bundle of N_f filaments is

$$\Lambda = \bar{L}(3) = \sqrt{\frac{3\pi^2\ell_p d_0}{4N_f(1+\ln\hat{\rho}_1)}} \tag{3.57}$$

at reduced density $\hat{\rho}_1$. A bundle of flexible filaments hence exhibits a behavior that depends on its length. Let's see how this reflects on the velocity-load relationship.

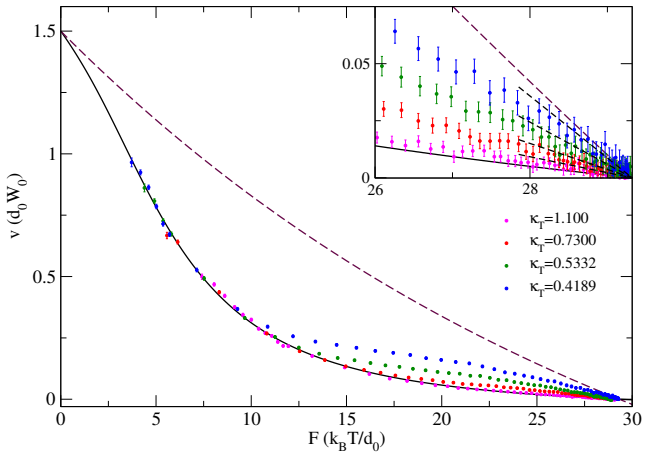

Figure 3.10. Velocity-load relationships obtained by optical trap relaxations for $N_f = 32$ at $\hat{\rho}_1 = 2.5$ and the indicated values of κ_T. The curves progressively deviate from the brownian ratchet (rigid) behavior as the trap strength decreases. Inset: magnification of the region close to stalling. The slopes of the curves are the same as calculated by the time autocorrelation function for the wall position at equilibrium, Eq. (3.50), indicated by black dashed lines.

Fig. 3.10 shows some of the velocity-load relationships obtained by optical trap relaxations for $N_f = 32$ at $\hat{\rho}_1 = 2.5$ and the indicated values of κ_T. The curves follow the rigid behavior for the largest κ_T and they progressively deviate from it for decreasing κ_T – at a given F value, the highest point belongs to the curve with the smallest κ_T. All the curves meet at stalling, where they present slopes whose absolute values increase with decreasing κ_T. In particular, these slopes result to be in good agreement with the values calculated through the characteristic time of the exponential relaxation of the time autocorrelation function for the wall position at equilibrium, Eq. (3.50). These latter values are shown in the inset of the figure by black dashed lines. At given F, besides, the corresponding L depends on κ_T – the smaller κ_T the larger L. At given F, hence, longer bundles move with a larger velocity. Indeed, by defining $\lambda = L/\Lambda$ as a degree of flexibility, it naturally appears that the velocity-load relationship $v(F; N_f, \hat{\rho}_1)$ can be generalized to the flexible case by including the dependence on λ, $v(F, \lambda; N_f, \hat{\rho}_1)$. The rigid behavior should be recovered for $\lambda \leqslant 1$.

Since in the optical trap experiments the average bundle length evolves from very short sizes at short times up to the final stalling length, the velocity-load relationship that we obtain by plotting the velocity at each time as a function of the optical trap force at the same time, is a collection of points characterized by different F and different λ values, cutting successive velocity-load curves at fixed λ. To map the full

$v(F,\lambda)$ relationship for the $N_f = 32$ bundle at $\hat{\rho}_1 = 2.5$, we performed 14 different optical trap experiments (averages over 992 individual trajectories in each case) at different trap strengths in the range $0.2094 k_B T/d_0^2 \leqslant \kappa_T \leqslant 1.10 k_B T/d_0^2$. Note that the expected average wall position for the smallest of these values is $L^{\mathrm{MF}} = 140.0 d_0$, well beyond the escaping threshold $L_{max} = 69.5 d_0$ (see Eq. (2.55)). In presence of escaping filaments, the analysis had to be performed carefully: for too long bundles, where eventually all the filaments escaped, we included in the analysis only the portion of the average relaxation before the manifestation of the phenomenon. For bundle lengths close to the threshold, where only few filaments were found to escape in some replica, we used only the replicas that didn't present the phenomenon[6] yet preserving a good statistics. Some of these trajectories are shown in Fig. 3.11. A horizontal line at a given $\langle L \rangle_t$ intersects with the trajectories at different times and dashed lines indicate the corresponding slopes (*i.e.* wall velocities); the values of the force acting on the wall at those times depend on κ_T. Collecting these (F, v) points belonging to different trajectories at given L provides a $v(F; \lambda, N_f, \hat{\rho}_1)$ curve, which is the velocity-load relationship *at given flexibility* λ. The justification of this procedure is again related to the observed separation of time scales between the slow load variation and the faster relaxation of filament lengths [54]. Fig. 3.12 shows the power developed by the pushing filaments, $P(F; \lambda, N_f, \hat{\rho}_1) = F \cdot v(F; \lambda, N_f, \hat{\rho}_1)$, at given λ for $N_f = 32$ and $\hat{\rho}_1 = 2.5$. The brownian ratchet (solid violet line) and the mean field (dashed violet line) predictions are also shown. This is the power of transduction of chemical into mechanical energy. For short filaments ($\lambda \leq 1$) the observed behavior is close to the brownian ratchet predictions and the effects of flexibility are negligible. As λ increases over unity, the power-load curves rise over the brownian ratchet prediction, moving towards the mean field behavior. This reflects the fact that flexibility induces better work sharing capacities, as anticipated by Schaus and Borizy [44]. The largest value of λ shown corresponds to the maximum bundle length before entering the escaping regime, $\lambda_{max} = L_{max}/\Lambda = 2.8$ – indeed, the perfect load sharing condition cannot be attained, filaments would be too long and finally escape and no more chemical energy would be transducted into mechanical work. Flexibility thus manifests through a remarkable enhancement of the power of transduction of chemical into mechanical energy, which is reasonably related to an enhanced degree of work sharing among the filaments: as seen in the previous chapter, longer bundles at equilibrium are characterized by a larger fraction of filaments touching the loaded wall ($N_0 \sim L^2$, see Chapter 2). At a given value of the load, longer bundles displace the wall with a larger velocity recruiting a larger number of filaments to sustain the load.

The velocity-load relationship of a bundle of semiflexible filaments thus moves from the brownian ratchet behavior (partial work sharing) to the mean field behavior (perfect work sharing) as the degree of flexibility increases, and we make the *ansatz* that it can be written as a linear combination of the brownian ratchet and the mean field behaviors, with coefficients that depend on the bundle length:

$$v(F, L) \simeq b(L) v^{\mathrm{MF}}(F) + [1 - b(L)]\, v^{\mathrm{SR}}(F) \tag{3.58}$$

with $b(L) = (L/L_l)^2$, suggested by the L^2 dependence of the number of filaments

[6] Nonetheless, in these cases we have verified that including the "escaping trajectories" in the analysis wouldn't have affected the analysis significantly.

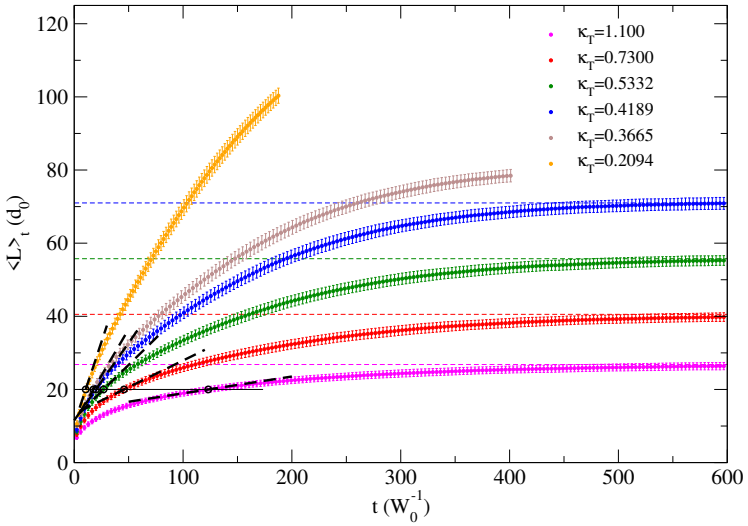

Figure 3.11. Optical trap relaxations for $N_f = 32$ at $\hat{\rho}_1 = 2.5$ and the indicated values of κ_T. The horizontal dashed colored lines indicate the mean field prediction for the stalling length, $L^{\mathrm{MF}} = F^{\mathrm{MF}}_{stall}/\kappa_T$ with F^{MF}_{stall} given by Eq. (1.9). The two relaxations corresponding to the smallest values of κ_T have been truncated as soon as escaping filaments started to massively manifest. The horizontal line shows how the slopes (*i.e.* velocities) at a given length (but different loads, depending on κ_T) increase for decreasing trap strength. Collecting points (F, v) at given L provides a $v(F; \lambda, N_f, \hat{\rho}_1)$ curve, which is the velocity-load relationship *at given flexibility* λ.

recruited to produce a given permanent force F at different trap widths; $b(L) = 1$ for $L = L_l = \sqrt{\frac{\ell_p d_0}{\ln \hat{\rho}_1}}$, *i.e.* the perfect load sharing condition would be attained for a bundle which is already massively escaped. The dashed colored lines in Fig. 3.12 represent Eq. (3.58) for the corresponding values of $L = \lambda\Lambda$. The agreement is not perfect, yet still good for small λ values, while it worsens approaching λ_{max}.

In Fig. 3.13, data obtained for the optical trap relaxation of bundles of 64 and 128 flexible filaments are compared with the prediction Eq. (3.58) to stress the general validity of the *ansatz* illustrated in Fig. 3.12 for the $N_f = 32$ case only. These results show the pertinence of Fig. 3.13 for a full characterization of the flexibility effects based on analytical expressions, hence relatively easy to use in interpreting future in-vivo experimental data.

3.4 Concluding remarks

In this chapter, using a realistic model for semi-flexible filaments and by means of numerical simulations, the effects of flexibility on the dynamics of actin bundles in supercritical conditions pressing against a loaded obstacle have been studied. Taking inspiration from ref. [10], we simulate the behavior at equilibrium (stalling) and the

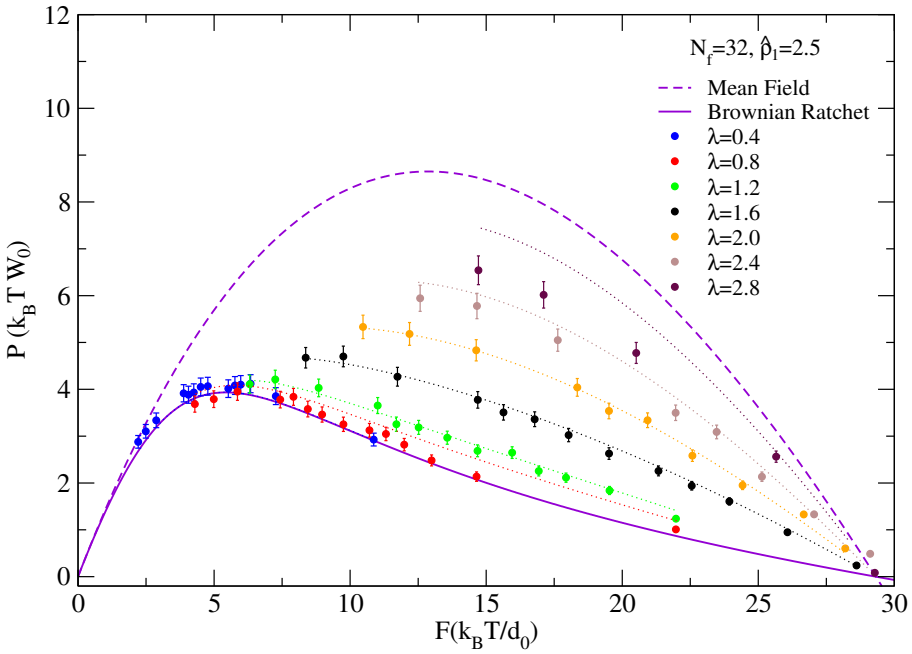

Figure 3.12. Power-load relationship, $P = vF$ versus F, at given λ obtained by optical trap relaxations for $N_f = 32$ and $\hat{\rho}_1 = 2.5$. The brownian ratchet and mean field predictions are shown by a solid and a dashed violet line respectively. For $\lambda < 1$ the observed behavior is in quite good agreement with the brownian ratchet prediction, but for $\lambda > 1$ the curves move towards the mean field behavior. The perfect work sharing condition though is never attained because of the occurrence of escaping filaments. The dotted lines represent linear combinations between the mean field and brownian ratchet laws, see text.

relaxation towards equilibrium of bundles in optical trap setup, applying a harmonic external force to the wall which opposes to the bundle growth. In such conditions the wall moves under the combined action of the polymerization force of a staggered actin bundle and the external load. At equilibrium, all the results obtained by the theoretical analysis in the previous chapter have been re-obtained and confirmed. Moreover, through the analysis of the time autocorrelation function for the wall position, we found that the wall is subject to an additional friction, which we call "chemical", linked to the slope of the velocity-load relationship at stalling.

In non-equilibrium situations, where bundles were let grow from a small initial size up to stalling, the relaxation of the trap is found to be mostly adiabatic as the reorganization of the filament sizes against the loaded wall is one-two orders of magnitude faster than the time over which the load varies. This fundamental fact allows to consider most states visited during the dynamical relaxations as stationary states for the bundle and, by eliminating the time from the analysis of the results,

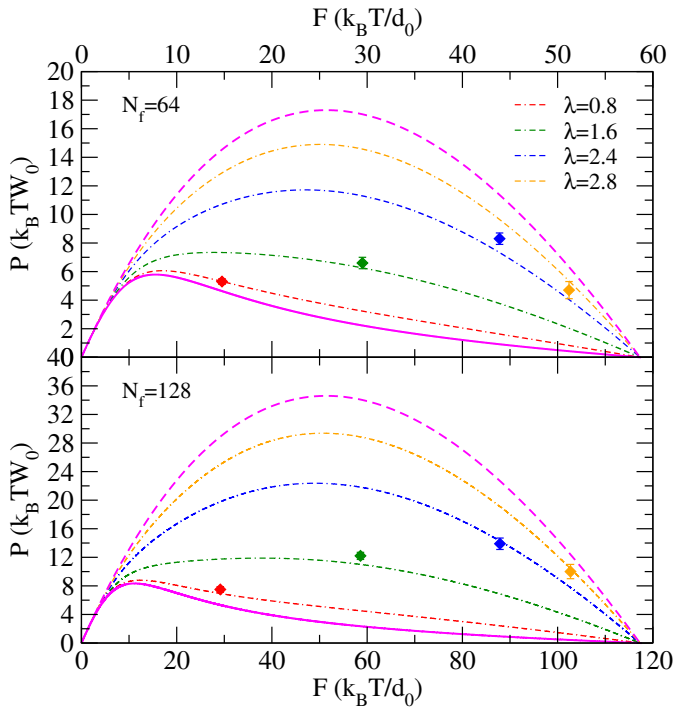

Figure 3.13. Flexible bundles relaxation experiments against an harmonic load with trap strength $\kappa_T = 0.011453 N_f$ chosen to cover a similar L window between the bundle initial size $L_0 \approx 5d_0$ up to a common equilibrium value $L_{stall} \approx 80d_0$. The plot show the power predicted by Eq. (3.58).

to obtain the velocity-load relationship of semiflexible bundles. Filament flexibility greatly enriches the theoretical scenario: first, the velocity-load relationship results to depend on the reduced bundle length $\lambda = L/\Lambda$ which is a measure of its degree of flexibility. Second, the power of transduction of chemical energy into mechanical work is considerably enhanced as the bundle length (and hence filaments flexibility) increases. The perfect load sharing condition, nonetheless, cannot be attained because of the massive occurrence of escaping filaments. Fig. 3.14 illustrates these features and their dependence on the filament persistence length ℓ_p. It shows the three regimes observed: 1) a rigid regime at $L < \Lambda$ ($\lambda < 1$) where flexibility effects are negligible; 2) the intermediate regime where flexibility effects are present with an increase of the obstacle velocity with flexibility (*i.e.* bundle length at fixed ℓ_p) at fixed external load; 3) the escaping regime at large enough trap width ($L > L_l$). We see that the non-escaping flexible regime gets wider for increasingly flexible filaments. It is illuminating to consider the ratio $L_l/\Lambda = \sqrt{\frac{4N_f(1+\ln\hat{\rho}_1)}{3\pi^2 \ln\hat{\rho}_1}}$, which is independent of ℓ_p. In supercritical conditions ($\hat{\rho}_1 > 1$) $L_l/\Lambda \geq \sqrt{\frac{4N_f}{3\pi^2}}$, therefore a wide flexible regime before escaping requires bundles with a large number of filaments.

Using the optical trap set up for different values of κ_T the three regimes were characterized and their boundaries established. We have shown that the power of the bundle is strongly increased by the flexibility in the intermediate regime and

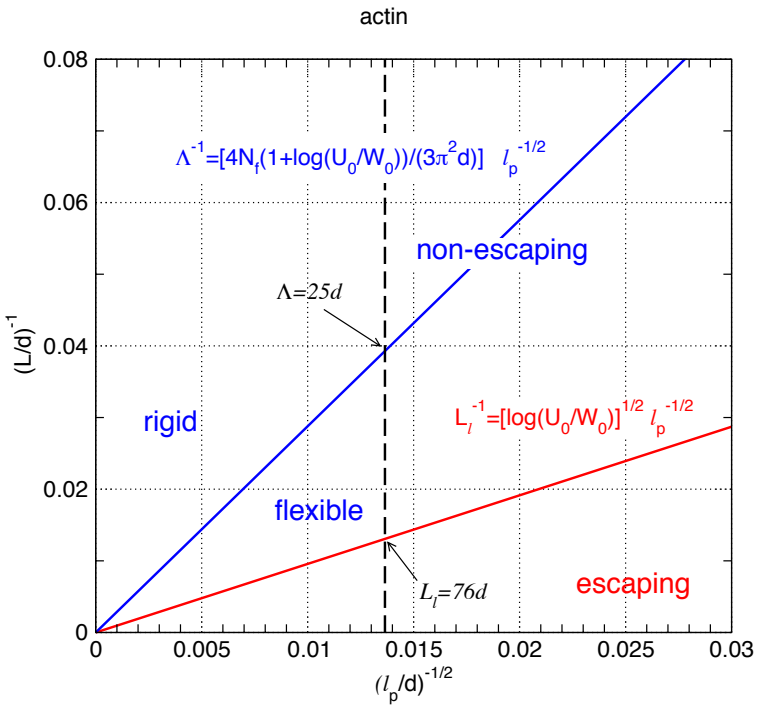

Figure 3.14. The three different regimes for a bundle of filaments with finite flexibility indicated by the filament persistence length illustrated here for $N_f = 32$ and $\hat{\rho}_1 = 2.5$. The case of actin $\ell_p = 5370 d_0$ is indicated by a vertical dashed line. The non escaping regime for a homogeneous bundle is further divided into a rigid filament regime and a flexible filament regime by the line at $L = \Lambda$, Eq. (3.57). The escaping regime is met for $L = L_l$ with $L_l = \sqrt{\ell_p d_0 / \ln \hat{\rho}_1}$ (see Eq. (2.55)). From [54].

can almost cover the entire gap between the brownian ratchet (rigid) and the mean field (perfect load sharing) behaviors, which appears to be an upper bound for a many flexible filaments bundle, as the filament length reaches the crossover value between non-escaping and escaping domains. The power increase with L at a given load F is the result of an improved work sharing capacity of the bundle due to the increasing fraction of filaments pressing on the wall ($\propto L^2$) when developing the polymerization force opposing the load F. A simple ansatz combining linearly the perfect load sharing behavior and the brownian ratchet behavior provides a satisfactory description of the data. Our work shows how filament flexibility could be easily considered in interpreting future experiments, in a way that enriches considerably the present dominant theoretical model [6].

Despite a consistent treatment of filament flexibility including the escaping regime, our model is unable to reproduce the in-vivo experimental results of ref. [10], which remain once more unexplained.

Part II

The Cell Membrane and the Cytoskeleton

Chapter 4

Biomembranes: an introduction

It is essential for cells' life that the intracellular environment is kept different from the extracellular one: this is guaranteed by the plasma membrane that has the purpose to isolate the interior of the cell from the surroundings, not contributing to the mechanical strength of the cell – task that is assigned to the cytoskeleton. The plasma membrane is a thin, fluid, flexible and selectively permeable thin sheet, with a particular structure and chemical composition. It completely embeds the cytoskeleton, and the activity of the cytoskeletal filaments pushing beneath the membrane determines the onset of temporary structures, such as lamellipodia *and* filopodia*, which are fundamental for cell motility.*

This chapter is intended to provide an introduction to the subject of biomembranes and it is organized as follows: Section 4.1 will provide a brief description of the phospholipid bilayers and their fundamental properties. Section 4.2 will be focused on the interactions between the cytoskeleton and the overlying membrane with particular interest in the lamellipodial and filopodial structures. Finally, Section 4.3 is devoted to a concise review of one of the first models attempting to give a physical and mathematical interpretation of the filopodial protrusions [4].

4.1 Cell membrane: structure and functions

Membranes play a central role in both the structure and function of all cells, either prokaryotic or eukaryotic, vegetal or animal. The main function carried by cell membranes is to create compartments, dividing an "inside" form an "outside". Yet, their role is not limited to this partitioning: it is also the main regulator of all the communications between the cell and the extracellular environment, which mostly translates into ions and molecules passing through the membrane.

The first membrane we can think of is the *plasma membrane*, enveloping the whole cell and dividing it from the extracellular environment, but there are also many membraneous organelles inside the cell (Golgi apparatus, mitochondria, nucleus...), and each membrane has a different composition, structural details and functions. Still, it is possible to study all these membranes on a common ground, focusing on their universal properties.

In the following, I will focus on the plasma membrane only, starting from the analysis of its building blocks: *phospholipids*.

4.1.1 Phospholipids aggregates

Phospholipids are the cellular membrane's main components, as it was discovered already in the end of the XIX century [63]; they are *amphiphilic molecules*, meaning that they present two zones with different behaviors when in contact with water. They have a round domain called "head" that is *hydrophilic* – literally "in love with water" – attached by a phosphate group to (typically two) hydrocarbon chains called "tails" that are *hydrophobic* – literally "frightened by water". When groups of amphiphilic molecules are put in water, they develop collective strategies to avoid contact between water and the hydrophobic tails: they self-assemble forming aggregates, which can be spheres (micelles), cylinders (cylindrical or wormlike micelles) or double sheets (lipid bilayers), which expose the hydrophilic heads to the water contact in the surface while shielding the tails, which point towards the inside of the aggregate. The kind of aggregate that phospholipids spontaneously form when put in water depends on their geometrical properties in the first place, as can be seen through the following simple argument [20, 64, 65].

Let a_0 be the cross-sectional area that the head group of the amphiphile occupies in the aggregate's surface, l_{hc} the length of its hydrocarbon tail and v_{hc} its volume. Let's take the case of a spherical micelle. If N is the number of amphiphiles, to a first approximation the total micelle area must be equal to N times the area of an amphiphile's head and its volume must be equal to N times the volume of an amphiphile, *i.e.* $4\pi R_{sphere}^2 = Na_0$ and $\frac{4}{3}\pi R_{sphere}^3 = Nv_{hc}$, which gives:

$$R_{sphere} = \frac{3v_{hc}}{a_0}. \tag{4.1}$$

In the meantime, the inner volume of the micelle must be filled by the tails (no holes must be left in the core), which implies $l_{hc} \geq R_{sphere}$. This requirement leads to the condition

$$P \equiv \frac{v_{hc}}{a_0 l_{hc}} \leq \frac{1}{3} \qquad \text{(spherical micelle)} \tag{4.2}$$

where P is the phospholipid *shape factor*; I will come back later on its meaning. Let's now consider a cylindrical micelle and repeat the same reasoning: we would have $2\pi R_{cylinder} t = Na_0$ and $\pi R_{cylinder}^2 t = Nv_{hc}$, where t is the cylinder height. This gives

$$R_{cylinder} = \frac{2v_{hc}}{a_0} \tag{4.3}$$

and the condition $l_{hc} \geq R_{cylinder}$ leads to

$$\frac{1}{3} < P \leq \frac{1}{2} \qquad \text{(cylindrical micelle)}. \tag{4.4}$$

Let's finally consider the case of phospholipids forming a double layer, with the phospholipid heads in the external surfaces and the tail toward the inside; in this case the interesting quantity is the distance between the heads, $D_{bilayer}$. We have $2A = Na_0$ and $AD_{bilayer} = Nv_{hc}$, being A the total area of the bilayer, from which we obtain

$$D_{bilayer} = \frac{2v_{hc}}{a_0}. \tag{4.5}$$

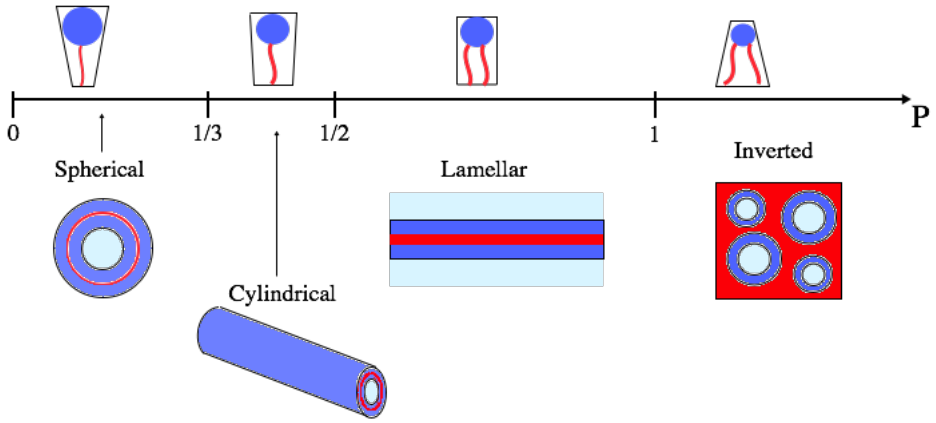

Figure 4.1. Schematic representation of the amphiphile's shape depending on its shape factor P and the relative kind of amphiphilic self-assemblies: spherical, cylindrical, lamellar and inverted micelle.

The condition on l_{hc} in this case is $l_{hc} \geq \frac{1}{2} D_{bilayer}$ leading to the following condition on the shape factor:

$$\frac{1}{2} < P \leq 1 \qquad \text{(bilayer)}. \tag{4.6}$$

The shape factor of the amphiphile thus relates the shape of the molecule to the kind of aggregate that a group of them spontaneously forms in water: at given l_{hc}, a small P means that the molecule has a big head attached to a relatively small tail, like an ice-cream cone, and it shouldn't surprise that such molecules tend to form spheres, where small tails will more easily fit in. On the other hand a large P means that the amphiphile's tail has dimensions similar to its head, and both cylindrical and planar configurations are "roomier" for large tails. There is also the possibility that the hydrocarbon tail volume is significantly larger than the head, which lies near the apex of a truncated cone. In this case, the lipids will tend to form *inverted micelles* with the head groups on the inside of the micelle, which contains water, and the hydrocarbon regions radiating away from the aqueous core. In this case

$$P > 1 \qquad \text{(inverted micelles)}. \tag{4.7}$$

Fig. 4.1 shows a schematic representation of these possible amphiphiles' shape factor and the relative aggregate. This is a very naive and not so predictive argument – still, it can be mapped quantitatively to model lipids collective behavior [20].

4.1.2 Bilayers in the cell

The interior of the cells is filled with the cytoplasm that is mostly made of an aqueous solution, the cytosol, in which the cellular organelles are suspended. The phospholipid bilayer is thus the optimal structure to separates the interior and the exterior of the cell, both water-like. The lipids that compose cellular membranes are indeed mostly double-tailed: this doubles their shape fraction, which is roughly

$P = 0.8$ for double-chain lipids [20]. Additionally, carbons along the chain are most likely joint by double rather than single bonds: this makes the tails more twisty and steric interactions between tails of neighboring lipids make the dense packing more difficult. Other lipids, like cholesterol, can fill the gaps left between the main phospholipids. This loose packing lets lipids diffuse among the bilayer, which shows a low lateral viscosity. Indeed, a property of the plasma membrane is its *fluidity*: it behaves like a 2D fluid where lipids can diffuse with certain diffusion coefficients. A typical lipid molecule exchanges places with its neighbors in a leaflet about 10^7 times per second and diffuses several micrometers per second at $37°C$. At this rate, a lipid could diffuse the length of a typical bacterial cell ($\approx 1\mu$m) in only 1 second and the length of an animal cell in about 20 seconds. Besides, the membrane composition is more varied than just phospholipids: in between them, there are membrane proteins that can be permanently anchored or part of the membrane (*integral membrane proteins*) or temporarily attached to the lipid bilayer or to other integral proteins (*peripheral membrane proteins*). Integral proteins can span across the two layers (*transmembrane proteins*) or be attached to only one side (*monotopic proteins*), all of them being typically much larger than lipids. Their size, together with the interactions with the underneath cytoskeleton [66], causes a dramatic reduction of the lateral diffusion coefficient; the rate of lateral diffusion of lipids in the plasma membrane is nearly an order of magnitude slower than in pure phospholipid bilayers: diffusion constants of 10^{-7} cm^2/s and $10^{-8} cm^2/s$ are characteristic of the plasma membrane and a pure lipid bilayer, respectively [67]. Fig. 4.2 represents schematically a bilayer membrane with examples of embedded

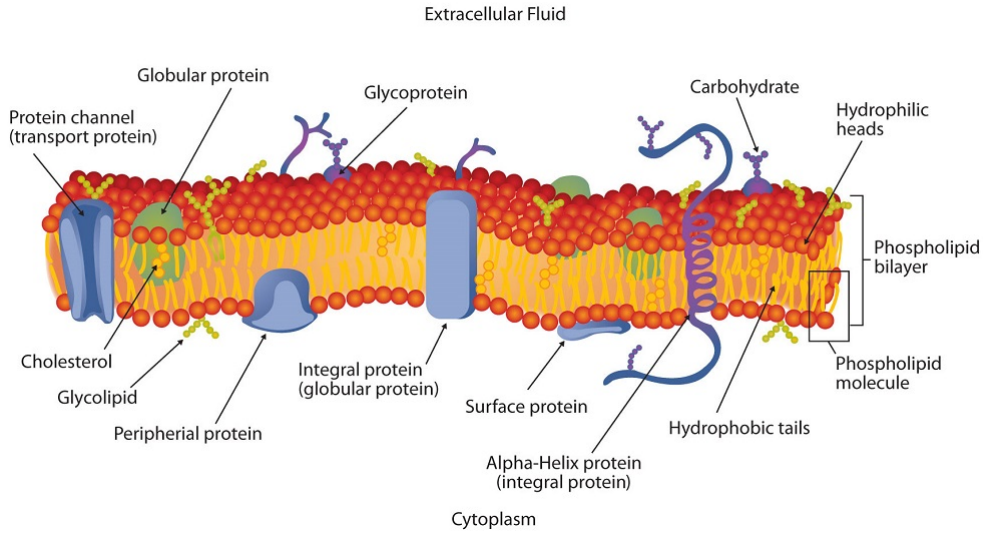

Figure 4.2. The cell membrane comprises different types of lipids, membrane proteins and small molecules. Lipids are organized in domains and are asymmetric, i.e. there are different lipid types in the opposing layers. Water molecules are present on both sides of the membrane. From [68].

membrane proteins. Some of the integral proteins, such the protein channel indicated at the left of the figure, are meant to make the membrane selectively permeable to

external objects – these proteins make channels which open or close to allow or not for molecules to enter the cell.

Beyond the large variety of structure and composition of plasma membranes (of which this section was intended to provide a far from exhaustive overview), the point we are interested in here is the (mechanical) interaction between the membrane and the cytoskeleton, which is located just beneath it. Indeed all the cell shape changes are driven by the cytoskeletal activity and involve strong local deformations of the membrane, still avoiding its rupture. In the next section I will review the kinds of structures that cytoskeletal filaments are able to form beneath the membrane inducing large deformations of it.

4.2 Cytoskeleton and cell membrane: integrated actin structures

The dynamic interplay between the soft plasma membrane and the underlying much stiffer cytoskeleton is essential for any cellular shape change or movement. We have seen in the first part of this thesis that actin filaments can generate significant forces by polymerization, and in real cellular processes these forces are employed to deform the membrane in the first place, e.g. during motility [69], phagocytosis [70], endocytosis [71] and cytokinesis [72]. In real cells, the spacial organization of actin filaments is mediated by specific protein-protein interactions that branch, crosslink and bundle filaments. Whether these proteins are indispensable or not is still an open question.

Actin filaments can be arranged in a variety of integrated structures to produce efficient forces, membrane deformations and finally movement of the cell as a whole. We have already seen (Chapter 1) that the most popular vision of the moving cell is largely inspired by studies of fibroblasts moving on rigid surfaces, and according to it cell motility is the result of a cyclic protruding of the leading edge of the cell, creation of adhesion points and further rear retraction (see Fig. 1.1b). All this process is essentially driven by actin polymerization (myosin being involved in the retraction stage). The main organelles driving forward motility are *filopodia* and *lamellipodia*, while the movement of the cell as a whole is assigned to contractile structures like transverse arcs, focal adhesion or anchored stress fibers and cell cortex [73]. Thanks to developments in *in-vivo* imaging of cell motility, it is becoming more and more clear that cell motility is more complex and varied than this simple picture, still the main ingredient remains actin filaments polymerization, initiated by either formin or the Arp2/3 complex [20].

4.2.1 Lamellipodia and filopodia

- A lamellipodium is a sheet-like actin-rich protrusion formed by a quasi-2D network of filaments polymerizing beneath the membrane at the leading edge of the moving cell, via the Arp2/3 complex activated by the WAVE complex, a specific nucleating-promoting factor; cofilin may also play an active role during the initiation of the lamellipodium by increasing the number of the free barbed ends due to filament severing [74, 75]. The flat shape of the lamellipodium

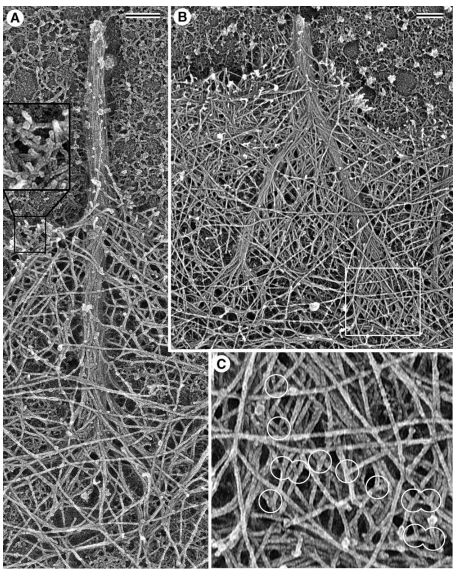

Figure 4.3. One of the most beautiful image of a filopodium obtained by electronic microscopy, from [81]. (A) A filopodium containing a tight F-actin bundle. Filaments in the roots are long compared with the branching network of the adjacent lamellipodium (inset). (B) A filopodium resulting from the fusion of two sub-bundles; the boxed region at the root of the right sub-bundle is enlarged in (C) and shows many branches (encircled) at which filopodial filaments originate.

is maintained by branched actin filaments, even if not all the branches grow in the leading edge direction: in *in-vitro* studies [73, 76] many barbed ends were observed to grow away from the surface, oppositely to the direction of cell migration. Similarly, in an *in-vivo* investigation of an intracellular wound healing system [77], primary filaments were observed to run parallel to the surface while secondary branches were oriented obliquely to the protruding membrane.

The lamellipodial protrusive force in a migrating cell has been directly measured, *e.g.* in [78] by recording the deflection of a cantilever in contact with the cell. There, the maximal force needed to stop the entire cell was found on the order of 35 nN, while the stalling force for the lamellipodium was on the order of 3 nN. The velocity-load relationship has been measured as well, finding a bent-down shaped curve [79]: it is much different from the single actin filaments velocity-load curves discussed in the first part of this thesis, suggesting that actin dynamics alone is not enough to explain cell measurements, but either motor activity or the length change of actin filaments under force should be taken into account [73, 80].

- Filopodia are finger-like protrusions at the front of the cell, typically growing from the lamellipodial protrusion, made up of bundled, parallel, unbranched actin filaments (see Fig. 4.3) with the barbed ends oriented towards the membrane. They have the role of sensing the extracellular environment, initiate

cell contacts and transmitting signals between cells; they may also attach to bacteria, retract once captured the hostile object and then allow for bacterial engulfment. Filopodia are also thought to be involved in cellular processes including wound healing, cell-cell adhesions or cell-matrix adhesion, but their exact biological contribution to these processes remains unclear [82, 83]. In the filopodia tip complex, formins and Ena/VASP proteins retain the growing barbed ends at the membrane and enhance actin growth [73]. The most unclear point about filopodia is how they are initiated: the main debate concerns whether Arp2/3 complexes have some role in the filopodia formation or if their nucleation demands only formin, or whether actin bundling proteins are needed for the filopodium formation and maintainance. Two alternative models have been proposed for the filopodium initiation, the *convergent elongation model* and the *de novo tip nucleation model*. According to the former, actin filaments branched by Arp2/3 grow, meet at the membrane and converge inside some basin on the membrane's surface initiating the filopodium; this filopodial seed then extends, not clearly if the presence of elongators and bundlers like Ena/VASP and fascin proteins is required [81] or not [84]. According to the latter mechanism, the Arp2/3 complex is not needed while filopodial filaments are newly nucleated and elongated by formins [85, 86].

The mechanism of retraction of the filopodium subsequent to engagement of bacteria-cell contact has been used to measure the force generated by filopodia, by covering a bead with a microorganism attachment proteins and coupling it with an optical tweezer set-up [73]. The force exerted by the filopodia was found on the order of 10 pN. In [87], optical tweezers were used to measure the force-extension curve for the formation of tubes from giant vesicles. The GUV was immobilized on a cover slip with a streptavidin-coated polystyrene bead, then another bead was brought into contact with the vesicle for a short time with the tweezers. Next, the vesicle was moved away with a piezoelectric stage for 10-15 μm at a constant velocity (0.5 μm/s). During this pull the force grew up to a maximum value, F_{over}, after which a tube was formed and the force dropped to a plateau value F_0. Overshoot forces much larger ($F_{over} \lesssim 40$ pN) than the plateau value ($F_0 \sim 4$ pN) were observed. The authors related the observation of this significant force barriers for the formation of the tube to the work needed for the initial deformation of the membrane.

4.2.2 Role of plasma membrane in the lamellipodia and filopodia dynamics

When starting polymerization to create a lamellipodium or a filopodium, the first resistance that filaments encounter is indeed the membrane tension: several physical models of membrane-cytoskeleton interaction treat the membrane just as an obstacle with fluctuating shape [88, 89], with a resisting load related to the membrane tension. It has indeed been clearly observed that a reduction in the membrane surface tension allows for more growth [90], still, the direct effect of membrane elasticity on cytoskeletal network organization is not clear.

In reproducing actin-membrane systems, large use is made of the aforementioned giant unilamellar vesicles (GUVs), which are spherical vesicles bounded by a single

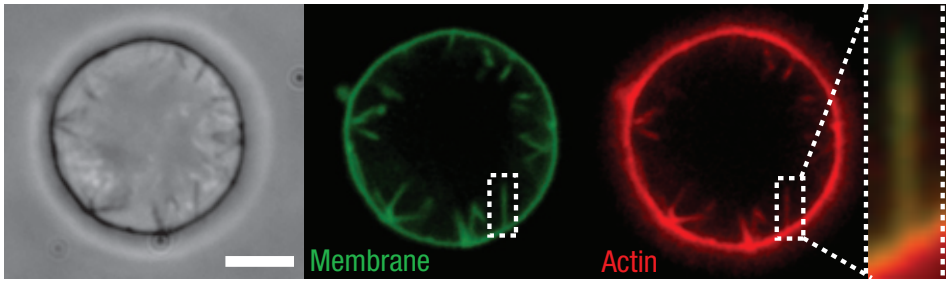

Figure 4.4. Thin actin protrusions emerging from dendritic actin networks. Green: phase-contrast and spinning-disc confocal images of membrane; red: actin. Multiple protrusions towards the inside of the GUV are clearly visible. The profiles of membrane protrusions and actin-reach regions can be perfectly superimposed, confirming that the membrane protrusions are supported by actin filaments. Scale bar: 5 μm. From [84].

bilayer of an amphiphilic lipid (or a mixture of them) containing aqueous solution inside the chamber. In [84], reconstituted actin networks containing only actin, N-WASP and Arp2/3 complex were assembled onto GUVs; as actin started polymerizing, dendritic actin network formed on the external leaflet of the GUVs. Protrusions emanating from the Arp2/3-branched network pointing towards the inside of the vesicle were observed in nearly 95% of the vesicles over 10μm in diameter, see Fig. 4.4. These protrusions initially grew at a rate of ~ 1 μm min^{-1}, gradually slowed down until stalling at a stationary length ranging from 1 to 25 μm. During elongation, protrusions remained straight with no visible lateral fluctuations. In that work, only a minimal set of purified proteins was used and the authors showed how a deformable membrane can gather and bundle nearby actin filaments into finger-like protrusions, *even in absence of tip-complex or bundling proteins*. The authors focused on the direct effect of membrane elasticity on growing filaments, which is not clear yet, and suggested that the mechanical properties of the membrane may play a central role in the cytoskeletal network organization driving several kinds of cellular shape change.

In this second part of the thesis I will focus on these filopodial protrusions created by bundles of parallel actin filaments. The interactions I will be interested in are mechanical – filaments growing against the resistance of the membrane – for which the knowledge of the membrane's elastic properties is needed. This will be the topic of the next chapter. To conclude this introducing chapter, in the next section I will briefly review a very popular work [4] attempting to mathematically model filopodial protrusions and interpret experimental evidences.

4.3 The Physics of Filopodial Protrusion

The work I shall present in this section is one of the first attempts of mathematical modeling of the filopodial protrusion, and it gives nice and neat results, in good agreement with some experimental observations, with a very simple mathematical approach. The authors modeled a filopodium protrusion as a bundle of N_f actin

filaments (typically $N_f \approx 10 \div 30$) growing from an extending lamellipodium against a membrane which opposes a constant resistance force, and found that depending on the number of filaments, different processes may limit the growth of filopodial extensions, even with a negligible depolymerization rate [4].

Buckling-limited elongation

Filaments growing in bundles beneath the membrane creating a filopodial protrusion need to win the membrane resistance F, which can be determined either experimentally or theoretically. Authors reported that the resistance force at the filopodial tip has been estimated theoretically as $F \sim 10 \div 20$ pN for a membrane cylinder of radius $50 \div 100$ nm [7]. From a mechanical point of view, the F-actin bundle is treated like an effective elastic rod, which can resist to a maximum force before buckling equal to

$$F_{buckle} = \frac{\pi^2}{4} \frac{k_B T \ell_p}{L^2} \times I(N_f) \tag{4.8}$$

where L is the length of the N_f-filaments bundle and $I(N_f)$ is a dimensionless factor accounting for the dependence of the bundle stiffness on the number of bundled filaments. If the filaments bundling is loose (*e.g.* in absence of cross-links or with very flexible bundling proteins), they buckle independently from each other and $I(N_f) = N_f$. Conversely, if filaments are tightly bundled, they will behave like a single thick rod, with total cross-section equal to N_f times the cross-section of a single filament, and hence effective radius $R \propto \sqrt{N_f}$; the stiffness scales with the radius to the fourth power, and hence $I(N_f) \propto N_f^2$. Numerical simulations performed in [4] suggest $I(N_f) \approx \frac{1}{2} N_f^2$.

From Eq. (4.8), as the bundle grows longer, the force that it is able to sustain before buckling decreases, and there will be a maximum length such as the buckling force equals the membrane resistance force and growth will stop. The maximum length of the filopodium due to buckling can be calculated in the two limiting cases of loose and tight bundling, giving respectively:

$$L^{\mathrm{B}}_{max}(N_f) = \frac{\pi}{2} \sqrt{\frac{k_B T \ell_p}{F}} \times \begin{cases} \sqrt{N_f} & \text{weakly cross-linked,} \\ \frac{1}{\sqrt{2}}\, N_f & \text{strongly cross-linked.} \end{cases} \tag{4.9}$$

The authors considered a membrane resistance force equal to $F \sim 20$ pN (experiments provided forces in the range $10 \div 50$ pN [7, 91]) and a persistence length equal to $\ell_p = 10$ μm, and obtained, for $N_f = 10$, $L^{\mathrm{B}}_{max} \sim 0.22$ μm in the case of weak cross-linking and 0.5 μm in the case of strong cross-linking, whereas for $N_f = 30$ they found $L^{\mathrm{B}}_{max} \sim 0.40$ μm in the case of weak cross-linking and 1.5 μm in the case of strong cross-linking. The authors found by numerical simulations that in cells a strong cross-linking of filaments in filopodia is more plausible. Moreover, this order of magnitude for the filopodial protrusion length was in agreement with several experimental observations; also the authors reported a case where filopodia of 25 filaments showed a (bundle) persistence length of 14 mm – in accordance with a quadratic scaling of the stiffness with the number of filaments (strong cross-linking) – but reached a length on the order of 40 μm, much larger than predicted. Possible explanations have been provided for this discrepancy, first of all the need of more

details in the model, together with a non adequate value of the membrane resistance, or possible adhesions of the filopodia to the substrate increasing its stiffness.

G-actin diffusion-limited elongation

Besides buckling, another phenomenon can limit the elongation of the filopodial protrusion: monomers diffusion. If the membrane offered no mechanical resistance, as long as filaments can polymerize, the filopodial protrusion will go on growing undefinitely. Still, in order for them to polymerize, actin filaments need supplies of free monomers in the proximity of their barbed ends. If free monomers take a very long time to diffuse to the leading edge of the protrusion, compared to the rate at which they are consumed for polymerization, the growth will eventually stop.

Let's $L(t)$ be the length of the bundle, and $\rho_1(x,t)$ the free monomer density, depending both on time and on the position along the filopodium (the x axis is oriented along the filopodium with the origin at its basis). G-actins drift with the cytoplasmic fluid and since the cytoplasm has to constantly fill the filopodium, the drift rate is equal to the filopodium elongation rate, $\frac{dL}{dt}$. The free monomer concentration varies in time according to the following equation [92]:

$$\frac{\partial \rho_1}{\partial t} = D\frac{\partial^2 \rho_1}{\partial x^2} - \frac{\partial}{\partial x}\left[\left(\frac{dL}{dt}\right)\rho_1\right] \tag{4.10}$$

where D is the effective G-actin diffusion coefficient, on the order of 5 μm^2/s [4, 93]. This equation describes the variation in time of the free monomer density due to both diffusion and advection of free monomers. The boundary conditions read:

$$\rho_1(0) = \rho_1^0 \tag{4.11}$$

with ρ_1^0 bulk free monomer density and:

$$-D\frac{\partial \rho_1}{\partial x}\Big|_{x=L(t)} = \frac{N_f v_{fil}}{\eta d_0} \tag{4.12}$$

because the flux at the leading edge, $-D\partial\rho_1/\partial x(x = L(t))$ must be equal to the number of monomers assembling per second onto the tips of N_f filaments. This number is equal to N_f times the elongation rate of the filopodial filaments v_{fil} divided by the monomer half size $d_0 = 2.7$ nm; η is a coefficient converting the number of monomers into micromolar units: a concentration of 1μM corresponds to roughly 600 molecules per μm^3, which gives $\pi(0.1\mu\text{m})^2 \times 600/\mu\text{m}^3 \simeq 20$ molecules per μm of filopodium. Hence $\eta \simeq 20\ \mu\text{M}^{-1}\mu\text{m}^{-1}$. The authors considered the case of a filopodium emerging from a lamellipodium, which in turn elongates with a velocity v_{lam}: the rate of the filopodial extension is thus $\frac{dL}{dt} = v_{fil} - v_{lam}$. The velocity v_{fil} was taken equal to Eq. (1.13) in the limit $U_0 \gg W_0$,

$$v_{fil} \approx d_0 k_{on}\rho_1(L(t))\exp\left(-\beta F d_0/N_f\right) \equiv d_0 k_{on}\rho_1(L(t))\exp\left(-N_0/N_f\right) \tag{4.13}$$

with $N_0 = \beta F d_0 \approx 13$ for $F \approx 20$ pN and $\rho_1(L(t))$ free monomers concentration at the leading edge, so that Eq. (4.12) becomes:

$$-D\frac{\partial \rho_1}{\partial x}\Big|_{x=L(t)} = \frac{N_f k_{on}\exp\left(-N_0/N_f\right)}{\eta}\,\rho_1(L(t)). \tag{4.14}$$

As for the lamellipodium velocity in the protrusion direction, v_{lam}, it is given by the elongation velocity of the filaments contained in it, which are oriented by a wide range of angles, times the cosine of the angle between the protrusion and the elongation directions, $v_{lam} = v_{elong} \cos\theta$; v_{elong} is considered to be the same for all filaments. Filaments growing at small θ generate larger forces and grow slower, those at large θ grow faster against smaller forces (see Fig. 4.5). There will be a

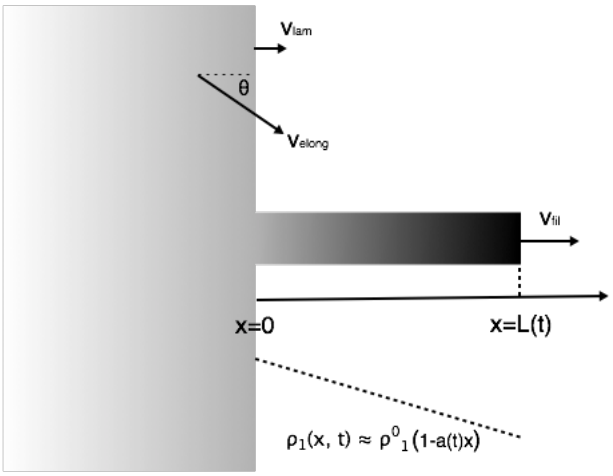

Figure 4.5. Schematic illustration of the filopodium-lamellipodium system and 2D G-actin density distribution $\rho_1(x,t)$ along the filopodium (illustrated by the color gradient and the dotted line). Adapted from [4].

value θ_c such that filaments growing at this angle elongate against zero force with an elongation velocity equal to the load-free velocity, $v_{elong} = v_0 = d_0 k_{on} \rho_1^0$. Hence $v_{lam} = v_0 \cos\theta_c = d_0 k_{on} \rho_1^0 \cos\theta_c$ and

$$\frac{dL}{dt} = v_{fil} - v_{lam} = d_0 k_{on} \left(\exp\left(-\frac{N_0}{N_f} \right) \rho_1(L) - \cos\theta_c \rho_1^0 \right) \tag{4.15}$$

Eqs. (4.10) and (4.15) represent a difficult free-boundary problem; though, considerations on the timescale separation between G-actin diffusion, filopodial growth and cytoplasmic drift allow for a strong simplification. The characteristic length, time and density scales are taken as: $\bar{l} = D\eta \exp(N_0/N_f)/k_{on}N_f \approx 1$ μm, $\bar{t} = \bar{l}/v_0 \approx 3$ s and $\rho_1^0 \approx 10$ μM. The corresponding dimensionless diffusion coefficient is $\bar{D} = D\bar{t}/\bar{l}^2 \approx 10$. Eq. (4.10) in terms of these dimensionless variables becomes:

$$\bar{D} \frac{\partial^2 \bar{\rho}_1}{\partial \bar{x}^2} = \frac{\partial \bar{\rho}_1}{\partial \bar{t}} + \frac{\partial}{\partial \bar{x}} \left[\left(\frac{d\bar{L}}{d\bar{t}} \right) \bar{\rho}_1 \right] \tag{4.16}$$

with boundary conditions:

$$\left. \frac{\partial \bar{\rho}_1}{\partial \bar{x}} \right|_{\bar{x}=\bar{L}(\bar{t})} = -\bar{\rho}_1(\bar{L}) \tag{4.17}$$

$$\bar{\rho}_1(0) = 1 \tag{4.18}$$

$$\tag{4.19}$$

while Eq. (4.15) becomes:

$$\frac{d\bar{L}}{d\bar{t}} = \exp\left(-\frac{N_0}{N_f}\right) - \cos\theta_c \tag{4.20}$$

where rescaled variables are indicated by a bar over the symbol. On the relevant scale, the G-actin diffusion is much faster than both the cytoplasmic drift and the filopodial growth, so that the r.h.s. of Eq. (4.16) can be neglected, resulting in a quasi-stationary gradient of the free monomers density along the filopodium.Eq. (4.16) becomes thus simply $\partial^2\bar{\rho}_1/\partial\bar{x}^2 \approx 0$ and applying Eqs. (4.17) and (4.18) one easily finds, going back to the dimensional variables:

$$\rho_1(x,t) \approx \rho_1^0\left(1 - \frac{k_{on}N_f}{k_{on}N_f L(t) + D\eta\exp(N_0/N_f)}\,x\right) \qquad 0 < x < L(t) \tag{4.21}$$

$$\rho_1(x = L(t), t) \approx \frac{D\eta\exp(N_0/N_f)}{k_{on}N_f L(t) + D\eta\exp(N_0/N_f)}\rho_1^0 \tag{4.22}$$

i.e. G-actin concentration decreases linearly along the filopodium, and this gradient induces G-actin flux, but the longer the filopodium, the smaller the G-actin density at the tip, resulting in a slower growth. Substituting Eq. (4.22) into Eq. (4.15) and setting $dL/dt = 0$ (stalled filopodium), one can find the maximum length, limited by G-actin diffusion:

$$L^{\mathrm{D}}_{max}(N_f) = \frac{D\eta}{k_{on}N_f}\left[\frac{1}{\cos\theta_c} - \exp\left(-\frac{N_0}{N_f}\right)\right]. \tag{4.23}$$

The dependence of this maximum length on N_f is non monotonic: at large N_f, $\exp\left(-\frac{N_0}{N_f}\right) \approx 1$ and the maximum filopodium length goes like N_f^{-1}: many filaments deplete the G-actin pool; at small N_f, $\exp\left(-\frac{N_0}{N_f}\right)$ increases with decreasing N_f and the filopodium maximum length rapidly decreases with decreasing N_f. There is indeed a minimum number of filaments to allow for filopodial protrusion, given by $N_f^{min} = N_0/\ln(1/\cos\theta_c) \approx 7 \div 9$ for a critical angle $\theta_c \approx 75^\circ \div 80^\circ$.

Both Eqs. (4.9) and (4.23) express the maximum filopodial length as a function of the number of filaments, in two cases where either buckling or monomer diffusion limits the filopodial growth; these different behaviors are shown in Fig. 4.6. At a given number of filaments, the observed maximum length will be the minimum between these two lengths, $L_{max}(N_f) = \min\left[L^{\mathrm{B}}_{max}(N_f), L^{\mathrm{D}}_{max}(N_f)\right]$. In Fig. 4.6 this quantity is represented by a solid black line, distinguishing three regimes: (1) for $N_f \lesssim 8$, the filopodial elongation is limited by the membrane resistance; (2) for $8 < N_f \lesssim 26$ filopodial length is limited by buckling and (3) for $N_f > 26$ filopodial length is limited by G-actin diffusion. These prediction resulted in agreement with several experimental observations [4], despite of the simplicity of this theoretical model.

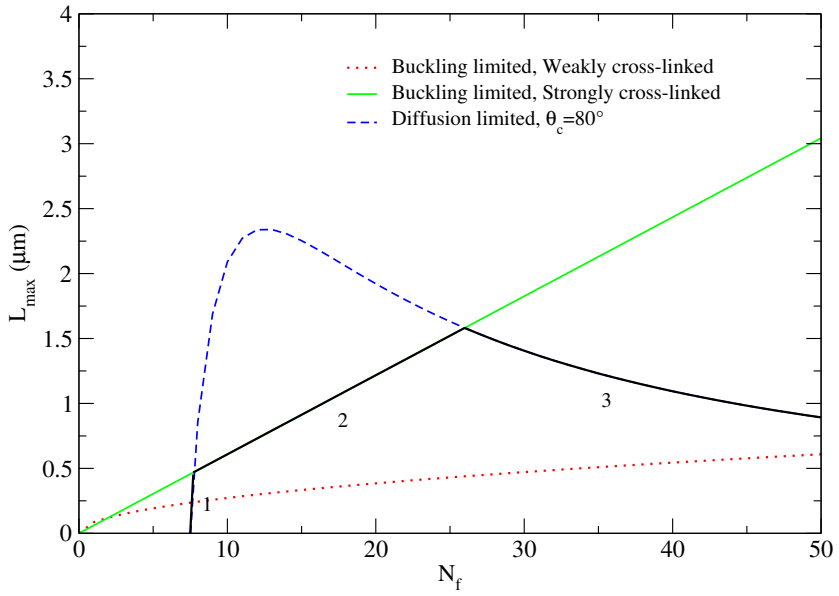

Figure 4.6. Maximum filopodial length in the case elongation is limited by buckling, Eq. (4.9), both for weakly cross-linked (red dotted line) and for strongly cross-linked bundles (green solid line), and in the case elongation is limited by G-actin diffusion (blue dashed line), Eq. (4.23) with $\theta_c = 80°$ as a function of the bundled number of filaments, N_f. A solid black line indicates the predicted filopodial length limited by membrane resistance (1), buckling (2) and diffusion (3).

Chapter 5

Membrane elasticity

Biomembranes are quite complex objects, made primarily by lipids of different kinds, also containing a number of proteins, carbohydrates, enzymes. To simplify the treatment, proteins and other objects can be disregarded and one can stick with a single-phospholipid bilayer – like in in-vitro *experiments with GUVs. Still, phospholipids have typical sizes on the order of a couple of nanometers while forming sheets extending over many microns. On relevant length scales, thus, membranes can be envisioned as simple, homogeneous two-dimensional surfaces embedded in 3D space and described by an effective larger-scale Hamiltonian. All the elastic properties of such objects can be derived from a continuum theory approach (or mean-field) in terms of phenomenological parameters that depend on the underlying microscopic physics [94]. The most popular model for the membrane curvature energy is the Helfrich theory, which provides a phenomenological Hamiltonian in terms of the membrane principal curvatures, and which has been successfully employed to describe phenomena of shaping, fusion and fission of cellular membranes. Considering a membrane in its flat phase, it gives a useful prediction on the spectrum of the height fluctuations at equilibrium relating it to the membrane elastic coefficients, namely the* surface tension *and the* bending modulus*, which are fundamental to understand the membrane elastic response to externally driven deformations (*e.g. *the suction within a micropipette or the push of underlying polymerizing filaments). Within the Helfrich theory, moreover, the radius of a cylindrical protrusion pulled from a flat membrane can be related via a simple expression to these elastic coefficients: in particular, it results to increase with the bending modulus and decrease with the surface tension – see Eq.* (5.47)*. Besides, the elastic constants of a fluid membrane can be calculated following a statistical mechanics approach and relating them to the interactions between the amphiphiles contained in it. In particular, a virial expression can be derived to relate the surface tension to the pressure tensor [95]. This expression is derived using a mechanical approach, namely by calculating the free energy variations resulting from the change in the area of a membrane patch.*

This chapter is structured as follows. In Sections 5.1 and 5.2 the continuum theory approach, referring mostly to differential geometry methods, will be briefly reviewed, with the purpose of providing some useful definitions and tools to treat the mathematics of manifolds embedded in three dimensional space. In Section 5.3 the most popular Helfrich's theory for the membrane curvature energy will be presented,

with particular emphasis on the derivation of the expression for the spectrum of height fluctuations. Also the expression relating the radius of a tubular protrusion to the membrane elastic coefficients will be derived. In Section 5.4 the virial expression for the membrane surface tension will be derived through a statistical mechanics approach [95].

5.1 Membrane elasticity: a simple continuum model

Let's consider a square piece of membrane, of lateral length L and thickness $h \ll L$. We want to know how the energy of such material changes when it undergoes a deformation, which can be in-plane, like stretching and shearing, or out-of-plane, like bending. In either case, a deformation causes the phospholipids, components of the double sheet, to get closer to or further from their next neighbors, and this costs energy. Following a simple continuum theory approach, we will consider the bilayer as a single sheet of a continuum material with given elastic coefficients which implicitly incorporate the microscopic details of the bilayer [94].

5.1.1 Stretching and shearing

Let's focus on the in-plane deformations, namely stretching and shearing. If we take the piece of membrane $A_0 = L^2$ and stretch it to a size $A > A_0$, we can assume that the bilayer behaves like a harmonic spring, with a stretching energy growing quadratically with the area variation [94]:

$$E_{stretch} = \frac{1}{2} K_{stretch} \frac{(A - A_0)^2}{A_0} \tag{5.1}$$

where $K_{stretch}$ is the membrane stretching modulus. The membrane lateral stress due to the strain, *i.e.* the surface tension Σ, is given by the derivative of the energy with respect to A:

$$\Sigma \equiv \frac{\partial E_{stretch}}{\partial A} = K_{stretch} \frac{A - A_0}{A_0} = K_{stretch} u \tag{5.2}$$

where $u = \frac{A - A_0}{A_0}$ is the dimensionless relative strain; the surface tension Σ has correctly the dimensions of an energy per area and it can be defined as the reversible work of formation of a unit area of surface. Eq. (5.2) expresses the stress-strain relation, assumed to be *linear*, which is correct at least for small deformations. The stretching modulus can be measured experimentally using micropipette aspiration techniques [96, 97]; a micropipette is a glass tube ending with a narrow tip with a diameter on the order of a micrometer. In typical micropipette aspiration experiments, a suction pressure is applied within the tube and if the tip is put in contact with a vesicle of large enough dimensions (many micrometers), it will be sucked inside the micropipette, forming a protrusion. All the vesicle surface will be consequenty put under tension. Measuring the difference between the inside and the outside pressure, the vesicle size and the radius of the protrusion inside the pipette, one can accurately probe the stress-strain relation. Typical values for the stretching modulus are on the order of 10^2 mJ/m^2 [96].

As for shear, since the membrane is fluid, it doesn't have a shear modulus: static shear doesn't imply an energy cost [94].

5.1.2 Bending

Bending is an out-of-plane deformation that can lead to substantial overall changes in the membrane's shape, without requiring a huge stress. This is true in general for materials whose extension over one or two of the three dimensions is much larger than the other(s) – this is the case of a rod or a plate, which can be easily bent even if the material is very strong (metallic wires or sheets can be easily bent but not stretched for instance).

Let's take the same piece of membrane as above, of total volume $V_0 = A_0 h$ at rest and let's imagine to bend it, for instance downwards, as illustrated in Fig. 5.1. By doing so, it will get compressed at some points and stretched at others: the bottom side, which is concave, is compressed, the upper side, which is convex, is stretched. Penetrating from the bottom layer inside the material thus the compression decreases and eventually it changes sign: there must be a surface, on which there is no extension or compression, which is called the *neutral surface*. If the material is homogeneous, the neutral surface lies midway through the membrane thickness [49].

Following a simple approach [65, 94], we can assume that locally a change in volume determines an energy variation which obeys a simple elastic law of the form of Eq. (5.2):

$$\Delta E_{stretch} = \frac{1}{2}\, Y\, \frac{(V - V_0)^2}{V_0} \tag{5.3}$$

where Y is the *Young's modulus* of uniaxial extension or compression: we assume that a deformation (stretching or compression) along a direction will not cause shape changes along other directions. If this is the case, assuming that the stretching is for instance along the x direction, it will only cause a deformation along the same direction and an element dx at depth z becomes $dx' = \frac{R+z}{R}\, dx = \left(1 + \frac{z}{R}\right)\, dx$ (see Fig. 5.1). If $z < 0$, the volume is compressed, *i.e.* $dx' < dx$, otherwise it is stretched, *i.e.* $dx' > dx$. Using Eq. (5.3), the energy change of a volume $dV = dx\, dy\, dz$ stretched to $dV' = \left(1 + \frac{z}{R}\right)\, dx\, dy\, dz$, will be

$$dE_{stretch} = \frac{1}{2} Y\, \frac{z^2}{R^2}\, dx\, dy\, dz \tag{5.4}$$

which, integrated over the whole volume, gives:

$$E_{bend} = \frac{1}{2} Y \int_0^L dx \int_0^L dy \int_{-h/2}^{h/2} dz\, \frac{z^2}{R^2} = \frac{L^2 Y h^3}{24 R^2}. \tag{5.5}$$

Dividing by the total area of the membrane, we get the bending energy density per unit area,

$$e_{bend} = \frac{E_{bend}}{L^2} = \frac{1}{24}\, Y \frac{h^3}{R^2}. \tag{5.6}$$

Notice the strong cubic dependence on the membrane thickness: decreasing the thickness determines a rapid decrease in the membrane bending energy. The three-dimensional Young's modulus Y can be re-expressed using the two-dimensional stretching modulus $K_{stretch}$ by $K_{stretch} = Yh$, valid in the case of uniaxial extension/compression. This leads to [94]

$$e_{bend} = \frac{1}{24} K_{stretch} \left(\frac{h}{R}\right)^2 = \frac{1}{2}\, \kappa\, \frac{1}{R^2}, \tag{5.7}$$

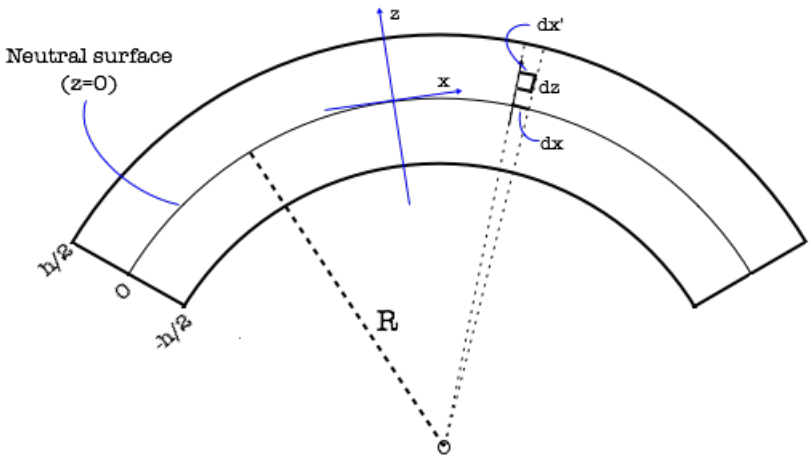

Figure 5.1. A thin elastic sheet bent along a direction into an arc of curvature radius R at the neutral surface. A volume element at distance z from the neutral surface is stretched along the x direction if it is above it, compressed if it is below. An element dx at $z = 0$ subtended by the angle $d\theta = dx/R$, becomes $dx' = (R + z)d\theta = \frac{R+z}{R}\, dx$ at $z \neq 0$.

even if the stretching modulus is very large, since $h \ll R$, the bending energy per unit area can be quite small. In the second equality of this equation the *bending modulus*

$$\kappa = \frac{1}{12} Y h^3 = \frac{1}{12} K_{stretch} h^2 \tag{5.8}$$

has been implicitly defined to highlight the quadratic dependence of the bending energy on the curvature, in a fashion similar to the bending energy density for a wormlike chain Eq. (2.5). In this case, however, the energy density is per unit area and not per unit length, so that κ has the dimensions of energy. Still, the energy, per area, is locally proportional to the square of the curvature (*quadratic curvature energy*).

This approach is very simplistic and at least two corrections can be made. First, the membrane comprises of two lipid sheets that can slide on top of each other: no stress can thus be transmitted across the neutral surface – which is the surface where the two layers meet. If the two layers were rigidly coupled, the stretching/compression would be larger; it would be indeed more appropriate to consider the total bending energy as twice the bending energy of a single sheet of thickness $\frac{h}{2}$ [94],

$$e_{bend}(h) = 2 \times e_{bend}\left(\frac{h}{2}\right) = \frac{1}{96} Y h \frac{h^2}{R^2}. \tag{5.9}$$

Second, we only considered uniaxial extension/compression, neglecting the *Poisson's ratio* ν: a uniaxial strain of some material with non-zero ν determines a compression or extension also in the direction perpendicular to the strain itself. It is in general defined as the ratio of lateral strain to axial strain [98]:

$$\nu = \left| \frac{\text{lateral strain}}{\text{axial strain}} \right| = -\frac{\text{lateral strain}}{\text{axial strain}} \tag{5.10}$$

where the negative sign is introduced to have a positive ν. Its value lies in the range $0 \leqslant \nu < 0.5$; a perfectly incompressible material has $\nu = 0.5$. To take into account the Poisson's ratio of the membrane, the Young modulus in Eq. (5.9) needs to be corrected to an effective value $\widetilde{Y} = \frac{Y}{1-\nu^2}$ [49, 94], so that

$$e_{bend} = \frac{1}{96} \frac{Y}{1-\nu^2} h \frac{h^2}{R^2}. \tag{5.11}$$

We have seen that typical values of the stretching modulus are on the order of 10^2 mJ/m^2, and taking a value $K_{stretch} = 250$ mJ/m^2 and a typical bilayer thickness $h = 4nm$, one gets a bending modulus $\kappa \approx (20 \div 27)\ k_BT$ depending on the Poisson's ratio. This value is fairly larger than thermal energy, so that thermal fluctuations don't induce dramatic bending of the membrane (stability against thermal fluctuations), but still not too much larger than thermal energy, so that nanoscopic sources of energy (like polymerizing filaments) are capable of deforming the lipid membrane. It should be noticed, though, that the relation between Young's modulus and bending modulus Eq. (5.8) is somehow tricky: it is not obvious which value for h should be used – the phosphate-phosphate distance in phospholipid or the width of the hydrophobic region are two possible choices, for instance. Since h enters quadratically in the $\kappa(Y)$ relation, small differences may be of great importance. The estimate given by Eq. (5.8) is still good enough but should be trusted within a factor of ~ 2. More reliable experimental methods have been designed with the aim of getting κ: besides the aforementioned micropipette aspiration technique, where the total area change can be directly related to the bending modulus in the so-called "low tension regime", other worth mentioning techniques are the Shape Fluctuation Optical Analysis and X-ray Scattering [99]. The first one is a direct analysis of thermal fluctuations of a giant vesicle, *e.g.* through the measurement of the vesicle radius autocorrelation function, which in turn can be obtained directly from optical microscopy images after digitalization [99]. In X-ray Scattering, stacks of bilayers are mounted on solid substrate and measurements of the scattered X-ray intensity at different wavevectors let determine κ [99]. Still, the range of experimental values obtained in different studies is rather wide ($(4 \div 16) \times 10^{-20}$ J$\approx (10 \div 40) k_BT$); The value most commonly used for κ in literature is $20 k_BT$ [65].

5.2 Differential geometry of surfaces

Let's now move to a less naive treatment of the membrane elasticity, using a more solid mathematical approach. Unlike semiflexible polymers that can be locally well characterized through a single radius of curvature, dealing with membranes is more complicated: surfaces embedded in 3D space can present a large variety of bending at a single point, and a more precise mathematical treatment is required. The common mathematical language in which surface curvature is properly discussed is *differential geometry*; in the following, a brief introduction of the subject will be given, in order to set the basis for a fair discussion of the bending free energy of a curved membrane.

5.2.1 Surface curvature

We want to find a mathematical representation of a two-dimensional object embedded in three-dimensional space, and this can be done in terms of the coordinates of that space. Since we are dealing with a surface, two local coordinates will be needed to parametrize it. Unfortunately, there is not a unique way to define them, nor a choice which looks like more natural or obvious than others, and a particular choice may be valid only locally [100]. Let's call this set of arbitrary coordinates (x_1, x_2); we will make sure that the results obtained in terms of them do not depend on the particular choice we will have made. The set of points $\mathcal{S}$ belonging to the surface can be written as:

$$\mathcal{S} = \{\mathbf{r}(x_1, x_2) | x_1, x_2 \in \mathcal{U}\} \tag{5.12}$$

where $\mathcal{U} \in \mathbb{R}^2$ is the domain of (x_1, x_2) and $\mathbf{r}$ is a three-component vector identifying the position of the point on the surface in the 3D space in terms of (x_1, x_2). We can further define the two vectors

$$\mathbf{e}_1 = \frac{\partial \mathbf{r}(x_1, x_2)}{\partial x_1} \qquad \mathbf{e}_2 = \frac{\partial \mathbf{r}(x_1, x_2)}{\partial x_2} \tag{5.13}$$

which are tangent to the surface in $\mathbf{r}(x_1, x_2)$ along the two directions x_1 and x_2. These vectors aren't necessarily normalized, nor perpendicular to each other. Nonetheless, they span a plane which is tangent to the surface at $\mathbf{r}(x_1, x_2)$. Their normalized cross product will give a unitary vector which is a proper surface normal:

$$\mathbf{n} = \frac{\mathbf{e}_1 \times \mathbf{e}_2}{||\mathbf{e}_1 \times \mathbf{e}_2||}. \tag{5.14}$$

The infinitesimal area element at $\mathbf{r}(x_1, x_2)$ is given by $dx_1\, dx_2$ times the area of the parallelogram spanned by $\mathbf{e}_1$ and $\mathbf{e}_2$, in turn equal to the magnitude of their cross product, namely

$$d\mathcal{A} = ||\mathbf{e}_1 \times \mathbf{e}_2|| dx_1\, dx_2 = \sqrt{||\mathbf{e}_1||^2 ||\mathbf{e}_2||^2 - (\mathbf{e}_1 \cdot \mathbf{e}_2)^2} dx_1\, dx_2. \tag{5.15}$$

The *metric* or *first fundamental form* on the surface is defined as $g_{ij} = \mathbf{e}_i \cdot \mathbf{e}_j$ [100], which is a symmetric second rank tensor:

$$\mathbf{g}(x_1, x_2) = \begin{bmatrix} \mathbf{e}_1(x_1, x_2) \cdot \mathbf{e}_1(x_1, x_2) & \mathbf{e}_1(x_1, x_2) \cdot \mathbf{e}_2(x_1, x_2) \\ \mathbf{e}_2(x_1, x_2) \cdot \mathbf{e}_1(x_1, x_2) & \mathbf{e}_2(x_1, x_2) \cdot \mathbf{e}_2(x_1, x_2) \end{bmatrix} \tag{5.16}$$

It can be immediately seen that the area element $d\mathcal{A}$ is equal to $dx_1\, dx_2$ times the square root of the determinant of this tensor, so that the total area of the manifold can be written as

$$\mathcal{A} = \int_{\mathcal{U}} \sqrt{\det \mathbf{g}(x_1, x_2)} dx_1\, dx_2. \tag{5.17}$$

It can be easily shown that, although it makes use of an explicit parametrization of the surface, this expression is independent of the parametrization chosen (see Appendix B.1).

For objects like soap films, which have no bending resistance, the only contribution to the total energy is proportional to the area $\mathcal{A}$ via the *surface tension* Σ,

$$E_{\mathcal{A}} = \Sigma \mathcal{A}. \tag{5.18}$$

The shape of a soap film between two coaxial circular rings (*catenoid*) is known to minimize this kind of "area energy". Unfortunately, membranes are not simple objects as such, even if they are fluid in their lateral extension; their characteristic bilayer structure makes bending of the membrane energetically costly, because it deforms its intrinsic structure, and a proper energy functional for the membrane shape must include curvature contributions.

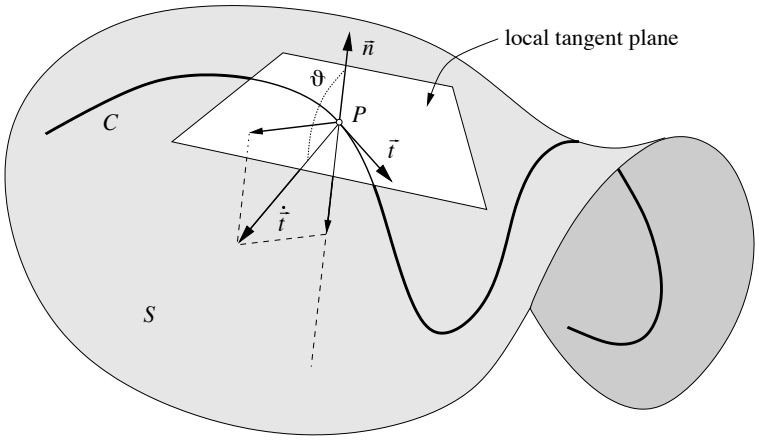

Figure 5.2. Illustration of the definition of the normal curvature $c_n = c\cos\theta$ (Eq. (5.23)) and the geodesic curvature $c_g = c\sin\theta$ (Eq. (5.24)). They are essentially given by the magnitude of the projections of $\dot{\mathbf{t}}$ onto the local normal vector and onto the local tangent plane, respectively. From [100].

Determining the curvature of a surface is not straightforward: given a particular choice of (x_1, x_2), the vector couples $(\mathbf{e}_1, \mathbf{n})$ and $(\mathbf{e}_2, \mathbf{n})$ will span two planes intersecting with each other on the surface at $\mathbf{r}(x_1, x_2)$, while their intersections with the surface define two curves in $\mathbb{R}^3$, λ_1 and λ_2, whose curvature can be defined as we did for the WLC model in Section 2.1.2. Considering one of these curves (or any other curve defined on the surface), let $\mathbf{t}$ be the tangent vector at $\mathbf{r}(x_1, x_2)$; if $(x_1(s), x_2(s))$ is the curve parametrization (s curvilinear coordinate), let's indicate by $\mathbf{n}_{curv} = \left(\frac{\partial \mathbf{t}(s)}{\partial s}\right)/c \equiv \dot{\mathbf{t}}/c$ the principal normal vector to the curve with $c = |\dot{\mathbf{t}}|$ its curvature; being $\mathbf{n}$ the normal vector to the surface at the same point, we have:

$$\dot{\mathbf{t}} \cdot \mathbf{n} = c\cos\theta \tag{5.19}$$

with θ angle between $\mathbf{n}_{curv}$ and $\mathbf{n}$. We thus have:

$$\dot{\mathbf{t}}(s) = \ddot{\mathbf{r}}(s) = \frac{\partial^2}{\partial s^2}\mathbf{r}(s) = \frac{\partial}{\partial s}\left(\sum_{i=1,2}\frac{\partial \mathbf{r}}{\partial x_i}\dot{x}_i\right)$$
$$= \sum_{i,j=1,2}\dot{x}_i\frac{\partial^2\mathbf{r}}{\partial x_i \partial x_j}\dot{x}_j + \sum_{i=1,2}\frac{\partial \mathbf{r}}{\partial x_i}\ddot{x}_i \equiv \sum_{i,j=1,2}\dot{x}_i\mathbf{e}_{ij}\dot{x}_j + \sum_{i=1,2}\mathbf{e}_i\ddot{x}_i \tag{5.20}$$

where $\mathbf{e}_{ij} = \frac{\partial^2\mathbf{r}}{\partial x_i \partial x_j}$. Since $\mathbf{e}_i \cdot \mathbf{n} = 0$ by definition,

$$c\cos\theta = \dot{\mathbf{t}} \cdot \mathbf{n} = \sum_{i,j=1,2}(\mathbf{e}_{ij}\cdot\mathbf{n})\,\dot{x}_i\dot{x}_j \tag{5.21}$$

where the expression in brackets is a property of the surface alone, independent of the curve. It is the so-called *second fundamental form*, defined as

$$b_{ij} \equiv \mathbf{e}_{ij}\cdot\mathbf{n} = \frac{\partial \mathbf{e}_i}{\partial x_j}\cdot\mathbf{n} \tag{5.22}$$

which is a symmetric second rank tensor, since $\mathbf{e}_{ij} = \mathbf{e}_{ji}$.

The curvature c of the curve depends both on its intrinsic curvature and on the surface curvature: we want to disentangle these two effects and univocally define the curvature of the surface. This can be done by defining two different curvatures, the *normal* and the *geodesic* curvature. Eq. (5.21) expresses the component of the curvature of the curve in the direction of the surface unit normal $\mathbf{n}$, and it is called the normal or *directional* curvature c_n of the surface along the direction $\mathbf{t}$:

$$c_n \equiv c\cos\theta = \sum_{i,j=1,2} b_{ij}\dot{x}_i\dot{x}_j. \tag{5.23}$$

In contrast to the curvature c, which is always non-negative, the normal curvature can be either positive, or zero, or negative. The normal curvature is a measure of how much the surface (rather than the curve) is curving. On the other hand, the so-called geodesic curvature measures the curvature of the curve due to itself and not to the surface curvature. It is obtained by projecting the vector $\dot{\mathbf{t}}$ onto the local tangent plane to the surface,

$$c_g = c\sin\theta \tag{5.24}$$

so that

$$c^2 = c_n^2 + c_g^2. \tag{5.25}$$

Let's take for instance the case of a curve on a the xy plane: in this case the normal to any point of the curve lies in the xy plane while the surface normal is along z, so that $\theta = \frac{\pi}{2}$ at any point of the curve, and the geodesic curvature is maximal, while the directional curvature is zero (*i.e.* the surface is flat). If we take on the contrary a straight curve on a curved surface, like the diameter of a sphere, $\theta = 0$ (or π) at any point of the curve, and the directional curvature is maximal, while the geodesic curvature is zero.

The normal curvature c_n, Eq. (5.21), is a quadratic form of the $\dot{x}_i$, and a quadratic form can always be diagonalized: the corresponding eigenvectors are

the two directions along which the curvature is extremal. These are the *principal directions* and the corresponding eigenvalues are the *principal curvatures*, c_1 and c_2 [101]. Let's rewrite Eq. (5.23) as

$$c_n = \frac{\sum_{i,j=1,2} b_{ij}\dot{x}_i\dot{x}_j}{\sum_{i,j=1,2} g_{ij}\dot{x}_i\dot{x}_j} \tag{5.26}$$

which is valid since $\sum\limits_{i,j=1,2} g_{ij}\dot{x}_i\dot{x}_j = 1$ [102]. Eq. (5.26) in turn can be rewritten as

$$\sum_{i,j=1,2} (b_{ij} - c_n g_{ij})\, v_i v_j = 0 \tag{5.27}$$

with $v_i = \dot{x}_i$, and differentiating it with respect to v_k, we get:

$$\sum_{i=1,2} (b_{ik} - c_n g_{ik})\, v_i = 0. \tag{5.28}$$

By defining the first form *dual* tensor g^{ij} such as $\sum_i g_{ki}g^{ij} = \delta_{kj}$ (Kronecker symbol), and $b^j_k = \sum_i b_{ki}g^{ij}$, if we multiply this last equation by g^{kl} and sum over k,

$$\sum_{i=1,2} \left(b^l_i - c_n\delta_{il}\right) v_i = 0. \tag{5.29}$$

which shows that the search for extremal curvatures is indeed an eigenvalue problem: the directions along which the normal curvature is extremal are given by the eigenvectors of the matrix b^l_i. The sum and the product of the principal curvatures are respectively the trace and the determinant of b^l_i, and they define the *mean curvature* H and the *Gaussian curvature* K_G respectively:

$$H = \frac{c_1 + c_2}{2} = \frac{1}{2}\mathrm{tr}\left(\mathbf{b}\mathbf{g}^{-1}\right) = \frac{1}{2}\sum_{i=1,2} b^i_i = \frac{1}{2}\sum_{ij} b_{ji}g^{ij} \qquad \text{Mean curvature,} \tag{5.30}$$

$$K_G = c_1c_2 = \det\left(\mathbf{b}\mathbf{g}^{-1}\right) = \frac{\det\mathbf{b}}{\det\mathbf{g}} \qquad \text{Gaussian curvature} \tag{5.31}$$

with $\mathbf{g}^{-1}$ dual tensor of the first fundamental form. It can be shown that both H and K_G are coordinate-independent [94, 100].

To practically calculate the surface curvature, a parametrization for the surface shall be chosen: I will proceed in the following revisiting the most popular *Monge parametrization*.

5.2.2 Monge parametrization

One of the most straightforward parametrizations for 2D surfaces embedded in 3D space is the Monge parametrization, in which each point of the surface is described in terms of its height h over some plane, as a function of orthonormal coordinates in

the plane. If we take such plane as the yz plane, the position vector $\mathbf{r}$ and the two tangent vectors $\mathbf{e}_y$ and $\mathbf{e}_z$ are:

$$\mathbf{r}(y,z) = \begin{pmatrix} h(y,z) \\ y \\ z \end{pmatrix} \qquad \mathbf{e}_y = \frac{\partial \mathbf{r}}{\partial x} = \begin{pmatrix} h_y \\ 1 \\ 0 \end{pmatrix} \qquad \mathbf{e}_y = \frac{\partial \mathbf{r}}{\partial y} = \begin{pmatrix} h_z \\ 0 \\ 1 \end{pmatrix} \tag{5.32}$$

where h_y and h_z are h partial derivatives with respect to y and z respectively. The normal vector is

$$\mathbf{n} = \frac{\mathbf{e}_y \times \mathbf{e}_z}{||\mathbf{e}_y \times \mathbf{e}_z||} = \frac{1}{\sqrt{1+h_y^2+h_z^2}} \begin{pmatrix} 1 \\ -h_y \\ -h_z \end{pmatrix}. \tag{5.33}$$

The first and second fundamental forms can be readily calculated:

$$\mathbf{g} = \begin{pmatrix} 1+h_y^2 & h_y h_z \\ h_y h_z & 1+h_z^2 \end{pmatrix} \qquad \mathbf{b} = \frac{1}{\sqrt{1+h_y^2+h_z^2}} \begin{pmatrix} h_{yy} & h_{yz} \\ h_{yz} & h_{zz} \end{pmatrix} \tag{5.34}$$

whose determinants are

$$g = (1+h_y^2)(1+h_z^2) - h_y^2 h_z^2 = 1 + h_y^2 + h_z^2 \tag{5.35}$$

$$b = \frac{h_{yy}h_{zz} - hyz^2}{\sqrt{1+h_y^2+h_z^2}} \tag{5.36}$$

To get the mean curvature, the inverse of the first fundamental form is needed as well:

$$\mathbf{g}^{-1} = \frac{1}{1+h_y^2+h_z^2} \begin{pmatrix} 1+h_z^2 & -h_y h_z \\ -h_y h_z & 1+h_y^2 \end{pmatrix}. \tag{5.37}$$

Straightforward calculations lead to the mean and Gaussian curvatures:

$$H = \frac{h_{yy}(1+h_z^2) + h_{zz}(1+h_y^2) - 2h_{yz}h_y h_z}{2\left(1+h_y^2+h_z^2\right)^{3/2}} \tag{5.38}$$

$$K_G = \frac{h_{yy}h_{zz} - h_{yz}^2}{\left(1+h_y^2+h_z^2\right)^{3/2}}. \tag{5.39}$$

Defining the transverse two-dimensional Nabla operator $\nabla_{/\!/} = (\frac{\partial}{\partial y}, \frac{\partial}{\partial z})^{\mathrm{T}}$, the mean curvature can be written compactly as

$$H = \frac{1}{2}\nabla_{/\!/} \cdot \left(\frac{\nabla_{/\!/} h}{\sqrt{1+\left(\nabla_{/\!/} h\right)^2}} \right) \overset{|\nabla_{/\!/} h| \ll 1}{\approx} \frac{1}{2} \triangle_{/\!/} h(\mathbf{r}) \tag{5.40}$$

with $\triangle_{/\!/} = \partial_y^2 + \partial_z^2$ the Laplace operator in the plane. The last identity represents a good approximation when the gradient $\nabla_{/\!/} h$ is small compared to unity; it is usually referred to as the *small gradient approximation.*

5.3 Canham-Helfrich Theory

In 1970 Canham [103] proposed a generalization of the bending energy density Eq. (5.11) which could interpret the biconcave shape of the human red blood cells, describing the contribution to the total free energy of the membrane. The curvature energy had to be coordinate invariant, thus it shall be expressed in terms of the principal curvatures introduced in the previous section, or equivalently in terms of the mean and Gaussian curvatures. The curvature energy density proposed by Canham was of the form:

$$e_{bend}^{Canham} = \frac{1}{2}\kappa(c_1^2 + c_2^2) = \frac{1}{2}\kappa(K^2 - 2K_G) \tag{5.41}$$

with $K = 2H$ so-called *extrinsic curvature*, so that the total energy would be given by a surface integral,

$$E_{bend}^{Canham} = \frac{1}{2}\kappa \int_{\text{surface}} d\mathcal{A}\ (K^2 - 2K_G) \tag{5.42}$$

where the integral extends over the entire membrane and $d\mathcal{A}$ is the area element on the membrane. These expressions, though, considered only one curvature modulus, while since there are two independent curvatures, one would expect in general two different moduli. The generalization of Eq. (5.41) was proposed three year later by Helfrich [14]

$$e_{bend}^{Helfrich} = \frac{1}{2}\kappa(c_1 + c_2 - c_0)^2 + \bar{\kappa}c_1c_2 = \frac{1}{2}\kappa(K - c_0)^2 + \bar{\kappa}K_G \tag{5.43}$$

where κ is the bending modulus, $\bar{\kappa}$ is the *saddle splay* modulus and c_0 is the *spontaneous curvature* of the membrane. If $c_0 \neq 0$ it means that the membrane has a natural tendency to be bent, which can happen only if the membrane is not up-down symmetric (different leaflets compositions); we will consider only the simpler case $c_0 = 0$. In this case, the total Helfrich free energy is given by

$$E_{bend}^{Helfrich} = \int_{\text{surface}} d\mathcal{A}\ \left\{\frac{1}{2}\kappa K^2 + \bar{\kappa}K_G\right\}. \tag{5.44}$$

Eqs. (5.42) and (5.44) look like different, still they are equivalent: by virtue of the Gauss-Bonnet Theorem [100, 104], any surface integral of the Gaussian curvature leads to a constant term, which is irrelevant to the subsequent physics. We can thus rewrite this last expression getting rid of the Guassian curvature and introducing a term which accounts for energy penalties due to area variations:

$$E^{Helfrich} = \int_{\text{surface}} d\mathcal{A}\ \left\{\frac{1}{2}\kappa K^2 + \Sigma\right\} \tag{5.45}$$

where Σ is the surface tension of the membrane. The shape of a given membrane of area $\mathcal{A}$ that minimizes Eq. (5.45) is the one that minimizes the overall mean curvature. If the shape is a sphere of radius $R = \sqrt{\mathcal{A}/4\pi}$, the energy turns out to be $E^{Helfrich} = 8\pi\kappa$, independent of the radius. Or more interestingly, let's consider a large spherical membrane vesicle and imagine to apply a point force on it, as it is done in *in-vitro* experiments on GUVs (*e.g.* [87]); it has been observed the formation

of a cylindrical membrane tube in such conditions. The total energy for a cylindrical tube of radius R and length L, pulled by a force f, would be:

$$\begin{aligned} E_{tube}^{Helfrich} &= \int_{\text{surface}} d\mathcal{A} \left\{ \frac{1}{2}\kappa K^2 + \Sigma \right\} - fL \\ &= \left(\frac{\kappa}{2}\frac{1}{R^2} + \Sigma \right) 2\pi RL - fL. \end{aligned} \tag{5.46}$$

This expression for the total energy contains two opposite contributions, the bending rigidity trying to increase the tube radius ($\propto \frac{1}{R}$), and the surface tension trying to reduce it ($\propto R$). If we want a stable solution for a given force f_0, *i.e.* the radius R_0 which gives a stable condition, we have to impose vanishing derivatives of the energy with respect to R and L, getting:

$$\left\{ \begin{array}{l} -\dfrac{\kappa}{2R_0^2} + \Sigma = 0 \\ \left(\dfrac{\kappa}{2R_0^2} + \Sigma \right) 2\pi R_0 - f_0 = 0 \end{array} \right. \Rightarrow \left\{ \begin{array}{l} R_0 = \sqrt{\dfrac{\kappa}{2\Sigma}} \\ f_0 = 2\pi\sqrt{2\kappa\Sigma} \end{array} \right. \tag{5.47}$$

for given surface tension and bending modulus [105]. These expressions give the radius of a tube pulled out of a flat membrane of surface tension Σ and bending modulus κ by a local force f_0. We will make use of this equation for R_0 later on.

We can further use the Monge parametrization introduced in Section 5.2.2: the expression for the area element Eq. (5.15) becomes $d\mathcal{A} = \sqrt{1 + \left(\nabla_\parallel h\right)^2}\, dy\, dz$ and in the small gradient approximation $d\mathcal{A} = \left(1 + \frac{1}{2}\left(\nabla_\parallel h\right)^2\right) dy\, dz$, so that:

$$\begin{aligned} E^{Helfrich} &= \int_{\text{base plane}} dy\, dz \left(1 + \frac{1}{2}\left(\nabla_\parallel h\right)^2\right) \left\{ \frac{1}{2}\kappa \left(\triangle_\parallel h\right)^2 + \Sigma \right\} \\ &\approx \frac{1}{2} \int_{\text{base plane}} dy\, dz \left\{ \kappa \left(\triangle_\parallel h\right)^2 + \Sigma \left(\nabla_\parallel h\right)^2 \right\} \end{aligned} \tag{5.48}$$

where in the first line the small gradient approximation on the extrinsic curvature K (or equivalently on the mean curvature H), Eq. (5.40), has been applied and in the second line only terms up to the fourth order in the h derivatives have been kept (the constant term has been disregarded).

Membrane elasticity has been traditionally studied using this last expression as an effective surface Hamiltonian, which successfully describes shape and phase diagram of complex interfaces [95] and yields a correct description of the thermal fluctuations of h at equilibrium. Still, the same expression Eq. (5.48) has traditionally been used also as the membrane free energy and referred to as the *Helfrich free energy*, mostly in theories trying to relate the elastic coefficients to microscopic quantities [95].

In the following subsection I will analyze the equilibrium fluctuations of the membrane height h within this theory.

5.3.1 Membrane fluctuations

Let's consider a rectangular membrane patch $L_y \times L_z$, and let's assume 2D periodic boundary conditions along y and z directions. Let's first define the inverse

Fourier transforms based on an expansion over all the wave vectors $\mathbf{q} = (q_y, q_z) = \left(2\pi\frac{n_y}{L_y}, 2\pi\frac{n_z}{L_z}\right)$, with n_y, n_z integers, compatible with the periodicity of the system, and the direct Fourier transform as a double integral on the projected plane variables (y, z). For an arbitrary function $f(y, z)$ they are defined as:

$$f(\mathbf{r}) = \sum_{\mathbf{q}} \widehat{f}_{\mathbf{q}} \exp\left(i\mathbf{q}\cdot\mathbf{r}\right) \tag{5.49}$$

and

$$\widehat{f}_{\mathbf{q}'} = \frac{1}{L_y L_z}\int_0^{L_y} dy \int_0^{L_z} dz\; f(\mathbf{r}) \exp\left(-i\mathbf{q}'\cdot\mathbf{r}\right) \tag{5.50}$$

Indeed, substitution of Eq. (5.49) in Eq. (5.50) gives

$$\widehat{f}_{\mathbf{q}'} = \sum_{\mathbf{q}} \widehat{f}_{\mathbf{q}} \left[\frac{1}{L_y L_z}\int_0^{L_y} dy \int_0^{L_z} dz \exp\left(i(\mathbf{q}-\mathbf{q}')\cdot\mathbf{r}\right)\right] = \sum_{\mathbf{q}} \widehat{f}_{\mathbf{q}} \delta_{(\mathbf{q}-\mathbf{q}'),\mathbf{0}} = \widehat{f}_{\mathbf{q}'} \tag{5.51}$$

where the delta function is defined in each direction as:

$$\delta_{q_\alpha,0} = \frac{1}{L_\alpha}\int_0^{L_\alpha} dr_\alpha \exp\left(iq_\alpha r_\alpha\right) \tag{5.52}$$

with $\alpha = y, z$. The function we are interested in, $h(y, z)$, is real and therefore its Fourier components shall satisfy the condition $\hat{h}_{-\mathbf{q}} = \hat{h}^*_{\mathbf{q}}$. Using Eq. (5.49), we get

$$\begin{aligned}
\nabla_\parallel h &= \sum_{\mathbf{q}} \hat{h}_{\mathbf{q}} i\mathbf{q} \exp\left(i\mathbf{q}\cdot\mathbf{r}\right)\\
(\nabla_\parallel h)^2 &= \sum_{\mathbf{q},\mathbf{q}'} \hat{h}_{\mathbf{q}}\hat{h}_{\mathbf{q}'}(-\mathbf{q}\cdot\mathbf{q}') \exp\left(i\left(\mathbf{q}+\mathbf{q}'\right)\cdot\mathbf{r}\right)\\
\triangle_\parallel h &= \sum_{\mathbf{q}} \hat{h}_{\mathbf{q}}(-q^2) \exp\left(i\mathbf{q}\cdot\mathbf{r}\right)\\
(\triangle_\parallel h)^2 &= \sum_{\mathbf{q},\mathbf{q}'} \hat{h}_{\mathbf{q}}\hat{h}_{\mathbf{q}'}(q^2 q'^2) \exp\left(i\left(\mathbf{q}+\mathbf{q}'\right)\cdot\mathbf{r}\right)
\end{aligned}$$

and finally:

$$\begin{aligned}
E^{Helfrich} &= \int_{L_y\times L_z} d^2r \sum_{\mathbf{q},\mathbf{q}'} h_{\mathbf{q}} h_{\mathbf{q}'} \exp\left(i\left(\mathbf{q}+\mathbf{q}'\right)\cdot\mathbf{r}\right)\left\{\frac{1}{2}\kappa\left(q^2 q'^2\right) + \frac{1}{2}\Sigma\left(-\mathbf{q}\cdot\mathbf{q}'\right)\right\}\\
&= \sum_{\mathbf{q},\mathbf{q}'} h_{\mathbf{q}} h_{\mathbf{q}'} L_y L_z \delta_{\mathbf{q}+\mathbf{q}',0}\left\{\frac{1}{2}\kappa\left(q^2 q'^2\right) + \frac{1}{2}\Sigma\left(-\mathbf{q}\cdot\mathbf{q}'\right)\right\}\\
&= L_y L_z \sum_{\mathbf{q}} h_{\mathbf{q}} h_{-\mathbf{q}}\left\{\frac{1}{2}\kappa q^4 + \frac{1}{2}\Sigma q^2\right\} = L_y L_z \sum_{\mathbf{q}} |h_{\mathbf{q}}|^2\left\{\frac{1}{2}\kappa q^4 + \frac{1}{2}\Sigma q^2\right\}.
\end{aligned} \tag{5.53}$$

Looking at this expression for the membrane energy, it can readily be noted that either bending or tension energy dominates depending on the wave vector: for $q < q_{\text{crossover}} \equiv \sqrt{\Sigma/\kappa}$ (small length scales) tension is the dominant energy, for

$q > q_{\text{crossover}}$ (large length scales) bending dominates. Another observation to be made is that different Fourier modes decouple (diagonal membrane energy):

$$\langle h_{\mathbf{q}} h_{\mathbf{q}'} \rangle = \langle |h_{\mathbf{q}}|^2 \rangle \delta_{\mathbf{q},-\mathbf{q}'} \tag{5.54}$$

with energy quadratic in the amplitudes [106]. Invoking the equipartition theorem, each quadratic degree of freedom will possess an energy $\frac{1}{2}k_BT$ on average:

$$\frac{1}{2} L_y L_z \left(\kappa q^4 + \Sigma q^2 \right) \langle |h_{\mathbf{q}}|^2 \rangle = \frac{1}{2} k_B T \tag{5.55}$$

where $\langle \cdots \rangle$ denotes a statistical average over membrane configurations, and hence:

$$\langle |h_{\mathbf{q}}|^2 \rangle = \frac{k_B T}{L_y L_z \left[\kappa q^4 + \Sigma q^2 \right]}. \tag{5.56}$$

This is an important result and we will make use of it later on. Eq. (5.56) is the *fluctuation spectrum* or*static structure factor* of the membrane. The mean-square amplitude of the membrane modes result correctly proportional to the temperature and are also dependent on the elastic constant κ and the tension Σ. The undulation amplitude of the whole membrane can be calculated as the sum over all individual modes [65]:

$$\langle h^2 \rangle = \sum_{\mathbf{q}} \frac{k_B T}{L_y L_z \left[\kappa q^4 + \Sigma q^2 \right]} \tag{5.57}$$

which can be approximated by an integral between $q_{min} = \frac{2\pi}{\max(L_y, L_z)}$ and $q_{max} = \frac{2\pi}{a}$ with a characteristic length on the order of the bilayer thickness:

$$\begin{aligned}
\langle h^2 \rangle &\approx \frac{L_y L_z}{(2\pi)^2} \int_{q_{min}}^{q_{max}} dq\, 2\pi\, q \frac{k_B T}{L_y L_z \left[\kappa q^4 + \Sigma q^2 \right]} \\
&= \frac{k_B T}{4\pi\Sigma} \ln \frac{q_{max}^2 \left(\kappa q_{min}^2 + \Sigma \right)}{q_{min}^2 \left(\kappa q_{max}^2 + \Sigma \right)} = \frac{k_B T}{4\pi\Sigma} \left[\ln \left(1 + \frac{\Sigma}{q_{min}^2 \kappa} \right) - \ln \left(1 + \frac{\Sigma}{q_{max}^2 \kappa} \right) \right] \\
&\overset{\Sigma \to 0}{\approx} \frac{k_B T}{4\pi\Sigma} \left[\frac{\Sigma}{q_{min}^2 \kappa} - \frac{\Sigma}{q_{max}^2 \kappa} \right] = \frac{k_B T}{4\pi\kappa} \frac{q_{max}^2 - q_{min}^2}{q_{max}^2 q_{min}^2} \\
&\overset{q_{min} \ll q_{max}}{\approx} \frac{k_B T}{16\pi\kappa} L_{max}^2
\end{aligned} \tag{5.58}$$

with $L_{max} = \max(L_y, L_z)$. The last identity gives an estimate for the root mean-square amplitude of the height fluctuations: since typical vales for the bending rigidity are on the order of $\kappa = 20 k_B T$, $\Delta h = \langle h^2 \rangle^{1/2} \simeq \frac{L_{max}}{100}$ for $\Sigma = 0$, *i.e.* the root mean square amplitude of the membrane fluctuations are typically 1% of the lateral extension of the membrane patch.

5.4 Thermodynamic expressions for the elastic constants

The elastic constants of a fluid membrane can be calculated following a statistical mechanics approach and relating them to the interactions between the amphiphiles

contained in it. In particular, let's see how to derive a thermodynamic expression for the surface tension [95].

To calculate the surface tension Σ, let's consider a *flat* membrane and slightly increase its area (still leaving it flat), and let's calculate the induced free energy difference. The *characteristic surface* on which the free energy is calculated is taken as the mid surface between the two phospolipid layers, while the total volume of the membrane is assumed to be fixed, so that the volume compression modulus can be disregarded [95]. To calculate the free energy of the membrane, first we need to write the partition function Z, related to the microscopic nature of the membrane and the interaction energy E between the amphiphiles. Being $R^{\alpha\beta} = \left|\mathbf{R}^{\alpha} - \mathbf{R}^{\beta}\right|$ the distance between interaction sites (amphiphiles) α and β, we assume that the energy E can be written as the sum of pair interactions:

$$E = \sum_{\langle\alpha\beta\rangle} \phi(R^{\alpha\beta}) \tag{5.59}$$

and the partition function can be written as

$$Z = \int_{V_0} \prod_{\gamma=1}^{N} d\mathbf{R}^{\gamma} \exp\left(-\frac{\sum_{\langle\alpha\beta\rangle} \phi(R^{\alpha\beta})}{k_B T}\right) \tag{5.60}$$

where the integral is performed over the coordinates of all particles (or pseudo-particles for this coarse-grained representation) over the entire volume of the container embedding the membrane. It is necessary to specify the boundary conditions for the positions of the amphiphiles near the walls of the container [95]: we can take, for instance, a container with square cross section with size L_p, $-L_p/2 \leqslant y, z < L_p/2$. Let's denote by $\mathbf{R}$ the position of a point on the undeformed membrane, and by $\mathbf{r}$ its strained position; let's apply a small deformation causing a strain in the x direction, linear in y (see Fig. 5.3):

$$\begin{cases} r_x &= R_x + \epsilon R_y \\ r_y &= R_y \\ r_z &= R_z \end{cases} \qquad \text{or:} \qquad \mathbf{r} = \begin{pmatrix} 1 & \epsilon & 0 \\ 0 & 1 & 0 \\ 0 & 0 & 1 \end{pmatrix} \mathbf{R} \tag{5.61}$$

From simple geometric considerations, it results that the strained cell size is $L' = L_p\sqrt{1+\epsilon^2}$ (see Fig. 5.3), and the area of the characteristic surface thus becomes:

$$A' = A_p\sqrt{1+\epsilon^2} = A_p\left(1 + \frac{\epsilon^2}{2} + \mathcal{O}(\epsilon^4)\right) \tag{5.62}$$

where $A_p = L_p^2$ is the area of the unstrained surface. The free energy difference of the strained flat surface and the unstrained one can be written as the surface tension times the area difference, namely:

$$F = F(\epsilon = 0) + \Sigma A_p \frac{\epsilon^2}{2} + \mathcal{O}(\epsilon^4) \tag{5.63}$$

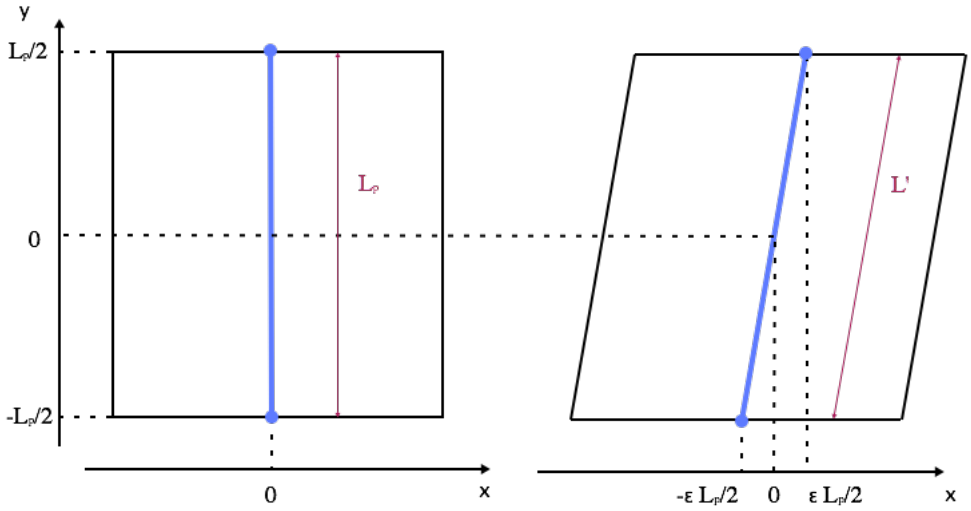

Figure 5.3. A schematic representation of the side view (thick blue line) of the characteristic surface of a membrane enclosed in a cell of size L_p, deformed according to Eq. (5.61).

from which the surface tension can be written as:

$$\Sigma = \frac{1}{A_p}\left.\frac{\partial^2 F}{\partial \epsilon^2}\right|_{\epsilon=0} = -\frac{1}{A_p}\left.\frac{\partial^2 k_B T \ln Z}{\partial \epsilon^2}\right|_{\epsilon=0}$$
$$= \frac{k_B T}{A_p}\frac{\partial}{\partial \epsilon}\left[\frac{1}{Z}\frac{\partial Z}{\partial \epsilon}\right]_{\epsilon=0} = \frac{k_B T}{A_p}\left[\frac{1}{Z}\frac{\partial^2 Z}{\partial \epsilon^2} - \frac{1}{Z^2}\left(\frac{\partial Z}{\partial \epsilon}\right)^2\right]_{\epsilon=0} \tag{5.64}$$

where the relation $F = -k_B T \ln Z$ has been used. To calculate this expression, we need to write the strained distance between two atoms:

$$r^{\alpha\beta}(\epsilon) = \left[\left(R^{\alpha\beta}\right)^2 + 2\epsilon R_x^{\alpha\beta} R_y^{\alpha\beta} + \epsilon^2\left(R_y^{\alpha\beta}\right)^2\right]^{1/2} \tag{5.65}$$

from which

$$Z = \int_{V_0}\prod_{\gamma=1}^{N} d\mathbf{R}^\gamma \exp\left(-\sum_{\langle\alpha\beta\rangle}\phi\left[\sqrt{\left(R^{\alpha\beta}\right)^2 + 2\epsilon R_x^{\alpha\beta} R_y^{\alpha\beta} + \epsilon^2\left(R_y^{\alpha\beta}\right)^2}\right]/k_B T\right) \tag{5.66}$$

being the Jacobian of the transformation unitary. Hence:

$$\left.\frac{\partial Z}{\partial \epsilon}\right|_{\epsilon=0} = \int_{V_0}\prod_{\gamma=1}^{N} d\mathbf{R}^\gamma \exp\left(-\sum_{\langle\alpha\beta\rangle}\phi\left(R^{\alpha\beta}\right)\right) \times \left[-\sum_{\langle\alpha\beta\rangle}\frac{\phi'\left(R^{\alpha\beta}\right)}{k_B T}\frac{R_x^{\alpha\beta} R_y^{\alpha\beta}}{R^{\alpha\beta}}\right] \tag{5.67}$$

and

$$\left.\frac{\partial^2 Z}{\partial \epsilon^2}\right|_{\epsilon=0} = \int_{V_0} \prod_{\gamma=1}^{N} d\mathbf{R}^\gamma \exp\left(-\sum_{\langle\alpha\beta\rangle} \phi\left(R^{\alpha\beta}\right)\right) \times \left\{ \left(\sum_{\langle\alpha\beta\rangle} \frac{\phi'\left(R^{\alpha\beta}\right)}{k_B T} \frac{R_x^{\alpha\beta} R_y^{\alpha\beta}}{R^{\alpha\beta}} \right)^2 - \sum_{\langle\alpha\beta\rangle} \left[\frac{\phi''\left(R^{\alpha\beta}\right)}{k_B T} \left(\frac{R_x^{\alpha\beta} R_y^{\alpha\beta}}{R^{\alpha\beta}} \right)^2 + \frac{\phi'\left(R^{\alpha\beta}\right)}{k_B T} \left(\frac{\left(R_y^{\alpha\beta}\right)^2}{R^{\alpha\beta}} - \frac{\left(R_x^{\alpha\beta} R_y^{\alpha\beta}\right)^2}{\left(R^{\alpha\beta}\right)^3} \right) \right] \right\} \tag{5.68}$$

where $\phi' = d\phi/dR$. The surface tension Eq. (5.64) thus reads:

$$\begin{aligned} \Sigma = \frac{1}{A_p k_B T} & \left\{ \left[\left\langle \sum_{\langle\alpha\beta\rangle} \phi'\left(R^{\alpha\beta}\right) \frac{R_x^{\alpha\beta} R_y^{\alpha\beta}}{R^{\alpha\beta}} \right\rangle \right]^2 - \left\langle \left[\sum_{\langle\alpha\beta\rangle} \phi'\left(R^{\alpha\beta}\right) \frac{R_x^{\alpha\beta} R_y^{\alpha\beta}}{R^{\alpha\beta}} \right]^2 \right\rangle \right\} \\ & + \frac{1}{A_p} \left\langle \sum_{\langle\alpha\beta\rangle} \phi''\left(R^{\alpha\beta}\right) \left(\frac{R_x^{\alpha\beta} R_y^{\alpha\beta}}{R^{\alpha\beta}} \right)^2 \right\rangle + \frac{1}{A_p} \left\langle \sum_{\langle\alpha\beta\rangle} \phi'\left(R^{\alpha\beta}\right) \frac{\left(R_y^{\alpha\beta}\right)^2}{R^{\alpha\beta}} \right\rangle \\ & - \frac{1}{A_p} \left\langle \sum_{\langle\alpha\beta\rangle} \phi'\left(R^{\alpha\beta}\right) \frac{\left(R_x^{\alpha\beta} R_y^{\alpha\beta}\right)^2}{\left(R^{\alpha\beta}\right)^3} \right\rangle \end{aligned} \tag{5.69}$$

where $\langle \cdots \rangle$ indicates a statistical average evaluated at the equilibrium reference state ($\epsilon = 0$). If the system is invariant with respect to the transformation $x \to -x$, then the first term in r.h.s. of Eq. (5.69) vanishes. If it is furthermore invariant with respect to rotation around the x axis ($y \to z$; $z \to -y$), then an equivalent expression can be found with $R_y^{\alpha\beta}$ replaced by $R_z^{\alpha\beta}$. We can sum these expressions and divide by two, and defining $R_t^{\alpha\beta} = \sqrt{\left(R_y^{\alpha\beta}\right)^2 + \left(R_z^{\alpha\beta}\right)^2}$, we find:

$$\begin{aligned} \Sigma = & -\frac{1}{2A_p k_B T} \left\langle \left[\sum_{\langle\alpha\beta\rangle} \phi'\left(R^{\alpha\beta}\right) \frac{R_x^{\alpha\beta} R_y^{\alpha\beta}}{R^{\alpha\beta}} \right]^2 + \left[\sum_{\langle\alpha\beta\rangle} \phi'\left(R^{\alpha\beta}\right) \frac{R_x^{\alpha\beta} R_z^{\alpha\beta}}{R^{\alpha\beta}} \right]^2 \right\rangle \\ & + \frac{1}{2A_p} \left\langle \sum_{\langle\alpha\beta\rangle} \phi''\left(R^{\alpha\beta}\right) \left(\frac{R_x^{\alpha\beta} R_t^{\alpha\beta}}{R^{\alpha\beta}} \right)^2 \right\rangle + \frac{1}{2A_p} \left\langle \sum_{\langle\alpha\beta\rangle} \phi'\left(R^{\alpha\beta}\right) \frac{\left(R_t^{\alpha\beta}\right)^2}{R^{\alpha\beta}} \right\rangle \\ & - \frac{1}{2A_p} \left\langle \sum_{\langle\alpha\beta\rangle} \phi'\left(R^{\alpha\beta}\right) \frac{\left(R_x^{\alpha\beta} R_t^{\alpha\beta}\right)^2}{\left(R^{\alpha\beta}\right)^3} \right\rangle \\ & = L_x \left[\frac{C_{xyxy} + C_{xzxz} - P_{yy} - P_{zz}}{2} \right] \equiv L_x \mu_{xt} \end{aligned} \tag{5.70}$$

where L_x is the linear size of the system in the x direction (normal to the membrane), and $\mathbf{P}$ and $\mathbf{C}$ are the pressure tensor and the tensor of elastic constants of the system. The quantity μ_{xt} is the shear modulus associated with the deformation [95].

An analogous (and more popular) expression can be obtained considering the variation of the free energy due to the variation of the *projected* area A_p, which is the

area of the projection of the surface on the yz reference plane, $\widetilde{\Sigma} = [\partial F/\partial A_p]_V$. It results that these two expressions differ by $L_x \mu_{xt}$, and in the case of fluid membranes (no shear modulus) the two coincide. This second expression reads [95, 107]:

$$\widetilde{\Sigma} = \frac{1}{2A_p} \left\langle \sum_{\langle \alpha\beta \rangle} \phi' \left(R^{\alpha\beta} \right) \frac{\left(R_t^{\alpha\beta} \right)^2 - 2 \left(R_x^{\alpha\beta} \right)^2}{R^{\alpha\beta}} \right\rangle = L_x \left[\frac{2P_{xx} - P_{yy} - P_{zz}}{2} \right] \quad (5.71)$$

This expression represents the "virial route" to the calculation of the membrane's surface tension, mostly useful in computer simulations, as it shall be discussed in the next chapter.

Chapter 6

Numerical simulations of biomembranes

Similar to any other complex system, numerical simulations have been a powerful tool to get insight on the dynamics of lipid membranes. In this chapter I will present the algorithms and techniques that I have used to numerically simulate the lipid membranes, and study their elastic properties, as well as the mutual interaction between membranes and biofilaments in the onset of filopodial protrusions. This chapter reports the work I have performed in the second part of this thesis, which has been mostly a technical effort of code developing – the resulting code has been written in Fortran90, all from scratch.

*In order to perform numerical simulations of biomembranes, a convenient discretization must be chosen: the most typical choice is to discretize it into beads connected by bonds in a triangular network (*triangulated surface model*). The tethers can be taken fixed or stretchable, while the bending resistance can be introduced based on the reciprocal orientation of adjacent triangle faces, the minimum of the energy being attained for all coplanar triangles [17, 108]. While the usual technique employed to study such system is the Monte Carlo simulation, here the dynamics of such beads will be defined following a Langevin approach and the corresponding equations of motion numerically integrated using a second-order integration scheme [111], in a Molecular Dynamics fashion. The fluid character of the membrane can be reproduced by introducing a* bond-flipping *procedure [15, 16]: given two adjacent triangles, the bond shared by the two is flipped on the diagonal, connecting in the end the two opposite beads. This procedure leads to a fluid-like behavior of the surface, as can be verified e.g. by the analysis of the beads mean squared displacement in the long time limit. Moreover, to let the membrane deform when subject to out-of-plane forces, the number of constituents is let vary in time via grand-canonical Monte Carlo insertion/deletion moves [19] that preserve the correct triangulation of the network.*

This chapter is structured as follows. Section 6.1 presents the basic triangulated surface model, the corresponding interaction potentials (bonding, bending, excluded volume) and the dynamical model. In Section 6.2 an inset on the bond-flipping procedure is provided and from numerical simulation data the mean squared displacement is shown to correctly have a linear time dependence in the long time limit (fluid-like

behavior). In Section 6.3 the numerical procedures used to get the surface tension via analysis of height fluctuations and the virial expression (introduced in the previous chapter) are described, and results obtained with these two protocols are compared, with an unprecedented level of agreement between the two. Section 6.4 reports the grand-canonical procedure of beads insertion/deletion and presents results obtained by simulations of membranes pushed by a hard sphere that induces the formation of a cylindrical protrusion; from these data the surface tension has been calculated, finding again a perfect agreement with the other methods. Finally, in Section 6.5 the numerical modeling of the actin filaments, which will grow in contact with the membrane to create a filopodium, is presented. Some numerical results on these filaments/membrane system simulations are shown, which are semiquantitative only at this stage but let envisioning interesting future developments, as discussed in Section 6.6.

6.1 Triangulated surface model

Numerical models of biomembranes are based in general on the membrane discretization and can be divided in two large groups: on one hand, *atomistic models* start from the actual individual molecules (amphiphiles) and their interactions; they can be very accurate and relate the membrane properties to realistic microscopic details, such as the amphiphiles chain length, which can be accessed experimentally. Yet, due to the large number of degrees of freedom, atomistic models are restricted to ensembles of a few thousand amphiphilic molecules. On the other hand, *coarse-grained models* start from the continuum description of a membrane in terms of an elastic energy and discretize it in a network of large beads, which can represent groups of real atoms; the size of the beads should be adapted to the physical situation under consideration and to the properties of interest. These models can be used to study membrane behavior on the scale of micrometers [17]. In order to make coarse-grained models suitable for computer simulations, the discretization is usually performed in the form of a triangulated network [15–17]: the membrane is represented as an ensemble of beads at the vertices of triangles (see Fig. 6.3), whose edges are bonds linking the beads. These bonds can be taken as fixed or stretchable (*e.g.* harmonic), and typically adjacent triangles tend to stay coplanar due to an explicit interaction which represents a bending rigidity.

Let's consider a canonical ensemble of N such beads forming the membrane, at positions $\{\mathbf{r}_1, \ldots, \mathbf{r}_N\}$, and let's connect them to each other by N_b bonds forming N_t triangles (each bead must be connected at least with 3 next neighbors to get a properly triangulated surface). The membrane is embedded in a box $H \times L_y \times L_z$ with periodic boundary conditions along y and z. For both closed vesicles and planar patches with 2D periodicity, the relationship $N_t = \frac{2N_b}{3}$ is valid for any microscopic configuration, since each bond is common to two triangles in a triangulated surface. The idea is to realize a numerical time evolution of the system, for which a model of the dynamics must be defined – a Langevin approach will be chosen – and the forces acting on the beads – namely bonding, bending and excluded-volume interactions – must be specified.

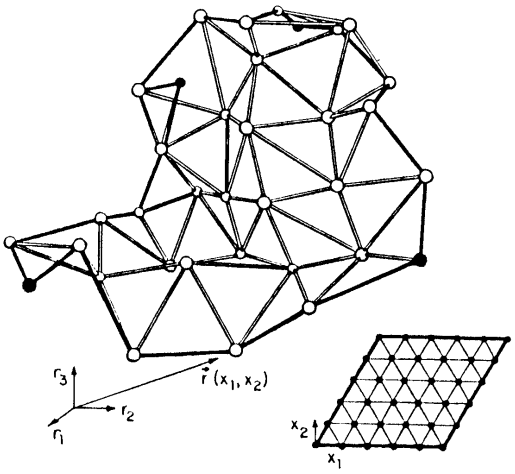

Figure 6.1. Triangulated surface embedded in a three dimensional space. From [108].

Bonding and excluded-volume interactions

The simplest form of bonding and excluded volume interactions would be to take the beads as hard spheres with diameter σ (excluded volume apply between all bonded and unbonded pairs); bonded pairs would be characterized by a square well potential which is zero (constant) as long as the pair distance l is in the range $\sigma = l_{min} \leqslant l \leqslant l_{max}$ and infinite below σ and above l_{max}. To avoid membrane self-penetrability, one must choose [15] $l_{max} < \sqrt{3}\sigma$, so that a bead of diameter σ does not fit in the void space at the center of a triangle of edge l_{max}. This choice is particularly suitable for Monte Carlo simulations, where trial displacements of beads are attempted and accepted or refused based on the new distances between the spheres. Here we want to dynamically evolve the system, solving the equations of motion of every bead (Molecular Dynamics approach), and a continuum potential would be more appropriate. A suitable potential is the Stillinger-Weber [109] for both bond and excluded-volume interactions: it is a kind of smooth-square-well potential (see Fig. 6.2), amenable for molecular dynamics simulations. It has the following form:

$$U^{mb}_{bond}(r_{ij}) = \begin{cases} b\,\dfrac{\exp\left[\left(\frac{\ell_{0,mb}}{\ell_{c,bond}-r_{ij}}\right)\right]}{(\ell_{max}-r_{ij})/\ell_{0,mb}} & \text{for } r_{ij} > \ell_{c,bond} \\ 0 & \text{for } r_{ij} \leqslant \ell_{c,bond} \end{cases} \tag{6.1}$$

$$U^{mb}_{\mathrm{EV}}(r_{ij}) = \begin{cases} b\,\dfrac{\exp\left[\left(\frac{\ell_{0,mb}}{r_{ij}-\ell_{c,\mathrm{EV}}}\right)\right]}{(r_{ij}-\ell_{min})/\ell_{0,mb}} & \text{for } r_{ij} < \ell_{c,\mathrm{EV}} \\ 0 & \text{for } r_{ij} \geqslant \ell_{c,\mathrm{EV}} \end{cases} \tag{6.2}$$

where $\ell_{c,bond}$ and $\ell_{c,\mathrm{EV}}$ are two cutoff distances, $\ell_{0,mb}$ the length scale of the distances between membrane beads, and b is a constant with energy dimensions determining the energy scale. These potentials are smoothly connected at the cutoff lengths with $d^n U^{mb}_{bond,\mathrm{EV}}/dr^n = 0$ for all n at $r = \ell_{c,bond}$ and $r = \ell_{c,\mathrm{EV}}$, and diverge for $r \to \ell^+_{min}$

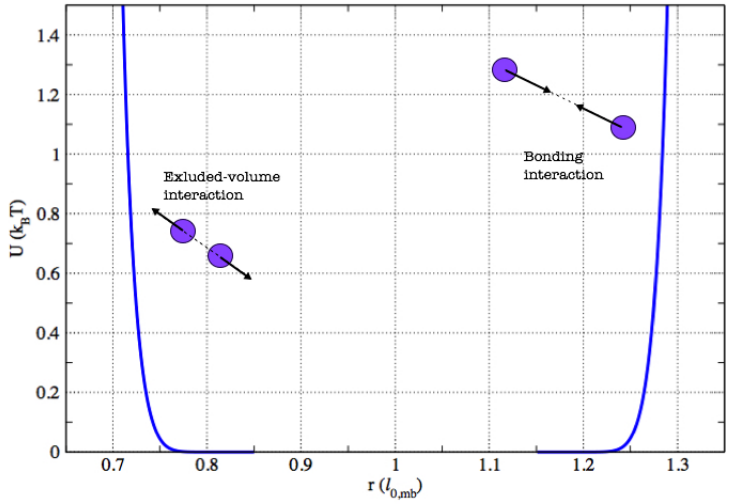

Figure 6.2. Stillinger-Webber potential Eqs. (6.1) and (6.2) for $b = 80k_BT$, $\ell_{min} = 0.67$, $\ell_{c,\mathrm{EV}} = 0.85$, $\ell_{c,bond} = 1.15$ and $\ell_{max} = 1.33$ (in $\ell_{0,mb}$ units).

and $r \to \ell_{max}^-$. When two nodes, i and j, are bonded, the bonding forces acting on them are:

$$\mathbf{F}_i^{bond} = -\mathbf{F}_j^{bond} = -\frac{b\exp\left(\frac{\ell_{0,mb}}{\ell_{c,bond}-r_{ij}}\right)}{\left(\ell_{max}-r_{ij}\right)/l_{0,mb}}\left[\frac{\ell_{0,mb}}{\left(\ell_{max}-r_{ij}\right)^2}+\frac{\ell_{0,mb}}{\left(\ell_{c,bond}-r_{ij}\right)^2}\right]\frac{\mathbf{r}_{ij}}{r_{ij}} \quad (6.3)$$

for $\ell_{c,bond} \leqslant r_{ij} < \ell_{max}$, with $\mathbf{r}_{ij} = \mathbf{r}_j - \mathbf{r}_i$. The excluded-volume interaction forces have a similar expression:

$$\mathbf{F}_i^{\mathrm{EV}} = -\mathbf{F}_j^{\mathrm{EV}} = \frac{b\exp\left(\frac{\ell_{0,mb}}{r_{ij}-\ell_{c,\mathrm{EV}}}\right)}{\left(r_{ij}-\ell_{min}\right)/l_{0,mb}}\left[\frac{l_{0,mb}}{\left(r_{ij}-\ell_{min}\right)^2}+\frac{\ell_{0,mb}}{\left(r_{ij}-\ell_{c,\mathrm{EV}}\right)^2}\right]\frac{\mathbf{r}_{ij}}{r_{ij}} \quad (6.4)$$

for $\ell_{min} \leqslant r_{ij} < \ell_{c,\mathrm{EV}}$.

Bending interactions

The calculation the bending forces acting on the membrane nodes relates to the reciprocal orientation of the flat triangles covering the surface: in any case, the minimum bending energy is attained for all the triangles being coplanar (in a 2D periodic surface); as the angles between the normal vectors of adjacent triangles become different from zero, the energy rises. With this idea in mind, there's a number of ways to discretize the Helfrich's energy Eq. (5.45), but here I will briefly describe the two most popular options for the form of this bending energy:

Option 1: The bending energy is formulated as a sum over all bonds, each bond being the common edge of two adjacent triangles and hence a possible hinge

for local bending. It is equivalent to sum over all the different pairs of adjacent triangles $\langle nm \rangle$. Defining $\mathbf{n}_n$ the normal unity vector to the n-th triangle, the bending energy can be written as

$$U_{bend}^{mb} = \lambda_b \sum_{\langle nm \rangle} (1 - \mathbf{n}_n \cdot \mathbf{n}_m) \tag{6.5}$$

where the sum runs over all the adjacent triangles. λ_b is an input bending modulus parameter, which turns out to be related to the bending modulus appearing in Eq. (5.45) in a way that depends on the curvature: for a spherical or flat surface, $\lambda_b = \sqrt{3}\kappa$, while for a cylinder $\lambda_b = 2\kappa/\sqrt{3}$ [16].

Option 2: The second option is way more complicated, with the advantage that the input bending modulus parameter coincides with the same κ appearing in Eq. (5.45), independently of the topology. The curvature energy is written as a sum over all the nodes, each of them involving all the nodes connected to it; let's denote by $V(i)$ the set of all the nodes bonded to node i. Let's l_{ij} be the distance between the two nodes i and $j \in V(i)$; these two nodes will form with two other nodes, k and l, connected to both of them, two adjacent triangles. The length of the bond in the dual lattice is [16]

$$\sigma_{ij} = l_{ij} \frac{\cot \theta_{ikj} + \cot \theta_{ilj}}{2} \tag{6.6}$$

where θ_{ikj} (θ_{ilj}) is the internal angle at vertex k (l) in triangle (ikj) ((ilj)). The area of the virtual dual cell of vertex i is [16]

$$\sigma_i = \frac{1}{4} \sum_{j \in V(i)} \sigma_{ij} l_{ij}. \tag{6.7}$$

The bending energy can be expressed as

$$E_{bend}^{mb} = \frac{\kappa}{2} \sum_{i=1}^{N} \frac{1}{\sigma_i} \left[\sum_{j \in V(i)} \frac{\sigma_{ij}}{l_{ij}} (\mathbf{r}_i - \mathbf{r}_j) \right]^2 . \tag{6.8}$$

In Monte Carlo simulations the second option is usually preferred because the cartesian forces (whose calculation would be rather cumbersome) are not needed, while in Molecular Dynamics simulations the first option is to be preferred. As mentioned, though, this choice implies an issue related to the value of the bending modulus parameter λ_b, which depends on the shape of the object; still, Eq. (6.5) can be used if the goal is not to best approximate the Helfrich model, but to just include some bending resistance in the model: in this case, this method can be taken as the *model itself* [110], and this is what I have done.

Let's thus take Eq. (6.5) as our bending energy; each term of the sum in it involves four atoms, let's say i, j, k and l. Let's take the ij bond as the common edge of the two triangles, while k and l are in the opposing vertices (see Fig. 6.3). The normals to the two adjacent triangles $n \equiv (ijk)$ and $m \equiv (ijl)$ are:

$$\mathbf{n}_n = \frac{\mathbf{r}_{ij} \times \mathbf{r}_{ik}}{|\mathbf{r}_{ij} \times \mathbf{r}_{ik}|} \qquad \mathbf{n}_m = \frac{\mathbf{r}_{il} \times \mathbf{r}_{ij}}{|\mathbf{r}_{il} \times \mathbf{r}_{ij}|} \tag{6.9}$$

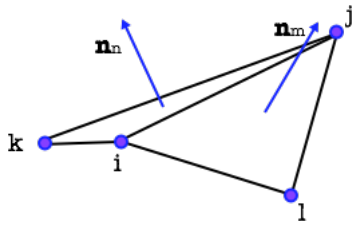

Figure 6.3. Adjacent triangles $n \equiv (ijk)$ and $m \equiv (ijl)$, with normal vectors $\mathbf{n}_n$ and $\mathbf{n}_m$.

with $\mathbf{r}_{ij} = \mathbf{r}_j - \mathbf{r}_i$ (vector going from i to j). The order of the vectors in the cross product has been chosen referring to Fig. 6.3. To get the forces acting on all the vertices, we need the gradient of Eq. (6.5) with respect to $\mathbf{r}_i$, $\mathbf{r}_j$, $\mathbf{r}_k$ and $\mathbf{r}_l$, which enter in the energy expression through the normal vectors. Straightforward calculation leads to the following expressions:

$$\mathbf{F}_i^{bend} = \frac{\lambda_b}{R_{ijk}R_{ilj}}\left\{\mathbf{R}_{ilj}\times\mathbf{r}_{jk} - \mathbf{R}_{ijk}\times\mathbf{r}_{jl} - (\mathbf{R}_{ijk}\cdot\mathbf{R}_{ilj})\left[\frac{\mathbf{R}_{ijk}\times\mathbf{r}_{jk}}{R_{ijk}^2} - \frac{\mathbf{R}_{ilj}\times\mathbf{r}_{jl}}{R_{ilj}^2}\right]\right\} \tag{6.10}$$

$$\mathbf{F}_j^{bend} = \frac{\lambda_b}{R_{ijk}R_{ilj}}\left\{\mathbf{R}_{ijk}\times\mathbf{r}_{il} - \mathbf{R}_{ilj}\times\mathbf{r}_{ik} - (\mathbf{R}_{ijk}\cdot\mathbf{R}_{ilj})\left[\frac{\mathbf{R}_{ilj}\times\mathbf{r}_{il}}{R_{ilj}^2} - \frac{\mathbf{R}_{ijk}\times\mathbf{r}_{ik}}{R_{ijk}^2}\right]\right\} \tag{6.11}$$

$$\mathbf{F}_k^{bend} = \frac{\lambda_b}{R_{ijk}R_{ilj}}\left\{\mathbf{R}_{ilj}\times\mathbf{r}_{ij} - \frac{\mathbf{R}_{ijk}\cdot\mathbf{R}_{ilj}}{R_{ijk}^2}(\mathbf{R}_{ijk}\times\mathbf{r}_{ij})\right\} \tag{6.12}$$

$$\mathbf{F}_l^{bend} = \frac{\lambda_b}{R_{ijk}R_{ilj}}\left\{\mathbf{R}_{ijk}\times\mathbf{r}_{ij} - \frac{\mathbf{R}_{ijk}\cdot\mathbf{R}_{ilj}}{R_{ilj}^2}(\mathbf{R}_{ilj}\times\mathbf{r}_{ij})\right\} \tag{6.13}$$

where $\mathbf{r}_{ab} = \mathbf{r}_b - \mathbf{r}_a$, $\mathbf{R}_{ijk} = \mathbf{r}_{ij}\times\mathbf{r}_{ik}$ and $\mathbf{R}_{ilj} = \mathbf{r}_{il}\times\mathbf{r}_{ij}$.

Dynamical model

To get a numerical simulation of the time evolution of the system (triangulated membrane), I will assume that the motion of each node in it can be described by a simple Langevin equation:

$$m_{mb}\frac{d^2\mathbf{r}_i}{dt^2} = -\zeta_{mb}\frac{d\mathbf{r_i}}{dt} + \mathbf{F}_i(t) + \eta(t) \tag{6.14}$$

where m_{mb} is the bead mass, ζ_{mb} is the solvent friction coefficient, $\mathbf{F}_i = -\nabla_i E_i = \mathbf{F}_i^{bend} + \mathbf{F}_i^{bond} + \mathbf{F}_i^{\text{EV}}$ is the total force acting on the node and η is a white noise with

$$\langle\eta_\alpha(\mathbf{t})\rangle = 0 \qquad \langle\eta_\alpha(t)\eta_\beta(t')\rangle = 2k_BT\zeta_{mb}\delta_{\alpha\beta}\delta(t-t') \tag{6.15}$$

where $\alpha, \beta = x, y, z$. This set of equations can be integrated numerically following *e.g.* the algorithm proposed by Vanden-Eijnden and Ciccotti in [111] (see Appendix B.2).

6.2 Membranes simulations: algorithm and results

All the parameters chosen for the simulations are reported in Tables 6.2 to 6.4 at the end of the chapter.

6.2.1 Polymerized membranes

The model presented so far describes a *polymerized membrane*, where lipids cannot diffuse along the surface, being permanently attached to the same neighbors and the network has a permanent topology directly following from the choice of the starting configuration. The membrane initialization has been done in any case starting from a triangular lattice of step $\ell_{0,mb}$ in a rectangular box ($L_y \times L_z$), with PBC along y and z. The initial velocities of each node is sampled from the Maxwell distribution. When the membrane patch is initiated, three neighbor lists are created:

- `list_bond(1:nn_k,k)` contains all the membrane nodes bonded to the k-th. Here $nn_k \in [3, \max_{nn}]$ and $k \in [1, N_{nodes}]$ with $\max_{nn}$ maximum number of allowed bonds per node. nn_k has also to be larger than 3, as mentioned.

- `list_bend(1:4,k_b)` contains the four nodes forming the k_b-th couple of adjacent triangles (*i.e.* the k_b-th bond). $i = 1, 2$ are the two bonded beads, with the bond forming the edge shared by the two triangles and $i = 3, 4$ are the beads at the opposite vertices; $k_b \in [1, N_b]$.

- `list_EVmb(1:nn_k,k)` contains all the membrane nodes closer to the k-th than a distance $r_{\rm EV}^{list} > \ell_{c,\rm EV}$, which are not bonded to it. Here $nn_k \in [1, \max_{nn}]$ and $k \in [1, N_{nodes}]$.

These lists are used to compute forces at each integration step; the first two lists remain unchanged along the simulation, while the third is updated as soon as the largest of the nodes' displacements from the position they occupied when the list had been created is larger than $\left(r_{\rm EV}^{list} - \ell_{c,\rm EV}\right)/2 \equiv \left(1.5\ell_{c,\rm EV} - \ell_{c,\rm EV}\right)/2 = 0.25\ell_{c,\rm EV}$. Starting from the initial configuration, at each step the positions and velocities of each node is evolved using Eq. (B.5), and the displacements are calculated to check whether the EV list must be updated; periodically an output file is printed with all the coordinates for further analysis.

6.2.2 Fluid membranes: bond-flipping procedure

If we want to include *fluidity* in the membrane model, the connectivity of the nodes needs to be transformed into a dynamical variable. This can be done by introducing Monte Carlo *bond flipping moves*: every Δ_{bf} steps, before the positions and velocities integration, a number $\psi_{bf} N_b$ of bonds ($0 < \psi_{bf} < 1$) is selected at random and a "flip move" on each of them is attempted: let's suppose that the tether ij is selected, with k and l at the opposed vertices of triangles (ijk) and (ijl) (see Fig. 6.4). The move consists in cutting the ij tether and substituting it by a new bond connecting k and l. The new attempted bond must be of suitable length, $\ell_{min} < r_{kl} < \ell_{max}$; if this is the case, the bonding energies $U_{bond}^{old} = U_{bond}^{mb}(r_{ij})$ and $U_{bond}^{new} = U_{bond}^{mb}(r_{kl})$ are calculated, as well as the bending energies $U_{bend}^{old} = U_{bend}^{mb}(ijk - ijl) + \dots$ and

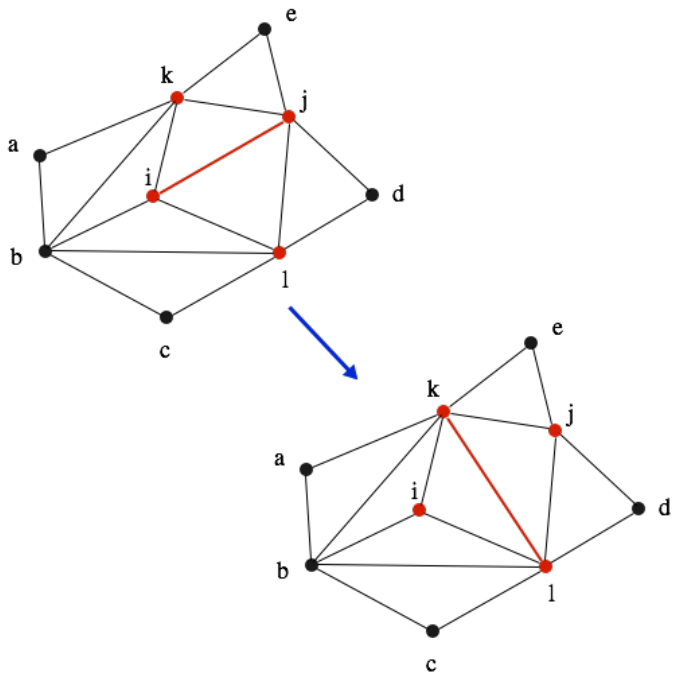

Figure 6.4. Bond flipping procedure: when the triangles couple $(ijk) - (ijl)$ is selected, the tether ij is (attempted to be) removed and substituted by the new bond kl.

$U^{new}_{bend} = U^{mb}_{bend}(kli - klj) + \dots$ for all the pairs of triangles involving nodes i, j, k or l in the old and the new configuration respectively. The acceptance probability for the Metropolis check is taken equal to

$$P^{acc}_{bond-flip} = \min\left\{1, \exp\left[-\beta\left((U^{new}_{bond} + U^{new}_{bend}) - (U^{old}_{bond} + U^{old}_{bend})\right)\right]\right\} \qquad (6.16)$$

If the Metropolis test succeeds and the move is accepted, both `list_bond` and `list_bend` need to be updated.As for the latter, the couple $(ijk) - (ijl)$ (listed as `ijkl`) is changed into $(kli) - (klj)$ (`klij` in the updated list). Also other triangles pairs need to be changed: any time a bond-flipping move is accepted, four other triangle pairs change, namely those involving both i and j – referring to Fig. 6.4, for instance $(ikb) - (ikj)$ becomes $(ikb) - (ikl)$. An automatized procedure substitutes the old with the new pairs in the list any time a bond flipping move is accepted. The time-step interval Δ_{bf} has been chosen such that these moves did not affect the dynamics dramatically, checking for instance that the energy was correctly conserved between two successive moves. This interval indeed must be large enough to let the membrane re-equilibrate after the bond-flipping procedure.

Mean square displacement: polymerized vs fluid membranes

The bond-flipping procedure described above should reproduce the lipids diffusion along the membrane surface, and hence the mean square displacement of the nodes

in the membrane should be linear with time in the long time limit:

$$\text{MSD}(t) = \left\langle ((\mathbf{R}(t) - \mathbf{R}_{cm}(t)) - (\mathbf{R}(t_0) - \mathbf{R}_{cm}(t_0)))^2 \right\rangle \tag{6.17}$$

where the average is taken over the membrane nodes, the time origin t_0 and different trajectories. For a fluid this quantity is expected to increase in time like $\text{MSD}(t) = 6D_{eff}t$ (D_{eff} effective diffusion coefficient), while for a solid it is expected to saturate to a plateau value related to the characteristic vibrational frequency. Fig. 6.5 reports the MSD for membranes with periodic boundary conditions along y and z, for three different values of ψ_{bf}: for $\psi_{bf} = 0$ the behavior is solid-like, and the black dashed line corresponds to the static average

$$\sigma^2 = \overline{\left\langle (\mathbf{R} - \mathbf{R}_{cm})^2 \right\rangle} \tag{6.18}$$

where the average is performed over particles, time and different trajectories. Non-zero ψ_{bf} values (0.01 and 0.25 in the figure) provide a MSD linearly increasing in time (fluid-like behavior) with a slope increasing with ψ_{bf}. This result has been used and presented as a test for the code reliability.

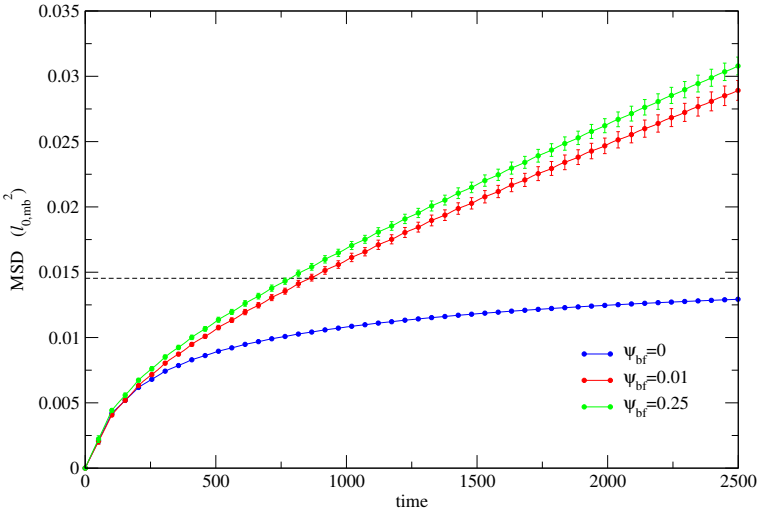

Figure 6.5. Mean Square Displacement (MSD) versus time for different values of the bond-flipping probability: for $\psi_{bf} = 0$ no bond is flipped and the membrane behaves like a solid, with the MSD saturating at long times to a plateau value related to the characteristic vibrational frequency. Non-zero values of ψ_{bf} give a fluid behavior to the membrane: the MSD grows linearly in time with a slope increasing with ψ_{bf} and proportional to the diffusion coefficient.

6.3 "Fluctuation route" and "virial route" to the surface tension

The main membrane property I have been interested in was the *surface tension*, which can be calculated via several methods, as sketched in the previous chapter. The first route was presented in Section 5.3.1, and it is through the analysis of the spectrum of height fluctuations. The second route is through the virial expression Eq. (5.71). The results obtained by these two methods are in excellent agreement, providing a strong evidence of the reliability of the code and a strong support to the equivalence of these two rather different ways to obtain this crucial property. From previous attempts, based on shorter simulations of smaller membranes (smaller boxes), the numerical evidence of the equivalence was rather weak (see e.g. [95]).

6.3.1 Spectrum of height fluctuations

As detailed in the previous chapter, in the Monge parametrization the membrane is described by specifying the height $h(y,z)$ (with respect to a reference plane) of the surface as a function of the coordinates of the flat base plane (yz in the present work case). In the simulations, the set of positions $S = \{x_j, y_j, z_j\}_{j=1,N_{nodes}}$ localizes all nodes for a given microscopic configuration of the membrane, and the height information must be extracted from these available data. Let $\widehat{u}(y,z;S)$ be the height of the membrane surface at (y,z) to be estimated from the data set S, and $\widehat{\rho}(y,z;S)$ the in-plane number density, defined as

$$\widehat{\rho}(\mathbf{r}) \equiv \widehat{\rho}(y,z;S) = \sum_{j=1}^{N_{nodes}} \delta(y_j - y)\, \delta(z_j - z) \tag{6.19}$$

which gives the following average membrane density (for a given microscopic configuration)

$$\begin{aligned}
\bar{\rho} &= \frac{1}{L_y}\int_0^{L_y} dy \frac{1}{L_z}\int_0^{L_z} dz\, \widehat{\rho}(\mathbf{r}) \\
&= \frac{1}{L_y L_z}\sum_{j=1}^{N_{nodes}} \int_0^{L_y} dy \int_0^{L_z} dz\, \delta(y_j - y)\, \delta(z_j - z) \\
&= \frac{N_{nodes}}{L_y L_z},
\end{aligned} \tag{6.20}$$

as expected. Note that by $\mathbf{r}$ I indicate the two-component vector $\mathbf{r} \equiv (y,z)$. The height $\widehat{h}(y,z;S)$ to be estimated from the data set S can be written as:

$$\begin{aligned}
\widehat{h}(\mathbf{r}) \equiv \widehat{h}(y,z;S) &= \frac{\widehat{\rho}(y,z;S)}{\bar{\rho}}\, \widehat{u}(y,z;S) \\
&= \frac{L_y L_z}{N_{nodes}} \sum_{j=1}^{N_{nodes}} \delta(y_j - y)\, \delta(z_j - z)\, u(y_j, z_j; S)
\end{aligned} \tag{6.21}$$

where the height of the surface $u(y_j, z_j; S) \equiv u(y_j, z_j)$ at the j-th node location can be defined as

$$u(y_j, z_j) = x_j - \bar{x} \tag{6.22}$$

with $\bar{x} = \frac{1}{N_{nodes}} \sum_{i=1}^{N_{nodes}} x_i$ average over the nodes in a single configuration. These definitions give zero membrane average height:

$$\begin{aligned}\bar{h} &= \frac{1}{L_y}\int_0^{L_y} dy \frac{1}{L_z}\int_0^{L_z} dz\ \widehat{h}(\mathbf{r}) \\ &= \frac{1}{N_{nodes}} \sum_{j=1}^{N_{nodes}} \int_0^{L_y} dy \int_0^{L_z} dz\ \delta(y_j - y)\ \delta(z_j - z)\ (x_j - \bar{x}) \\ &= \frac{1}{N_{nodes}} \sum_{i=1}^{N_{nodes}} x_i - \bar{x} = 0 \end{aligned} \tag{6.23}$$

as expected.

We are interested in the spectrum of the height and density fluctuations, the former being related to the membrane elastic constants, as detailed in Section 5.3.1; let's take the Fourier transforms of $\widehat{\rho}(y,z;S)$ and $\widehat{h}(y,z;S)$, as defined there:

$$\begin{aligned}\widehat{\rho}_{\mathbf{q}} &= \frac{1}{L_y L_z}\int_0^{L_y} dy \int_0^{L_z} dz \exp\left(-iq_y y - iq_z z\right)\widehat{\rho}(y,z;S) \\ &= \frac{1}{L_y L_z} \sum_{j=1}^{N_{nodes}} \exp\left(-iq_y y_j - iq_z z_j\right) \end{aligned} \tag{6.24}$$

$$\begin{aligned}\widehat{h}_{\mathbf{q}} &= \frac{1}{L_y L_z}\int_0^{L_y} dy \int_0^{L_z} dz \exp\left(-iq_y y - iq_z z\right)\widehat{h}(y,z;S) \\ &= \frac{1}{N_{nodes}} \sum_{j=1}^{N_{nodes}} (x_j - \bar{x}) \exp\left(-iq_y y_j - iq_z z_j\right). \end{aligned} \tag{6.25}$$

Eq. (6.24) computed for $\mathbf{q} = (0,0)$ gives the average density $\bar{\rho} = \frac{N_{nodes}}{L_y L_z}$, while Eq. (6.25) applied to the $\mathbf{q} = (0,0)$ case gives the average height $\bar{h} = 0$. This expression for $\widehat{h}_{\mathbf{q}}$ corresponds to Eq.(15) of [112] citing Brandt et al. work [113], and they referred to it as the "direct Fourier method". Let's now write explicitly the averages of the square modulus of $\widehat{\rho}_{\mathbf{q}}$ and $\widehat{h}_{\mathbf{q}}$, taken over many microscopic configurations (produced by a long time trajectory for instance):

$$\begin{aligned}\left\langle |\widehat{\rho}_{\mathbf{q}}|^2 \right\rangle &= \frac{1}{L_y^2 L_z^2}\left(\left\langle \sum_{j=1}^{N_{nodes}} \sum_{k=1}^{N_{nodes}} \exp\left(-iq_y y_j - iq_z z_j\right)\exp\left(iq_y y_k + iq_z z_k\right)\right\rangle\right) \\ &= \frac{1}{L_y^2 L_z^2}\left(N_{nodes} + \left\langle \sum_{j\neq k}^{N_{nodes}} \exp\left(-i\ \mathbf{q}\cdot(\mathbf{r}_j - \mathbf{r}_k)\right)\right\rangle\right) \end{aligned} \tag{6.26}$$

$$\begin{aligned}\left\langle |\widehat{h}_{\mathbf{q}}|^2 \right\rangle &= \frac{1}{N_{nodes}^2}\left(\left\langle \sum_{j=1}^{N_{nodes}} \sum_{k=1}^{N_{nodes}} (x_j - \bar{x})(x_k - \bar{x})\exp\left(-iq_y y_j - iq_z z_j\right)\exp\left(iq_y y_k + iq_z z_k\right)\right\rangle\right) \\ &= \frac{1}{N_{nodes}^2}\left(N_{nodes}\sigma_x^2 + \left\langle \sum_{j\neq k}^{N_{nodes}} (x_j - \bar{x})(x_k - \bar{x})\exp\left(-i\ \mathbf{q}\cdot(\mathbf{r}_j - \mathbf{r}_k)\right)\right\rangle\right) \\ &= \frac{\sigma_x^2}{N_{nodes}} + \frac{1}{N_{nodes}^2}\left\langle \sum_{j\neq k}^{N_{nodes}} (x_j - \bar{x})(x_k - \bar{x})\exp\left(-i\ \mathbf{q}\cdot(\mathbf{r}_j - \mathbf{r}_k)\right)\right\rangle \end{aligned} \tag{6.27}$$

with $\sigma_x^2 = \langle (x - \bar{x})^2 \rangle$ the square of the width of the height distribution. Note that $\langle \cdots \rangle$ indicates a *statistical* average over the Boltzmann measure. Introducing δ-functions centered on the nodes positions:

$$\left\langle |\widehat{\rho}_{\mathbf{q}}|^2 \right\rangle = \frac{N_{nodes}}{L_y^2 L_z^2} + \frac{1}{L_y^2 L_z^2} \int \int_{L_y^2 L_z^2} d\mathbf{r}\, d\mathbf{r}' \exp\left(-i\, \mathbf{q} \cdot (\mathbf{r} - \mathbf{r}')\right) \times \left\langle \sum_{j \neq k}^{N_{nodes}} \delta\left(\mathbf{r} - \mathbf{r}_j\right) \delta\left(\mathbf{r}' - \mathbf{r}_k\right) \right\rangle \tag{6.28}$$

$$\left\langle |\widehat{h}_{\mathbf{q}}|^2 \right\rangle = \frac{\sigma_x^2}{N_{nodes}} + \frac{1}{N_{nodes}^2} \int \int_{L_y^2 L_z^2} d\mathbf{r}\, d\mathbf{r}' \exp\left(-i\, \mathbf{q} \cdot (\mathbf{r} - \mathbf{r}')\right) \times \left\langle \sum_{j \neq k}^{N_{nodes}} \left(x(\mathbf{r}) - \bar{x}\right) \left(x(\mathbf{r}') - \bar{x}\right) \delta\left(\mathbf{r} - \mathbf{r}_j\right) \delta\left(\mathbf{r}' - \mathbf{r}_k\right) \right\rangle \tag{6.29}$$

The terms in brackets can be regarded as radial distribution functions, which can be defined as

$$g(r = |\mathbf{r}' - \mathbf{r}''|) = \frac{L_y^2 L_z^2}{N_{nodes}^2} \left\langle \sum_{j \neq k}^{N_{nodes}} \delta\left(\mathbf{r}' - \mathbf{r}_j\right) \delta\left(\mathbf{r}'' - \mathbf{r}_k\right) \right\rangle \tag{6.30}$$

$$g_h(r = |\mathbf{r}' - \mathbf{r}''|) = \frac{L_y^2 L_z^2}{N_{nodes}^2 \sigma_x^2} \left\langle \sum_{j \neq k}^{N_{nodes}} \left(x(\mathbf{r}') - \bar{x}\right) \left(x(\mathbf{r}'') - \bar{x}\right) \delta\left(\mathbf{r}' - \mathbf{r}_j\right) \delta\left(\mathbf{r}'' - \mathbf{r}_k\right) \right\rangle \tag{6.31}$$

Eqs. (6.28) and (6.29) can be then rewritten as:

$$\begin{aligned} \langle |\widehat{\rho}_{\mathbf{q}}|^2 \rangle &= \frac{N_{nodes}}{L_y^2 L_z^2} + \frac{N_{nodes}^2}{L_y^3 L_z^3} \int_{L_y L_z} d\mathbf{r}\ \exp\left(-i\, \mathbf{q} \cdot \mathbf{r}\right) g(r) \\ &= \frac{N_{nodes}}{L_y^2 L_z^2} + \frac{2\pi N_{nodes}^2}{L_y^3 L_z^3} \int_{L_0} dr\ r\ J_0(qr) g(r) \end{aligned} \tag{6.32}$$

$$\begin{aligned} \langle |\widehat{h}_{\mathbf{q}}|^2 \rangle &= \frac{\sigma_x^2}{N_{nodes}} + \frac{\sigma_x^2}{L_y L_z} \int_{L_y L_z} d\mathbf{r}\ \exp\left(-i\, \mathbf{q} \cdot \mathbf{r}\right) g_h(r) \\ &= \frac{\sigma_x^2}{N_{nodes}} + \frac{2\pi \sigma_x^2}{L_y L_z} \int_{L_0} d\, r\ r\ J_0(qr) g_h(r) \end{aligned} \tag{6.33}$$

where L_0 is the linear system size (radius) and $J_0(x)$ is the zeroth-order Bessel function of the first kind, with $J_n(x) = \frac{1}{2\pi} \int_0^{2\pi} d\tau\ \exp\left[i\left(n\tau - x \sin(\tau)\right)\right]$.

It is interesting to analyze the large-q limits of Eqs. (6.32) and (6.33): the zeroth-order Bessel function is known to go to zero as its argument goes to infinity, so we immediately get the large-q limits of $\langle |\widehat{\rho}_{\mathbf{q}}|^2 \rangle$ and $\langle |\widehat{h}_{\mathbf{q}}|^2 \rangle$:

$$\lim_{q \to \infty} \langle |\widehat{\rho}_{\mathbf{q}}|^2 \rangle = \frac{N_{nodes}}{L_y^2 L_z^2} \qquad \text{and} \qquad \lim_{q \to \infty} \langle |\widehat{h}_{\mathbf{q}}|^2 \rangle = \frac{\sigma_x^2}{N_{nodes}}. \tag{6.34}$$

At high q, hence, we have:

$$\langle |\widehat{h}_{\mathbf{q}}|^2 \rangle = \sigma_x^2 \left(\frac{L_y L_z}{N_{nodes}} \right)^2 \langle |\widehat{\rho}_{\mathbf{q}}|^2 \rangle \tag{6.35}$$

Notice that the average square modulus of $\widehat{\rho}_q$ and $\widehat{h}_q$ Eqs. (6.24) and (6.25) can be rewritten using the Euler's formula for complex numbers:

$$\langle|\widehat{\rho}_{\mathbf{q}}|^2\rangle = \frac{1}{L_y^2 L_z^2}\left[\left\langle\left(\sum_{j=1}^{N_{nodes}}\cos\left(\mathbf{q}\cdot\mathbf{r}_j\right)\right)^2\right\rangle + \left\langle\left(\sum_{j=1}^{N_{nodes}}\sin\left(\mathbf{q}\cdot\mathbf{r}_j\right)\right)^2\right\rangle\right] \tag{6.36}$$

$$\langle|\widehat{h}_{\mathbf{q}}|^2\rangle = \frac{1}{N_{nodes}^2}\left[\left\langle\left(\sum_{j=1}^{N_{nodes}}\left(x_j-\langle x\rangle\right)\cos\left(\mathbf{q}\cdot\mathbf{r}_j\right)\right)^2\right\rangle + \left\langle\left(\sum_{j=1}^{N_{nodes}}\left(x_j-\langle x\rangle\right)\sin\left(\mathbf{q}\cdot\mathbf{r}_j\right)\right)^2\right\rangle\right] \tag{6.37}$$

which have been used to extract these spectra from the simulation data. In particular, anticipating the following, the numerical result for $\langle|\widehat{h}_{\mathbf{q}}|^2\rangle$ will be compared at small q values with Eq. (5.57) to extract information on the membrane surface tension and the bending modulus.

6.3.2 Virial expression for the surface tension

Eq. (5.71) gives a relation between the membrane surface tension and the pressure tensor, $\mathbf{P}$. In the following, details on the computation of this quantity starting from a numerical simulation of the model described in Sections 6.1 and 6.2 will be provided.

The global pressure tensor $\mathbf{P}$ for a collection of N particles in a volume V is related to the global virial tensor [114],

$$\mathbf{P}V = \langle\sum_{i=1}^{N} m_i\mathbf{v}_i\otimes\mathbf{v}_i + \mathbf{W}(\mathbf{r}^N)\rangle \tag{6.38}$$

where m_i and $\mathbf{v}_i$ are the mass and instantaneous velocity of the ith node; $\otimes$ indicates the outer product. The scalar virial is related to the global virial tensor by $W = \mathrm{Tr}\ \mathbf{W} = W_{xx} + W_{yy} + W_{zz}$. In the case of pair interactions, the virial is given

$$\mathbf{W}(\mathbf{r}^N) = \sum_{i=1}^{N}\sum_{j>i}^{N}\mathbf{r}_{ij}\otimes\mathbf{F}_{ij} \tag{6.39}$$

where $\mathbf{F}_{ij}$ is the force on atom i due to the pair interaction with atom j. This expression under periodic boundary conditions along two directions becomes

$$\mathbf{W}(\mathbf{r}^N) = \sum_{\mathbf{n}\in\mathbb{Z}^2}\sum_{i=1}^{N}\sum_{j>i}^{N}\mathbf{r}_{ij\mathbf{n}}\otimes\mathbf{F}_{ij\mathbf{n}} \tag{6.40}$$

where $\mathbf{F}_{ij\mathbf{n}}$ is the force acting on atom i due to the pair interaction with the image of atom j located at $\mathbf{r}_j + (L_y, L_z)\mathbf{n}$.

As already mentioned, however, our bending energy is not a pair potential, but it is a four-body potential. The general expression for the virial in the case of many-body potential has been derived in [114]: let's define the potential energy

for a finite nonperiodic system as the sum of K group energy terms, each of which depends only on the position of a small group of N_k atoms (four in our case):

$$U(\mathbf{r}^N) = \sum_{k=1}^{K} u_k(\mathbf{r}^{N_k}), \qquad \mathbf{r}^{N_k} = \mathbf{r}_1^k, \mathbf{r}_2^k, \ldots, \mathbf{r}_{N_k}^k \tag{6.41}$$

where $\mathbf{r}_w^k$ is the position of the wth atom in the kth group. The expression for the virial in a finite nonperiodic system is given by:

$$\mathbf{W}(\mathbf{r}^N) = \sum_{k=1}^{K} \sum_{w=1}^{N_k} \mathbf{r}_w^k \otimes \mathbf{F}_w^k \tag{6.42}$$

where $\mathbf{F}_w^k$ is the force due to the atoms in the kth group on the wth atom of that group, $\mathbf{F}_w^k = -\frac{d}{d\mathbf{r}_w^k} u_k(\mathbf{r}^{N_k})$.

Let’s now consider an infinite periodic system. Each group will have an infinite number of equivalent periodic group images, and each of them must be associated to one and only one of the infinite cell replicas. One criterion to chose such cell replicas is to associate each group image with the replica cell containing its center of mass. Alternatively, each group image can be associated to the replica cell containing the *first* atom of the group – and this is what I have done. Figure 6.6 shows four images of a group of four atoms, all of them having an atom in the local cell. The first atom in the group surrounded by the red circle is in the local cell and so this group is the one associated with the local cell.

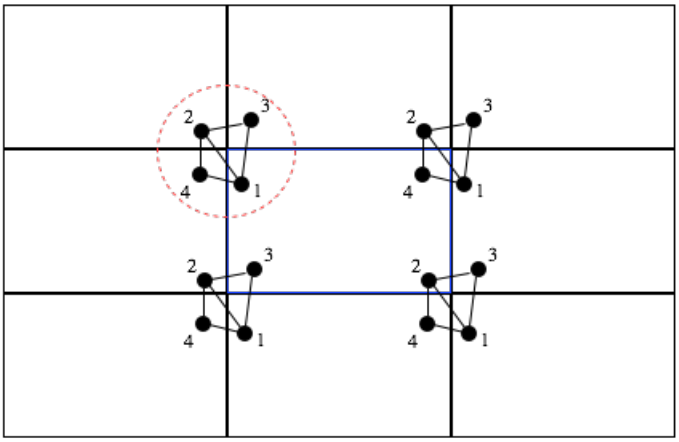

Figure 6.6. Example of how group images are associated with periodic replicas. The blue central rectangle indicates the local cell, surrounded by infinite periodic replicas. The red circle indicates the group image associated with the local cell.

The potential energy of the local cell can then be written unambiguously:

$$U(\mathbf{r}^N) = \sum_{k \in \mathbf{0}} u_k(\mathbf{r}^{N_k}), \qquad \mathbf{r}^{N_k} = \mathbf{r}_1^k, \mathbf{r}_2^k, \ldots, \mathbf{r}_{N_k}^k \tag{6.43}$$

where the sum is taken over all group images associated with the local cell; the first atom of each group is by construction in the local cell. The virial of the local cell in

an infinite periodic system results in the following expression [114]

$$\mathbf{W}(\mathbf{r}^N) = \sum_{k\in\mathbf{0}} \sum_{w=1}^{N_k} \mathbf{r}_w^k \otimes \mathbf{F}_w^k. \tag{6.44}$$

where $k \in \mathbf{0}$ means that the sum is performed over all the groups contained in the local cell.

I used Eq. (6.44) for the contribution to the virial coming from the bending potential: as each group is defined by a ordered quartet of particles (i, j, k, l) – the bond between i and j being the common edge of the triangle pair – I loop over the bonds and take the corresponding quartet. Then I take the position of particle i inside the local cell $L_y \times L_z$, and look at the distances from the others. If the distance from j, for instance, is not appropriate for bonding, I look for the corresponding image of j which is at a suitable distance. Then I used Eq. (6.40) for the contribution of the bonding and EV potentials, and finally Eqs. (5.71) and (6.38) to get the membrane surface tension.

Numerical tests

Numerical simulations of a fluid membrane with $N_{nodes} = 6400$ and $\psi_{bf} = 0.25$ have been realized to get information on the surface tension, both from the analysis of the height fluctuations spectrum and the virial expression. $N_{traj} = 24$ trajectories have been realized starting from a planar configuration of equilateral triangles of edge $\ell_{0,mb} = 3d_0$ ($d_0 = 2.7$ nm half G-actin diameter, see Part I and Table 6.1). The parameters used in the simulations are summarized in Tables 6.1 and 6.3; the size of the simulation box (local cell) was $L_y = 80\ell_{0,mb} \equiv 240\ d_0 \approx 650$ nm and $L_y = 80\frac{\sqrt{3}}{2}\ell_{0,mb} \equiv 207.8\ d_0 \approx 560$ nm.

Fig. 6.7 shows the height fluctuations and density spectra for this system, $\langle|h_{\mathbf{q}}|^2\rangle$ (blue) and $\langle|\rho_{\mathbf{q}}|^2\rangle$ (magenta) respectively; the theoretical large-q limits Eq. (6.34) are well satisfied, and the two curves correctly present the same oscillations in that region [113], inherent to the molecular structure of fluid phases (structure factor).

Fig. 6.8 shows $\langle|h_{\mathbf{q}}|^2\rangle$ in the small-q region: these data have been used to extract the membrane surface tension value by fitting Eq. (5.56) to the data in a suitable q range (at small q, the data deviate from the expected behavior, probably due to finite-size effects). The effective value of bending rigidity λ_b (κ in Eq. (5.56)), which I will denote by λ_b^{eff} hereafter, has been also extracted from the fitting procedure. The values I get are:

$$\lambda_b^{eff} = (14.7 \pm 0.2)\ k_BT \tag{6.45}$$

$$\Sigma = (1.75 \pm 0.08)\ \frac{k_BT}{\ell_{0,mb}^2} \qquad \text{(height fluctuations)} \tag{6.46}$$

The behavior of $\langle|h_{\mathbf{q}}|^2\rangle$ is correctly dominated by the surface tension for $q < q_{crossover} = \sqrt{\frac{\Sigma}{\lambda_b^{eff}}} = 0.345\ell_{0,mb}^{-1}$ and by the bending energy for $q > 0.345\ell_{0,mb}^{-1}$, as anticipated in Section 5.3.1.

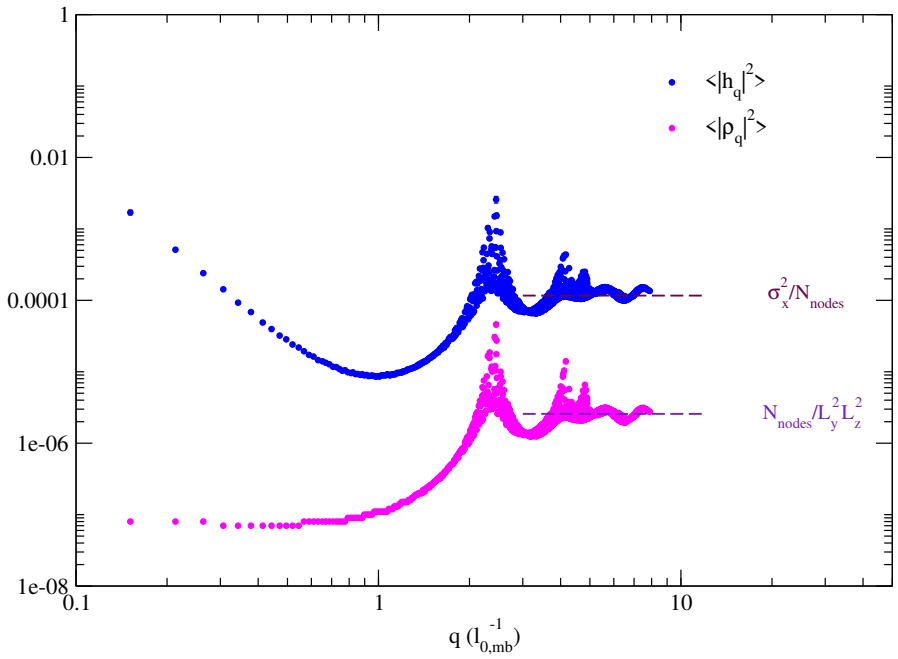

Figure 6.7. Height fluctuations and density spectra, $\langle|h_{\mathbf{q}}|^2\rangle$ (blue) and $\langle|\rho_{\mathbf{q}}|^2\rangle$ (magenta) respectively; the large-q limits are indicated by dashed horizontal lines, respectively at σ_x^2/N_{nodes} and $N_{nodes}/L_y^2L_z^2$, as expected (see Eq. (6.34)). The large-q tail of $\langle|h_{\mathbf{q}}|^2\rangle$ reflects the same oscillations of $\langle|\rho_{\mathbf{q}}|^2\rangle$ (see Eq. (6.34)) [113].

The same trajectories have been used to calculate the surface tension using Eq. (5.71), as previously detailed, and the resulting value is:

$$\Sigma = (1.724 \pm 0.004)\ \frac{k_B T}{\ell_{0,mb}^2} \qquad \text{(virial)} \tag{6.47}$$

which is in perfect agreement with the value obtained through the spectrum of height fluctuations.

6.4 Grand-Canonical simulations of triangulated membranes

What has been described so far is a *canonical* model for a fluid triangulated membrane, with a fixed number of beads, and it has been useful to study membrane fluctuations at equilibrium. Our purpose being to simulate the onset and development of a filopodial protrusion, we need this membrane to be also *deformable*: if the number of beads is kept fixed and we somehow push the membrane keeping some nodes frozen [19], it can't vertically shift nor deform – the bonded beads cannot step away

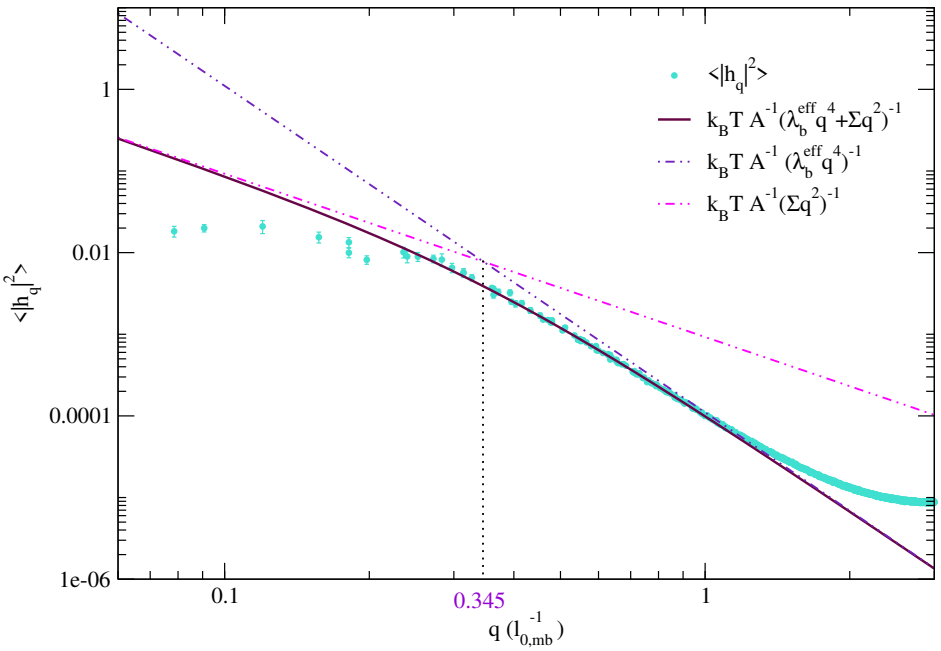

Figure 6.8. Height fluctuations spectrum at small-q values: the solid line represents Eq. (5.56), and the dashed-dotted lines represent the q^{-2} and the q^{-4} behaviors. The numerical values of λ_b^{eff} and Σ have been extracted from the data set by a linear fit; the Σ value obtained by the virial calculation has not been drawn since the lines would be perfectly superimposed. The agreement is not excellent at the smallest q values, probably symptomatically of finite-size effects. The crossover value of q, at which the contributions coming from the surface tension and the bending resistance are equal, is indicated in violet.

further than ℓ_{max}. The idea is then to allow for the number of beads to vary, using a *grand-canonical* model [19]: the simulated membrane patch can be regarded as a small portion of a large GUV or a cell, which provides a fixed reference frame supporting the deformation and constitutes a reservoir of lipid molecules which are drawn as the protrusion elongates. In this view, the filopodial protrusion constitutes only a small fraction of the total vesicle or cell, and the surface tension is fixed and maintained constant by the much larger lipid reservoir.

6.4.1 Statistical mechanics foundations

Let's consider a triangulated membrane as a 2D network of connected beads in chemical equilibrium with an ideal solution of similar free beads at temperature T. The system is enclosed in an orthonormal box of section $A = L_y \times L_z$ and height H along the x direction, the volume $V = AH$.The membrane has an area A and thickness $h \ll H$ taking into account its height fluctuations. Periodic boundary conditions apply in the yz plane. The number of beads in the membrane, N_{nodes}, fluctuates as exchanges beads with a reservoir of $M - N_{nodes}$ non-interacting free beads (no bead-bead and no membrane-beads interactions); they participate to a chemical exchange with the membrane by transferring a bead from/to the solution to/from the membrane, leading to change $N_{nodes} \to N_{nodes} \pm 1$ within the membrane, while the total number of beads M is conserved. This leads to the same chemical potential at equilibrium for both the free beads reservoir and the membrane network [115]. The effective Hamiltonian of the membrane for a given number of beads and for a particular triangulation t (with N_b bonds and N_t triangles) connecting the beads with elementary triangles, comprises a standard kinetic part and a potential part $E^{mb}(\mathbf{r}^{N_{nodes}}; t)$ containing bonding, excluded-volume and bending terms, as already detailed above. The canonical partition function for the global system (membrane and solution) with total number of particles M is:

$$\mathcal{Z}(M, V, A, T) = \sum_{N_{nodes}=0}^{M} \frac{V^{M-N}}{(M - N_{nodes})! \Lambda^{3(M-N_{nodes})}} \mathcal{Z}_{mb}(N_{nodes}, h, A, T) \tag{6.48}$$

$$\mathcal{Z}_{mb}(N_{nodes}, h, A, T) = \frac{Ah}{N_{nodes}! \Lambda^{3N_{nodes}}} \sum_t \int_h dx^{N_{nodes}} \int_A d\mathbf{r}^{N_{nodes}} \exp\left(-\beta E^{mb}(\mathbf{r}^{N_{nodes}}; t)\right) \tag{6.49}$$

where $\sum_t$ implies a sum over the distinct possible triangulations that can be realized given a microscopic configuration $\mathbf{r}^{N_{nodes}}$ of N_{nodes} particles. Taking the limit $M \to \infty$, $H \to \infty$ keeping constant the beads density $\rho_s = \frac{M}{AH}$, we get the Grand-Canonical partition function for the membrane:

$$\Xi_{mb}(\mu, A, h, T) = \sum_{N_{nodes}=0}^{\infty} \exp\left(\beta \mu N_{nodes}\right) \mathcal{Z}_{mb}(N_{nodes}, h, A, T) \tag{6.50}$$

where the chemical potential is $\mu = k_B T \ln\left(\Lambda^3 \rho_s\right)$ with $\Lambda = \sqrt{\frac{2\pi\hbar^2}{m_{mb} k_B T}}$ thermal de Broglie wavelength. The membrane grand-potential is related to Eq. (6.50) by

$$\Omega_{mb}(\mu, A, h, T) = -k_B T \ln \Xi_{mb}(\mu, A, h, T) \tag{6.51}$$

which satisfies the thermodynamic relation

$$d\Omega_{mb} = -SdT + \Sigma dA - pdV - N_{nodes}d\mu. \tag{6.52}$$

From this thermodynamic relationship one can get for instance the average number of beads in the membrane in the grand canonical ensemble taking the derivative of $\Omega_{mb}(\mu, A, h, T)$ with respect to the chemical potential μ at fixed A, h, T:

$$\langle N_{nodes}\rangle^{gc} = \left(\frac{\partial\Omega_{mb}}{\partial\mu}\right)_{A,h,T} = \frac{\sum_{N_{nodes}=0}^{\infty}\exp(\beta\mu N_{nodes})N_{nodes}\mathcal{Z}_{mb}(N_{nodes},h,A,T)}{\sum_{N_{nodes}=0}^{\infty}\exp(\beta\mu N_{nodes})\mathcal{Z}_{mb}(N_{nodes},h,A,T)} \tag{6.53}$$

or the average surface tension Σ taking the derivative of $\Omega_{mb}(\mu, A, h, T)$ with respect to the area A at given μ, h, T:

$$\begin{aligned}\langle\Sigma\rangle^{gc} &= \left(\frac{\partial\Omega_{mb}}{\partial A}\right)_{\mu,h,T} = -k_BT\frac{\left(\frac{\partial\Xi_{mb}}{\partial A}\right)_{\mu,h,T}}{\Xi_{mb}(\mu,A,h,T)} \\ &= -k_BT\frac{\langle N_{nodes}\rangle^{gc}}{A} + \frac{1}{2A}\left\langle\sum_{j=1}^{N_{nodes}}\nabla_j E^{mb}(\mathbf{r}^{N_{nodes}};t)\cdot\mathbf{r}_j\right\rangle^{gc}.\end{aligned} \tag{6.54}$$

Eq. (6.54) is a standard virial equation, where $\langle\cdots\rangle^{gc}$ implies a grand-canonical average over N_{nodes} beads, the beads positions $\mathbf{r}^{N_{nodes}}$ and the possible triangulations t.

If the free beads solution has a (critical) density ρ_c such as at equilibrium the membrane has no tendency to loose nor incorporate beads, then the membrane has *zero* surface tension. The corresponding chemical potential can be written as

$$\mu_c = k_BT\ln\left(\Lambda^3\rho_c\right). \tag{6.55}$$

If the free beads density is smaller than ρ_c, the surface tension is expected to be positive, with the membrane tending to loose beads, and it can be estimated writing the chemical potential as

$$\mu \approx \mu_c - \Sigma a \tag{6.56}$$

where a is the area per inserted bead. This relation states that to insert a new bead in the membrane, the reversible work $-\Sigma a$ has to be done in order to create a gap a in the membrane and insert the bead in the available hole, as if the membrane were tensionless. It is convenient to define the *fugacity* as

$$z \equiv \exp(\beta\mu) = \exp(\beta\mu_c)\exp(-\beta\Sigma a) = C\exp(-\beta\Sigma a). \tag{6.57}$$

The constant C combines specific parameters of the system which are not easy to control, still this fugacity can be used in numerical simulations as a direct tuning parameter, from which the surface tension value derives [19].

6.4.2 Grand-Canonical insertion/deletion moves

In the following I'll detail the procedure used to simulate the membrane patch in the grand canonical ensemble, through insertion or deletion of beads to or from the network.

Let's consider two related microscopic states of the membrane having respectively a number $N'_{nodes} = \mathrm{N}$ (state ν') and $N_{nodes} = \mathrm{N}+1$ of beads (state ν), as depicted in Fig. B.1. These two states ν and ν' have in common $\mathrm{N}-1$ beads, at the same positions and with the same connections in the triangulated network. In the state ν' there is an additional N-th bead, located at position $\mathbf{r}'_{\mathrm{N}}$, and it is connected to its nearest neighbors by specific connections yielding the global triangulation $t_{\nu'}$. In the state ν, there are two additional beads, N and $\mathrm{N}+1$, which we take[1] located at positions symmetric with respect to $\mathbf{r}'_{\mathrm{N}}$:

$$\mathbf{r}_{\mathrm{N}} = \mathbf{r}'_{\mathrm{N}} - \frac{l}{2}\hat{\mathbf{p}} \qquad \mathbf{r}_{\mathrm{N}+1} = \mathbf{r}'_{\mathrm{N}} + \frac{l}{2}\hat{\mathbf{p}} \tag{6.58}$$

with $\hat{\mathbf{p}} = (\sin\theta\cos\phi, \sin\theta\sin\phi, \cos\phi)$ unitary vector with arbitrary orientation and $\ell_{min} < l < \ell_{max}$ valid distance for bonding. These two beads are connected to each other and to the other nearest neighbors forming the global triangulation t_ν. Eq. (6.58) can be inverted to recover the position of the N-th bead in the state ν',

$$\mathbf{r}'_{\mathrm{N}} = \frac{1}{2}\left(\mathbf{r}_{\mathrm{N}} + \mathbf{r}_{\mathrm{N}+1}\right) \tag{6.59}$$

which can be seen as a *fusion* of two beads. The two states ν and ν' have a number of bonds, triangles and beads related to each other by

$$N_b = N'_b + 3 \tag{6.60}$$
$$N_t = N'_t + 2 \tag{6.61}$$
$$N_{nodes} = N'_{nodes} + 1. \tag{6.62}$$

It should be noticed that in state ν there is a number of possible connections between beads leading to different possible triangulations. In state ν', the triangulation $t_{\nu'}$ results from connecting the N-th bead with its N_v nearest neighbors, these N_v beads being bonded to each other. They are indeed the vertices of a non-planar polygon whose edges are their bonds and which will be divided into N_v triangles by tethering the N-th bead to them. The triangulation is valid if every distance is suitable for bonding ($\ell_{min} < d_{\mathrm{N}j} < \ell_{max}$, $j = 1, \ldots, N_v$). In state ν, the two additional beads, N and $\mathrm{N}+1$, are connected to each other, in the middle of the same non-planar polygon of N_v vertices. Among these vertices, only two will be connected to both bead N and $\mathrm{N}+1$, acting as "hinge" vertices. Looking along the polygon ring, these two hinge vertices separate two contiguous regions of beads connected either to bead N or $\mathrm{N}+1$ only. Fig. 6.9 shows three of the possible triangulation schemes given the two beads N and $\mathrm{N}+1$ in the middle of a convex hull of beads connected to each other. The hinge vertices are colored in purple, dividing those connected to N (green) and those tethered to $\mathrm{N}+1$ (light blue).

In the simulation scheme, every Δ_{GC} steps a Grand Canonical Monte Carlo move is attempted, choosing uniformly between insertion and deletion; how the respective procedures work is detailed in Appendix B.3.

[1] This is the same method implemented in [19], but it is not the only possible.

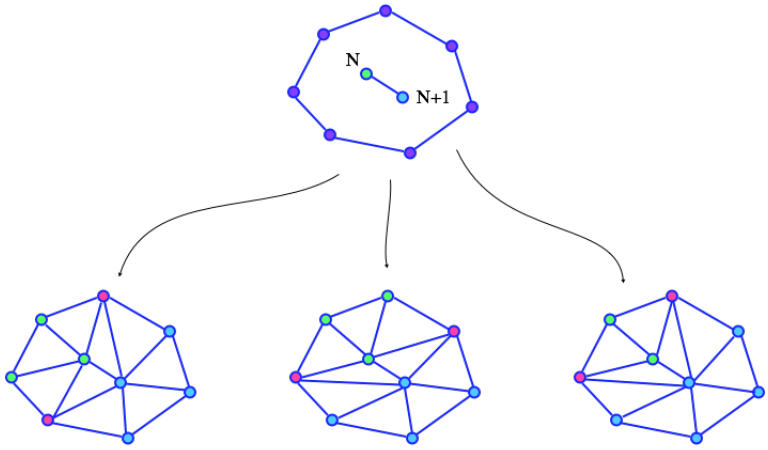

Figure 6.9. Three examples of possible triangulation schemes, given two beads surrounded by a convex hull of connected beads. The hinge beads are colored in purple, the beads connected to the N-th alone are colored in green, those connected to $N+1$ only are colored in light blue.

6.4.3 Numerical tests

First, numerical simulations on membranes in the grand-canonical ensemble have been performed with no external forces, so that after equilibration the number of beads in the membrane remains constant (within fluctuations), and the surface tension has been calculated from the spectrum of height fluctuations at equilibrium as done before. The simulated membrane patch was initially made of 30×30 nodes put on a regular triangular network of size $\ell_{0,mb}$; the bond-flipping probability has been set equal to $\psi_{bf} = 0.25$ and three different values for the effective fugacity z^{eff}, input parameter for the model appearing the expression for the acceptance probability (see Appendix B.3, Eqs. (B.12) to (B.14)), have been used: 5, 13 and 30. The relationship between z^{eff} and the resulting membrane tension has indeed been verified to be logarithmic,

$$\Sigma = \alpha_1 \ln\left(\frac{\alpha_2}{z^{eff}}\right) \tag{6.63}$$

as expected from Eq. (6.57); Fig. 6.10 shows the surface tension as obtained by the height fluctuation analysis at equilibrium (blue points) together with the latter best-fit function (dashed line). The numerical values of α_1 and α_2 have been found to be 0.653 ± 0.004 $(k_B T \ell_{0,mb})^{-2}$ and 78.4 ± 0.9 respectively. Regarding at Eq. (6.57), the factor α_1 would be expected to be equal to $\frac{1}{\beta a}$, with a area per added node. Loosely speaking, we would expect a value between $\frac{1}{\beta \ell_{max}^2} \approx 0.6$ $(k_B T \ell_{0,mb})^{-2}$ and $\frac{1}{\beta \ell_{min}^2} \approx 2$ $(k_B T \ell_{0,mb})^{-2}$, and the value we get fits within this range. As for α_2, it is

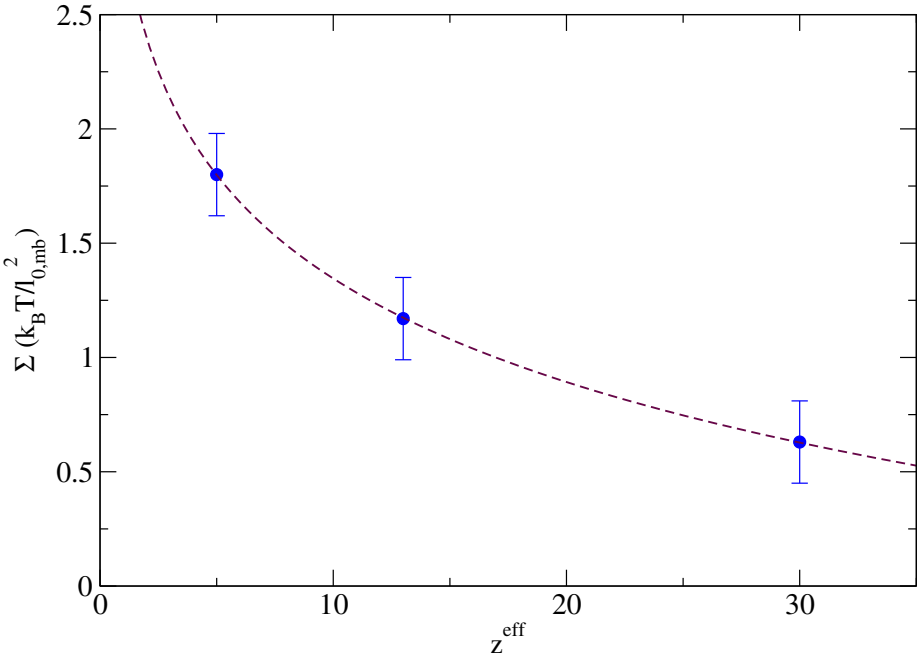

Figure 6.10. Membrane surface tension in the grand canonical ensemble as a function of the input fugacity; the blue points are the values obtained from the numerical simulations, while the dashed line is the fitting function Eq. (6.63) with $\alpha_1 = (0.653 \pm 0.004)\ k_B T \ell_{0,mb}^{-2}$ and $\alpha_2 = 78.4 \pm 0.9$.

related to the critical chemical potential μ_c (see Eqs. (B.14) and (6.57)) and it is not easy to predict a reasonable value for this quantity. As for the bending modulus λ_b^{eff}, the following values have been found through the height fluctuations analysis:

z^{eff}	λ_b^{eff} $(k_B T)$
5	13.8 ± 0.2
13	14.0 ± 0.2
30	13.6 ± 0.2

Successively, to induce the formation of a finger-like protrusion on a larger membrane patch ($N_{nodes} = 6400$) a local upward force on its central beads has been applied. In this case three nodes – at $(0, 0)$, $(0, L_z/2)$ and $(L_y/2, 0)$, plus periodic images – have been kept fixed, in order to avoid a shift along x of the membrane as a whole. The tubular deformation can be induced *e.g.* by applying an extra force on one of the membrane beads, or by pushing an extra sphere from beneath the membrane upwards. I chose this second option: the extra sphere was initially

put under the membrane patch, in its center, and a purely repulsive Lennard-Jones potential has been taken for the interaction between this extra sphere and the above membrane beads:

$$V_{es}^{\mathrm{EV}}(r_{is}) = \begin{cases} 4\epsilon_{es}\left[\left(\dfrac{r_{is}}{\sigma_{es}}\right)^{12} - \left(\dfrac{r_{is}}{\sigma_{es}}\right)^{6}\right] + V_{cut-off} & \text{if } r_{is} \leq r_{cut-off}, \\ 0 & \text{otherwise.} \end{cases} \tag{6.64}$$

where r_{is} is the distance between the i-th node and the sphere center, $\sigma_{es} = \frac{4}{3}\ell_{0,mb}$ and $V_{cut-off}$ the potential at the cut-off distance, $r_{cut-off} = 2^{1/6}\sigma_{es}$, which is the position of the minimum of the Lennard-Jones potential. The sphere was pushed upwards of a small step δ as the gap between the position of its center plus δ and the overlying beads was of sufficient size (*i.e.* larger than σ_{es}). The sphere pulling was interrupted when the tubule had reached a satisfying height ($\sim 40 \div 50\ \ell_{0,mb}$). This procedure led to the formation of a tubule, see Fig. 6.11 for an illustrative sketch; in the figure, a side view of the protrusion is shown (enlarged top view in the inset). An ensemble of 24 trajectories has been generated and, once let the system equilibrates after the sphere has been stopped, the average radius of the protrusion has been calculated averaging both over time and trajectories using the following procedure: I considered a section $20\ \ell_{0,mb} = x_{min} < x < x_{max} = 40\ \ell_{0,mb}$ (indicated in figure by the two horizontal dashed lines), divided it into slices of height $\delta x = \frac{2}{3}\ell_{0,mb}$ and at any time, for each slice, I calculated the center of mass of the beads belonging to it and the average radius as the average distance of every bead from this center. Then I averaged the values obtained for every slice, and then averaged over time. The value I get with this procedure, picking as effective fugacity $z^{eff} = 13$, is:

$$\langle R_0 \rangle = (2.430 \pm 0.003)\ \ell_{0,mb}. \tag{6.65}$$

In the inset of Fig. 6.11 an enlarged top view is shown together with a circle of radius $\langle R_0 \rangle$, superimposed to the larger-nodes-density area. This value of the radius, according to Eq. (5.47) and using an average bending modulus $\lambda_b^{eff} = (13.8 \pm 0.4)\ k_B T$, gives a surface tension equal to

$$\Sigma = (1.17 \pm 0.07)\ \frac{k_B T}{\ell_{0,mb}^2} \tag{6.66}$$

in perfect agreement with results shown in Fig. 6.10.

Before moving to discuss membrane-filaments simulations, let's notice once more that computing the surface tension with three different methods – spectrum of height fluctuations, virial and tubule radius – and getting results in so nice agreement with each other is to be considered a remarkable achievement of this part of the work, since so far only weak numerical evidence of the equivalence between these methods had been provided in the literature [95].

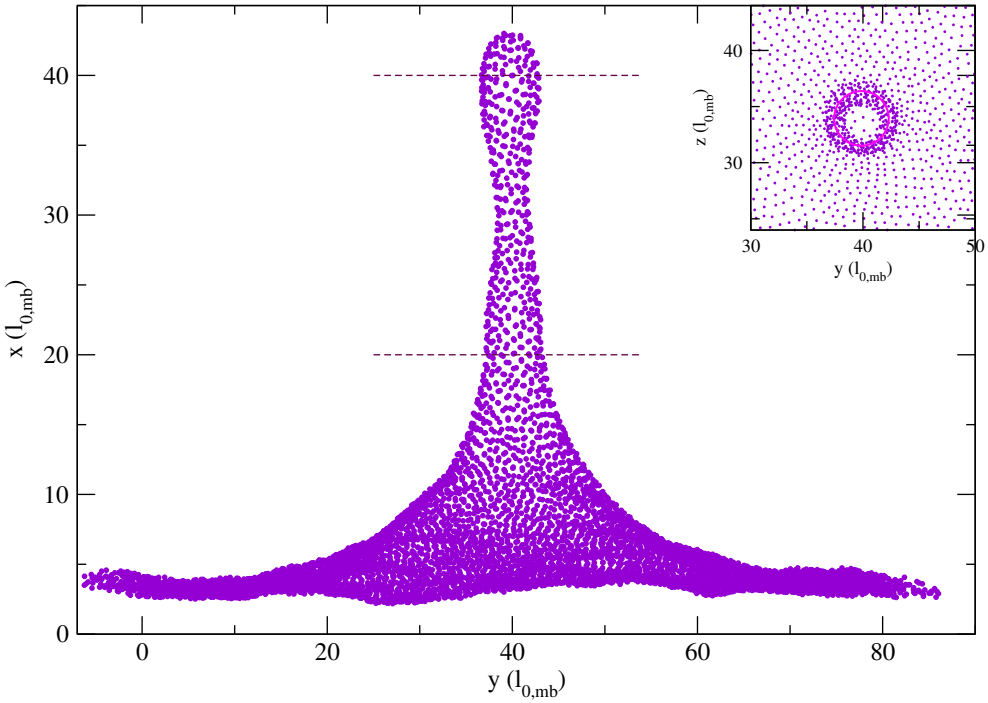

Figure 6.11. Filopodium-like protrusion generated by pushing a sphere beneath the membrane patch ($N_{nodes} = 6400$, simulation parameters reported in Tables 6.1 and 6.3). Inset: top view of the protrusion; the solid line is a circle of radius $\langle R_0 \rangle = 2.43\ \ell_{0,mb}$ calculated as a time and ensemble (*i.e.* over trajectories) average. The horizontal dashed lines indicate the region used for the calculation of $\langle R_0 \rangle$.

6.5 Membrane-filaments simulations

Now that all the ingredients for the membrane simulation have been settled, we can proceed with simulating (membrane+filaments) systems; to do so, the filaments model needs to be specified.

6.5.1 MD simulation of living filaments

Actin filaments, growing beneath the membrane, are modeled as discrete chains of N_{mon} monomers linked to each other by permanent bonds, except for the last monomer that can detach from the chain by depolymerization. Polymerization, on the other hand, implies the addition of a monomer at the end of the chain. The bonding potential is taken to be harmonic,

$$U^{ac}_{bond}(r_{i,i\pm1}) = \frac{1}{2}k^{ac}_{bond}\left(r_{i,i\pm1} - d_0\right)^2 \tag{6.67}$$

where $r_{i,i\pm1}$ is the distance between monomer i and $i \pm 1$ (to which i is bonded) and d_0 is the filament incremental size per added monomer. (Superscript ac stands for *actin*). Adjacent monomers are also subject to the bending potential

$$U^{ac}_{bend}(\theta_{i-1,i,i+1}) = k^{ac}_{bend}\left(1 - \cos\theta_{i-1,1,i+1}\right) \tag{6.68}$$

where $\theta_{i-1,i,i+1}$ is the angle between the bonds $\mathbf{r}_{i+1} - \mathbf{r}_i$ and $\mathbf{r}_i - \mathbf{r}_{i-1}$. This is essentially equal to Eq. (2.16), the wormlike chain bending energy (up to a constant). The bending modulus is related to the actin filaments persistence length, $\ell_p = d_0 \frac{k^{ac}_{bend}}{k_B T}$; taking a realistic persistence length ($\ell_p \sim 5\times10^3 d_0$) allows to simulate actin filaments, while a much larger ℓ_p will be chosen to simulate rigid filaments. Moreover, (non-bonded) excluded volume interactions with the other monomers are taken into account:

$$U^{ac}_{\text{EV}}(r_{ij}) = 4\epsilon_{ac}\left[\left(\frac{\sigma_{ac}}{r_{ij}}\right)^{12} - \left(\frac{\sigma_{ac}}{r_{ij}}\right)^{6}\right]\Theta(r^{ac}_{cutoff} - r_{ij}) \qquad \text{for } |i-j| \geq 3 \tag{6.69}$$

and a similar potential has been taken between monomers belonging to different filaments, to avoid filaments reciprocal penetration. The dynamics of monomers composing the filaments has been assumed to be described by a Langevin equation analogous to Eq. (6.14):

$$m_{ac}\frac{d^2\mathbf{r}_i}{dt^2} = -\zeta_{ac}\frac{d\mathbf{r_i}}{dt} + \mathbf{F}_i(t) + \xi(t) \tag{6.70}$$

where m_{ac} is the actin monomer mass, ζ_{ac} is the solvent friction coefficient, $\mathbf{F}_i = -\nabla_i E_i = \mathbf{F}^{bend}_i + \mathbf{F}^{bond}_i + \mathbf{F}^{\text{EV}}_i$ the total force acting on the monomer and ξ white noise with

$$\langle\xi_\alpha(\mathbf{t})\rangle = 0 \qquad \langle\xi_\alpha(t)\xi_\beta(t')\rangle = 2k_B T\zeta_{ac}\delta_{\alpha\beta}\delta(t-t') \tag{6.71}$$

where $\alpha, \beta = x, y, z$. This set of equations has been integrated numerically following the same algorithm presented in Appendix B.2 [111].

Additionally to the Langevin dynamics, filaments have been assumed to grow and shrink in time by gaining or loosing a monomer by polymerization and depolymerization, occurring with probability per unit of time U_0 and W_0 respectively. The ratio between the two is the reduced monomer density $\hat{\rho}_1$, as usual (see Part I). Free monomers are implicit in the model: they are not followed in time, but it is assumed that the free monomer density stays constant, fixed by the phenomenological rates. In other words, any time a filament tries to polymerize, a free monomer is assumed to be at its disposal. This is at variance with the method proposed in [116], where a more sophisticated (de)polymerization scheme was used, but with a much lower efficiency.

This is how the (de)polymerization moves work: Polymerization and depolymerization are assumed to be Poisson processes with rates U_0 and W_0 respectively, so that the distribution function of the waiting times between successive events is [58]

$$P_p(\tau_p) = 1 - \exp\left(-U_0\tau_p\right) \qquad \text{and} \qquad P_d(\tau_d) = 1 - \exp\left(-W_0\tau_d\right). \tag{6.72}$$

If h is the timestep (with hU_0, $hW_0 \ll 1$), the probability that in one timestep a polymerization or depolymerization occurs is:

$$P_p(h) \approx hU_0 \qquad \text{and} \qquad P_d(h) \approx hW_0 \tag{6.73}$$

where the exponential has been Taylor expanded to first order. At each timestep a random number, ξ, is generated and compared to the (de)polymerization probability (cumulative distribution):

1. if $\xi \leq N_f W_0 h$ then depolymerization is attempted for one of the filaments randomly chosen;
2. if $N_f W_0 h < \xi \leq N_f(W_0 + U_0)h$ then polymerization is attempted for one of the filaments randomly chosen;
3. otherwise no polymerization nor depolymerization is attempted,

where it has been taken into account the fact that there are N_f filaments that can undergo polymerization or depolymerization.

Considering one of the N_f filments and denoting by $\mathcal{I}$ the state of the filament with N monomers and by $\mathcal{J}$ the state of the filament with $N+1$ monomers, the detailed balance reads:

$$\pi(\mathcal{I})\; T_p(\mathcal{I} \to \mathcal{J})\; A_p(\mathcal{I} \to \mathcal{J}) = \pi(\mathcal{J})\; T_d(\mathcal{J} \to \mathcal{I})\; A_d(\mathcal{J} \to \mathcal{I}) \tag{6.74}$$

with $\pi(\mathcal{I}) \propto \exp\left(-\beta E(\mathcal{I})\right)$ Boltzmann weight. $E(\mathcal{I})$ is the energy of state $\mathcal{I}$ and $E(\mathcal{J})$ is the energy of the state $\mathcal{J}$, which differ only by terms involving the added monomer, all the others being in the same positions:

$$E(\mathcal{I}) = \sum_{i=1}^{N-1} U^{ac}_{bond}(r_{i,i+1}) + \sum_{i=2}^{N-1} U^{ac}_{bend}(r_{i-1,i,i+1}) + \frac{1}{2}\sum_{|i-j|>3} U^{ac}_{\text{EV}}(r_{ij}) - N\epsilon_0 + \frac{1}{2}\sum_{i=1}^{N} m\; v_i^2 \tag{6.75}$$

$$E(\mathcal{J}) = E(\mathcal{I}) + U^{ac}_{bond}(r_{N,N+1}) + U^{ac}_{bend}(r_{N-1,N,N+1}) + U^{ac}_{\text{EV}}(N+1) - \epsilon_0 + \frac{1}{2} m\; v^2_{N+1} \tag{6.76}$$

where ϵ_0 is a bonding energy term accounting for the energy gain due to polymerization (in supercritical conditions), $\frac{1}{2}m\ v_i^2$ the kinetic energy of monomer i and $U_{\rm EV}^{ac}(N+1)$ is the EV energy of monomer $N+1$. $T_p(\mathcal{I}\to\mathcal{J})$ is the a-priori probability of attempting the polymerization move, $T_d(\mathcal{J}\to\mathcal{I})$ of attempting the depolymerization. Given the above energies Eqs. (6.75) and (6.76), the detailed balance equation is satisfied by the following acceptances and a-priori probabilities:

$$T_p = hU_0 \exp\left(-\beta\left(U_{bond}^{ac}(r_{N,N+1}) + U_{bend}^{ac}(r_{N-1,N,N+1}) + \frac{1}{2}m\ v_{N+1}^2\right)\right) \tag{6.77}$$

$$T_d = hW_0 \tag{6.78}$$

$$A_p = \min\left[1; \exp\left(-\beta U_{\rm EV}^{ac}(N+1)\right)\right] \tag{6.79}$$

$$A_d = \min\left[1; \exp\left(\beta U_{\rm EV}^{ac}(N+1)\right)\right] \tag{6.80}$$

The ratio U_0/W_0 (or W_0/U_0) cancels with the factor $\exp(-\beta\epsilon_0)$ (or $\exp(\beta\epsilon_0)$) which is contained in the ratio between $\pi(\mathcal{I})$ and $\pi(\mathcal{J})$, related to the reversible work of the polymerization force.

Polymerization move

The filament to be grown is selected at random. The polymerization move is attempted only if the filament is shorter than a maximum allowed size.

To get the position of the (attempted) added monomer, the algorithm samples the bond length, the bending angle (notice that $\theta = 0$ for aligned bonds) and the angle ϕ around the direction of the last bond, $\mathbf{t}_{N-1} = \mathbf{r}_N - \mathbf{r}_{N-1}$, according to the following probability distributions:

$$P(r) = \frac{1}{\sqrt{2\pi\beta k_{bond}^{ac}}} \exp\left[-\frac{1}{2}\beta k_{bond}^{ac}\left(r-d\right)^2\right] \tag{6.81}$$

$$P(\cos\theta) = \frac{\beta k_{bend}^{ac}}{1-\exp\left(-2\beta k_{bend}^{ac}\right)} \exp\left[-\beta k_{bend}^{ac}\left(1-\cos\theta\right)\right] \tag{6.82}$$

$$P(\phi) = \frac{1}{2\pi} \tag{6.83}$$

using the inversion generating method [60]:

$$r = d + \xi\sqrt{\frac{k_B T}{2k_{bond}^{ac}}} \tag{6.84}$$

$$\cos\theta = 1 + \frac{k_B T}{k_{bend}^{ac}} \ln\left[\exp(-2\beta k_{bend}^{ac}) + \eta\left(1-\exp\left(-\beta k_{bend}^{ac}\right)\right)\right] \tag{6.85}$$

$$\phi = 2\pi\psi \tag{6.86}$$

with ξ normally distributed random number (obtained by Box-Muller method) and η, ψ uniformly distributed in $[0,1)$. The last two lines are got by putting the random number equal to the cumulative function of $P(\cos\theta)$ and $P(\phi)$ respectively. Being k_{bend}^{ac} very large, in practice $\cos\theta = 1 + \frac{k_B T}{k_{bend}^{ac}} \ln\eta$.

To get the coordinate of the added monomer in the global reference system, we define a local reference system, centered at $\mathbf{r}_N$ and with the abscissa axis along the

direction of $\mathbf{t}_{N-1} = \mathbf{r}_N - \mathbf{r}_{N-1}$. In the translated system this vector is characterized by the following polar and azimuthal angles:

$$\theta_{N-1} = \arccos\left(\frac{z_N - z_{N-1}}{t_{N-1}}\right) \tag{6.87}$$

$$\phi_{N-1} = \arctan\left(\frac{y_N - y_{N-1}}{x_N - x_{N-1}}\right) \tag{6.88}$$

The rotation which leads the x axis to superpose to this direction is made up of a rotation around the z axis of ϕ_{N-1} and then a rotation around the y axis of $\frac{\pi}{2} - \theta_{N-1}$. The corresponding matrix will be:

$$\begin{aligned}\mathbf{R}_y\mathbf{R}_z &= \begin{bmatrix} \cos\left(\frac{\pi}{2} - \theta_{N-1}\right) & 0 & \sin\left(\frac{\pi}{2} - \theta_{N-1}\right) \\ 0 & 1 & 0 \\ -\sin\left(\frac{\pi}{2} - \theta_{N-1}\right) & 0 & \cos\left(\frac{\pi}{2} - \theta_{N-1}\right) \end{bmatrix} \begin{bmatrix} \cos\phi_{N-1} & -\sin\phi_{N-1} & 0 \\ \sin\phi_{N-1} & \cos\phi_{N-1} & 0 \\ 0 & 0 & 1 \end{bmatrix} \\ &= \begin{bmatrix} \sin\theta_{N-1}\cos\phi_{N-1} & -\sin\theta_{N-1}\sin\phi_{N-1} & \cos\theta_{N-1} \\ \sin\phi_{N-1} & \cos\phi_{N-1} & 0 \\ -\cos\theta_{N-1}\cos\phi_{N-1} & \sin\phi_{N-1}\cos\theta_{N-1} & \sin\theta_{N-1} \end{bmatrix}. \end{aligned} \tag{6.89}$$

The kinetic energy of the new monomer is sampled from the Maxwell-Boltzmann distribution. Once the global coordinates are known, the energy of the new monomer is computed and the acceptance probability A_p is calculated according to Eq. (6.79). Then the acceptance test is performed as usual: a random number α is sampled from the uniform distribution in $[0, 1)$, and if $\alpha < A_p$ the move is accepted, otherwise it is rejected.

Depolymerization move

The filament to be shrunk is selected at random. The depolymerization is tried only if the filament has more than three monomers. This move is much more straightforward than polymerization: the energy of the last monomer and, from it, the acceptance probability are calculated, the acceptance check is performed by extracting a random number α from the uniform distribution in $[0, 1)$, and if $\alpha < A_d$ the move is accepted, otherwise it is rejected.

Numerical tests on this scheme for the (de)polymerization events have been conducted, as reported in Appendix B.4, proving that it is equivalent to – yet much nimbler than – the more cumbersome procedure proposed in [116].

6.5.2 Numerical simulations of filaments pushing against a membrane

Once tested that both the algorithm for the membrane and the algorithm for the filaments gave satisfactory results, simulations of (membrane + filaments) systems have been performed. To do so, a local excluded-volume interaction between the

membrane beads and the actin monomers has been introduced in the form of a purely repulsive Lennard-Jones potential:

$$U_{\text{EV}}^{ac\text{-}mb}(r_{i_nj}) = 4\epsilon_{ac}\left[\left(\frac{\sigma_{ac\text{-}mb}}{r_{i_nj}}\right)^{12} - \left(\frac{\sigma_{ac\text{-}mb}}{r_{i_nj}}\right)^{6}\right]\Theta(r_{cutoff}^{ac\text{-}mb} - r_{i_nj}) \tag{6.90}$$

where r_{i_nj} is the distance between the i-th monomer belonging to the n-th filament and the j-th membrane node and $r_{cutoff}^{ac\text{-}mb} = 2^{1/6}\sigma_{ac\text{-}mb}$. This potential determines an extra force on some of the membrane beads and filament monomers, to be included in the equations of motion, and it must be also considered in the acceptance probability for both the (de)polymerization moves and the GC insertion/deletion moves for the membrane beads. An additional list for the membrane beads and filament monomers closer than a cutoff distance $r_{list}^{ac\text{-}mb}$ is created and regularly updated to efficiently calculate forces. The values of membrane and actin parameters are reported in Tables 6.1 to 6.4.

Several simulations for different values of N_f and staggered and unstaggered disposition of the seeds have been performed, both for rigid and flexible filaments, to appreciate the influence of filament flexibility. In the rigid case, as mentioned, the same model as for flexible filaments has been used but with a persistence length artificially increased by a factor 10^3, in order to eliminate bending fluctuations[2].

The membrane patch has been taken by 30×30 nodes, at an initial height $x_0 = 10d_0$ over the filament grafting plane ($x = 0$), $d_0 = 2.7$ nm actin monomer half diameter (see Part I). The transverse coordinates of filaments' seeds are randomly distributed on the yz plane, inside a circle centered on the membrane patch center and with radius increasing as $\sqrt{N_f}$. The distance between any two seeds is checked to be larger than a minimum distance equal to $2d_0$. At the beginning of the simulation, all the filaments are composed by 3 monomers and then let (de)polymerize. As filaments grow, they reach the overlying membrane and start pushing it locally with a force equal to the gradient of Eq. (6.90). If this force is strong enough to overcome the membrane resistance, a membrane protrusion embedding the growing filaments should form.

In the following, details on the simulations results shall be given.

Staggered bundles: flexible *vs* rigid filaments

Simulations of bundles with different $N_f \geq 1$ and staggered seeds disposition (see Eq. (1.17)) have been performed; in any case an initial unhindered growth (before reaching the membrane height) has been observed. After that stage, in the single filament case the growth stopped: *a single filament results to be not sufficient to create a protrusion in the membrane*, in either flexible and rigid case. This agrees with Mogilner's prediction that a minimum number of filaments is needed in order

[2] We observe that the small contour length fluctuations (related to bond stretching between adjacent monomers) are present in both the flexible and the "rigid" model used in our experiments. We could have alternatively treated a strictly rigid model freezing all vibrational modes by considering the straight alignment of monomers at equal distances d_0 as a time-independent external field acting on the membrane degrees of freedom between the occurrence of instantaneous (de)polymerizing steps: this approach should be preferred in future studies as it simplifies the rigid filament model and corresponds better to the concept of a rigid filament.

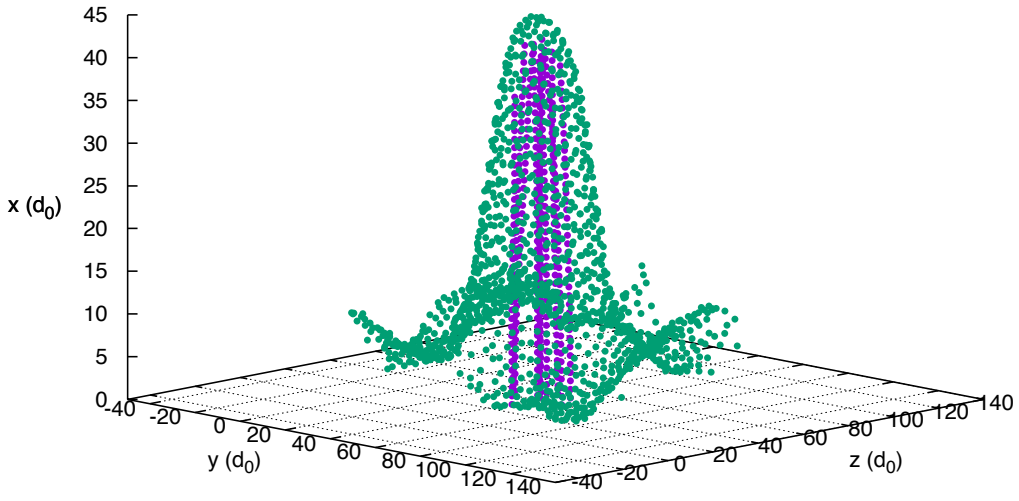

Figure 6.12. Illustrative sketch of a filopodium generated by $N_f = 10$ filaments, in the case of a staggered flexible bundle. Similar configurations have been observed for other N_f either flexible or rigid filaments.

to protrude a filopodium (see Section 4.3, [4]). Yet, bundles with $N_f = 3$ are already large enough, in the present simulation model, to create a protrusion. Fig. 6.12 shows an illustrative sketch of a filopodium generated by $N_f = 10$ flexible filaments in the staggered case. Similar conformations have been observed for other N_f either flexible or rigid filaments.

Fig. 6.13 shows the average bundle length (averaged over the filaments and different trajectories) as a function of time for four values of N_f (1, 3, 7 and 10), for both rigid and flexible filaments: for $N_f > 1$, the average bundle length grows above the membrane initial height, creating a protrusion, and the growth appears faster as N_f increases. Interestingly enough, again flexible filaments appear faster than rigid ones, as found in Part I of this thesis, and as can be seen from the flexible-rigid filaments comparison in each panel of Fig. 6.13.

Unstaggered bundles: flexible *vs* rigid filaments

Simulation of unstaggered bundles, *i.e* with all the seeds lined up at the yz plane ($h_n = 0\ \forall n$), for $N_f = 3$, 7 and 10 have been realized for both flexible and rigid filaments, finding results similar to the staggered case: the first observation to be made is that the larger the bundle the faster the growth, the second one is that flexible filaments also grow faster than rigid, at given N_f. The deviation of the flexible bundles growth from the rigid behavior is in this case even more pronounced than in the staggered bundles case, as it can be seen in the comparison shown in Fig. 6.14.

In both the staggered and the unstaggered cases, no escaping filament has been observed. This is due partly to the enveloping membrane that keeps the filaments

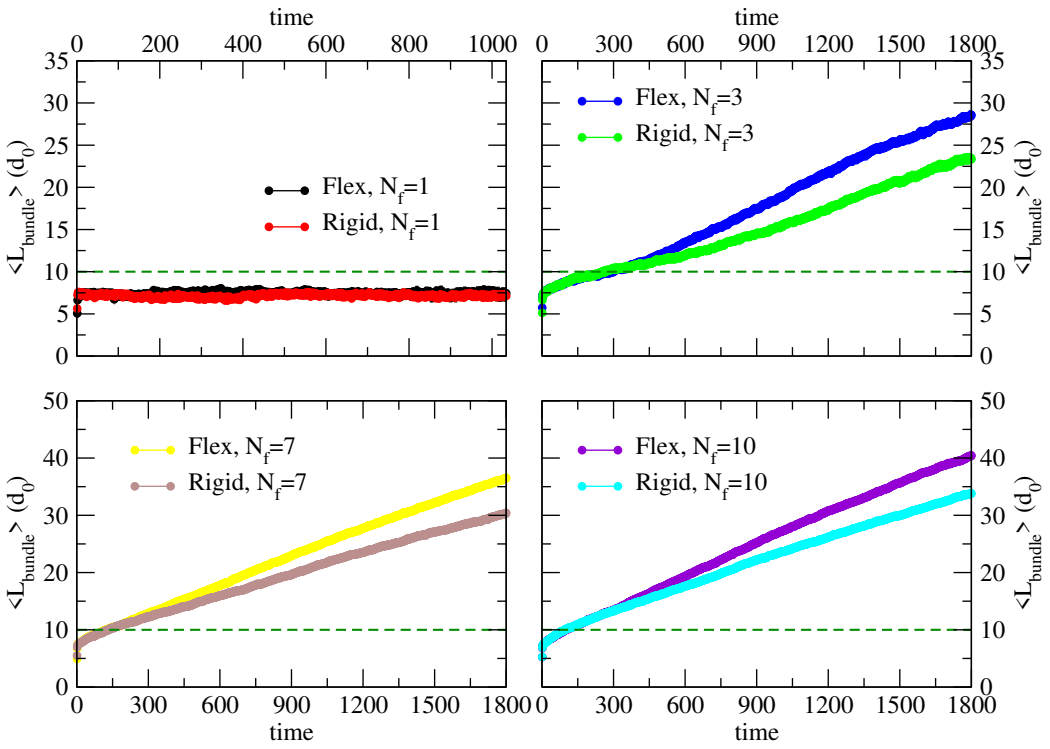

Figure 6.13. Average bundle length at the indicated N_f values as a function of time, for *staggered* bundles. For $N_f = 1$ the filament average length remains below the membrane height ($x_0 = 10d_0$), for $N_f > 1$ the bundles grow in time above the initial membrane height, creating a protrusion. As N_f increases, the average bundle length grows faster with time. Also, comparison between flexible and rigid filaments is shown: flexible filaments are always faster than rigid ones. A horizontal dashed line is located at the initial membrane height.

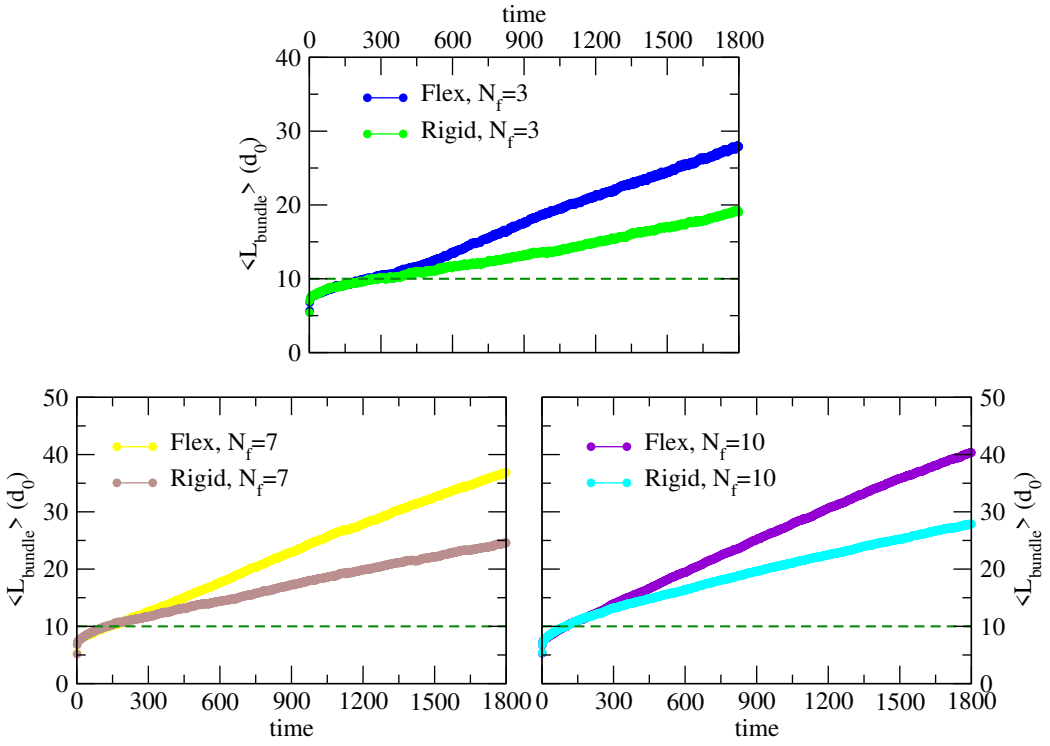

Figure 6.14. Average bundle length at the indicated $N_f > 1$ values as a function of time, for *unstaggered* bundles. Bundles grow in time above the initial membrane height, creating a protrusion. As N_f increases, the average bundle length grows faster with time. Again, flexible filaments are always faster than rigid ones. A horizontal dashed line is located at the initial membrane height.

straight and partly to the choice of the distance between the grafting plane and the membrane initial height ($10d_0$): this implies that filaments meet the above membrane when their size is still too small to make flexibility effects manifest. Indeed, in the $N_f = 1$ staggered case, the filament remains stalled without growing parallel to the membrane. If the size were close to the escaping limit length, some escaping filament would have probably been detected, as reported in [19].

Staggered *vs* unstaggered bundles

Fig. 6.15 shows the same data as before, but comparing staggered/unstaggered bundles behaviors separately for flexible and rigid filaments.

It is evident that flexible bundles' behavior (left panels) is to first approximation independent of the seeds disposition: flexibility allows filaments to bend and more easily accommodate monomers intercalation at the tip-membrane gap, in addition to the membrane flexibility itself.

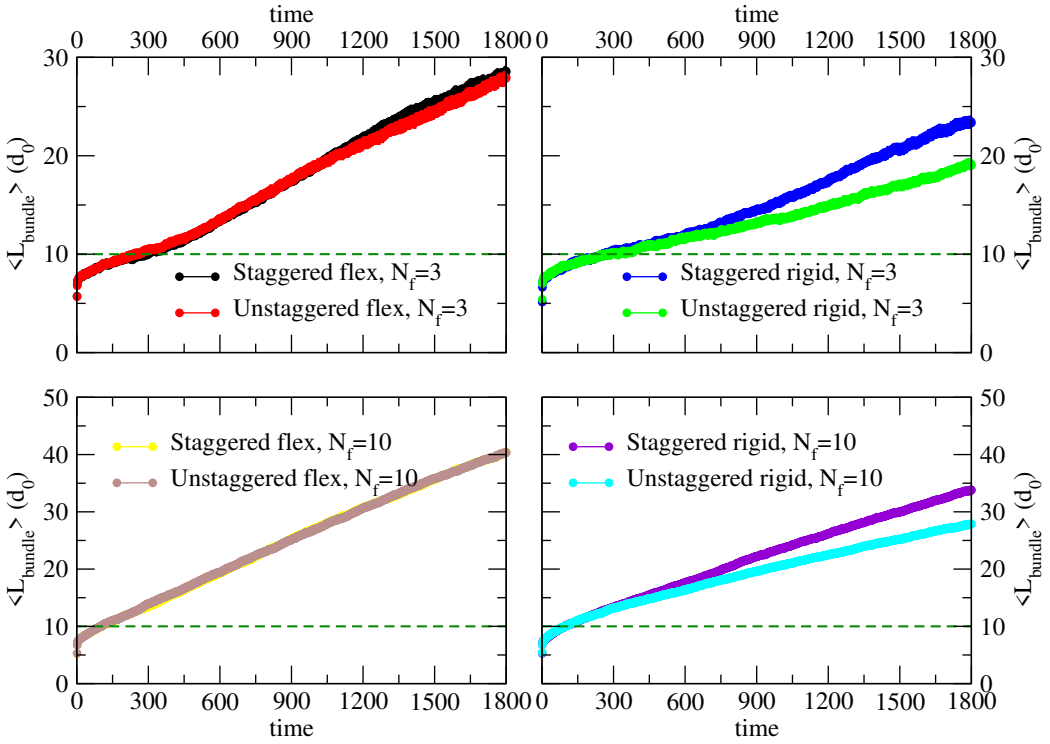

Figure 6.15. Comparison between the average bundle length as a function of time between staggered and unstaggered bundles, both for the flexible and the rigid case: in the former, there is no appreciable difference between the staggered and unstaggered dispositions, while in the latter the staggered bundles grow faster than the unstaggered. A horizontal dashed line is located at the initial membrane height.

In the case of rigid filaments (right panels), staggered bundles are evidently faster than the corresponding unstaggered: in the case of rigid filaments the subsidy effect emerging in the brownian ratchet model (see Section 1.3.2) plays again an important role, despite of the membrane fluctuations.

6.6 Concluding remarks

In this chapter, I have presented the simulation scheme that has been developed to reproduce the dynamics of a cell membrane, alone or pushed by polymerizing filaments. The main features of the model are: i. the membrane discretization into a triangulated surface; ii. the bond-flipping procedure that leads to a correct reproduction of the fluid character of the membrane; iii. the grand-canonical insertion/removal moves, which allow for membrane non-trivial deformations as the onset of a cylindrical protrusion.

It has been shown that the membrane surface tension – which determines, together with the bending modulus, the membrane resistance to external deforming forces – can be calculated via several methods, namely height fluctuations spectrum analysis, virial calculation and measurement of the radius of a tube pulled out of a membrane patch. The first remarkable result of this part of the work has been the numerical evidence of the equivalence of these three method: the values obtained by the three methods are in perfect agreement with each other, which is quite an unprecedented result. This result has been also taken as a validation of the simulation procedure for the membrane, providing a fair level of confidence in the validity of this coarse-grained model for this complex system.

As for the filaments, they have been included in the simulations by modeling them as chains of monomers linked by harmonic bonds and subject to excluded volume forces and bending interactions tending to keep them straight. This part of the code has been tested by means of simulations of bundles at equilibrium in contact with a rigid wall in an optical trap set up and comparing results with those presented in Part I of this thesis and in ref. [116]. The improvement with respect to the method presented there, is related to the much larger efficiency of the (de)polymerizations procedure introduced here.

Preliminary simulations of membrane+filaments systems have been performed, and the results presented here seem to confirm that filament flexibility essentially increases the bundle velocity also in the formation of filopodial protrusions from beneath the membrane: Figs. 6.13 to 6.15 show the average bundle length as a function of time comparing flexible and rigid bundles with $N_f = 1$, 3, 7 and 10 for staggered and unstaggered seeds dispositions, suggesting the following considerations:

- In any case, *flexible bundles grow faster than rigid ones.* Filament flexibility is an important property, also when filaments grow in contact with a fluctuating flexible membrane.

- The *seeds disposition plays a role only for rigid filaments*: staggered rigid bundles protrude faster than unstaggered ones, showing that also in the presence of membrane fluctuations, the "subsidy" effect proposed for the SR model (see Part I).

- In the case of flexible bundles, *escaping filaments do not appear* when it is enveloped by the membrane. This is also due to the fact that filaments meet the membrane when their size is $9 \div 11$, too short for the flexibility effects to manifest, as discussed in Part I; if they had a size close to the escaping threshold size, filaments growing parallel to the (flat) membrane would have probably been observed.

These results on membrane-filaments systems are still preliminary, but let envisioning further developments, possibly leading to more quantitative results. Further and more refined data analysis could be used to extract a velocity-load relationship for the filopodium elongation, which could be interestingly compared to the rigid wall case. Moreover, a length dependence of the free monomer density could be introduced to reproduce the diffusion-limited elongation suggested by [4]. Before concluding, it should be noticed that these arguments are implicitly based on a timescale separation between the membrane relaxation and the filaments dynamics, so that the membrane can be considered at equilibrium between two polymerization

events. This timescale separation, which has been basically assumed so far, still needs to be verified in depth and once it is done, this model will provide a successful method to simulate this complex system and extract informations on its physical properties otherwise inaccessible.

In the following and last section, the units and values of the physical parameters chosen for the simulations so far presented are resumed in four tables.

6.7 Simulations parameters

Table 6.1. Unit system for the MD program - actin filaments against the membrane

Physical quantity	**Unit**	**Comments**
Energy	$k_BT = 4.14 \times 10^{-21}\ J$	Thermal energy at standard temperature.
Length	$d_0 = 2.7\ nm$	Actin monomer size.
Mass	$m_{ac} = 42\ kDa = 6.97 \times 10^{-23} kg$	Actin monomer mass. This fixes the time unit at $u_t = d_0\sqrt{\frac{m_{ac}}{k_BT}} = 0.35\ ns$. We take, as in [116], a monomer mass sensibly larger than the real one, namely $m_{ac}^{mod} = 2.8 \times 10^{-15} kg$, fixing the time unit at $u_t = d_0\sqrt{\frac{m_{ac}}{k_BT}} = 2.22\ \mu s$

Table 6.2. F-actin parameters.

Physical quantity	**Unit**	**Comments**
Depolymerization rate	$W_0 = 0.05 u_t^{-1}$	This value corresponds to $W_0 = 2.3 \times 10^3 s^{-1}$, the same enhanced rate used in [116]. The chemical timescale is thus $\tau_{chem} = 1/W_0 = 200 u_t$.
Free monomers reduced density	$\hat{\rho}_1 = 10$	This value fixes the polymerization rate to $U_0 = \hat{\rho}_1 W_0 = 0.5 u_t^{-1}$.
Persistence length	$\ell_p = 14.5$ μm$= 5370$ d_0	Numerical simulations of rigid filaments have been done using a thousandfold larger persistence length.
Force constant (bonding)	$k_{bond}^{ac} = 4000$ $k_B T/d_0^2$	The resulting vibrational time is $\tau_{vib} = \sqrt{\frac{m_{ac}}{k_{bond}^{ac}}} = \frac{\sqrt{k_B T}}{d_0} \frac{1}{\sqrt{k_{bond}^{ac}}}$ $u_t = 0.016$ u_t.
Friction coefficient	$\zeta_{ac} = 8$ $k_B T u_t/d^2$	The typical radius of a G-actin protein is $R_{ac} = 2.9nm = 1.074 d_0$. From the Stokes law, $\xi_{ac} = 6\pi\eta R_{ac} \simeq 5.5 \times 10^{-11} Js/m^2$, with $\eta = 0.001$ Js/m^3. The inertial time of free monomer is thus $\tau_{inertia}^{ac} \sim m_{ac}/\xi_{ac} \simeq 1.3$ ps$= 0.6 \times 10^{-6} u_t$. The value in the central column corresponds to that chosen in [116], which gives $\tau_{inertia}^{ac} = 0.125 u_t$. $\zeta_{ac} = 6\pi\eta R_{ac} \simeq 5.5 \times 10^{-11} Js/m^2$, with $\eta = 0.001$ $Js/m^3 = 0.0021$ $k_B T$ u_t/d_0^3.
LJ potential: depth of the potential well	$\epsilon_{ac} = 0.1$ $k_B T$	
LJ potential: σ	$\sigma_{ac} = 3.1$ d_0	The value of σ_{ac} comes from the usual estimation of the F-actin diameter of 8 nm.

Table 6.3. Membrane parameters.

Physical quantity	**Unit**	**Comments**
Bending modulus	$\lambda_b = 20\ k_BT$	
Force constant (bonding and EV)	$b = 80\ k_BT$	
Membrane length scale	$\ell_{0,mb} = 3\ d_0$	
Minimum beads distance	$\ell_{min} = 0.67\ \ell_{0,mb} = 2\ d_0$	
Maximum beads distance	$\ell_{max} = 1.33\ \ell_{0,mb} = 4\ d_0$	$\ell_{0,mb}$, ℓ_{min} and ℓ_{max} have been chosen to ensure that an actin bead does not cross the membrane.
Bead mass	$m_{mb} = 1$	
Friction coefficient	$\zeta_{mb} = 8\ k_BTu_t/d_0^2$	This value, together with m_{mb}, gives $\tau^{mb}_{inertia} = \tau^{ac}_{inertia} = 0.125\ u_t$.

Table 6.4. Membrane-filaments interaction parameters.

Physical quantity	**Unit**	**Comments**
LJ potential: depth of the potential well	$\epsilon_{ac,mb} = 1\ k_BT$	
LJ potential: σ	$\sigma_{ac,mb} = 0.5(\sigma_{ac} + \ell_{min}) = 2.89\ d_0$	
Time step	$h = 1 \times 10^{-5}\ u_t$	This value has to be much smaller than the fastest time scales in our system, $\tau^{ac}_{inertia} = 0.125\ u_t$ and $\tau_{vib} = 0.016\ u_t$. We get $\tau_{vib} = 1581\ h$ which is a reasonable number.

Appendices

Appendix A

Appendices to Part I

A.1 Calculation of the probability distribution of the tip position of a compressed wormlike chain in the weak bending limit

Let's consider a grafted worm-like chain of contour length $L_c \ll \ell_p$, grafted perpendicularly at one end to the yz plane, and let's define the stiffness parameter as $\epsilon = L_c/\ell_p$: the smaller ϵ, the stiffer the chain. Let's $\mathbf{t}(s)$ be the tangent unitary vector at arc length s, if ϵ is small (*weak bending limit*), its transverse components will be small as well. Let's parametrize $\mathbf{t}(s)$ as follows:

$$\mathbf{t}(s) = \frac{1}{\sqrt{1 + a_y^2 + a_z^2}} (1, a_y, a_z) \tag{A.1}$$

with boundary conditions $\mathbf{t}(0) = (1, 0, 0)$ (tangent at the origin perpendicular to the grafting yz plane) and $\dot{\mathbf{t}}(L_c) = (0, 0, 0)$ (vanishing curvature at the free end), or equivalently $\mathbf{a}(0) = (a_y(0), a_z(0)) = (0, 0)$ and $\dot{\mathbf{a}}(L_c) = (\dot{a_y}(L_c), \dot{a_z}(L_c)) = (0, 0)$.

Let's choose the following normal mode decomposition:

$$a_y(s) = \sum_{k=1}^{\infty} \tilde{a}_{y,k} \sin\left(\lambda_k \frac{s}{L_c}\right) \tag{A.2}$$

$$\tilde{a}_{y,k} = \frac{2}{L_c} \int_0^{L_c} ds\; a_y(s) \sin\left(\lambda_k \frac{s}{L_c}\right) \tag{A.3}$$

and similarly for z. The boundary condition $\dot{\mathbf{a}}(L_c) = (\dot{a_y}(L_c), \dot{a_z}(L_c)) = (0, 0)$ leads to $\lambda_k = \frac{\pi}{2}(2k - 1)$.

The x component of the tip position $r_x(L_c)$, at second order in a_y, a_z is:

$$\begin{aligned} r_x(L_c) &= \int_0^{L_c} ds\; t_x(s) = \int_0^{L_c} ds\; \frac{1}{\sqrt{1+a_y^2+a_z^2}} \approx \int_0^{L_c} ds\; \left[1 - \frac{1}{2}\left(a_y^2 + a_z^2\right)\right] \\ &= L_c - \frac{1}{2}\int_0^{L_c} ds \sum_{k,j=1}^{\infty} \sum_{\beta=y,z} \tilde{a}_{\beta,k}\tilde{a}_{\beta,j} \sin\left(\lambda_k \frac{s}{L_c}\right) \sin\left(\lambda_j \frac{s}{L_c}\right) \\ &= L_c - \frac{1}{2}\sum_{k,j=1}^{\infty} \sum_{\beta=y,z} \tilde{a}_{\beta,k}\tilde{a}_{\beta,j} \int_0^{L_c} ds\; \sin\left(\lambda_k \frac{s}{L_c}\right) \sin\left(\lambda_j \frac{s}{L_c}\right) \\ &= L_c - \frac{1}{2}\sum_{k,j=1}^{\infty} \left(\tilde{a}_{y,k}\tilde{a}_{y,j} + \tilde{a}_{z,k}\tilde{a}_{z,j}\right) \frac{L_c}{2}\delta_{k,j} \\ &= L_c - \frac{L_c}{4}\sum_{k=1}^{\infty} \left(\tilde{a}_{y,k}^2 + \tilde{a}_{z,k}^2\right). \end{aligned} \tag{A.4}$$

The bending hamiltonian $\beta H = \frac{\ell_p}{2}\int_0^{L_c} ds\; (\partial \mathbf{t}(s)/\partial s)^2$ can be evaluated to second order in a_y, a_z, using

$$\left(\frac{\partial \mathbf{t}}{\partial s}\right)^2 = \frac{1}{1+a_y^2+a_z^2}(\dot{a}_y^2 + \dot{a}_z^2) \approx \dot{a}_y^2 + \dot{a}_z^2 \tag{A.5}$$

with $\dot{a}_\beta = \sum_{k=1}^{\infty} \tilde{a}_{\beta,k}\frac{\lambda_k}{L_c}\cos\left(\lambda_k \frac{s}{L_c}\right)$ with $\beta = y, z$, so that

$$\begin{aligned} \beta H &= \frac{\ell_p}{2}\int_0^{L_c} ds\; \left(\frac{\partial \mathbf{t}(s)}{\partial s}\right)^2 \\ &= \frac{\ell_p}{2}\int_0^{L_c} ds \sum_{\beta=y,z}\sum_{k,j=1}^{\infty} \frac{\lambda_k\lambda_j}{L_c^2}\left[\tilde{a}_{\beta,k}\tilde{a}_{\beta,j}\cos\left(\lambda_k\frac{s}{L_c}\right)\cos\left(\lambda_j\frac{s}{L_c}\right)\right] \\ &= \frac{\ell_p}{2}\sum_{k,j=1}^{\infty}\frac{\lambda_k\lambda_j}{L_c^2}\left[\left(\tilde{a}_{y,k}\tilde{a}_{y,j} + \tilde{a}_{z,k}\tilde{a}_{z,j}\right)\frac{L_c}{2}\delta_{kj}\right] \\ &= \frac{\ell_p}{4L_c}\sum_{k,j=1}^{\infty}\lambda_k^2\left(\tilde{a}_{y,k}^2 + \tilde{a}_{z,k}^2\right). \end{aligned} \tag{A.6}$$

We can now proceed with the calculation of the probability density for the position of the polymer tip, using the moment-generating function defined as follows:

$$\begin{aligned} \mathfrak{P}_{/\!/}(f) &\equiv \langle \exp\left(-\beta(L_c - r_x(L_c))f\right)\rangle_0 \\ &= \int_{-L_c}^{L_c} dx\; \exp\left(-\beta(L_c - x)f\right) P_{/\!/}(x) \\ &= \int_0^{2L_c} d\rho\; \exp(-\beta f\rho) P_{/\!/}(L_c - \rho) \end{aligned} \tag{A.7}$$

with $\rho = L_c - x$. Since we are in the weak bending limit, x configurations with large values of ρ are rather unlikely, and hence the upper boundary of the last integral can be extended to infinity, making the moment generating function the Laplace

transform of the distribution function $P_{/\!/}(x)$. From the definition of $\langle \cdots \rangle_0$, we can also write:

$$\begin{aligned}
\mathfrak{P}_{/\!/}(f) &= \int \mathcal{D}\left[\mathbf{r}(s)\right] \exp\left(-\beta f(L_c - r_x(L_c)\right) \exp\left(-\beta H\right) \\
&= \int \mathcal{D}\left[\mathbf{r}(s)\right] \exp\left[-\beta f \frac{L_c}{4} \sum_{k=1}^{\infty} \left(\tilde{a}_{y,k}^2 + \tilde{a}_{z,k}^2\right) - \frac{\ell_p}{4L_c} \sum_{k=1}^{\infty} \lambda_k^2 \left(\tilde{a}_{y,k}^2 + \tilde{a}_{z,k}^2\right)\right] \\
&= \int \mathcal{D}\left[\mathbf{r}(s)\right] \exp\left[-\frac{1}{4} \sum_{k=1}^{\infty} \left(\beta f L_c + \frac{\ell_p}{L_c}\right) \left(\tilde{a}_{y,k}^2 + \tilde{a}_{z,k}^2\right)\right] \\
&= \frac{1}{\mathcal{N}^2} \int \prod_{k=1}^{\infty} d\tilde{a}_{y,k}\, d\tilde{a}_{z,k}\ \exp\left[-\frac{1}{4} \left(\beta f L_c + \frac{\ell_p}{L_c}\right) \left(\tilde{a}_{y,k}^2 + \tilde{a}_{z,k}^2\right)\right] \\
&= \left\{\frac{1}{\mathcal{N}} \int \prod_{k=1}^{\infty} d\tilde{a}_{y,k}\ \exp\left[-\frac{1}{4} \left(\beta f L_c + \frac{\ell_p}{L_c}\right) \tilde{a}_{y,k}^2\right]\right\}^2
\end{aligned} \tag{A.8}$$

where $\mathcal{N}$ is the normalization factor that ensures that $\mathfrak{P}_{/\!/}(0) = 1$. This normalization factor can be directly calculated:

$$\begin{aligned}
\mathfrak{P}_{/\!/}(0) =& \left\{\frac{1}{\mathcal{N}} \int \prod_{k=1}^{\infty} d\tilde{a}_{y,k}\ \exp\left(-\frac{1}{4} \frac{\ell_p}{L_c} \tilde{a}_{y,k}^2\right)\right\}^2 = \frac{1}{\mathcal{N}^2} \left(\prod_{k=1}^{\infty} \sqrt{\frac{4\pi L_c}{\ell_p \lambda_k^2}}\right)^2 = 1 \\
\Rightarrow \mathcal{N} &= \prod_{k=1}^{\infty} \frac{4\pi L_c}{\ell_p \lambda_k^2}
\end{aligned} \tag{A.9}$$

Eq. (A.8) can be integrated as well, and substituting the found expression for $\mathcal{N}$, we find:

$$\mathfrak{P}_{/\!/}(f) = \prod_{k=1}^{\infty} \left(1 + \frac{\beta f L_c^2}{\ell_p \lambda_k^2}\right)^{-1}. \tag{A.10}$$

Finally the probability density for the filament's tip position can be calculated, using the inverse Laplace transform of $\mathfrak{P}_{/\!/}(f)$:

$$P_{/\!/}(x) = \int_{-i\infty}^{i\infty} \frac{d(\beta f)}{2\pi i} \exp\left(\beta f(L_c - x)\right) \prod_{k=1}^{\infty} \frac{\ell_p \lambda_k^2}{\beta f L_c^2 + \ell_p \lambda_k^2} \tag{A.11}$$

which presents poles at $\beta f_k = -\lambda_k^2 \ell_p / L_c^2$ with $k = 1, 2, 3, \ldots$, only along the negative real axis. Since the integrand function vanishes for $|f| \to \infty$, we can close the contour path of integration in the half-plane $f < 0$ and calculate the above integral

using the Residue Theorem:

$$\begin{aligned}
P_{/\!/}(x) &= 2\pi i \sum_{k=1}^{\infty} \mathrm{Res}\left(\frac{1}{2\pi i}\exp\left(\beta f(L_c-x)\right)\prod_{l=1}^{\infty}\frac{\ell_p\lambda_l^2}{\beta f L_c^2+\ell_p\lambda_l^2}, \beta f_k\right) \\
&= \sum_{k=1}^{\infty}\left[\lim_{\beta f\to-\lambda_k^2\ell_p/L_c^2}\exp\left(\beta f(L_c-x)\right)\prod_{l=1}^{\infty}\frac{\ell_p\lambda_l^2}{\beta f L_c^2+\ell_p\lambda_l^2}\left(\beta f+\frac{\lambda_k^2\ell_p}{L_c^2}\right)\right] \\
&= \sum_{k=1}^{\infty}\left[\lim_{\beta f\to-\lambda_k^2\ell_p/L_c^2}\exp\left(\beta f(L_c-x)\right)\frac{\ell_p\lambda_1^2}{\ell_p\lambda_1^2+\beta f L_c^2}\cdots\frac{\ell_p\lambda_k^2}{\ell_p\lambda_k^2+\beta f L_c^2}\cdots\frac{\beta f L_c^2+\lambda_k^2\ell_p}{L_c^2}\right] \\
&= \sum_{k=1}^{\infty}\exp\left(-\frac{\lambda_k^2\ell_p}{L_c^2}(L_c-x)\right)\prod_{l\neq k}\frac{\lambda_l^2}{\lambda_l^2-\lambda_k^2}\cdot\frac{\lambda_k^2\ell_p}{L_c^2} \\
&= \sum_{k=1}^{\infty}\exp\left(-\frac{\lambda_k^2\ell_p}{L_c^2}(L_c-x)\right)\prod_{l\neq k}\left(1-\frac{(2k-1)^2}{(2l-1)^2}\right)^{-1}\cdot\frac{\lambda_k^2\ell_p}{L_c^2}
\end{aligned} \tag{A.12}$$

and using the identity $\cos(x)=\prod_{k=1}^{\infty}\left(1-\frac{4x^2}{\pi^2(2k-1)^2}\right)$,

$$\begin{aligned}
\prod_{l\neq k}\left(1-\frac{(2k-1)^2}{(2l-1)^2}\right)^{-1} &= \lim_{k'\to k}\prod_{l\neq k}\left(1-\frac{(2k'-1)^2}{(2l-1)^2}\right)^{-1}\left(1-\frac{(2k'-1)^2}{(2k-1)^2}\right) \\
&= \lim_{k'\to k}\left(\cos\left((2k'-1)\frac{\pi}{2}\right)\right)^{-1}\left(1-\frac{(2k'-1)^2}{(2k-1)^2}\right) \\
&= \frac{2}{\pi}(-1)^{k+1}\frac{2}{2k-1} \\
&= 2(-1)^{k+1}\frac{1}{\lambda_k}
\end{aligned} \tag{A.13}$$

we finally get Eq. (2.32),

$$P_{/\!/}(x) = \frac{2\ell_p}{L_c^2}\sum_{k=1}^{\infty}(-1)^{k+1}\lambda_k\,\exp\left(-\frac{\lambda_k^2(L_c-x)\ell_p}{L_c^2}\right) \tag{A.14}$$

valid in the weak bending limit.

A.2 Grand potential of a grafted, compressed bundle of semiflexible living filaments

Let's consider a fixed number of filaments N_f and let the total number of monomers N_t, the temperature T and the volume V be fixed as well (canonical ensemble). The solution of filaments and free monomers is enclosed in a cuboid with bases of area A and height L; the filaments are grafted normally to one of the bases. The volume is thus given by the product of the distance between the confining and the grafting walls, L, and the constant transverse area, A; the total number of particles will be given by the sum of the amount of free monomers and the number j of monomers in each filament,

$$N_t = \rho_1 AL + \sum_{n=1}^{N_f}\sum_{j_n=2}^{z_n^*(L_n)} j_n P(j_n|L_n,\hat{\rho}_1) \tag{A.15}$$

where $P(j_n|L_n, \hat{\rho}_1)$ is the probability for the n-th filament to have j_n monomers.

Let's label by q_1 the free monomers canonical partition function, by $q^0_{j_n}(L_n)$ the uncompressed filament canonical partition function ($2 \leq j_n \leq z_n(L_n)$, with $z_n(L_n)$ the maximum number of monomers in the filament before it feels the presence of the wall, Eq. (2.51)) and by $q_{j_n}(L_n)$ the compressed filament canonical partition function ($z_n(L_n) < j_n < z^*_n(L_n)$, with $z^*_n(L_n)$ the maximum number of monomers in the filament before it becomes escaping, Eq. (2.40)). These latter two partition functions can be related to each other by introducing the *wall factors* $\alpha_{j_n}(L_n)$:

$$q_{j_n}(L_n) = \alpha_{j_n}(L_n) q^0_{j_n}(L_n) \tag{A.16}$$

These wall factors depend on the distance between the wall and the grafting point and embody the effect of the wall on the single filament partition function; they are given by the ratio between $q_{j_n}(L_n)$ and $q^0_{j_n}(L_n)$, and hence they are smaller than one only for $z_n(L_n) < j_n < z^*_n(L_n)$. Under the condition of independent and non-interacting monomers, the free monomer partition function is given by:

$$q_1 = \frac{1}{h} \int d^3r \int d^3p \, \exp\left(-\beta \frac{p^2}{2m}\right) = \frac{1}{h} \left(\frac{2\pi m}{\beta}\right)^{3/2} V = \frac{V}{\Lambda^3} \tag{A.17}$$

where $\Lambda = \sqrt{\beta h^2 / 2\pi m}$ is the free monomers de Broglie wavelength.

To calculate the single filament partition function we need to determine its Hamiltonian: it shall contain the kinetic energy and intramolecular interactions – bonding and bending energy –, a term accounting for the energy gain in forming a new bond and the interaction with the obstacle $U^{wall}_j(L)$, that can be again regarded as a hard wall potential. Denoting by H_j the Hamiltonian of the filament with j monomers we can write [117]

$$\begin{aligned} H_j = & \frac{1}{2m} \sum_{k=1}^{j} \mathbf{p}_k^2 - (j-1)\epsilon_0 + \frac{k_s}{2} \sum_{k=2}^{j} (d_k - d_0)^2 \\ & + \frac{\ell_p k_B T}{d_0} \sum_{k=2}^{j-1} (1 - \cos\theta_k) + \frac{j-1}{2} k_B T \ln\left(\frac{2\pi k_B T}{k_s d_0^2}\right) + U^{wall}_j(L) \end{aligned} \tag{A.18}$$

where ϵ_0 is the energy released in forming a new bond, bonds have been represented by springs of constant k_s and equilibrium length d_0, $d_k = |\mathbf{r}_k - \mathbf{r}_{k-1}|$, θ_k is the angle between bonds k and $k-1$; the fifth term is a constant needed to normalize the exponential of $\beta k_s (d_k - d_0)^2 / 2$ which will appear in the partition function

$$q_j(L_n) = \frac{1}{h^{3j}} \int d^{3j}r \int d^{3j}p \, \exp(-\beta H_j) \delta(x_1 - h_n) \delta(y_1) \delta(z_1) \delta(x_2 - h_n - d_0) \delta(y_2) \delta(z_2) \tag{A.19}$$

where the δ functions ensure that the anchored end is perpendicular to the grafting plane with the first monomer at $(h_n, 0, 0)$ and the second at $(h_n + d_0, 0, 0)$. The expression for the filament partition function in absence of the wall is analogous to this latter one, provided that the hamiltonian be H^0_j not containing the wall

interaction term. The wall factor will be thus:

$$\begin{aligned}\alpha_j(L_n) &= \frac{q_j(L_n)}{q_j^0(L_n)} \\ &= \frac{\frac{1}{h^{3j}}\int d^{3j}r \int d^{3j}p \, \exp(-\beta H_j^0 + U_j^{wall}(L_n)) \prod_{k=1,2} \delta(x_k - h_n - (k-1)d_0)\delta(y_k)\delta(z_k)}{\frac{1}{h^{3j}}\int d^{3j}r \int d^{3j}p \, \exp(-\beta H_j^0(L_n)) \prod_{k=1,2} \delta(x_k - h_n - (k-1)d_0)\delta(y_k)\delta(z_k)} \\ &= \left\langle \exp\left(-\beta U_j^{wall}(L_n)\right)\right\rangle_0 \end{aligned} \tag{A.20}$$

where the subscript 0 means that the canonical average is taken with the Hamiltonian of the filament in absence of the obstacle.

Let's consider now the reactivity of the mixture: the series of possible chemical reactions can be denoted as

$$A_{j-1} + A_1 \rightleftharpoons A_j \qquad j > 2 \tag{A.21}$$

where A_j represents the grafted filament of size j and A_1 a free monomer. At equilibrium, if we denote by μ_j the chemical potential of the filament of size j, it must be:

$$\mu_j = \mu_{j-1} + \mu_1 \qquad 2 < j < z^*(L) \tag{A.22}$$

where $z^*(L)$ has been defined in Eq. (2.40). In terms of the temperature T, the volume $V = AL$, the total number of monomers N_t and the total number of filaments N_f, the reversible change of the relevant Helmholtz thermodynamic potential $\mathcal{F}^R$ for this reactive system is:

$$d\mathcal{F}^R = -S\, dT - p_\perp A\, dL + p_{/\!/} L\, dA + \mu_1 dN_t + \sum_{j=2}^{z^{**}} \mu_j\, dN_j \tag{A.23}$$

where S is the system entropy, $p_\perp A$ and $p_{/\!/} A$ are the total normal and tangential forces acting on the wall, N_j is the number of filaments with j monomers and $z^{**} = \max_n(z_n^*)$. Being N_1 the number of free monomers, the total number of monomers can be written as $N_t = N_1 + \sum_{j=2}^{z^{**}} j\, N_j$, while the number of filament shall be $N_f = \sum_{j=2}^{z^{**}} N_j$, so that, applying Eq. (A.22):

$$\begin{aligned}\mu_1\, dN_t = \mu_1 dN_1 + \sum_{j=2}^{z^{**}} j\, dN_j &= \mu_1 dN_1 + \mu_2 dN_2 + (\mu_2 + \mu_1)dN_3 + (\mu_3 + \mu_1)dN_4 \\ &\quad + (\mu_4 + \mu_1)dN_5 + \cdots + (\mu_{z^{**}} + \mu_1)dN_{z^{**}} \\ &= \mu_1 dN_1 + \mu_2 dN_2 + (\mu_2 + \mu_1)dN_3 + (\mu_2 + 2\mu_1)dN_4 \\ &\quad + (\mu_2 + 3\mu_1)dN_5 + \cdots + (\mu_2 + (z^{**} - 2)\mu_1)dN_{z^{**}} \\ &= \mu_1 dN_1 + \mu_2 \sum_{j=2}^{z^{**}} dN_j + \mu_1 \sum_{j=2}^{z^{**}} (j-2)dN_j \\ &= \mu_1 \left(dN_1 + \sum_{j=2}^{z^{**}} j\, dN_j - 2\sum_{j=2}^{z^{**}} dN_j \right) + \mu_2 dN_f \\ &= \mu_1 dN_t + (\mu_2 - 2\mu_1)dN_f. \end{aligned} \tag{A.24}$$

Eq. (A.23) thus becomes:

$$d\mathcal{F}^R = -S\, dT - p_\perp A\, dL + p_{/\!/} L\, dA + \mu_1 dN_t + (\mu_2 - 2\mu_1) dN_f. \tag{A.25}$$

Let's the single filament case $N_f = 1$: applying equilibrium statistical mechanics, the canonical partition function $Q^R = \exp(-\beta \mathcal{F}^R)$ can be written as the sum of all distinct states compatible with the boundary conditions [53]:

$$Q^R(A, L, T, N_t, N_f = 1) = \frac{q_1^{N_t-2}}{(N_t-2)!}\, q_2 + \frac{q_1^{N_t-3}}{(N_t-3)!}\, q_3 + \cdots + \frac{q_1^{N_t-z^*}}{(N_t-z^*)!}\, q_{z^*} \tag{A.26}$$

where each term corresponds to a particular size of the grafted filament and the remaining free monomers.

The equilibrium constant for the chemical reaction Eq. (A.21), given by the ratio of the concentrations of the product and that of reactants [118], resultss related to the wall factors Eq. (A.20) as follows:

$$\begin{aligned} K_j(L) &= \frac{\frac{q_j(L)}{V}}{\frac{q_{j-1}(L)}{V}\frac{q_1}{V}} = \frac{q_j(L)}{q_{j-1}(L)}\Lambda^3 \\ &= \frac{\alpha_j(L)}{\alpha_{j-1}(L)}\frac{q_j^0(L)}{q_{j-1}^0(L)}\Lambda^3 \\ &= \frac{\alpha_j(L)}{\alpha_{j-1}(L)}\, K_j^0 \end{aligned} \tag{A.27}$$

where K_j^0 is the equilibrium constant for the same reaction in absence of the obstacle. As detailed in Appendix A.3, this equilibrium constant results to be independent of j:

$$\begin{aligned} K_0 = 2\pi \exp(\beta\epsilon_0)\, \frac{d_0^4}{\ell_p}\left(1 - \exp\left(-2\frac{\ell_p}{d_0}\right)\right)\sqrt{\frac{\beta k_s d_0^2}{2\pi}} \times \\ \left[\frac{1 + \operatorname{erf}\left(\frac{\beta k_s d_0^2}{\sqrt{2}}\right)}{2}\left(1 + \frac{1}{\beta k_s d^2}\right) + \frac{\exp\left(-\frac{\beta k_s d_0^2}{2}\right)}{\sqrt{2\pi\beta k_s d_0^2}}\right] \end{aligned} \tag{A.28}$$

which in the large k_s limit reduces to:

$$K_0 = 2\pi \exp(\beta\epsilon_0)\, \frac{d_0^4}{\ell_p}\left(1 - \exp\left(-2\frac{\ell_p}{d_0}\right)\right). \tag{A.29}$$

Applying recursively Eq. (A.27) we thus have:

$$q_j(L) = q_2^0 \alpha_j(L) \left(\frac{K_0}{\Lambda^3}\right)^{j-2} \tag{A.30}$$

where q_2^0 is the partition function of the grafted seed. Eq. (A.26) can be now

combined with this last expression to give

$$
\begin{aligned}
Q^R &= q_2^0 q_1^{N_t-2} \times \left[\frac{\alpha_2(L)}{(N_t-2)!} + \frac{q_1^{-1}\alpha_3(L)\left(\frac{K_0}{\Lambda^3}\right)}{(N_t-3)!} + \cdots + \frac{q_1^{-(z^*-2)}\alpha_{z^*}(L)\left(\frac{K_0}{\Lambda^3}\right)^{z^*-2}}{(N_t-z^*)!} \right] \\
&= q_2^0 q_1^{N_t-2} \times \left[\frac{\alpha_2(L)}{(N_t-2)!} + \frac{\alpha_3(L)\left(\frac{K_0}{V}\right)}{(N_t-3)!} + \cdots + \frac{\alpha_{z^*}(L)\left(\frac{K_0}{V}\right)^{z^*-2}}{(N_t-z^*)!} \right] \\
&= \frac{q_2^0 q_1^{N_t-2}}{(N_t-2)!} \times \left[\alpha_2(L) + \alpha_3(L)\left(\frac{K_0}{V}\right)(N_t-2) + \cdots + \alpha_{z^*}(L)\left(\frac{K_0}{V}\right)^{z^*-2} \frac{(N_t-2)!}{(N_t-z^*)!} \right] \\
&= \frac{q_2^0 V^2}{K_0^2} \frac{q_1^{N_t-2}}{(N_t-2)!} \times \left[\alpha_2(L)\left(\frac{K_0}{V}\right)^2 + \alpha_3(L)\left(\frac{K_0}{V}\right)^3 (N_t-2) + \cdots + \alpha_{z^*}(L)\left(\frac{K_0}{V}\right)^{z^*} \frac{(N_t-2)!}{(N_t-z^*)!} \right] \\
&= \frac{q_2^0 V^2}{K_0^2} \frac{q_1^{N_t-2}}{N_t!} \times \sum_{j=2}^{z^*} \alpha_j(L)\left(\frac{K_0}{V}\right)^j \frac{N_t!}{(N_t-j)!} \\
&\approx \frac{q_2^0 V^2}{K_0^2} \frac{q_1^{N_t-2}}{N_t!} \times \sum_{j=2}^{z^*} \alpha_j(L)\hat{\rho}_t^j \\
&= \frac{q_2^0 \Lambda^6}{K_0^2} \frac{q_1^{N_t-2}}{N_t!} \times D(L,\hat{\rho}_t)
\end{aligned}
\tag{A.31}
$$

where in the second-to-last line we applied the thermodynamic limit $N_t \to \infty$, $A \to \infty$ with fixed ratio $N_t/A = \rho_t L$ (ρ_t total monomers density), so that $\frac{N_t!}{N_t^j (N_t-j)!} \approx 1$, and where we defined:

$$\hat{\rho}_t = \rho_t K_0 \tag{A.32}$$

$$D(L,\hat{\rho}_t) = \sum_{j=2}^{z^*} \alpha_j(L)\hat{\rho}_t^j. \tag{A.33}$$

The Helmholtz free energy is now:

$$\beta\mathcal{F}^R(A,L,T,N_t,N_f=1) = N_t\left[\ln(\Lambda^3\rho_t)-1\right] - \ln\left(\frac{q_2^0\Lambda^6}{K_0^2}\right) - \ln D(L,\hat{\rho}_t). \tag{A.34}$$

Note that in the thermodynamic limit we can replace the total number of monomer by the number of free monomers, being the number of monomers bound in the filament relatively small. Hence $\hat{\rho}_t \to \hat{\rho}_1$ and Eq. (A.33) coincides with Eq. (2.42); the first term in the r.h.s. of Eq. (A.34) becomes the Helmholtz free energy of the bath of free monomers, the last term is the relevant free energy of the living filament while the middle term is linked to the free energy required to graft the filament seed. We are now able to get the probability for the living filament to have size j, $P(j|L,\hat{\rho}_t)$: it is the term of index j in the global partition function, properly normalized:

$$P(j|L,\hat{\rho}_t) = \frac{\alpha_j(L)\hat{\rho}_t^j}{D(L,\rho_t)}. \tag{A.35}$$

A more suitable ensemble to describe real experiments is the grand-canonical ensemble where the free monomers density becomes constant. Performing a Legendre

transform of the reactive Helmholtz free energy Eq. (A.34) to get the reactive grand-canonical potential $\Omega^R = \mathcal{F}^R - \mu_1 N_t$ we can write:

$$d\Omega^R = -S\ dT - p_\perp A\ dL + p_{/\!/} L\ dA - N_t d\mu_1 + (\mu_2 - 2\mu_1)\ dN_f \tag{A.36}$$

from which

$$\begin{aligned}\beta\mu_1 = \frac{\partial\beta\mathcal{F}^R}{\partial N_t} &= \ln(\Lambda^3\rho_t) - \frac{\partial D(\hat{\rho}_t)/\partial\hat{\rho}_t}{D(\hat{\rho}_t)}\frac{K_0}{V} \\ &= \ln(\Lambda^3\rho_t) - \frac{\partial D(\hat{\rho}_t)/\partial\hat{\rho}_t}{D(\hat{\rho}_t)}\frac{\hat{\rho}_t}{N_t} = \ln(\Lambda^3\rho_t) - \frac{l_{fil}}{N_t}\end{aligned} \tag{A.37}$$

where the average length of the filament has been introduced as

$$l_{fil}(L,\hat{\rho}_t) = \frac{\sum_{j=2}^{z^*} j\ \alpha_j(L)\hat{\rho}_t^j}{D(L,\hat{\rho}_t)}. \tag{A.38}$$

Using Eq. (A.34) and Eq. (A.37), we get:

$$\begin{aligned}\beta\Omega^R(A,L,T,\mu_1,N_f=1) &= \Big[\beta\mathcal{F}^R(A,L,T,N_t,N_f=1) - N_t\beta\mu_1\Big]_{N_t=N_t(\mu_1)} \\ &= \left[-N_t + l_{fil} - \ln\left(\frac{q_2^0\Lambda^6}{K_0^2}\right) - \ln D(L,\hat{\rho}_t)\right]_{N_t=N_t(\mu_1)} \\ &\approx \left[-N_t + l_{fil} - \frac{l_{fil}^2}{N_t} - \ln\left(\frac{q_2^0\Lambda^6}{K_0^2}\right) - \ln D(L,\hat{\rho}_1)\right]_{N_t=N_t(\mu_1)}\end{aligned} \tag{A.39}$$

where we have developed $D(\hat{\rho}_t)$ around $\hat{\rho}_1$ to first order. Neglecting the term l_{fil}/N_t in Eq. (A.37) and the term l_{fil}^2/N_t in Eq. (A.39), we get:

$$\hat{\rho}_1 = \frac{K_0}{\Lambda^3}\exp(\beta\mu_1) \tag{A.40}$$

$$\beta\Omega^R(A,L,T,\mu_1,N_f=1) = \left[-N_1 - \ln\left(\frac{q_2^0\Lambda^6}{K_0^2}\right) - \ln D(L,\hat{\rho}_1)\right]_{\hat{\rho}_1=\frac{K_0}{\Lambda^3}\exp(\beta\mu_1)} \tag{A.41}$$

which, re-expressed in terms of the reduced free monomers density $\hat{\rho}_1$, becomes:

$$\beta\Omega^R(A,L,T,\mu_1,N_f=1) = \beta\Omega^{free}(A,L,T,\hat{\rho}_1) + \beta\Omega^{fil}(L,T,\hat{\rho}_1) \tag{A.42}$$

$$\beta\Omega^{free}(A,L,T,\hat{\rho}_1) = -\frac{AL}{K_0}\hat{\rho}_1 \tag{A.43}$$

$$\Omega^{fil}(L,T,\hat{\rho}_1) = -k_BT\left[\ln\left(\frac{q_2^0\Lambda^6}{K_0^2}\right) + \ln D(L,\hat{\rho}_1)\right] \tag{A.44}$$

where $\beta\Omega^{free}(A,L,T,\hat{\rho}_1)$ is the free monomers contribution and $\beta\Omega^{fil}(L,T,\hat{\rho}_1)$ is the grafted living filament contribution to the total grand potential. From this expression, the grand-canonical partition function Eq. (2.41) is readily recovered.

The single filament size distribution function, the single filament partition function and the average size take the final form

$$P(j) \equiv P(j|L,\hat{\rho}_1) = \frac{\alpha_j(L)\hat{\rho}_1^j}{D} \tag{A.45}$$

$$D(L,\hat{\rho}_1) = \sum_{j=2}^{z^*} \alpha_j(L)\hat{\rho}_1^j \tag{A.46}$$

$$l_{fil}(L,\hat{\rho}_1) = \frac{\sum_{j=2}^{z^*} j\ \alpha_j(L)\hat{\rho}_1^j}{D} = \hat{\rho}_1 \frac{\partial \ln D}{\partial \hat{\rho}_1} = \frac{\partial \ln D}{\partial \beta\mu_1} \tag{A.47}$$

corresponding to Eqs. (2.42), (2.44) and (2.45).

As for the force, according to Eq. (A.36), the total normal pressure on the wall is given by the partial derivative with respect to L of the grand potential: the force of the living single filament is thus

$$f_\perp(L,\hat{\rho}_1) = \frac{\partial \Omega^{fil}}{\partial L} = k_B T \sum_{j=2}^{z^*(L)} \frac{\partial \ln \alpha_j(L)}{\partial L}\ P(j|L,\hat{\rho}_1) = \sum_{j=2}^{z^*(L)} \bar{f}_j(L)\ P(j|L,\hat{\rho}_1) \tag{A.48}$$

as in Eq. (2.46).

The generalization to a bundle of N_f independent filaments is straightforward: the canonical partition function will be the product of N_f terms if the kind of Eq. (A.26),

$$Q^R(A,L,T,N_t,N_f) = \prod_{n=1}^{N_f} \sum_{j_n=2}^{z_n^*} \frac{q_1^{N_t-j_n}}{(N_t-j_n)!} q_{j_n}(L_n) \tag{A.49}$$

while to get the grand-canonical partition function we need to sum over all the possible N_t values the canonical partition function weighted by the corresponding activity:

$$\begin{aligned}
\Xi^R(A,L,T,\mu_1,N_f) &= \sum_{N_t=2N_f}^{\infty} \exp(\beta\mu_1 N_t)\, Q^R(A,L,T,N_t,N_f) \\
&= \sum_{N_t=2N_f}^{\infty} \exp(\beta\mu_1 N_t) \sum_{j_1=2}^{z_1^*} \cdots \sum_{j_{N_f}=2}^{z_{N_f}^*} \frac{q_1^{N_1}}{N_1!} q_{j_1}(L_1)\cdots q_{j_{N_f}}(L_{N_f}) \Bigg|_{N_t=N_1+\sum_{n=1}^{N_f} j_n} \\
&= \sum_{N_1=0}^{\infty} \frac{q_1^{N_1}}{N_1!} \sum_{j_1=2}^{z_1^*} \cdots \sum_{j_{N_f}=2}^{z_{N_f}^*} q_{j_1}(L_1)\cdots q_{j_{N_f}}(L_{N_f}) \exp(\beta\mu_1 N_t) \\
&= \sum_{N_1=0}^{\infty} \frac{q_1^{N_1}}{N_1!} \exp(\beta\mu_1 N_1) \prod_{n=1}^{N_f} \left[\sum_{j_n=2}^{z_n^*} q_{j_n}(L_n) \exp(\beta\mu_1 j_n) \right] \\
&= \Xi^{free}(A,L,T,\mu_1) \left(\frac{q_2^0 \Lambda^6}{K_0^2} \right)^{N_f} \prod_{n=1}^{N_f} \left[\sum_{j_n=2}^{z_n^*} \alpha_{j_n}(L_n) \hat{\rho}_1^{j_n} \right]
\end{aligned} \tag{A.50}$$

where again $\hat{\rho}_1 = K_0 \exp(\beta\mu_1)/\Lambda^3$ and $\Xi^{free}(A, L, T, \mu_1)$ is the free monomer ideal gas partition function in the accessible volume at the same temperature and chemical potential. The grand potential $\beta\Omega^R(A, L, T, \mu_1, N_f) = \ln \Xi^R(A, L, T, \mu_1, N_f)$ takes the form [47]

$$\beta\Omega^R(A, L, T, \mu_1, N_f) = \beta\Omega^{free}(A, L, T, \hat{\rho}_1) + \beta\Omega^{bun}(L, T, \hat{\rho}_1) \tag{A.51}$$

$$\beta\Omega^{free}(A, L, T, \hat{\rho}_1) = -\frac{AL}{K_0}\hat{\rho}_1 \tag{A.52}$$

$$\Omega^{bun}(L, T, \hat{\rho}_1) = -k_B T \left[N_f \ln\left(\frac{q_2^0 \Lambda^6}{K_0^2}\right) + \sum_{n=1}^{N_f} \ln D(L_n, \hat{\rho}_1) \right] \tag{A.53}$$

with $L_n = L - h_n$ and h_n seed position. As for the probability for the n-th filament to have j_n monomers, given L_n, is:

$$P(j_n | L_n, \hat{\rho}_1) = \frac{\alpha_{j_n}(L_n)\hat{\rho}_1^{j_n}}{D(L_n, \hat{\rho}_1)} \tag{A.54}$$

which is identical to Eq. (A.45), provided $L \to L_n$. The same applies to the other quantities.

A.3 Calculation of the equilibrium constant K_0 in absence of loads

Starting from the definition of K_0 given implicitly in Eq. (A.27) we have

$$\begin{aligned}
K_0 &= \frac{q_j^0(L)}{q_{j-1}(L)}\,\Lambda^3 \\
&= \Lambda^3\,\frac{h^{-3j}\int d^{3j}p \int d^{3j}r \exp(-\beta H_j^0)}{h^{-3(j-1)}\int d^{3j-3}p \int d^{3j-3}r \exp(-\beta H_{j-1}^0)} \\
&= \left(\frac{\Lambda}{h}\right)^3 \left(\frac{2\pi}{\beta k_s d_0^2}\right)^{-1/2} \frac{\left(\int dp\ \exp\left(-\beta\frac{\mathbf{p}^2}{2m}\right)\right)^{3j}}{\left(\int dp\ \exp\left(-\beta\frac{\mathbf{p}^2}{2m}\right)\right)^{3j-3}} \exp\left(\beta\epsilon_0\right) \\
&\times \frac{\int d^{3j}r\ \exp\left(-\beta\sum_{k=1}^{j-1} k_s d_0^2\left(\frac{d_k}{d_0}-1\right) - \frac{\ell_p}{d_0}\sum_{k=2}^{j-1}(1-\cos\theta_k)\right)}{\int d^{3j-3}r\ \exp\left(-\beta\sum_{k=1}^{j-2} k_s d_0^2\left(\frac{d_k}{d_0}-1\right) - \frac{\ell_p}{d_0}\sum_{k=2}^{j-2}(1-\cos\theta_k)\right)}.
\end{aligned} \tag{A.55}$$

The ratio between the integrals in dp cancels out with the prefactor $\left(\frac{\Lambda}{h}\right)^3$ and hence, setting $u = \frac{r}{d}$:

$$\begin{aligned} K_0 &= \left(\frac{2\pi}{\beta k_s d_0^2}\right)^{-1/2} \exp(-\beta\epsilon_0)\, 2\pi d_0^3 \int_0^\infty du\; u^2\; \exp\left(-\beta\frac{k_s d_0^2}{2}(u-1)^2\right) \\ &\quad \times \int_{-1}^{1} d\cos\theta\; \exp\left(-\frac{\ell_p}{d_0}(1-\cos\theta)\right) \\ &= \left(\frac{2\pi}{\beta k_s d_0^2}\right)^{-1/2} \exp(-\beta\epsilon_0)\, 2\pi\frac{d_0^4}{\ell_p}\left(1-\exp\left(-2\frac{\ell_p}{d_0}\right)\right) \int_0^\infty du\; u^2\; \exp\left(-\beta\frac{k_s d_0^2}{2}(u-1)^2\right) \\ &= \exp(-\beta\epsilon_0)\, 2\pi\frac{d_0^4}{\ell_p}\left(1-\exp\left(-2\frac{\ell_p}{d_0}\right)\right)\; I(\xi) \end{aligned} \tag{A.56}$$

with

$$\begin{aligned} I(\xi) &= \sqrt{\frac{\xi^2}{2\pi}} \int_0^\infty du\; u^2 \exp\left(-\frac{\xi^2}{2}(u-1)^2\right) \\ &= \frac{\xi}{\sqrt{2\pi}}\left[\frac{1+\operatorname{erf}\left(\frac{\xi}{\sqrt{2\pi}}\right)}{2}\left(1+\frac{1}{\xi^2}\right) + \frac{1}{\sqrt{2\pi}\,\xi}\exp\left(-\frac{\xi^2}{2}\right)\right] \end{aligned} \tag{A.57}$$

This function goes to 1 for $\xi \to \infty$, and Eq. (A.29) is recovered.

A.4 Optical Trap Ensamble

Let's consider a large volume filled with free monomers at fixed chemical potential μ_1 and hence fixed grand-canonical average reduced density $\hat{\rho}_1$, in contact with a heat bath at temperature T, and let's take a central volume of transverse area A and length L_R. A bundle of N_f filaments is grafted onto one of the two bases A and hits a mobile wall, parallel to A and connected to a spring of constant κ_T and rest length L_R (so that the restoring force is $\kappa_T L$); on the other side of the moving wall there are only free monomers (see Fig. 2.6). The total free energy of this subvolume AL_R is

$$\Omega^{OT}(A, L, L_R, T, N_f, \mu_1, \kappa_T) = \Omega_1(A, L, T, N_f, \mu_1) + \Omega_2(A, L - L_R, \mu_1) + \frac{1}{2}\kappa_T L^2 \tag{A.58}$$

where by 1 and 2 I indicate the chamber containing the bundle and the chamber containing only free monomers respectively, and $\frac{1}{2}\kappa_T L^2$ is the contribution due to the compressional energy stored in the spring. The grand potential of chamber 2 (free monomers only) is given by Eq. (A.52) with $L \to L - L_R$, while the grand potential of chamber 1 is given by Eq. (A.53), so that:

$$\Omega^{\mathrm{OT}}(L, T, N_f, \mu_1, \kappa_T) = -\frac{AL_R}{\beta K_0}\hat{\rho}_1 - k_B T\left[N_f \ln\left(\frac{q_2^0 \Lambda^6}{K_0^2}\right) + \sum_{n=1}^{N_f} \ln D(L_n, \hat{\rho}_1)\right] + \frac{1}{2}\kappa_T L^2 \tag{A.59}$$

The equilibrium distribution Eq. (2.61) for the variable L is related to this grand potential through:

$$\mathcal{P}^{\mathrm{OT}}(L) = \frac{\exp\left(-\beta\Omega^{\mathrm{OT}}(L,T,N_f,\mu_1,\kappa_T)\right)}{\int_{2d_0}^{L_R} dL' \ \exp\left(-\beta\Omega^{\mathrm{OT}}(L',T,N_f,\mu_1,\kappa_T)\right)} \tag{A.60}$$

which gives Eq. (2.61). The average of the bundle force $F_{bun} = \sum_{n=1}^{N_f} f_{\perp}(L_n, \hat{\rho}_1)$ over the optical trap ensemble is

$$\langle F_{bun}\rangle^{\mathrm{OT}} = \int_{2d_0}^{L_R} dL \ \mathcal{P}^{\mathrm{OT}}(L) \ F_{bun}(L,\hat{\rho}_1) \tag{A.61}$$

and since from Eqs. (A.59), (2.46) and (2.56) we have $\frac{\partial\Omega^{\mathrm{OT}}}{\partial L} = \kappa_T - F_{bun}(L)$,

$$\begin{aligned}\langle F_{bun}\rangle^{\mathrm{OT}} &= \int_{2d_0}^{L_R} dL \ \mathcal{P}^{\mathrm{OT}}(L) \ \left(\kappa_T L - \frac{\partial\Omega^{\mathrm{OT}}}{\partial L}\right) \\ &= \int_{2d_0}^{L_R} dL \ \mathcal{P}^{\mathrm{OT}}(L) \ (\kappa_T L) = \langle L\rangle^{\mathrm{OT}}\kappa_T\end{aligned} \tag{A.62}$$

where the second line comes from the boundary conditions. Thus, $\langle L\rangle^{\mathrm{OT}} = \langle F_{bun}\rangle^{\mathrm{OT}}/\kappa_T$: the measurement of the colloid position in an optical trap experiment is equivalent to the optical trap average of the bundle force expression, as requested by mechanical equilibrium.

A.5 Polymerization/depolymerization rates

The reaction given in Eq. (A.21) is usually associated to phenomenological rate constants k_{on}^{j-1} and k_{off}^{j}, in terms of which the microreversibility condition – number of events $j-1 \to j$ per unit of time equal to the number of events $j \to j-1$ – can be written as:

$$k_{on}^{j-1}\rho_1 P(j-1) = k_{off}^{j} P(j) \tag{A.63}$$

The equilibrium constant K_j given by Eq. (A.27) is also equal to k_{on}^{j-1}/k_{off}^{j}. Introducing the polymerization and depolymerization rates $U_{j-1} = k_{on}^{j-1}\rho_1$ and $W_j = k_{off}^{j}$, the latter equation can be written equivalently as follows:

$$\frac{U_{j-1}}{W_j} = \frac{P(j)}{P(j-1)} = \frac{\alpha_j(L)}{\alpha_{j-1}(L)}\,\hat{\rho}_1 \tag{A.64}$$

The bulk (de)polymerization rates denoted by U_0 and W_0, with $U_0/W_0 = \hat{\rho}_1$, are valid as long as the filament does not interact with the wall. For (de)polymerization reactions implying filaments hitting the wall, the rates satisfying Eq. (A.64) are often chosen in applications assuming that the depolymerization rates are not affected by the presence of the wall, namely,

$$W_j = W_0 \tag{A.65}$$

$$U_j = \frac{\alpha_{j+1}(L)}{\alpha_j(L)}\,U_0 \tag{A.66}$$

A.6 Average wall position for a single rigid filament in optical trap setup: link with Hill's formula

Let's explicitly calculate the average wall position in the case of a rigid single filament in an optical trap of strength constant κ_T. We have:

$$\langle L \rangle^{\mathrm{OT}} = \int_0^\infty dL\, L\, \mathcal{P}^{\mathrm{OT}}(L) \tag{A.67}$$

$$= \frac{\displaystyle\int_0^\infty dL\, L\, \left(\hat{\rho}_1^{\,\mathrm{int}\left(\frac{L}{d_0}\right)} - 1 \right) \exp\left(-\beta \frac{\kappa_T L^2}{2} \right)}{\displaystyle\int_0^\infty dL\, \left(\hat{\rho}_1^{\,\mathrm{int}\left(\frac{L}{d_0}\right)} - 1 \right) \exp\left(-\beta \frac{\kappa_T L^2}{2} \right)} \tag{A.68}$$

where I have used Eqs. (A.59), (2.61) and (2.69) for the single filament case. Let's now define the reduced variable $x \equiv \frac{L}{d_0}$ and $a \equiv \beta \kappa_T d_0^2$. We have for the variable x:

$$\langle x \rangle^{\mathrm{OT}} = \frac{\displaystyle\int_0^\infty dx\, x\, \left(\hat{\rho}_1^{\mathrm{int}(x)} - 1 \right) \exp\left(-\frac{a x^2}{2} \right)}{\displaystyle\int_0^\infty dx\, \left(\hat{\rho}_1^{\mathrm{int}(x)} - 1 \right) \exp\left(-\frac{a x^2}{2} \right)} \tag{A.69}$$

and noticing that $x \exp\left(-\frac{ax^2}{2}\right) = -\frac{1}{a}\frac{d}{dx} \exp\left(-\frac{ax^2}{2}\right)$, the numerator can be integrated by parts:

$$\begin{aligned} \int_0^\infty dx\, x\, \left(\hat{\rho}_1^{\mathrm{int}(x)} - 1 \right) \exp\left(-\frac{a x^2}{2} \right) &= -\frac{1}{a} \exp\left(-\frac{a x^2}{2} \right) \left(\hat{\rho}_1^{\mathrm{int}(x)} - 1 \right) \Big|_0^\infty \\ &\quad + \frac{1}{a} \int_0^\infty dx\, \exp\left(-\frac{a x^2}{2} \right) \frac{d\hat{\rho}_1^{\mathrm{int}(x)}}{dx} \\ &= \frac{1}{a} \int_0^\infty dx\, \exp\left(-\frac{a x^2}{2} \right) \hat{\rho}_1^{\mathrm{int}(x)} \ln \hat{\rho}_1 \frac{d}{dx} \mathrm{int}\,(x) \end{aligned} \tag{A.70}$$

while the denominator can be splitted as

$$\int_0^\infty dx\, \left(\hat{\rho}_1^{\mathrm{int}(x)} - 1 \right) \exp\left(-\frac{a x^2}{2} \right) = \int_0^\infty dx\, \hat{\rho}_1^{\mathrm{int}(x)} \exp\left(-\frac{a x^2}{2} \right) - \sqrt{\frac{\pi}{2a}}. \tag{A.71}$$

The function $\frac{d}{dx}\mathrm{int}\,(x)$ is a singular function, since $\mathrm{int}\,(x)$ is discontinuous. Nevertheless, we can approximate this function by 1, which corresponds to taking the "average" slope of $\mathrm{int}\,(x)$. With this approximation, and splitting the integrals into sums of integrals to be performed in intervals $[n, n+1]$ where $\mathrm{int}(x)$ is continuous,

we can write:

$$\begin{aligned}\langle x\rangle^{\mathrm{OT}} &= \frac{\ln\hat{\rho}_1}{a}\frac{\displaystyle\int_0^\infty dx\; x\;\hat{\rho}_1^{\mathrm{int}(x)}\exp\left(-\frac{ax^2}{2}\right)}{\displaystyle\int_0^\infty dx\;\hat{\rho}_1^{\mathrm{int}(x)}\exp\left(-\frac{ax^2}{2}\right)-\sqrt{\frac{\pi}{2a}}} \\ &= \frac{\ln\hat{\rho}_1}{a}\frac{\displaystyle\sum_{n=0}^{\infty}\hat{\rho}_1^n\int_n^{n+1}dx\;\exp\left(-\frac{ax^2}{2}\right)}{\displaystyle\sum_{n=0}^{\infty}\hat{\rho}_1^n\int_n^{n+1}dx\;\exp\left(-\frac{ax^2}{2}\right)-\sqrt{\frac{\pi}{2a}}}\end{aligned} \tag{A.72}$$

where $\frac{\ln\hat{\rho}_1}{a}$ corresponds to Hill's result (1.8) divided by $\kappa_T d_0$; this equation corresponds to Eq. (2.74). Rewriting each integral as the difference of two integrals calculated between n and infinity and $n+1$ and infinity respectively, we get sums of complementary error functions both in the numerator and in the denominator, and simplifying we get

$$\langle x\rangle^{\mathrm{OT}} = \frac{\ln\hat{\rho}_1}{a}\left(1+\frac{1}{\frac{\hat{\rho}_1-1}{\hat{\rho}_1}\displaystyle\sum_{n=0}^{\infty}\hat{\rho}_1^n\mathrm{erfc}\left(n\sqrt{\frac{a}{2}}\right)}\right) \tag{A.73}$$

where the term in parenthesis goes to 1 for $\kappa_T \to 0$, since the complementary error function would go to 1 correspondingly and the sum in the denominator would diverge.

A.7 Average wall position for a homogeneous bundle of rigid filaments

According with the definition in Section 1.3.2, the seeds of a homogeneous bundle are positioned at

$$h_n^* = \frac{h_n}{d_0} = \frac{n}{N_f} - \frac{1}{2N_f} - \frac{1}{2} \tag{A.74}$$

for $n = 1, \cdots, N_f$. The bundle partition function is

$$\mathcal{D}(L,\hat{\rho}_1,N_f) = \prod_{n=1}^{N_f} D(L_n,\hat{\rho}_1) = \left(\frac{\hat{\rho}_1^2}{\hat{\rho}_1-1}\right)^{N_f}\prod_{n=1}^{N_f}\left(\hat{\rho}_1^{z_n-1}-1\right) \tag{A.75}$$

and the normalization of $\mathcal{P}^{OT}(L)$, Eq. (2.61):

$$\begin{aligned}\mathcal{N} &= \int_{2d_0}^{\infty} dL'\;\exp\left(-\beta\frac{\kappa_T L'^2}{2}\right)\prod_{n=1}^{N_f}\frac{\hat{\rho}_1^2}{\hat{\rho}_1-1}\left(\hat{\rho}_1^{z_n(L')-1}-1\right) \\ &= \left(\frac{\hat{\rho}_1^2}{\hat{\rho}_1-1}\right)^{N_f} d_0\int_{2d_0}^{\infty}dx\;\prod_{n=1}^{N_f}\left(\hat{\rho}_1^{z_n-1}-1\right)\exp\left(-\frac{x^2}{2\sigma^2}\right)\end{aligned} \tag{A.76}$$

with $\sigma^2 = (\beta\kappa_T d_0^2)^{-1}$ and $x = L/d$. From the definition of h_n, one has $h_{N_f} > h_{N_f-1} > \cdots > h_1$, which implies $x - h_{N_f} < x - h_{N_f-1} < \cdots < x - h_1$ for any $x > 2d_0$. Let's now change variable to $y = x - h_{N_f}$:

$$\mathcal{N} = \left(\frac{\hat{\rho}_1^2}{\hat{\rho}_1 - 1}\right)^{N_f} d_0 \sum_{i=2}^{\infty} \left(\hat{\rho}_1^i - 1\right) \int_i^{i+1} dy \left(\hat{\rho}_1^{\operatorname{int}\left(y+1-\frac{1}{N_f}\right)} - 1\right) \cdots \times \left(\hat{\rho}_1^{\operatorname{int}\left(y+1-\frac{N_f-1}{N_f}\right)} - 1\right) \exp\left(-\frac{(y+h_{N_f})^2}{2\sigma^2}\right) \tag{A.77}$$

and split the integral into N_f intervals in which each of the $N_f - 1$ terms in the integral has a constant value:

$$\mathcal{N} = \left(\frac{\hat{\rho}_1^2}{\hat{\rho}_1 - 1}\right)^{N_f} d_0 \sum_{i=2}^{\infty} \left(\hat{\rho}_1^i - 1\right) \sum_{k=0}^{N_f-1} \int_{i+\frac{k}{N_f}}^{i+\frac{k+1}{N_f}} dy \left(\hat{\rho}_1^{\operatorname{int}\left(y+1-\frac{1}{N_f}\right)} - 1\right) \cdots \times \left(\hat{\rho}_1^{\operatorname{int}\left(y+1-\frac{N_f-1}{N_f}\right)} - 1\right) \exp\left(-\frac{(y+h_{N_f})^2}{2\sigma^2}\right) \tag{A.78}$$

These intervals are such that in the k-th $N_f - k$ terms have the value $(\hat{\rho}_1^i - 1)$, while the remaining k have the value $(\hat{\rho}_1^{i+1} - 1)$. The generic term of the double sum is thus:

$$\begin{aligned}
&(\hat{\rho}_1^i - 1)^{N_f-k} (\hat{\rho}_1^{i+1} - 1)^k \int_{i+\frac{k}{N_f}}^{i+\frac{k+1}{N_f}} dy \, \exp\left(-\frac{(y+h_{N_f})^2}{2\sigma^2}\right) \\
&= (\hat{\rho}_1^i - 1)^{N_f-k} (\hat{\rho}_1^{i+1} - 1)^k \int_{i+h_{N_f}+\frac{k}{N_f}}^{i+h_{N_f}+\frac{k+1}{N_f}} dy \, \exp\left(-\frac{x^2}{2\sigma^2}\right) \\
&= (\hat{\rho}_1^i - 1)^{N_f-k} (\hat{\rho}_1^{i+1} - 1)^k \sqrt{\frac{\pi}{2}}\, \sigma \left[\operatorname{erfc}\left(\frac{i + h_{N_f} + k/N_f}{\sqrt{2}\sigma}\right) - \operatorname{erfc}\left(\frac{i + h_{N_f} + (k+1)/N_f}{\sqrt{2}\sigma}\right)\right]
\end{aligned} \tag{A.79}$$

so that

$$\mathcal{N} = d_0 \sqrt{\frac{\pi}{2}}\, \sigma \left(\frac{\hat{\rho}_1^2}{\hat{\rho}_1 - 1}\right)^{N_f} \sum_{i=2}^{\infty} \sum_{k=0}^{N_f-1} \left(\hat{\rho}_1^i - 1\right)^{N_f-k} \left(\hat{\rho}_1^{i+1} - 1\right)^k \times \left[\operatorname{erfc}\left(\frac{i + h_{N_f} + k/N_f}{\sqrt{2}\sigma}\right) - \operatorname{erfc}\left(\frac{i + h_{N_f} + (k+1)/N_f}{\sqrt{2}\sigma}\right)\right] \tag{A.80}$$

In the end the wall position distribution function reads:

$$\mathcal{P}^{OT}(L) = \sqrt{\frac{2}{\pi}} \sqrt{\frac{\kappa_T}{k_B T}} \times \frac{\prod_{n=1}^{N_f} \left(\hat{\rho}_1^{z_n+1} - 1\right) \exp\left(-\frac{(L/d_0)^2}{2\sigma^2}\right)}{\sum_{i=2}^{\infty} \sum_{k=0}^{N_f-1} \left(\hat{\rho}_1^i - 1\right)^{N_f-k} \left(\hat{\rho}_1^{i+1} - 1\right)^k \left[\operatorname{erfc}\left(\frac{i+h_{N_f}+k/N_f}{\sqrt{2}\sigma}\right) - \operatorname{erfc}\left(\frac{i+h_{N_f}+(k+1)/N_f}{\sqrt{2}\sigma}\right)\right]}. \tag{A.81}$$

Correspondingly, for $\langle L\rangle^{OT}$ we obtain

$$\langle L\rangle^{OT} = \sqrt{\frac{2}{\pi}}\sqrt{\frac{\kappa_T}{k_BT}} \times \frac{\sum_{i=2}^{\infty}\sum_{k=0}^{N_f-1}\left(\hat{\rho}_1^i-1\right)^{N_f-k}\left(\hat{\rho}_1^{i+1}-1\right)^k\left[\exp\left(-\frac{(i+h_{N_f}+k/N_f)^2}{2\sigma^2}\right)-\exp\left(-\frac{(i+h_{N_f}+(k+1)/N_f)^2}{2\sigma^2}\right)\right]}{\sum_{i=2}^{\infty}\sum_{k=0}^{N_f-1}\left(\hat{\rho}_1^i-1\right)^{N_f-k}\left(\hat{\rho}_1^{i+1}-1\right)^k\left[\mathrm{erfc}\left(\frac{i+h_{N_f}+k/N_f}{\sqrt{2}\sigma}\right)-\mathrm{erfc}\left(\frac{i+h_{N_f}+(k+1)/N_f}{\sqrt{2}\sigma}\right)\right]}. \tag{A.82}$$

A.8 Wall jump rates

Let's focus on the diffusive part of Eq. (3.3) for the wall position probability at a given set of filament sizes; abbreviating $\mathcal{P}_{j_1,\ldots,j_{N_f}}(L,t)$ by $\mathcal{P}_{\mathbf{j}}(L,t)$, we have

$$\frac{\partial\mathcal{P}_{\mathbf{j}}(L,t)}{\partial t} = D\frac{\partial}{\partial L}\left(\frac{\partial\mathcal{P}_{\mathbf{j}}(L,t)}{\partial L}+\frac{1}{k_BT}\frac{d\Phi}{dL}\mathcal{P}_{\mathbf{j}}(L,t)\right) \tag{A.83}$$

with $\frac{d\Phi}{dL} = -F(L)$. Let $p_k(t)$ be the probability for the wall to be in the k-th grid point, represented by the interval of width δ centered on $k\delta$, $L\in[(k-1/2)\delta,(k+1/2)\delta)$. For a given filaments' state, it will be given by the integral of $\mathcal{P}_{\mathbf{j}}(L,t)$ over that interval, so that:

$$p_k(t) = \int_{(k-1/2)\delta}^{(k+1/2)\delta} dL\ \mathcal{P}_{\mathbf{j}}(L,t) \tag{A.84}$$

$$p_{k+1}(t) = \int_{(k+1/2)\delta}^{(k+3/2)\delta} dL\ \mathcal{P}_{\mathbf{j}}(L,t) \tag{A.85}$$

for two adjacent grid points. Let's further define the wall *forward rate* $F_{k+1/2}$ of going from k to $k+1$ ($F_{k-1/2}$ from $k-1$ to k) and the *backward rate* $B_{k+1/2}$ of going from $k+1$ to k ($B_{k-1/2}$ from k to $k-1$). For a given k, the time evolution of the probability $p_k(t)$ can be written straightforwardly considering the possible jumps from/to k with the corresponding rates:

$$\begin{aligned}\frac{dp_k(t)}{dt} &= F_{k-1/2}p_{k-1} - (F_{k+1/2}+B_{k-1/2})p_k + B_{k+1/2}p_{k+1}\\ &= -(F_{k+1/2}p_k - B_{k+1/2}p_{k+1}) + (F_{k-1/2}p_{k-1} - B_{k-1/2}p_k)\\ &= -(J_{k+1/2}-J_{k-1/2})\end{aligned} \tag{A.86}$$

where $J_{k+1/2}$ is the net probability flux between sites k and $k+1$ ($J_{k-1/2}$ between $k-1$ and k).

To get the backward and forward rates, let's consider the stationary solution of Eq. (A.83) in the interval $(k-1/2,k+3/2)$, which will be denoted by $\mathcal{P}_{EQ}^{(k)}(L)$, and let's discretize Eq. (A.83) ensuring that the detailed balance is satisfied. According to the *detailed balance equations*,

$$F_{k+1/2}\mathcal{P}_{EQ}^{(k)}(L) = B_{k+1/2}\mathcal{P}_{EQ}^{(k+1)}(L) \tag{A.87}$$

i.e. at equilibrium each elementary process is equilibrated by its reverse process. To get the proper forward and backward jump rates, let's consider the interval $(k-1/2, k+3/2)$ and let's make the assumption that for any k the derivative of the potential $\frac{d\Phi}{dL}$ can be approximated by the constant $\frac{\Delta\Phi_{k+1/2}}{\delta} = \frac{\Phi((k+1)\delta)-\Phi(k\delta)}{\delta}$. Eq. (A.83) then becomes

$$D\frac{\partial}{\partial L}\left(\frac{\partial \mathcal{P}_{EQ}^{(k)}(L)}{\partial L} + \frac{\Delta\Phi_{k+1/2}}{k_BT\delta}\mathcal{P}_{EQ}^{(k)}(L)\right) = 0 \tag{A.88}$$

for $L \in ((k-1/2)\delta, (k+3/2)\delta)$. This equation can be readily solved, and the general solution is the exponential $\mathcal{P}_{EQ}^{(k)}(L) = \zeta_k \exp\left(-\frac{\Delta\Phi_{k+1/2}}{k_BT\delta}L\right) + \theta_k$, with ζ_k and θ_k constants to be found. Plugging this expression into Eqs. (A.84) and (A.85), these constants can be easily written in terms of p_k and p_{k+1}, leading finally to

$$\begin{aligned}\mathcal{P}_{EQ}^{(k)}(L) = &\frac{\Delta\Phi_{k+1/2}(p_k - p_{k+1})}{k_BT\delta\left(\exp\left(-\frac{\Delta\Phi_{k+1/2}}{k_BT}\right)-1\right)^2}\exp\left(-\frac{\Delta\Phi_{k+1/2}}{k_BT}\left(k-\frac{1}{2}\right)\right)\exp\left(-\frac{\Delta\Phi_{k+1/2}}{k_BT\delta}L\right)\\ &+\frac{p_k\exp\left(-\frac{\Delta\Phi_{k+1/2}}{k_BT}\right)-p_{k+1}}{\delta\left(\exp\left(-\frac{\Delta\Phi_{k+1/2}}{k_BT}\right)-1\right)}\end{aligned} \tag{A.89}$$

for $L \in ((k-1/2)\delta, (k+3/2)\delta)$. The corresponding probability flux in the same interval is

$$\begin{aligned}J_{EQ}^{(k)}(L) &= -D\left[\frac{d\mathcal{P}_{EQ}^{(k)}(L)}{dL} + \frac{\Delta\Phi_{k+1/2}}{k_BT\delta}\mathcal{P}_{EQ}^{(k)}(L)\right]\\ &= -\frac{D}{\delta^2}\frac{\Delta\Phi_{k+1/2}}{k_BT}\frac{p_k\exp\left(-\frac{\Delta\Phi_{k+1/2}}{k_BT}\right)-p_{k+1}}{\left(\exp\left(-\frac{\Delta\Phi_{k+1/2}}{k_BT}\right)-1\right)}.\end{aligned} \tag{A.90}$$

for $L \in ((k-1/2)\delta, (k+3/2)\delta)$. Comparing this current with the probability flux defined in Eq. (A.86), $J_{k+1/2} = F_{k+1/2}p_k - B_{k+1/2}p_{k+1}$, we finally get the following forward and backward jump rates:

$$F_{k+1/2} = \frac{D}{\delta^2}\frac{\Delta\Phi_{k+1/2}}{k_BT\left(\exp\left(-\frac{\Delta\Phi_{k+1/2}}{k_BT}\right)-1\right)} \tag{A.91}$$

$$B_{k+1/2} = -\frac{D}{\delta^2}\frac{\Delta\Phi_{k+1/2}\exp\left(-\frac{\Delta\Phi_{k+1/2}}{k_BT}\right)}{k_BT\left(\exp\left(-\frac{\Delta\Phi_{k+1/2}}{k_BT}\right)-1\right)} \tag{A.92}$$

which respect the detailed balance Eq. (A.87), as can be verified by direct substitution into Eq. (A.89).

A.9 Fokker-Planck equation: $\epsilon = 0$ expansion

Let's write the joint probability distribution function $\widetilde{\mathcal{P}}_{j_1,\ldots,j_{N_f}}(x,\tilde{t}\,)$ as an expansion in ϵ and truncate the Fokker-Planck Eq. (3.19) to the first order:

$$\widetilde{\mathcal{P}}_{j_1,\ldots,j_{N_f}}(x,\tilde{t}\,) = \widetilde{\mathcal{P}}^{(0)}_{j_1,\ldots,j_{N_f}}(x,\tilde{t}\,) + \epsilon\widetilde{\mathcal{P}}^{(1)}_{j_1,\ldots,j_{N_f}}(x,\tilde{t}\,) + \ldots \tag{A.93}$$

$$\begin{aligned}
&\frac{\partial\widetilde{\mathcal{P}}^{(0)}_{j_1,\ldots,j_{N_f}}(x,\tilde{t}\,)}{\partial\tilde{t}} + \frac{\partial}{\partial x}\widetilde{J}^{(1)}_{j_1,\ldots,j_{N_f}}(x,\tilde{t}\,) \\
&= \hat{\rho}_1 \sum_{n=1}^{N_f}\left[(1-\delta_{2,j_n})\frac{\alpha_{j_n}(x)}{\alpha_{j_n-1}(x)}\widetilde{\mathcal{P}}^{(0)}_{j_1,\ldots,j_n-1,\ldots,j_{N_f}}(x,\tilde{t}\,) - \frac{\alpha_{j_n+1}(x)}{\alpha_{j_n}(x)}\widetilde{\mathcal{P}}^{(0)}_{j_1,\ldots,j_{N_f}}(x,\tilde{t}\,)\right] \\
&+ \sum_{n=1}^{N_f}\left[\widetilde{\mathcal{P}}^{(0)}_{j_1,\ldots,j_n+1,\ldots,j_{N_f}}(x,\tilde{t}\,) - (1-\delta_{2,j_n})\widetilde{\mathcal{P}}^{(0)}_{j_1,\ldots,j_{N_f}}(x,\tilde{t}\,)\right]
\end{aligned} \tag{A.94}$$

where I have divided both sides of Eq. (A.94) by ϵ and applied Eq. (3.21) to $\frac{\partial}{\partial x}\widetilde{J}^{(0)}_{j_1,\ldots,j_{N_f}}(x,\tilde{t}\,)$. This equation can be integrated from x^* to ∞ applying the boundary conditions on $\widetilde{J}^{(1)}_{j_1,\ldots,j_{N_f}}(x,\tilde{t}\,)$, the normalization of $\widetilde{P}_{EQ}(x|j_1,\ldots,j_{N_f})$, and Eq. (3.25); we get:

$$\begin{aligned}
&\frac{\partial\widetilde{P}_0(j_1,\ldots,j_{N_f},\tilde{t}\,)}{\partial\tilde{t}} \\
&= \hat{\rho}_1 \sum_{n=1}^{N_f}\left[(1-\delta_{2,j_n})\int_{x^*}^{\infty} dx\;\Theta\left(x - \frac{X_n(j_n)}{d_0}\right)\widetilde{\Pi}^{(0)}_{EQ}(x|j_1,\ldots,j_n-1,\ldots,j_{N_f})\right. \\
&\times \widetilde{P}_0(j_1,\ldots,j_n-1,\ldots,j_{N_f},\tilde{t}\,) \\
&\left. - \int_{x^*}^{\infty} dx\;\Theta\left(x - \frac{X_n(j_n+1)}{d_0}\right)\widetilde{\Pi}^{(0)}_{EQ}(x|j_1,\ldots,j_n,\ldots,j_{N_f})\widetilde{P}_0(j_1,\ldots,j_n,\ldots,j_{N_f},\tilde{t}\,)\right] \\
&+ \sum_{n=1}^{N_f}\left[\widetilde{P}_0(j_1,\ldots,j_n+1,\ldots,j_{N_f},\tilde{t}\,) - (1-\delta_{2,j_n})\widetilde{P}_0(j_1,\ldots,j_n,\ldots,j_{N_f},\tilde{t}\,)\right] \\
&= \hat{\rho}_1 \sum_{n=1}^{N_f}\left[(1-\delta_{2,j_n})A^{(n)}(j_1,\ldots,j_n-1,\ldots,j_{N_f})\widetilde{P}_0(j_1,\ldots,j_n-1,\ldots,j_{N_f},\tilde{t}\,)\right. \\
&\left. - A^{(n)}(j_1,\ldots,j_n,\ldots,j_{N_f})\widetilde{P}_0(j_1,\ldots,j_n,\ldots,j_{N_f},\tilde{t}\,)\right] \\
&+ \sum_{n=1}^{N_f}\left[\widetilde{P}_0(j_1,\ldots,j_n+1,\ldots,j_{N_f},\tilde{t}\,) - (1-\delta_{2,j_n})\widetilde{P}_0(j_1,\ldots,j_n,\ldots,j_{N_f},\tilde{t}\,)\right].
\end{aligned} \tag{A.95}$$

The factors $A^{(n)}(j_1, \ldots, j_{N_f})$ have been defined implicitly as

$$A^{(n)}(j_1, \ldots, j_n, \ldots, j_{N_f}) = \int_{x^*}^{\infty} dx\, \Theta\left(x - \frac{X_n(j_n+1)}{d_0}\right) \widetilde{\Pi}^{(0)}_{EQ}(x|j_1, \ldots, j_n, \ldots, j_{N_f})$$
$$= \begin{cases} \exp\left(-f(x^{*'} - x^*)\right) & \text{constant load,} \\ \dfrac{\operatorname{erfc}\left(\sqrt{\tilde{\kappa}_T/2}x^{*'}\right)}{\operatorname{erfc}\left(\sqrt{\tilde{\kappa}_T/2}x^*\right)} & \text{optical trap} \end{cases} \tag{A.96}$$

where $x^{*'} \geq x^*$ is the most advanced tip's position once filament n has polymerized ($j_n \to j_n + 1$). These factors correct the polymerization rates, and take into account the reduction in U_0 due to the presence of the wall.

Appendix B

Appendices to Part II

B.1 Total area of a manyfold: invariance under reparametrization

For the total area of a manyfold parametrized by (x_1, x_2), we have found the elegant formula Eq. (5.17),

$$\mathcal{A} = \int_{\mathcal{U}} \sqrt{\det \mathbf{g}(x_1, x_2)} dx_1 \, dx_2. \tag{B.1}$$

We want now to prove that it is independent of the parametrization chosen. Let's make the change of coordinates from $(x_1, x_2) \in \mathcal{U}$ to $(y_1, y_2) \in \mathcal{V}$. The position of a point on the surface can be written in terms of these new coordinates, and

$$\mathbf{e}_{x_1} = \frac{\partial \mathbf{r}}{\partial x_1} = \sum_{k=1,2} \frac{\partial \mathbf{r}}{\partial y_k} \frac{\partial y_k}{\partial x_1} = \frac{\partial y_1}{\partial x_1} \mathbf{e}_{y_1} + \frac{\partial y_2}{\partial x_1} \mathbf{e}_{y_2} \tag{B.2}$$

and similarly for $\mathbf{e}_{x_2}$. Applying this transformation to the metric, we have

$$g_{ij}(x_1, x_2) = \mathbf{e}_{x_i} \cdot \mathbf{e}_{x_j} = \sum_{k,m=1,2} \frac{\partial y_k}{\partial x_i} \frac{\partial y_m}{\partial x_j} \tilde{g}_{km}(y_1, y_2). \tag{B.3}$$

If we now define the transformation matrix $\mathbf{X}$ as $X_{ij} = \frac{\partial y_j}{\partial x_i}$, we can write Eq. (B.3) as $\mathbf{g} = \mathbf{X}^T \tilde{\mathbf{g}} \mathbf{X}$. If we apply this to Eq. (B.1), we get:

$$\begin{aligned}
\mathcal{A} &= \int_{\mathcal{U}} \sqrt{\det \mathbf{g}(x_1, x_2)} dx_1 \, dx_2 \\
&= \int_{\mathcal{U}} \sqrt{\det \left(\mathbf{X}^T \tilde{\mathbf{g}} \mathbf{X} \right)} dx_1 \, dx_2 \\
&= \int_{\mathcal{U}} \sqrt{\det \tilde{\mathbf{g}}} \, |\det \mathbf{X}| \, dx_1 \, dx_2 \\
&= \int_{\mathcal{V}} \sqrt{\det \tilde{\mathbf{g}}(y_1, y_2)} dy_1 \, dy_2
\end{aligned} \tag{B.4}$$

since the determinant of a matrix product of square matrices equals the product of their determinants, the determinant of a transpose of a matrix is equal to the determinant of the matrix itself and $|\det \mathbf{X}|$ is the Jacobian for the coordinate transformation $(x_1, x_2) \to (y_1, y_2)$. We have thus proved that this formula holds for any parametrization.

B.2 Second order integrator for Langevin Equations

Let's consider a one-dimensional system with velocity v and position x, whose time evolution is described by a second order Langevin equation of the kind of Eq. (6.14). Let h be the integration time step, the position and velocity at time $(n+1)h$ are calculated from those at time nh as follows (Eq.(23) in [111]):

$$\begin{cases} v^{(n+1/2)} = & v^{(n)} + \frac{1}{2}\sqrt{h}\sigma\phi^{(n)} + \frac{1}{2}h\left(f(x^{(n)}) - \gamma v^{(n)}\right)\left(1 - \frac{h\gamma}{4}\right) - \frac{1}{4}h^{3/2}\gamma\sigma\left(\frac{1}{2}\phi^{(n)} + \frac{1}{\sqrt{3}}\xi^{(n)}\right) \\ x^{(n+1)} = & x^{(n)} + hv^{(n+1/2)} + h^{3/2}\sigma\frac{1}{2\sqrt{3}}\xi^{(n)} \\ v^{(n+1)} = & v^{(n+1/2)} + \frac{1}{2}\sqrt{h}\sigma\phi^{(n)} + \frac{1}{2}h\left(f(x^{(n+1)}) - \gamma v^{(n+1)}\right)\left(1 - \frac{h\gamma}{4}\right) - \frac{1}{4}h^{3/2}\gamma\sigma\left(\frac{1}{2}\phi^{(n)} + \frac{1}{\sqrt{3}}\xi^{(n)}\right) \end{cases} \tag{B.5}$$

where γ and $f(x)$ are the friction coefficient and the force divided by the mass, $\phi^{(n)}$ and $\xi^{(n)}$ are independent Gaussian variables with zero mean and unitary variance and $\sigma = \sqrt{2k_BT\gamma/m}$.

B.3 Membrane Grand Canonical insertion/deletion moves

In the following, the simulation schemes for the Grand Canonical MC moves will be explained in detail. These moves are introduced to let the membrane grow as an external force acts locally on some beads to deform it. Each Δ_{GC} steps a Grand Canonical Monte Carlo move is attempted, choosing uniformly between insertion and deletion.

As for the *insertion*, a bead, let's call it j', is selected at random among the N_{nodes} and it is attempted to be replaced by two new beads, $i(\equiv N_{nodes}+1)$ and $j(\equiv j')$, located at symmetric positions with respect to $\mathbf{r}_{j'}$,

$$\mathbf{r}_i = \mathbf{r}_{j'} + \frac{l}{2}\hat{\mathbf{p}} \qquad \mathbf{r}_j = \mathbf{r}_{j'} - \frac{l}{2}\hat{\mathbf{p}} \tag{B.6}$$

where $\hat{\mathbf{p}} = (\sin\theta\cos\phi, \sin\theta\sin\phi, \cos\theta)$, with θ and ϕ distributed according to the probability densities $P(\theta) = \frac{1}{2}\sin\theta$, $\theta \in [0,\pi]$, and $P(\phi) = \frac{1}{2\pi}$, $\phi \in [0, 2\pi]$. l is the distance between i and j and it is taken uniformly distributed between ℓ_{max} and ℓ_{min}, $P(l) = \frac{1}{\ell_{max}-\ell_{min}}$. Defining $u = -\cos\theta$, the probability to sample the specific vector $l\hat{\mathbf{p}}$ is

$$P(l,u,\phi)dl\ du\ d\phi = \frac{1}{4\pi\left(\ell_{max} - \ell_{min}\right)}\ dl\ du\ d\phi. \tag{B.7}$$

Let's notice that the two-beads joint probability for the positions of the two new beads can be reduced to a single-bead probability:

$$\begin{aligned} P(\mathbf{r}_i, \mathbf{r}_j)d\mathbf{r}_i\ d\mathbf{r}_j &= P^{cond}(\mathbf{r}_i \mid \mathbf{r}_j)P(\mathbf{r}_j)d\mathbf{r}_i\ d\mathbf{r}_j \\ &= P(\mathbf{r}_j)d\mathbf{r}_i\ d\mathbf{r}_j = P(\mathbf{r}_i)d\mathbf{r}_i\ d\mathbf{r}_j \end{aligned} \tag{B.8}$$

where the conditional probability has to be one by symmetry. Further defining $R = \frac{l}{2}$ and noting that $d\mathbf{r}_i = R^2 dR\, du\, d\phi$, we have

$$\begin{aligned} P(\mathbf{r}_i)d\mathbf{r}_i &= P(R,u,\phi)dR\, du\, d\phi \\ &= \frac{1}{2\pi\left(\ell_{max}-\ell_{min}\right)}\, dR\, du\, d\phi = \frac{1}{2\pi\left(\ell_{max}-\ell_{min}\right)R^2}\, d\mathbf{r}_i \end{aligned} \tag{B.9}$$

The new attempted configuration is sampled as follows: the new beads i and j are connected to each other and all their possible connections with the N_v vertices in the external perimeter are listed for $3 \leqslant N_v \leqslant 8$, according to geometrical constraints only (see Section 6.4). Each of the external nodes must be connected to either i or j, except two of them who are connected to both ("hinge" nodes, k and l in figure B.1). These hinge nodes cannot be bonded to each other, and are such that they delimit two portions around the polygon contour (each having minimum one vertex) of vertices connected to i only or to j only. Among all these possible configurations, a number $T_{\nu'}$ of them will be compatible with the given distances (each bond must be shorter than ℓ_{max}). If $T_{\nu'} = 0$ the move is immediately rejected with no further calculation, if $T_{\nu'} \geqslant 1$ a configuration is picked at random among the valid ones. The global attempt probability to reach the state ν from ν' is

$$P_{ins}^{att}(\nu' \to \nu) = \frac{1}{N_{nodes}T_{\nu'}} \times \frac{4}{2\pi\left(\ell_{max}-\ell_{min}\right)l^2} \tag{B.10}$$

where the first factor accounts for the probability of choosing one bead over N_{nodes} and one triangulation over $T_{\nu'}$ valid (the factor 4 at the numerator comes from $l = 2R$).

As for the *deletion* move, a bond is selected at random over the existing N_b', and the two connected beads, i and j, are attempted to be replaced by a single bead, j', located at their center of mass. The distances between j' and the N_v vertices in the surrounding convex hull are immediately checked and if one of them is not suitable for bonding, the move is immediately rejected. The attempt probability to reach the state ν' from ν is simply

$$P_{del}^{att}(\nu \to \nu') = \frac{1}{N_b}. \tag{B.11}$$

We want these moves to satisfy micro-reversibility, and to this purpose the ratio between the acceptance probabilities to go from ν ($N_{nodes}+1$ beads) to ν' (N_{nodes} beads) and reverse must satisfy

$$\begin{aligned} \frac{P_{del}^{acc}}{P_{ins}^{acc}} &= \frac{P_{ins}^{att}(\nu' \to \nu)\; P_{\nu'}}{P_{del}^{att}(\nu \to \nu')\; P_{\nu}} \\ &= \frac{N_b}{N_{nodes}T_{\nu'}} \frac{8}{4\pi\left(\ell_{max}-\ell_{min}\right)l^2} \frac{\Lambda^3}{\exp\left(\beta\mu\right)}\; \exp\left[-\beta\left(E_{\nu'}-E_{\nu}\right)\right] \qquad \text{(B.12)} \\ &= \frac{N_b}{N_{nodes}T_{\nu'}} \frac{\ell_{min}^2}{z^{eff}l^2}\; \exp\left[-\beta\left(E_{\nu'}-E_{\nu}\right)\right] \qquad \text{(B.13)} \end{aligned}$$

where the effective fugacity has been defined as

$$z^{eff} = \frac{8\ell_{min}^2}{4\pi\left(\ell_{max}-\ell_{min}\right)} \frac{\Lambda^3}{\exp\left(\beta\mu\right)} = \frac{8\ell_{min}^2}{4\pi\left(\ell_{max}-\ell_{min}\right)} \frac{\Lambda^3}{C\exp\left(-\beta\Sigma a\right)} \tag{B.14}$$

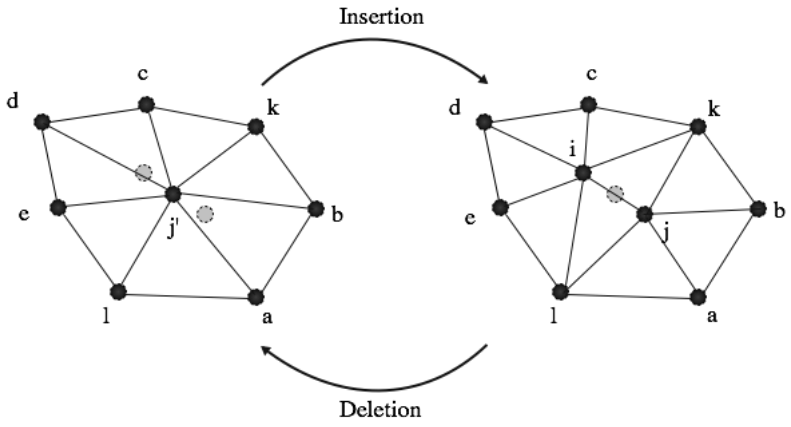

Figure B.1. Example of Grand Canonical Monte Carlo moves.

where Σ is the surface tension and a the area per inserted bead (see Section 6.4) This effective fugacity is an input parameter for the simulations, whose value can be fixed arbitrarily. It has been tested that indeed the surface tension is related to the fugacity according to an exponential relation (see Section 6.4.3).

In the following, the algorithm realizing these moves is explained in detail.

Insertion move

1. A bead j is chosen at random.

2. Check the number of beads connected to j, `NNj`. If `NNj` is not between 3 and 8, the move is rejected.

3. The beads connected to j form the external polygonal hull surrounding the two new beads. These are put in circular order in the list `hull(1:NNj)`. Referring to Fig. B.1, for instance, it would be `hull=(a,b,k,c,d,e,l)` (or cyclic permutations).

4. An exhaustive list of all the possible connections is constructed, basing on the number code: 1 if connected to i, 2 if connected to j, 3 if hinge. For example, for `NNj`=5 the possible connections satisfying all the above specified geometrical requirements (hinge beads divided by at least one bead, and in turn dividing two zones of 1-type and 2-type beads), are:

```
exhaustive_list(1:5,1)=(1, 1, 3, 2, 3)
exhaustive_list(1:5,2)=(1, 3, 2, 2, 3)
exhaustive_list(1:5,3)=(1, 3, 2, 3, 1)
exhaustive_list(1:5,4)=(2, 2, 3, 1, 3)
exhaustive_list(1:5,5)=(2, 3, 1, 1, 3)
exhaustive_list(1:5,6)=(2, 3, 1, 3, 2)
exhaustive_list(1:5,7)=(3, 1, 1, 3, 2)
```

```
exhaustive_list(1:5,8)=(3, 1, 3, 2, 2)
exhaustive_list(1:5,9)=(3, 2, 2, 3, 1)
exhaustive_list(1:5,10)=(3, 2, 3, 1, 1)
```

as there are 10 possibilities.

5. The two new positions are sampled:

```
ll=rng()*(lmax-lmin)+lmin
theta=2.d0*pi*rng()
phi=acos(2.d0*rng()-1.d0)
pp(1)=cos(theta)*sin(phi)
pp(2)=sin(theta)*sin(phi)
pp(3)=cos(phi)
pos1(:)=pos_mb(:,j)-ll*pp(:)/2.d0
pos2(:)=pos_mb(:,j)+ll*pp(:)/2.d0
```

6. For each configuration `k` in `exhaustive_list` the distances are checked: for `m=1,...,NNj`, the distance `r1` between `hull(m)` and `i` and `r2` between `hull(m)` and `j` are calculated; if `exhaustive_list(m,k)=1` and `r1`$\notin$ [`lmin`, `lmax`], or if `exhaustive_list(m,k)=2` and `r2`$\notin$ [`lmin`, `lmax`], or if `exhaustive_list(m,k)=3` and either `r1` or `r2`$\notin$ [`lmin`, `lmax`], then the configuration is not valid. The number of valid configuration is registered as `nvalidconf`. If `nvalidconf=0` the move is rejected, otherwise a configuration is picked at random and associated with the array `hull`.

7. A temporary list `bend_temp` is created; it contains the same triangles as in `list_bend`, with these differences: (i) triangle pairs containing j' (in the initial state) and beads that aren't hinges in the final state, will be unchanged, with $j' \to j$ or $j' \to i$ depending on the triangle; (ii) the two triangle pairs having as common bond $j'k$ and $j'l$ respectively (*i.e.* bonds between the central bead and the two hinges) are doubled: triangle `(j',k,b,c)` for instance (see Fig. B.1) splits into `(j,k,i,b)` and `(i,k,j,c)`; this implies two new triangles pairs in the list; (iii) the new triangle pair `(i,j,k,l)` is added. There are then three new triangle pairs (corresponding to three new bonds) in the temporary list.

8. Temporary lists `bond_temp` and `EV_temp` are created according to the new proposed configuration. The former is based on the chosen triangulation, the latter on the new distances between neighboring beads.

9. The old and new energies are computed and the acceptance probability is calculated as:

```
delta_e=enew-eold
acc=N_nodes*nvalidconf/(nbond+3)*z*ll**2/lmin_mb**2*exp(-delta_e)
```

where `nbond` is the number of bonds in the old configuration.

10. If the move is accepted, all the lists are set equal to the temporary ones, the number of nodes becomes `N_nodes+1`, the number of bonds `nbond+3`. The velocities of the new nodes `i` and `j` are taken from the Maxwell distribution and their positions are set equal to `pos1` and `pos2`.

GC deletion

1. A bond `ktr` is extracted at random from `list_bend`, involving the four beads i, j, k, l as follows:

```
i=max(list_bend(1,ktr),list_bend(2,ktr))
j=min(list_bend(1,ktr),list_bend(2,ktr))
k=list_bend(3,ktr)
l=list_bend(4,ktr)
```

   where `i` and `j` are the nodes to be merged.

2. The new position `pos_new` is computed as the center of mass of `i` and `j`.

3. Check the number of beads connected to i, `NNi`, and to j, `NNj`. The number of nodes in the external hull is `nb=NNi+NNj-4`. If `nb` is not between 3 and 8, the move is rejected.

4. All the nodes in the external hull are put in circular order in the list `hull(1:nb)` similarly to the insertion move.

5. Check that all the distances between the nodes in `hull` and the new position are suitable for bonding. If not, the move is rejected.

6. The exhaustive list of all the possible connections of nodes `i` and `j` to the external hull is constructed, as described for the insertion.

7. Similarly to the insertion procedure, all the valid configurations are listed by checking the distances. Here, `nvalidconf` must be positive and the current configuration of bonds must be included in the valid ones.

8. The temporary lists (bending, bonding, EV) are created similarly to what described above for the insertion move.

9. The old and new energies are calculated and:

```
delta_e=enew-eold
ll=distance(pos_mb(i),pos_mb(j))
acc=nbond/(N_nodes-1)/nvalidconf*lmin_mb/z/ll**2*exp(-delta_e)
```

   where `nbond` is the number of bonds in the old configuration.

10. If the move is accepted, all the lists are set equal to the temporary ones. The velocity and position of `i` are set to zero, and `pos_mb(:,j)=pos_new` with a velocity sampled from the Maxwell distribution. The zeros in the position and velocity arrays are moved to the end and all the nodes are renamed: if `m>i` `m`→`m-1` in all the lists. This is the corresponding part of the code:

```
! Remove node i from the position and velocity arrays...
    pos_mb(:,i)=0.d0
    vel_mb(:,i)=0.d0
    pos_mb(:,j)=pos_new(:)
    vel_mb(:,j)=(2.d0*rng()-1.d0)*vmx_mb
    do ii=i,N_nodes-1
      pos_mb(1:3,ii)=pos_mb(1:3,ii+1)
      vel_mb(1:3,ii)=vel_mb(1:3,ii+1)
    end do
    pos_mb(:,N_nodes:)=0.d0
    vel_mb(:,N_nodes:)=0.d0
! ...and rename all the beads n > i --> n-1 (if I remove the i=20 vertex, then the
! 21st becomes the 20th, the 22nd the 21st etc.
    do ii=1,N_nodes-1
      do n=1,point_bond(ii)
        jj=list_bond(n,ii)
        if(jj.ge.i) list_bond(n,ii)=jj-1
      end do
    end do

    do ii=1,nbond-3
      do n=1,4
        jj=list_bend(n,ii)
        if(jj.ge.i) list_bend(n,ii)=jj-1
      end do
    end do
```

Finally the number of nodes is changed from `N_nodes` to `N_nodes-1` and the number of bonds from `nbond` to `nbond-3`.

B.4 MD filaments simulations: results for the optical-trap set-up

The bundle in the optical trap set–up has been simulated using the same model as in the past: a mobile wall, rigid and smooth, is subject to the polymerization force and to the external harmonic force, $\kappa_T L$, opposite to the bundle growth. The interaction energy between the bonded monomers and the wall is taken as a 2D Lennard-Jones repulsion [116]:

$$U_{wall} = \frac{3\sqrt{3}}{2}\epsilon_{wall}\sum_{i=1}^{N}\left[\left(\frac{\sigma_{wall}}{L_{wall}-x_i}\right)^9 - \left(\frac{\sigma_{intra}}{L_{wall}-x_i}\right)^3\right]\Theta\left(r_{cutoff}^{wall} - (L_{wall}-x_i)\right) \tag{B.15}$$

where x_i is the x coordinate of the i-th monomer of one of the filaments. At each step, the equations of motion of filaments (monomers) and wall are integrated using the same scheme as for the membrane beads, see Section B.2, [111]. Two simulations have been performed: the first with $N_f = 1$ and $\kappa_T = 0.019375$, the

second with $N_f = 8$ and $\kappa_T = 0.275$, both at $\hat{\rho}_1 = 2.5$. All the other parameters for the simulations have been taken equal to those chosen in [116].

Results for the wall position distribution functions are shown in Fig. B.2, where the mean field prediction is indicated by the blue solid line; as for the average wall position, in the $N_f = 1$ case $\langle L \rangle^{\rm OT} = 47.9 d_0$ is slightly larger than what expected for rigid filaments, $L^{\rm MF} = 47.29 d_0$, as a manifestation of filament flexibility (see Part I). The same occurs for $N_f = 8$: $\langle L \rangle^{\rm OT} = 26.92 d_0$ versus $L^{\rm MF} = 26.65 d_0$.

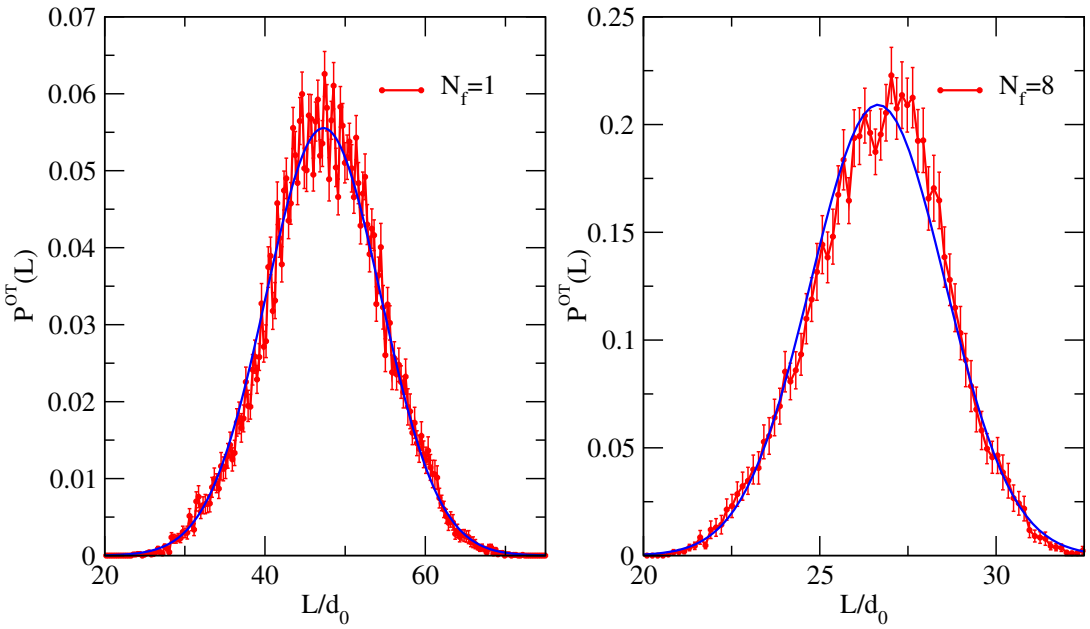

Figure B.2. Equilibrium wall distribution $P(L)$ for a single filament ($N_f = 1$, left panel) and a bundle of eight filaments ($N_f = 8$, right panel) growing at $\hat{\rho}_1 = 2.5$ against a mobile wall subject to a optical trap restoring force. The Gaussian curve indicates the equilibrium distribution based on the mean field model [5, 47, 116].

Other quantities have been investigated as well, following what has been done in [116]. Fig. B.3 reports three related correlation functions, relative to the $N_f = 8$ simulations:

1. the wall position autocorrelation function $C_{LL}(t) = \langle \delta L(t) \delta L(0) \rangle$, which provides the main relaxation, right panel. It exhibits a single exponential behavior well represented by $3.509 \exp(-t/\tau_L)$ with $\tau_L = 1440 \tau_D$ ($\tau_D = d_0^2/D$, see Part I);

2. the single filament size fluctuations, $C_{ii}(t) = \langle \delta i(t) \delta i(0) \rangle$, left top panel. It exhibits a relaxation with two characteristic times that can be well fitted by a linear combination of exponentials. The slow relaxation time is approximately equal to τ_L;

3. the correlation functions for the longitudinal part of the single filament end-to-end vector $C_{xx}(t) = \langle \delta x(t) \delta x(0) \rangle$, left bottom panel. It has a relaxation similar to $C_{ii}(t)$.

In any case, results are presented in comparison with data from [116], where a simulation scheme similar to what is presented in this thesis has been used, but with different procedures for the (de)polymerization moves, which were much slower and less efficient. The agreement is always good, enforcing the validity of our simulation algorithm.

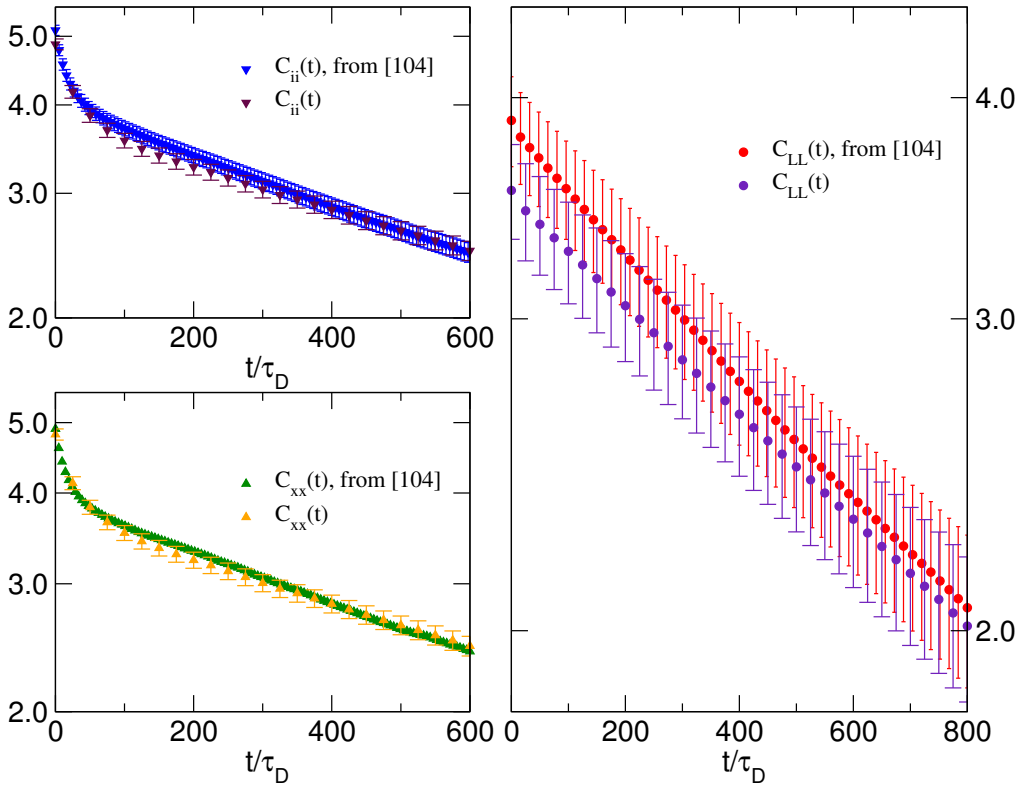

Figure B.3. Time correlation functions of the wall position (red circles), filaments size (blue triangles) and end-to-end distance (green triangles) for $N_f = 8$. The wall position correlation function is fitted by $3.509\exp(-t/\tau_L)$ with $\tau_L = 1440\tau_D$.

The last investigated quantity is the autocorrelation function of the fluctuations of the transverse component of the transverse single filament end-to-end vector, $R_\perp = \sqrt{(y_{j_n} - y_1)^2 + (z_{j_n} - z_1)^2}$ where j_n is the number of monomers in the n-th filament and y_1 and z_1 the transverse components of the filament's seed. Again, a linear combination of two exponential decays well represents the relaxations, the long relaxation time being again the wall position autocorrelation function relaxation time τ_L for the respective cases. The resulting autocorrelation functions are shown in Fig. B.4, showing again a very good agreement with results presented in [116].

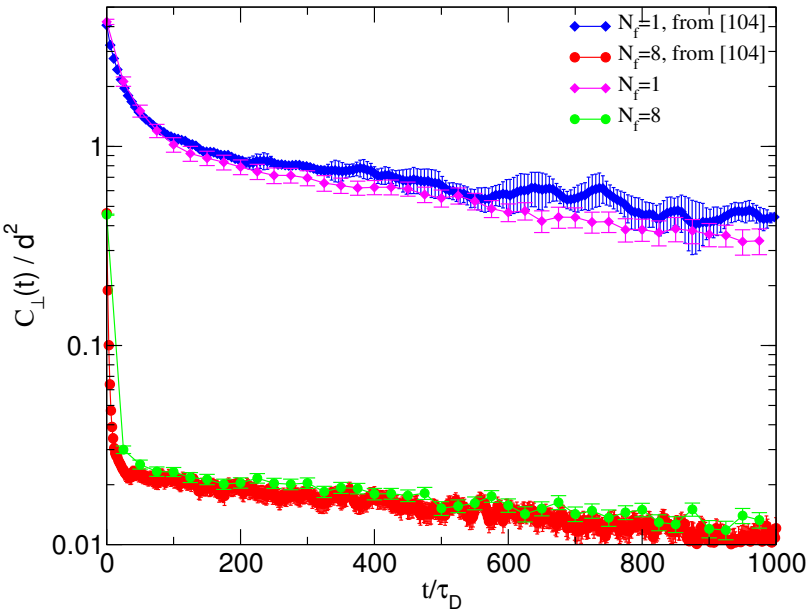

Figure B.4. Time correlation function of the fluctuation $\delta R_\perp(t) = R_\perp(t)\langle R_\perp\rangle$ of the modulus $R_\perp = \sqrt{(y_{jn} - y_1)^2 + (z_{jn} - z_1)^2}$ of the transverse part of the end-to-end vector of the single filament of the bundle with $N_f = 8$ (red circles) and $N_f = 1$ (blue diamonds).

Conclusions

The focus of the present work has been the mechanism of force production by polymerization of actin filaments, which are the cytoskeleton main components. In living cells polymerization forces drive the onset of temporary structures beneath the cell membrane, surrounding the cytoskeleton, which are fundamental for cell motility. These structures are the *lamellipodia*, a flat deformation protruding in the front of the cell filled by a quasi-2D actin filaments network, and the *filopodia*, finger-like protrusions composed by bundled parallel actin filaments surrounded by the cell membrane. Filopodium in particular has been the main subject of this thesis. The understanding of the mechanisms leading to the formation of such structures has started from fundamental questions related to the mechanism of force production by polymerizing actin filaments in simplified systems with respect to a real cell. Considering a bundle of actin filaments immersed in a solution of free monomers, it will tend to grow on average if the free monomer density is large enough to make the polymerization rate larger than the depolymerization rate (supercritical conditions). If their growth is opposed by an obstacle loaded with a pushing force, their growth velocity will be decreased or even stopped, if the force is large enough. The value of the force at which the filaments growth stops is the *stalling force*, F_s. Equivalently, if the filaments grow in contact with a resisting obstacle, loaded with a force F, this will be displaced by the growing filaments, with a velocity v depending on the intensity of the opposing force: the relation linking v to F is the *velocity-load relationship*. These two quantities have been central in theoretical and experimental investigations on actin polymerization forces.

Given the large persistence length of actin filaments, which measures their rigidity, most of the theories modeling the phenomenon picture them like *perfectly rigid rods*, with length that changes in time by adding or removing subunits, mimicking (de)polymerization reactions. Thermodynamic arguments (mean-field model [5]) and statistical mechanics treatments (brownian ratchet models [6–8]) have been developed to provide theoretical predictions for both the stalling force and the velocity-load relationship. All these models predict the same stalling force (given by Eq. (1.9)), while the velocity-load relationship is model-dependent – in particular it depends on how the work performed to push the obstacle is shared among the filaments: at the opposite extremes, the *Perfect Load Sharing* condition is attained when the work is equally divided among all the filaments, and the *No Load Sharing* condition, on the contrary, is realized when all the work is done by one filament (the longest one) while the others lag behind. A *Partial Load Sharing* condition is attained when the presence of the other filaments in the bundle decreases the amount of work that one filament needs to perform against the wall to polymerize

("subsidy" effect [6]). The velocity at a given load increases by increasing the level of work sharing among the filaments.

The aim of the present work has been to develop coarse-grained models of this complex system (actin filaments growing against obstacles) to study the dynamics of filopodia, and two different models have been developed, at different coarse-graining levels. The first one, presented in the first part of the thesis, is based on a stochastic approach for filaments with size changing in time and growing in contact with loaded rigid obstacles. This study is limited to the one dimensional case of a planar obstacle (wall) and filaments with an initial growth direction perpendicular to it (a generalization is possible but it has not been explored). Within this simple model, it is not clear how to introduce possible mutual interactions among filaments, and moreover it is independent on the lateral distribution of the filament seeds (*i.e.* perpendicular to the growth direction), while it does depend on their longitudinal distribution (*i.e.* parallel to the growth direction). The second model, presented in the second part of the thesis, is particle-based, hence at a lower coarse-graining level; this allows to consider more general cases, in particular inter-filament interactions can be explicitly introduced and, most importantly, the interaction with flexible and deformable obstacles (*i.e.* membranes) can be considered; this is a relatively new and definitely less popular approach, with few exceptions [19, 88, 116].

Within the first model, filaments have been treated as discrete wormlike chains with a realistic persistence length; the number of monomers in each filament can change by adding and removing one unit per time with a polymerization rate larger than the depolymerization (supercritical conditions). The seeds of the filaments (the first two anchored monomers) have been taken with a *staggered* disposition, *i.e.* homogeneously distributed within a distance d_0 (monomer size); calculations for the *unstaggered* disposition, *i.e.* all the seeds lined-up at the same distance from the obstacle, have been performed but not reported here, and also other dispositions (*e.g.* a random distribution) could be chosen. In the first part of the thesis, the Statistical Mechanics formalism to treat the bundle of (de)polymerizing filaments has been developed; we have studied the equilibrium properties of a bundle of filaments anchored at one end to a fixed plane and growing at the other end in contact with a mobile loaded wall. Mimicking the experimental conditions of ref. [10], we put the bundle in an optical trap set up, where the load is proportional to the distance between the grafting and the moving walls, $F = \kappa_T L$, with κ_T trap strength constant. At stalling, this force matches the bundle force (both equal to the stalling force F_s) at a value of L which depends on κ_T, $L_s = F_s/\kappa_T$; there, the bundle growth is stopped and a genuine equilibrium state is established [47]. Resuming the main findings:

1. Flexibility does not affect the stalling force significantly: the stalling force for a bundle of flexible filaments is very close to the value predicted by previous models [5–7] for rigid filaments – only few percents larger. Moreover, a Statistical Mechanics proof of this popular expression for F_s has been provided in the rigid filament case [47].

2. Since filaments can bend, the number N_0 of filaments simultaneously in contact with the obstacle can be larger than one, while for rigid filaments with the same seeds disposition it must be $N_0 = 1$ [6–8].

3. In particular, N_0 increases with the trap width like $\sim L^2$, but it cannot reach the value N_f since if filaments get too long they have a finite probability (increasing with their length) to escape laterally and grow parallel to the wall, not participating to the force production anymore. We label these filaments as *escaping filaments*.

4. In optical trap, the occurrence of escaping filaments can be avoided by properly choosing the value of the strength constant of the trap and hence the equilibrium bundle length. We have established the condition on κ_T to avoid entering in the escaping regime.

We used the same model to study the dynamical behavior of staggered actin bundles in optical trap set up, claiming that a relaxation experiment in optical trap can provide the full velocity-load relationship $v(F)$ in a much easier way than the usual constant load experiments: in the latter, the external force is fixed, the filaments are let grow against the loaded obstacle and a stationary velocity is established. In this case, one experiment gives *one point* of the $v(F)$ curve – one value of the stationary velocity given one value of the force. On the other hand, in an optical trap experiment the load evolves from a small value up to the stalling force, when the filaments growth is finally stopped; at any given moment, the value of the load is known, the velocity can be measured and the velocity-load relationship can be drawn for a wide range of forces, with only one experiment. The two velocity-load relationships are equivalent if there is a sufficiently wide time scale separation between the relaxation time needed by the wall to adjust to a change of the external force in the optical trap and the characteristic time needed by the chemistry (polymerization/depolymerization) to change the conformation of the bundle [45] – the load changes very slowly on the time interval over which the chemical events take place and the bundle tips relax. This separation of timescales implies that during the slow variation of the trap amplitude, and thus of the load, the distribution of the filament lengths (with respect to the position of the obstacle) remains equivalent to the distribution in a hypothetical constant load experiment with load value set the force in optical trap at the current stage of the relaxation process [45, 54]. Formulating the problem in a suitable Markovian formalism, numerical realizations of the time evolution of the system (filaments+moving wall) have been performed using a classical Gillespie algorithm [57] for both rigid and flexible bundles in optical trap; in the case of rigid filaments experiments with a constant load have been performed as well. In the case of flexible filaments, establishing a stationary state at constant velocity in a constant-load experiment is impossible since for large enough time filament would grow too long and the escaping regime would be attained. In the optical trap, conversely, the final bundle length is controlled by a proper choice of the trap strength constant, so that the occurrence of escaping filaments can be avoided. We have obtained for the two protocols the classical force-velocity relationship: for rigid filaments, the two curves coincide with the popular brownian ratchet prediction [6, 7, 12]. This universality is due to the timescale separation discussed above, which has been verified for both rigid and flexible filaments. In the latter case, we have observed a dependence of the velocity-load relationship on the bundle length, which we have identified as a *pure flexibility effect* suggesting to generalize the velocity-load relationship as $v(F, \lambda)$ to include the filaments flexibility degree λ, here defined as the ratio between the bundle average length and a crossover length beyond which

flexibility effects start to manifest. For $\lambda \leq 1$ the velocity-load relationship closely follows the brownian ratchet prediction for staggered rigid bundles [6,7,12], for $\lambda > 1$ the velocity results to be significantly increased with respect to the rigid behavior. This effect is even more evident when plotting the power, $P = vF$, as a function of the load F (see Fig. 3.12): filament flexibility in this model manifests as a significant enhancement of the power of transduction of chemical into mechanical energy. The curves for increasing λ move from the rigid model prediction (partial load sharing condition) towards the perfect load sharing behavior. A linear combination of the corresponding $v(F)$ relationships, with coefficients depending on λ, is shown to well describe the curves $v(F, \lambda)$ observed for flexible filaments. The spectacular power increase with λ at a given load F is the result of an improved work sharing capacity of the bundle due to the increasing fraction of filaments touching the wall when developing the polymerization force opposite to the load F. Again, the perfect load sharing condition, which would correspond to all the filaments in contact with the wall ($N_0 = N_f$), cannot be reached since filaments start to escape. Three different regimes, namely rigid, flexible (non-escaping) and escaping, have been characterized using the optical trap set up for different values of the trap strength constant, and their boundaries have been quantitatively established. Our work shows how filament flexibility could be easily considered in interpreting future experiments, in a way which enriches considerably the present dominant theoretical model.

The second part of this thesis has been focused on cellular membranes and their interaction with pushing filaments, with the purpose of generalizing the treatment of filaments growing against rigid obstacles to the more realistic scenario in which filaments push and deform a flexible membrane – which is the case of filaments protruding into a filopodium. The cell membrane is a double phospholipid layer that behaves as an effective 2D fluid, with lipids diffusing among its surface. Large part of the work has been devoted to the treatment of membrane elasticity, first in a continuum theory framework and then translating it into a discrete model which could be employed in numerical simulations. In order to develop a numerical treatment of the membrane, it has been discretized into a triangulated surface, where the elementary units (*beads* or *nodes*) are connected to the next neighbors by tethers forming a triangular network. These beads interact with each other by bonding, non-bonding (excluded volume) and bending interactions, these latter reproducing the popular Helfrich free energy [14]. While the most of the studies exploited MC simulations to study the membrane behavior (see *e.g.* [19]) , in this work numerical simulations have been performed in a MD-like fashion – the dynamics of the system has been modeled choosing a Langevin approach and the position and velocity of every node were evolved in time, starting from a regular triangular lattice, solving the corresponding Langevin equations using a second-order integrator [111]. In order to reproduce the fluid character of the membrane, *bond-flipping* Monte Carlo moves [15,17,18] have been introduced: at given time intervals, a tether is selected at random and the adjacent two triangles having this bond as common edge are considered, the bond is attempted to be cut and replaced by a tether joining the beads at the opposite vertices of the two triangles (see Fig. 6.4). This procedure leads indeed to a fluid character of the membrane, as verified by analyzing the beads mean square displacement as a function of time in the long time limit (see Fig. 6.5). The membrane surface tension, which is an important quantity to determine the

force opposing to the filaments' growth, has been calculated by three methods:

1. First, simulations of a flat membrane with a fixed number of beads have been performed, and the surface tension has been calculated from the spectrum of the membrane height fluctuations, Eq. (5.56), at small wave vectors q.

2. Second, from the same simulation data, the surface bending has been calculated using the virial expression Eq. (5.71) relating the membrane surface tension to the pressure tensor.

3. Finally, *grand-canonical Monte Carlo moves* [19] have been introduced to let the number of beads change in time, adding or removing beads from the triangular mesh, carefully keeping the triangulation valid after each move. This lets simulating the formation of strong deformations of the membrane, like cylindrical protrusions: in this case the radius of the tube pulled out of a membrane is related to the surface tension by Eq. (5.47) [105], and hence measuring the radius of the cylindrical protrusion gives a measure of the surface tension.

All the surface tension measurements brought to compatible values, with a remarkable level of agreement. This is a noticeable result of this part of the work, providing a strong support to the equivalence of these three rather different ways to obtain this crucial property. From previous attempts, the numerical evidence of this equivalence was rather weak (see e.g. [95]). Moreover, this result gives general confidence in the model and the simulation algorithm, which result to provide a valid coarse-grained description of this complex system.

The last part of the work has been devoted to the simulation of bundles of filaments interacting with the membrane: starting from the seeds, filaments were let grow towards the overlying membrane, initially flat, pushing it from below. The simulation procedure let us observe the onset of filopodium-like protrusions in the membrane patch. Simulations of membrane+filaments systems have been performed with both rigid and flexible filaments, pointing out some interesting results:

1. Both flexible and rigid filaments in bundles ($N_f > 1$) are able to create filopodial protrusions, while single filaments cannot: both in the flexible and in the rigid case, a single filament remains stalled by the above membrane.

2. *Flexible filaments protrude faster than rigid filaments*: again, filament flexibility manifests as an enhancement of the bundle velocity with respect to the rigid case.

3. *Flexible filaments' behavior appears to be insensitive to the seeds disposition*: staggered or unstaggered (*i.e.* lined-up) seeds dispositions lead to similar protruding dynamics. Rigid filaments, on the reverse, protrude faster when in the staggered disposition, showing the ability to exploit the "subsidy" effect introduced by [6] even when in contact with flexible barriers.

4. *No escaping filaments* have been observed: this is due to the presence of the membrane embedding the bundle and preventing the filaments from bending too much, and to the choice of the initial distance between the seeds and the membrane – the filaments sizes at the moment they meet the membrane resistance are too small ($9 \div 11$ monomers) to enter the escaping regime.

These results, though preliminary and semi-quantitative, can inspire interesting further developments: first, more sophisticated analysis can be performed to extract a velocity-load relationship, to be compared with experimental results on GUVs for instance. Second, a length-dependent free monomer density could be introduced, as motivated by [4], in order to reproduce the diffusion-limited filopodium elongation. Finally, more realistic features can be introduced in the model: for instance, in this study the filament seeds have been taken parallel to each other and perpendicular to the grafting plane. This situation can be generalized taking random orientations within a suitable range of angles. Moreover, the action of other auxiliary proteins can be introduced by cross-linking the filaments (like fascin) or by allowing for lateral filament branches (as happens in presence of the Arp2/3 complex).

Bibliography

[1] H. E. Huxley and J. Hanson. Changes in the cross-striations of muscle during contraction and stretch and their structural interpretation. *Nature*, 173:973, 1954. 2

[2] H. E. Huxley and R. Niedergerke. Structural changes in muscle during contraction: Interference microscopy of living muscle fibres. *Nature*, 173:971, 1954. 2

[3] J. Zimmermann, C Brunner, M Enculescu, M Goegler, A Ehrlicher, J. Kas, and M. Falcke. Actin filament elasticity and retrograde flow shape the force-velocity relation of motile cells. *Biophysical Journal*, 102:287, 2012. 2

[4] A. Mogilner and B. Rubinstein. The physics of filopodial protrusion. *Biophys. J.*, 89:782, 2005. 3, 5, 94, 101, 102, 103, 104, 105, 154, 158, 198

[5] T. L. Hill. Microfilament or microtubule assembly or disassembly against a force. *Proc. Nat. Acad. Sci. USA*, 78:5614, 1981. 3, 4, 9, 18, 19, 62, 82, 190, 193, 194

[6] A. Mogilner and G. Oster. The polymerization ratchet model explains the force-velocity relation for growing microtubules. *Eur. Biophys. J.*, 28:235, 1999. 3, 4, 9, 23, 92, 193, 194, 195, 196, 197

[7] S. C. Peskin, G. M. Odell, and G. F. Oster. Cellular motions and thermal fluctuations: The brownian ratchet. *Biophys. J.*, 65:316, 1993. 3, 4, 9, 20, 21, 22, 23, 102, 193, 194, 195, 196

[8] K. Tsekouras, D. Lacoste, K. Mallick, and J.-F. Joanny. Condensation of actin filaments pushing against a barrier. *New J. Phys.*, 13:103032, 2011. 3, 19, 25, 26, 27, 193, 194

[9] M. Dogterom and B. Yurke. Measurement of the force-velocity relation for growing microtubules. *Science*, 278:856, 1997. 3, 13, 14, 15, 20, 27

[10] M. J. Footer, J. W. J. Kerssemakers, J. A. Theriot, and M. Dogterom. Direct measurement of force generation by actin filament polymerization using an optical trap. *Proc. Nat. Acad. Sci. USA*, 104(7):2181, 2007. 3, 4, 15, 16, 17, 27, 28, 45, 48, 49, 53, 55, 60, 62, 68, 72, 80, 89, 92, 194

[11] G. S. van Doorn, C. Tanase, B. M. Mulder, and M. Dogterom. On the stall force for growing microtubules. *Eur. Biophys. J.*, 29:2, 2000. 3, 19, 20, 82

[12] D. Démoulin, M.-F. Carlier, J. Bibette, and J. Baudry. Power transduction of actin filaments ratcheting in vitro against a load. *Proc. Nat. Acad. Sci. USA*, 111(50):17845, 2014. 3, 16, 17, 20, 23, 24, 28, 53, 82, 85, 195, 196

[13] A.E. Carlsson. Model of reduction of actin polymerization forces by atp hydrolysis. *Phys. Biology*, 5:036002, 2008. 3

[14] W. Helfrich. Elastic properties of lipid bilayers: theory and possible experiments. *Z. Naturforsch.*, 28c:693, 1973. 5, 117, 196

[15] G. Gompper and D.M. Kroll. Network models of fluid, hexatic and polymerized membranes. *J. Phys.: Condens. Matter*, 9:8795, 1997. 5, 125, 126, 127, 196

[16] G. Gompper and D.M. Kroll. Random surface discretizations and the renormalization of the bending rigidity. *J. Phys. I France*, 6:1305, 1996. 5, 125, 126, 129

[17] G. Gompper and D.M. Kroll. *Triangulated-Surface Models of Fluctuating Membranes,* In: Nelson, D. and Piran, T. and Weinberg, S. (Eds.), *Statistical Mechanics of Membranes and Surfaces*, chapter 12, page 359. World Scientific Publishing Co. Pte. Ltd., 2004. 5, 125, 126, 196

[18] D. Nelson, T. Piran, and S. Weinberg, editors. *Statistical Mechanics of Membranes and Surfaces*. World Scientific Publishing Co. Pte. Ltd., 2004. 5, 196

[19] J. Weichsel and P. L. Geissler. The more the tubular: dynamic bundling of actin filaments for membrane tube formation. *PLoS Comput. Biol.*, 12:1, 2016. 4, 5, 45, 125, 140, 142, 143, 144, 156, 194, 196, 197

[20] David Boal. *Mechanics of the Cell*. Cambridge University Press, Cambridge, UK, 2012. 9, 17, 95, 96, 97, 98

[21] F. Pamapaloni, G. Lattanzi, A. Jonas, T. Surrey, E. Frey, and E.-L. Florin. Thermal fluctuations of grafted microtubules provide evidence of a length-dependent persistence length. *Proc. Nat. Acad. Sci. USA*, 103(27):10248–10253, 2006. 9

[22] S. Inoué and E. D. Salmon. Force generation by microtubule assembly/disassembly in mitosis and ralated movements. *Mol. Biol. of the Cell*, 6:1619, 1995. 9

[23] T. Risler. *Cytoskeleton and Cell Motility,* In: Meyers R. (eds), *Encyclopedia of Complexity and System Science*, pages 1738–1774. Springer, 2009. 9, 10

[24] J. A. Theriot. Polymerization motors. *Traffic*, 1(1):19, 2000. 11, 12, 21

[25] H. E. Huxley. Muscular contraction and cell motility. *Nature*, 243:445, 1973. 12

[26] A. De Lozanne and J. A. Spudich. Disruptionof the *Dictyostelium* myosin heavy chain gene by homologous recombination. *Science*, 236:1086, 1987. 12

[27] J. D. Cortese, B. III Schwab, C. Frieden, and E. L. Elson. Actin polymerization induces a shape change in actin-containing vesicles. *Proc. Nat. Acad. Sci. USA*, 86:5773, 1989. 12

[28] D. A. Lauffenburger and A. F. Horwitz. Cell migration: A physically integrated molecular process. *Cell*, 84:359, 1996. 12

[29] T. D. Pollard and G. G. Borisy. Cellular motility driven by assembly and disassembly of actin filaments. *Cell*, 112:453, 2003. 12

[30] L. Santella, N. Limatola, and J. T. Chun. *Actin Cytoskeleton and Fertilization in Starfish Eggs,* In: Sawada, Inoue and Megumi (eds), *Sexual Reproduction in Animals and Plants*, pages 141–155. Springer, 2014. 12

[31] N. F. Wilson, M. J. Fogleson, and W. J. Snell. The chlamydomonas mating type plus fertilization tubule, a prototypic cell fusion organelle: Isolation, characterization, and in vitro adhesion to mating type minus gametes. *J. Cell. Biol.*, 137(7):1537, 1997. 12

[32] L. P. Cramer and T. J. Mitchison. Myosin is involved in postmitotic cell spreading. *J. Cell. Biol.*, 131(1):179, 1995. 12

[33] J. A. Theriot, T. J. Mitchison, L. G. Tilney, and D. A. Portnoy. The rate of actin-based motility of intracellular listeria monocytogenes equals the rate of actin polymerization. *Nature*, 357:257, 1992. 12

[34] J. A. Theriot and Mitchison. Actin microfilament dynamic in locomoting cells. *Nature*, 352:126, 1991. 12

[35] T. P. Loisel, R. Boujemaa, D. Pantaloni, and M. F. Carlier. Reconstitution of actin-based motility of listeria and shigella using pure proteins. *Nature*, 401(6753):613, 1999. 12, 13

[36] S. Cudmore, P. Cossart, G. Griffiths, and M. Way. Actin-based motility of vaccinia virus. *Nature*, 378:636, 1995. 13

[37] F. Frischknecht, V. Moreau, S. Röttger, S. Gonfloni, I. Reckmann, G. Superti-Furga, and M. Way. Actin-based motility of vaccinia virus mimics receptor tyrosine kinase signalling. *Nature*, 401(6756):926, 1999. 13

[38] C. J. Merrifield, S. E. Moss, C. Ballestrem, B. A. Imhof, G. Giese, I. Wunderlich, and Almers W. Endocytic vesicles move at the tips of actin tails in cultured mast cells. *Nat. Cell. Biol.*, 1(1):72, 1999. 13

[39] A. L. Rozelle, L. M. Machesky, M. Yamamoto, M. H. E. Driessens, R. H. Insall, M. G. Roth, K. Luby-Phelps, G. Marriott, A. Hall, and H. L. Yin. Phosphatidylinositol 4,5-bisphosphate induces actin- based movement of raft-enriched vesicles through wasp-arp2/3. *Curr. Biol.*, 10:311, 2000. 13

[40] J. W. J. Kerssemakers, M. E. Janson, A. van der Host, and M. Dogterom. Optical trap setup for measuring microtubule pushing forces. *Appl. Phys. Lett.*, 83(21):4441, 2003. 15, 16

[41] Y. Marcy, J. Prost, M.-F. Carlier, and C. Sykes. Forces generated during actin-based propulsion: A direct measurement by micromanipulation. *Proc. Nat. Acad. Sci. USA*, 101(16):5992, 2004. 15

[42] S. H. Parekh, O. Chaudhuri, J. A. Theriot, and D. A. Fletcher. Loading history determines the velocity of actin-network growth. *Nature Cell Biol.*, 7(12):1219, 2005. 15

[43] D. R. Kovar and T. D. Pollard. Insertional assembly of actin filament barbed ends in association with formins produces piconewton forces. *Proc. Nat. Acad. Sci. USA*, 101(41):14725, 2004. 15, 17, 27

[44] T. E. Schaus and G. G. Borisy. Performance of a population of independent filaments in lamellipodium protrusion. *Biophys. J.*, 95:1393, 2008. 19, 20, 88

[45] A. Perilli, C. Pierleoni, G. Ciccotti, and J.-P. Ryckarte. On the force-velocity relationship of a bundle of rigid bio-filaments. *J. Chem. Phys.*, 148:095101, 2018. 25, 64, 68, 81, 82, 85, 195

[46] A. Gholami, J. Wilhelm, and E. Frey. Entropic forces generated by grafted semi-flexible polymers. *Phys. Rev. E*, 144:041803, 2006. 29, 30, 37, 42, 44, 62

[47] A. Perilli, C. Pierleoni, and J.-P. Ryckaert. On the properties of a bundle of flexible actin filaments in an optical trap. *J. Chem. Phys.*, 144:245102, 2016. 30, 42, 43, 46, 50, 52, 53, 54, 55, 57, 84, 173, 190, 194

[48] J. Howard. *Mechanics of Motor Proteins and the Cytoskeleton*. Sinauer Associates, Inc, 2001. 30, 31, 32, 33, 34

[49] E. M. Lifshitz and L. D. Landau. *Theory of Elasticity*. Pergamon Press,New York, 3rd edition, 1986. 30, 32, 109, 111

[50] J. Kierfeld, K. Baczynski, P. Gutjahr, and R. Lipowsky. Semiflexible polymers and filaments: from variational problems to fluctuations. In E. García-Río O. J. Garay and R. Vásquez-Lorenzo, editors, *Curvature and Variational Modeling in Physics and Biophysics*, page 151. American Institute of Physics, 2008. 32

[51] H. Nagashima and S. Asakura. Dark-field light microscopic study of the flexibility of f-actin complexes. *J. Mol. Biol.*, 136:169, 1980. 33

[52] O. Kratky and G. Porod. Röntgenuntersuchung gelöster fadenmoleküle. *Rec. Trav. Chim. Pays-Bas.*, 68:1106, 1949. 34, 36

[53] C. Pierleoni, G. Ciccotti, and J.-P. Ryckaert. A semiflexible model for the polymerization force exerted by a living f-actin filament on a fixed wall. *J. Chem. Phys.*, 143:145101, 2015. 40, 42, 43, 44, 50, 169

[54] A. Perilli, C. Pierleoni, and J.-P. Ryckaert. Filament flexibility enhances power transduction of f-actin bundles. 2018. 40, 41, 43, 47, 48, 64, 80, 84, 86, 88, 92, 195

[55] N. J: Burroughs and D. Marenduzzo. Three-dimensional dynamic monte carlo simulations of elastic actin-like ratchets. *J. Chem. Phys.*, 123:174908, 2005. 42

[56] C. P. Brangwynne, G. H. Koenderink, E. Barry, Z. Dogic, F. C. MacKintosh, and D. A. Weitz. Bending dynamics of fluctuating biopolymers probed by automated high-resolution filament tracking. *Biophys. J.*, 93:346, 2007. 44

[57] D. T. Gillespie. Exact stochastic simulation of coupled chemical reactions. *J. Phys. Chem.*, 81(25):2340, 1977. 63, 67, 195

[58] J. R. Norris. *Markov Chains.* Cambridge University Press, 1997. 66, 67, 150

[59] H. Wang, C. Peskin, and T. Elston. A robust numerical algorithm for studying biomolecular transport processes. *J. Theor. Biol.*, 221:491, 2003. 66

[60] D. T. Gillespie. *Markov Processes: An Introduction for Physical Scientists.* Academic Press, Inc., 1992. 67, 151

[61] H. Risken. *The Fokker-Plank Equation: Methods of Solution and Applications.* Springer-Verlag, 1996. 71

[62] P. Ranjith, D. Lacoste, K. Mallik, and J.-F. Joanny. Nonequilibrium self-assembly of a filament coupled to atp/gtp hydrolysis. *Biophys. J.*, 96:2146, 2009. 79

[63] Robert B. Gennis. *Biomembranes: Molecular Structure and Function.* Springer-Verlag New York, 1989. 95

[64] J. N. Israelachvili, D. J. Mitchell, and B.W. Ninham. Theory of self-assembly of hydrocarbon amphiphiles into micelles and bilayers. *J. Chem. Soc., Faraday Trans. 2*, 72:1525, 1976. 95

[65] M. Deserno. Fluid lipid membranes: a primer. `https://www.cmu.edu/biolphys/deserno/pdf/membrane_theory.pdf`. 5, 95, 109, 111, 120

[66] M. P. Sheetz, M. Schindler, and D. E. Koppel. The lateral mobility of integral membrane proteins is increased in spherocytic erythrocytes. *Nature*, 285:510, 1980. 97

[67] H. Lodish, A. Berk, S. L. Zipursky, P. Matsudaira, D. Baltimore, and J. Darnell. *Molecular Cell Biology.* New York: W. H. Freeman, 4th edition, 2000. 97

[68] Chemistry libretext. `https://chem.libretexts.org/Textbook_Maps/Biological_Chemistry/Lipids/Applications_of_Lipids/Lipid_Bilayer_Membranes`. 97

[69] T. D. Pollard and G. G. Borisy. Cellular motility driven by assembly and disassembly of actin filaments. *Cell*, 112:453, 2003. 98

[70] T. Yeung, B. Ozdamar, P. Paroutis, and S. Grinstein. Lipid metabolism and dynamics during phagocytosis. *Curr. Opin. Cell Biol.*, 18:429, 2006. 98

[71] E. Smythe and K. R. Ayscough. Actin regulation in endocytosis. *J. Cell Sci.*, 119:4589, 2006. 98

[72] U. S. Eggert, T. J. Mitchison, and C. M. Field. Animal cytokinesis: From parts list to mechanisms. *Annu. Rev. Biochem.*, 75:543, 2006. 98

[73] L. Blanchoin, R. Boujemaa-Paterski, C. Sykes, and J. Plastino. Actin dynamics, architecture and mechanics in cell motility. *Physiol. Rev.*, 94:235, 2014. 98, 99, 100

[74] M. Ghosh, X. Song, G. Mouneimne, M. Sidani, D.S. Lawrence, and J.S. Condeelis. Cofilin promotes actin polymerization and defines the direction of cell motility. *Science*, 304:743, 2004. 98

[75] I. Ichetovkin, W. Grant, and J.S. Condeelis. Cofilin produces newly polymerized actin filaments that are preferred for dendritic nucleation by the arp2/3 complex. *Current Biology: CB*, 312:79, 2002. 98

[76] V. Achard, J.L. Martiel, A. Michelot, C. Guerin, A.c. Reymann, L. Blanchoin, and R. Boujemaa-Paterski. A “primer"-based mechanism underlies branched actin filament network formation and motility. *Curr. Biol.*, 20:423, 2010. 99

[77] M. Vinzenz, M. Nemethova, F. Schur, J. Mueller, A. Narita, E. Urban, C. Winkler, C. Schmeiser, S.A. Koestler, K. Rottner, G.P. Resch, Y. Maeda, and J.V. Small. Actin branching in the initiation and maintenance of lamellipodia. *J. Cell Sci.*, 125:2775, 2012. 99

[78] M. Prass, K. Jacobson, A. Mogilner, and M. Radmacher. Direct measurement of the lamellipodial protrusive force in a migrating cell. *J. Cell Biol.*, 174:767, 2006. 99

[79] F. Heinemann, H. Doschke, and M. Radmacher. Keratocyte lamellipodial protrusion is characterized by a concave force-velocity relation. *Proc. Nat. Acad. Sci. USA*, 101:5992, 2004. 99

[80] J. Zimmerman, C. Brunner, M. Enculescu, Goegler M., A. Ehrlicher, J. Käs, and M. Falcke. Actin filaments elasticity and retrograde flow shape the force-velocity relation of motile cells. *Biophys. J.*, 102:287, 2012. 99

[81] T.M. Svitkina, E.A. Bulanova, O.Y. Chaga, D.M. Vignjevic, S. Kojima, J.M. Vasiliev, and G.G. Borisy. Mechanism of filopodia initiation by reorganization of a dendritic network. *J. Cell Biol.*, 160:409, 2003. 99, 100

[82] S. Wong, W.H. Guo, and Y.L. Wang. Fibroblasts probe substrate rigidity with filopodia extensions before occupying an area. *Proc. Nat. Acad. Sci. USA*, 111:17176, 2014. 100

[83] P. K. Mattila and P. Lappalainen. Filopodia: molecular architecture and cellular functions. *Nature reviews*, 9:446, 2008. 100

[84] A. P. Liu, D. L. Richmond, L. Maibaum, S. Pronk, P. L. Geissler, and D. A. Fletcher. Membrane-induced bundling of actin filaments. *Nature Physics*, 4:789, 2008. 100, 101

[85] P. Beli, D. Mascheroni, D. Xu, and M. Innocenti. Wave and arp2/3 jointly inhibit filopodium formation by entering into a complex with mdia2. *Nat. Cell Biol.*, 10:849, 2008. 100

[86] A. Steffen, J. Faix, G.P. Resch, J. Linkner, J. Wehland, J.V. Small, K. Rottner, and T.E. Stradal. Filopodia formation in the absence of functional wave- and arp2/3- complexes. *Mol. Biol. of the Cell*, 17:2581, 2006. 100

[87] G. Koster, A. Cacciuto, I. Derényi, D. Frenkel, and M. Dogterom. Force barriers for membrane tube formation. *Phys. Rev. Lett.*, 94:068101, 2005. 100, 117

[88] N.J. Burroughs and D. Marenduzzo. Growth of a semi-flexible polymer close to a fluctuating obstacle: application to cytoskeletal actin fibres and testing of ratchet models. *J. Phys.: Condens. Matter*, 18:S357, 2006. 100, 194

[89] R. K. Sadhu and S. Chatterjee. Actin filaments growing against an elastic membrane: Effect of membrane tension. *Phys. Rev. E*, 97:032408, 2018. 100

[90] D. Raucher and M. P. Sheetz. Cell spreading and lamellipodial extension rate is regulated by membrane tension. *J. Cell. Biol.*, 148:127, 2000. 100

[91] J. Y. Shao and F. M. Hochmuth. Micropipette suction for measuring piconewton forces of adhesion and tether formation from neutrophil membranes. *Biophys. J.*, 71:2892, 1996. 102

[92] S. A. Socolofsky and G. H. Jirka. Advective diffusion equation. `https://ceprofs.civil.tamu.edu/ssocolofsky/cven489/downloads/book/ch2.pdf`. 103

[93] J. L. McGrath, Y. Tandy, C. F. Dewey, J. J. Meister, and J. H. Hartwig. Simultaneous measurements of actin filament turnover, filament fraction, and monomer diffusion in endothelial cells. *Biophys. J.*, 75:2070, 1998. 103

[94] M. Deserno. *Membrane elasticity and mediated interactions in continuum theory: a differential geometric approach,* In: Jue, Th. and Risbud, S. H. and Longo, M. L. and Faller, S. (Eds.), *Biomembrane Frontiers: Nanostructures, Models, and the Design of Life*, pages 41–74. Springer, 2009. 107, 108, 109, 110, 111, 115

[95] O. Farago and P. Pincus. Statistical mechanics of bilayer membrane with a fixed projected area. *J. Chem. Phys.*, 120:2934, 2004. 5, 107, 108, 118, 121, 123, 124, 134, 147, 197

[96] U. Seifert and R. Lipowsky. *Morphology of Vesicles,* In: Lipowsky, R. and Sackmann E. (Eds.), *Structure and Dynamics of Membranes. From Cells to Vesicles*, volume 1A, pages 403–460. Elsevier, 1995. 108

[97] E. Evansand and D. Needham. Physical properties of surfactant bilayer membranes: Thermal transitions, elasticity, rigidity, cohesion, and colloidal interactions. *J. Phys. Chem*, 91:4219, 1987. 108

[98] Stress-strain material laws. `https://www.colorado.edu/engineering/CAS/courses.d/Structures.d/IAST.Lect05.d/IAST.Lect05.pdf`. 110

[99] D. Bochicchio and L. Monticelli. *The membrane bending modulus in experiments and simulations: a puzzling picture,* In: I. Iglič, M. Rappolt, and García Sáez, A. (Ed.s), *Biomembranes and lipid self-assembly*, volume 23, page 117. Elsevier Inc., 2016. 111

[100] M. Deserno. Notes on differential geometry with special emphasis on surfaces in $\mathbb{R}^3$. `https://www.cmu.edu/biolphys/deserno/pdf/diff_geom.pdf`. 112, 113, 115, 117

[101] M. Deserno. Fluid lipid membranes: From differential geometry to curvature stresses. *Chemistry and Physics of Lipids*, 185:11, 2015. 115

[102] R. A. Sharipov. *Course of Differential Geometry.* Publ. of Bashkir State University - Ufa, 1996. 115

[103] P. B. Canham. The minimum energy of bending as a possible explanation of the biconcave shape of the human red blood cell. *J. Theoret. Biol.*, 26:61, 1970. 117

[104] E. Kreyszig. *Differential Geometry.* Dover, New York, 1991. 117

[105] E. Atilgan, D. Wirtz, and S.X. Sun. Mechanics and dynamics of actin-driven thin membrane protrusions. *Biophys. J.*, 90:65, 2006. 5, 118, 197

[106] O. Edholm. *Time and Length Scales in Lipid Bilayer Simulations,* In: Feller, S.E. (Ed.), *Computer modelling of membrane bilayers*, volume 60, page 91. Elsevier Inc., 2008. 120

[107] J. S. Rowlinson. A drop of liquid. *J. Phys.: Condens. Matter*, 6:A1, 1994. 124

[108] Y. Kantor. *Properties of tethered surfaces,* In: Nelson, D. and Piran, T. and Weinberg, S. (Eds.), *Statistical Mechanics of Membranes and Surfaces*, chapter 12, page 111. World Scientific Publishing Co. Pte. Ltd., 2004. 125, 127

[109] H. Noguchi and G. Gompper. Dynamics of fluid vesicles in shear flow: Effect of membrane viscosity and thermal fluctuations. *Phys. Rev. E*, 72:011901, 2005. 127

[110] A. Guckenberger, M. P. Schrame, P. G. Chen, M. Leonetti, and S. Gekle. On the bending algorithms for soft objects in flows. *Computer Phys. Comm.*, 207:1, 2016. 129

[111] E. Vanden-Eijnden and G. Ciccotti. Second-order integrators for langevin equations with holonomic constraints. *Chem. Phys. Lett.*, 429:310, 2006. 125, 130, 149, 184, 189, 196

[112] F. Schmid. Fluctuations in lipid bilayers: are they understood? *Biophysical Reviews and Letters*, 8(01n02):1, 2013. 135

[113] E.G. Brandt, A.R. Braun, J.N. Sachs, J.F. Nagle, and O. Edholm. Interpretation of fluctuation spectra in lipid bilayer simulations. *Biophys. J.*, 100:2104, 2011. 135, 139, 140

[114] A.P. Thompson, S.J. Plimpton, and W. Mattson. General formulation of pressure and stress tensor for arbitrary many-body interaction potentials under periodic boundary conditions. *J. Chem. Phys.*, 131:154107, 2009. 137, 139

[115] D. Frenkel and B. Smit. *Understanding Molecular Simulation: From Algorithms to Applications*. Academic Press, San Diego, 2002. 142

[116] T.A. Hunt, S. Mogurampelly, G. Ciccotti, C. Pierleoni, and J.-P. Ryckaert. Particle-based modeling of living actin filaments in an optical trap. *Polymers*, 8:343, 2016. 150, 152, 158, 159, 160, 189, 190, 191, 194

[117] S. Ramachandran and J.P. Ryckaert. Compressive force generation by a bundle of living biofilaments. *J. Chem. Phys.*, 139:064902, 2013. 167

[118] L. T. Hill. *An Introduction to Statistical Thermodynamics*. Dover Publications, Inc., New York, 1986. 169